BALLISTIC AND DIFFUSIVE TRANSPORT OF ACOUSTIC WAVES IN RANDOM MEDIA

BY

HENRY P. SCHRIEMER

A Thesis
Submitted to the Faculty of Graduate Studies
in Partial Fulfillment of the Requirements
for the Degree of

DOCTOR OF PHILOSOPHY

Department of Physics
University of Manitoba
Winnipeg, Manitoba

THE UNIVERSITY OF MANITOBA

FACULTY OF GRADUATE STUDIES

COPYRIGHT PERMISSION

BALLISTIC AND DIFFUSIVE TRANSPORT OF ACOUSTIC WAVES IN RANDOM MEDIA

by

HENRY P. SCHRIEMER

A Thesis submitted to the Faculty of Graduate Studies of the University of Manitoba in partial fulfillment of the requirements of the degree of

DOCTOR OF PHILOSOPHY

Acknowledgments

I am deeply grateful for the support and encouragement I have received during the course of my graduate studies. My deepest thanks, and love, are extended to my wife and children, who endured my absence for many evenings and Saturdays, especially this past year. Nancy, your love and encouragement have made this thesis possible. My deepest respect and appreciation are extended to my supervisor, John Page. His patient guidance and support have been unstinting these past many years. It has been said that many graduate students end up becoming like their supervisors; I can think of no higher honour. My advisory committee also deserves thanks for their guidance and instruction. Heartfelt thanks are also due my parents, for reasons too innumerable to mention, and to Nancy's parents (for the obvious reason).

Many other people deserve acknowledgment for their influence and contributions over the years. To my predecessor in the lab, Norbert Pachet, for his warning and for not saying "I told you so!", and to the irreplaceable Gilles Roy, for the technical advice and instruction (and the "lost" equipment). I am indebted to Xiadun Jing for providing the computer code used in the determination of the density of states, and to Michael Cowan for recompiling the program to run at the University of Manitoba. I am also indebted to A. E. Bailey for writing the original software necessary to remotely control the automated translation stages and the digitizing oscilloscope. My coworkers Ian Jones, Michael Cowan, and Kristen Beaty have my thanks for their assistance with portions of the data collection and analysis when this project grew completely out of control: Mike and Kristen for some of the phase and group velocity measurements, and Ian for extracting phase and

amplitude data from measurements of the field. A final thanks to Mike for his efforts this past year while I was at Queen's. Thanks are also extended to the co-authors of my various publications, in particular Ping Sheng and David Weitz, for their efforts and insight. Financial support from the University of Manitoba and from John Page is gratefully acknowledged.

I thank the LORD GOD, who in His Son Jesus Christ has blessed my life, for the opportunity to glorify His Name by the study of His creation.

The heavens declare the glory of God;
the skies proclaim the work of His hands.
Day after day they pour forth speech;
night after night they display knowledge.
There is no speech or language where their voice is not heard.
Their voice goes out into all the earth,
their words to the ends of the world.

Psalm 19:1–4a (NIV)

Abstract

The transport of ultrasonic waves through a resonantly scattering inhomogeneous medium, composed of randomly close-packed glass beads immersed in water, is investigated in the normalized intermediate frequency range $1 < k_w a < 10$, where k_w is the ultrasonic wave vector in water and a is the bead radius. Short pulses propagating ballistically retain coherence with their incident pulses, enabling the small ballistic component to be extracted from the much larger scattered signals, and allowing the scattering mean free path, the phase velocity and the group velocity to be measured. An effective medium model which goes beyond the limitations of the coherent potential approximation is used to interpret the experimental results. This model shows that the minima in the scattering mean free path can be identified with resonances in the total scattering cross section of a coated elastic sphere embedded in a homogeneous effective medium. These resonances also result in considerable frequency dispersion and a substantial reduction in the phase and group velocities. The theoretical model provides an excellent description of the velocities, and resolves a long-standing problem in the definition of the group velocity in strongly scattering media.

The application of the diffusion approximation to the transport of multiply scattered sound is critically tested. For short incident pulses and various experimental geometries, the time dependence of the ensemble-averaged transmitted intensity is shown to be well-described by the diffusion equation. This has permitted the measurement of the diffusion coefficient and the absorption time from these dynamic measurements. Static continuous-wave measurements of the absolute transmitted intensity were performed as a

function of sample thickness to determine the values of the transport mean free path. From these experimental results, the energy velocity of the diffusing waves was determined. The energy velocity was found to be similar in magnitude and frequency dependence to the group velocity; furthermore, it is accurately described by extending the same effective medium model, originally developed for ballistic propagation, to account for the angular dependence of the scattering delay experienced by a wave pulse. These results lead to a unified physical picture of energy transport by ballistic and diffusive waves in strongly scattering media.

Table of Contents

List of Figures

List of Tables

1 Introduction

Until almost the middle part of this century, the study of wave propagation was generally confined to "ideal" media: substances that could either be considered homogeneous at the length scale studied, or evidenced a regular periodicity. This was characteristic of the field of condensed matter as a whole. Media that departed in any way from the ideal were considered to be "dirty" or "full of junk" (Fisher *et al.*, 1988). The reigning paradigm held the investigation of such "disordered" systems to be unwarranted, partially due to the assumed intractability of such systems, and perhaps because of the wealth of information yet to be gleaned from ordered systems. This mindset was altered with the realization that random systems are ubiquitous, and that a physical understanding of such is necessary to comprehend and exploit diverse phenomena (Elliot *et al.*, 1974). The investigation of wave transport through random systems developed as a natural outgrowth from the study of particle scattering by a distribution of scatterers (Lax, 1951, and references therein). Since then, it has become a problem of considerable importance to many areas of physics, particularly when the random media are strongly scattering (Sheng, 1990, 1995).

Progress in physics is typically predicated in a reductionist manner, often explained as being able to ask the right questions. An understanding of the fundamentals of wave transport in strongly scattering media thus devolves into a proper conception of the wave itself, and its relation to the medium of propagation. At its simplest, a wave may be regarded as a propagating disturbance. Leonardo da Vinci explained the behaviour of a wave passing through a medium by likening it to the effect of wind on a field of grain; the

grain remains in place, but the wave (or disturbance) runs across the field. This analogy was borrowed by Einstein and Infeld (1961) for their introduction to basic wave phenomena, and they emphasized that it is not the motion of the medium that is to be considered, but rather the energy propagated through the medium. The fundamental problem of wave transport is thus reduced to the question of how energy propagates.

Broadly speaking, the energy transport may be described as ballistic, where the wave travels straight through the medium, or diffusive, where it covers a distribution of scattering paths. Ballistic propagation is temporally *coherent*, which means that at each time there exists a definite phase relation to the incident wave. By contrast, diffusely transported waves bear no definite phase relation to the incident wave because they are a *superposition* of waves that have traveled different scattering paths. The distinction between these two types of propagation may be illustrated by two common examples of acoustic wave transport. The sound that we hear propagates ballistically, and the phase of the waves plays a critical role in enabling us to distinguish between the different tones of musical instruments. Heat, on the other hand, is sound that propagates diffusively, and we are sensitive only to its intensity, the phase playing no role whatsoever. The parameters that characterize these different types of energy transport depend on the relation between the wave and the random medium through which it propagates.

Random media may generally be described as multicomponent systems assembled in a disordered manner, the simplest of which consists of random scattering inclusions in a host medium. The relation of the wave to the aggregate is governed by the length scale of the scatterers as compared to the wavelength, and by the density of scatterers. At high frequencies, where the wavelengths are small compared to the size of the scatterers, the

propagation in each constituent is essentially governed by the characteristics of that medium. By contrast, at low frequencies the wavelengths are large compared to the size of the scatterers, and the propagation is characterized by a simple average of the material properties; this is the basis of the elementary "effective medium" theories. Wave propagation is generally well-understood at these extremes. However, fundamental questions remain in the "intermediate frequency regime," where the wavelengths are comparable to the size of the scatterers.

Much of the recent progress in understanding the wave transport in this regime has been achieved using electromagnetic waves, such as light (Sheng, 1990). The Amsterdam group, in particular, has addressed very important questions regarding the transport velocities (van Albada *et al.*, 1991). The excitation of internal modes and the concomitant strong resonant scattering greatly attenuates propagating waves, even in the absence of absorption. Their calculations have demonstrated that the correspondingly large dispersion leads to unphysical values of the group velocity, supporting the ideas of Sommerfeld (1914) and Brillouin (1953, 1960) that the group velocity completely loses its meaning in these circumstances. One of the major goals of this thesis is an experimental investigation of this question, and the application of a new theoretical model to predict the coherent transport (Page *et al.*, 1996).

The successful application of the diffusion approximation, in the description of the multiple scattering of light, has formed the basis for interpreting such diverse phenomena as enhanced backscattering (van Albada and Lagendijk, 1985), and frequency (Drake and Genack, 1989) and temporal correlations of the intensity (Maret and Wolf, 1987; Pine *et al.*, 1988). As the essential physics of the diffusion approximation is general to all types of

classical waves, it should apply equally well to the description of the propagation of acoustic waves. This is of some significance, as many materials of technological importance scatter sound quite strongly. Furthermore, the underlying physics of diffusing sound may be considerably richer, given the possibility of exciting transverse and surface vibrational modes in solid scatterers (Jing *et al.*, 1991, 1992). However, to date, there have been few detailed investigations of the applicability of the diffusion approximation to the description of sound propagation through strongly scattering media (Bayer and Niederdrank, 1993; Weaver and Sachse, 1993). The second major concern of this thesis exploits the considerable knowledge of diffusive propagation gained from the study of light to critically test the applicability of the full diffusion treatment to sound (Page *et al.*, 1995); the key parameters essential for its application are measured (Schriemer *et al.*, 1997).

Underlying the two major concerns of this thesis is the relationship between the energy transport velocities in the ballistic and diffusive regimes. The ballistic and diffusive transport of acoustic waves is investigated by studying the propagation of ultrasonic waves through randomly close-packed glass beads in water. The large acoustic impedance mismatch between glass and water ensures strong scattering, significantly higher than the best index mismatches achieved for light scattering experiments. The scattering was further enhanced by choosing the glass bead radius a to be the same order of magnitude as the acoustic wavelength in water. This allowed the wave transport to be studied in the intermediate frequency regime, for normalized frequencies $1 < k_w a < 10$, where k_w is the ultrasonic wave vector in water.

The structural organization of the thesis is now presented. The main body of the thesis begins in chapter 2, where the theoretical basis for the prediction of the wave transport is delineated. Sec. 2.1 introduces the Green's function approach to the description of coherent transport, and explains the new effective medium model used to interpret the data and its application to the scattering model employed. Sec. 2.2 discusses the diffusive transport, beginning by analogy with the random walk; the diffusion equation is then constructed from the more general transfer equation, and both time dependent and steady state solutions derived after a careful consideration of the appropriate boundary conditions. This allows the determination of the diffusion parameters through fits to experimental data; predictions of these parameters are achieved using the new effective medium model, thus relating the coherent and diffusive transport mechanisms. Chapter 3 discusses the physical rationale for the particular samples studied, the sample preparation, and details of the material properties for the sample constituents. The experiment is presented in chapter 4, beginning with a discussion of the generation and detection of ultrasonic waves. A description of the measurement technique and a discussion of the various experimental geometries follows, and the chapter concludes with a presentation of the experimental setup and apparatus. The experimental results, with their theoretical predictions, are given in chapter 5. The main components of this chapter are the coherent transmission (Sec. 5.2) and the diffusive transmission (Sec. 5.5); the latter treats both dynamic and static measurements of the multiply scattered sound, and closes with a discussion of the frequency dependence of the diffusion parameters and the relation of the transport velocities. The main body of the thesis concludes with chapter 6, where the

central findings are summarized. Note should be taken of the extra material presented in the three appendices.

2 Theory

2.1 Coherent Propagation

2.1.1 Introduction

We now concern ourselves with a theoretical formulation for the description of the propagation of the coherent component of the transmitted sound pulse in a resonantly-scattering inhomogeneous medium. For the purpose of clarity, and to avoid any possible misapprehensions, it is wise to be rather explicit as to what is meant by the term *coherent pulse*. Following the generally accepted terminology (Lax, 1951), the coherent pulse is that which bears a definite phase relation to, and hence can be made to interfere with, the incident pulse. The coherent, or *ballistic*, pulse thus consists of both the unscattered and forward scattered components of the wave pulse.

A description of the transport characteristics of the ballistic pulse is given in this section. The Green's function formalism is first presented in the context of acoustic wave propagation in an arbitrary medium. The Green's function for waves in a uniform medium is then given in order to illustrate the physical interpretation of the Green's function. This is followed by the general Green's function formulation of the scattering problem. A model description of the scattering medium is presented at this point in order to simplify subsequent discussions. The effective medium is discussed, and the extension of the well-known coherent potential approximation (CPA) to the intermediate frequency regime is illustrated, for the case of the scalar wave equation. A quantitative approach is then

developed using the full elastic wave equation, and the derivation of the Green's function solutions described. Finally, the application of the resultant Green's function to the description of the propagation of the ballistic pulse is shown, in particular, for the derivation of the *density of states* (DOS), and hence the determination of the dispersion relation (Jing *et al.*, 1991, 1992; Sheng, 1995).

2.1.2 The Green's function: an introduction

For sound of a given angular frequency ω in a three-dimensional medium described by position vector r, the acoustic wave equation can be put in the form

$$\left(\nabla^2 + \kappa^2(r)\right)\phi(r) = 0, \tag{2.1}$$

where $\phi(r)$ is the wave amplitude function, and $\kappa(r)$ a wave vector that, in general, incorporates the effect of disorder in the medium. The Green's function G of the system is an exact solution to the wave equation with a specific initial source and boundary condition. The attractiveness of the Green's function is that its analysis can be easily interpreted physically.

We take the system to be excited, at time $t = 0$, by a delta function pulse localized at $r = r'$, where r' denotes the source position. The reason for considering such a source is that it can excite the natural resonances of *all* temporal and spatial frequencies in the system. This implies that a useful approach for analyzing the Green's function is through its frequency components. The wave equation for the frequency component ω, written in terms of the Green's function in the frequency and spatial domain, is then of the form (Sheng, 1995)

$$\left(\nabla^2 + \kappa^2(\omega, r)\right) G(\omega, r, r') = \delta(r - r'). \tag{2.2}$$

In addition to equation (2.2), a unique determination of the Green's function requires the specification of the boundary conditions, and the imposition of causality.

The propagation of an acoustic wave in a disordered medium being governed by the wave equation, a complete solution of this wave equation is represented by the knowledge of the Green's function G, for all frequencies and positions. However, it is not, in general, possible to accurately determine the Green's function in the presence of disorder. Moreover, even if this *were* possible, the problem would then arise as to how to extract useful information from G. This may be illustrated by analogy with the classical random walker. The specific path traversed by an acoustic wave through a *particular* arrangement of scattering sites (i.e. a particular sample) may be approximated by a random walk. The complete solution of the random walk problem requires the knowledge of the position of the random walker at every instant of time. This is equivalent to the knowledge of the Green's function for the wave equation. However, the ability to depict a *particular* path is not necessary in order to describe the *generic* behaviour of the propagation in statistically independent samples (i.e. samples with a different internal arrangement of glass beads, but identical occupied volume fractions). The customary means of describing the solution to the random walk problem is thus to determine the *probability* of traversing a path of length r between two points. This brings out the statistical character of the propagation, which experimentally is brought out by averaging over different random walk trajectories, that is, by performing an ensemble average of the intensity. Employing the ergodic hypothesis, this is analogous to the determination of the

configurational average $\langle r \rangle$, which for the random walk problem is equal to zero. Similarly, for the wave problem our objective must be the evaluation of $\langle G \rangle$. We note that, since the Green's function describes the amplitude of the excitation, a true propagating mode will manifest itself as a singularity in the wave vector representation of the Green's function. The effect of the disorder, in general, means that the configurationally-averaged Green's function will exhibit a peak, rather than a singularity. Since $\langle G \rangle$ does not depend on the local nature of the disorder, only the statistical properties of the disorder are relevant. The Green's function may be viewed as the field solution, in the forward direction, to the wave equation. The peaks of $\langle G \rangle$ exhibit an exponential decay due to the scattering out of the forward direction, which implies that the wave coherence, in the sense of a unique propagation direction and phase relation, is lost. This defines a decay length which may be identified with the scattering mean free path. The character of the coherent part of the wave propagation is thus given by $\langle G \rangle$.

2.1.3 Interpretation of the Green's function: the uniform medium

For *disordered* systems, the position of the source point is an important parameter for the Green's function since the response of the system will depend on it. In the case of a uniform medium, where $\kappa(\omega, r) = \kappa_0$, the response of the system is independent of the source position, and the Green's function depends only on the relative separation $r - r'$ between the source and the detector. Equation (2.2) may then be written as

$$\left(\nabla^2 + \kappa_0^2\right) G_0(\omega, r - r') = \delta(r - r'), \tag{2.3}$$

where G_0 is the Green's function for the uniform medium. The simplest way to determine G_0 is to write both the Green's function and the delta function in terms of their Fourier transforms to the wave vector representation. Substituting these into equation (2.3) and solving for $G_0(\omega, k)$ yields

$$G_0(\omega, k) = \frac{1}{\kappa_0^2(\omega) - k^2} \frac{N}{L^3}, \tag{2.4}$$

where L^3 is the sample volume, and N is the number of states in the sample (Sheng, 1995). The Green's function $G_0(\omega, k)$ gives the response of the uniform medium to a source excitation that has angular frequency ω and wave vector k. If this excitation is coincident with the wave dispersion relation, that is, if $k^2 = \kappa_0^2(\omega)$, then G_0 diverges. This divergence is expected since the dispersion relation is essentially the condition of natural resonance of the system; it describes the propagating modes. Note that even if the source frequency and wave vector do not coincide with any natural mode of the system, equation (2.4) indicates that many modes can be excited just by proximity to the resonance condition.

The divergence in the wave-vector-space Green's function poses difficulties when one wishes to Fourier transform back to the real-space Green's function. To avoid this problem, it is customary to add a small positive imaginary constant to the denominator of equation (2.4), and then to take the limit as this constant approaches zero. The result is (Merzbacher, 1970; Sheng, 1995)

$$\frac{L^3}{N} G_0(\omega, k) = \lim_{\eta \to 0} \frac{1}{\kappa_0^2(\omega) - k^2 + i\eta}$$

$$= \mathrm{P} \frac{1}{\kappa_0^2(\omega) - k^2} - i\pi\delta\left(\kappa_0^2(\omega) - k^2\right), \qquad (2.5)$$

where P denotes the Cauchy principle value, and the choice of η as positive (required by causality) implies that the real-space Green's function

$$G_0(\omega, r - r') = -\frac{\exp\left(i\kappa_0 |r - r'|\right)}{4\pi |r - r'|}, \qquad (2.6)$$

represents an outgoing spherical wave. In the time domain (Fourier transforming with respect to frequency), causality implies that $G_0 = 0$ for $t < 0$; thus G_0 is usually denoted the retarded Green's function.

The delta function in the imaginary part of the Green's function, equation (2.5), exactly picks out the modes of the system. The *number* of modes per unit frequency range and per unit volume is called the *density of states* (DOS) and is given by (Ashcroft and Mermin, 1976)

$$DOS(\omega) = \int \frac{dk}{(2\pi)^3} \delta\left(\omega_0 - \omega(k)\right). \qquad (2.7)$$

Writing the delta function in equation (2.7) in the wave vector representation, as in equation (2.5), yields

$$DOS(\omega) = \frac{2\omega}{v_0^2} \int \frac{dk}{(2\pi)^3} \delta\left(\kappa_0^2(\omega) - k^2\right), \qquad (2.8)$$

where v_0 is the phase velocity in the uniform medium, and we have used the general dispersion relation, $\omega = v_0\kappa$, and the properties of the delta function (Merzbacher, 1970)

in the conversion of the delta function from the frequency to the wave vector representation. Using equation (2.5), the integral in equation (2.8) may be re-expressed as

$$\int \frac{dk}{(2\pi)^3}\delta\left(\kappa_0^2(\omega)-k^2\right)=-\frac{1}{\pi}\frac{L^3}{N}\int \frac{dk}{(2\pi)^3}\mathrm{Im}\,G_0(\omega,k)$$

$$=-\frac{1}{\pi}\mathrm{Im}\,G_0(\omega,r=r'), \tag{2.9}$$

where Im implies taking the imaginary part of G_0, and the last equality follows from treating the preceding integral as the Fourier transform of G_0 with the phase factor $e^{ik\cdot(r-r')}$ set equal to unity (i.e., $r=r'$). The density of states, equation (2.8), may then be written, using equation (2.9), as

$$DOS(\omega)=-\frac{2\omega}{v_0^2}\left(\frac{1}{\pi}\mathrm{Im}\,G_0(\omega,r=r')\right). \tag{2.10}$$

This formula is also valid for waves in random media (Sheng, 1995). Hence, in the general case, the *local* density of states at r is

$$DOS(\omega,r)=-\frac{2\omega}{v_0^2}\left(\frac{1}{\pi}\mathrm{Im}\,G(\omega,r=r')\right). \tag{2.11}$$

The reason the density of states can always be obtained in this manner is due to the divergent behaviour of the Green's functions at the resonant modes of the system. The negative imaginary part of the Green's function allows these modes to be identified as seen from equation (2.5).

2.1.4 The single coated-sphere model

In this thesis, the scattering medium investigated is composed of randomly close-packed glass beads immersed in water, which may be considered as the limiting case of randomly dispersed spheres in a fluid, with volume fraction Φ (Jing *et al.*, 1992). The *single coated-sphere model* consists of the simplest possible basic scattering unit, which takes into account only the strong short-range correlation between the solid and liquid phases. This model considers each solid sphere of radius a to be enveloped by a liquid coating of thickness $(b - a)$ [see figure 2.1(a)], whence the volume fraction of the solid phase, $\Phi = a^3/b^3$, determines the thickness of the coating. The effective macroscopic properties of the system are calculated by embedding this coated sphere in a homogeneous effective medium [see figure 2.1(b)], consisting of similar coated spheres, educed by some self-consistent condition *vis-à-vis* the single scattering unit. This self-consistent condition

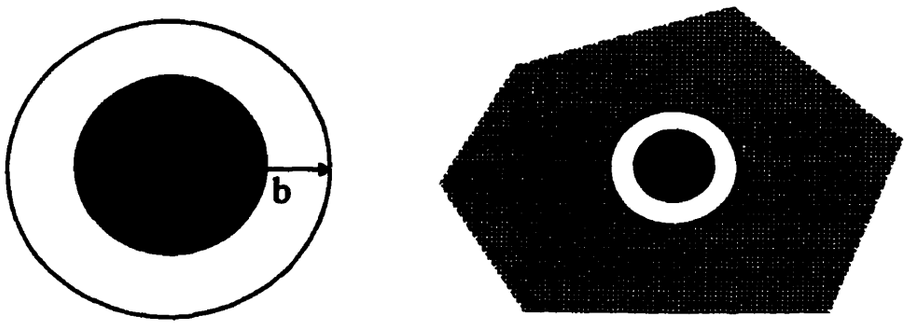

(a) (b)

Figure 2.1 (a) Fundamental scattering unit represented as a coated sphere; (b) scattering unit embedded in a uniform effective medium.

may be thought of as the requirement that, *on average*, there should be little difference in the scattering as the result of the local replacement of the effective medium by the actual medium (Economou and Soukoulis, 1990) (cf. Sec. 2.2.4).

2.1.5 The Green's function and the scattering medium

The treatment of the Green's function in the presence of disorder, within the effective medium approach, has been outlined by Jing *et al.* (1991, 1992). They have described a general Green's function formalism as part of their approach in identifying the quasimodes in colloidal suspensions of solid spheres. The difference between the colloidal suspension and the random close-packing of solid spheres being one of degree, and not kind, their approach is thus applicable to the discussions at hand. A more formal, and complete, treatment of the subject may be found in an excellent monograph written by Sheng (1995). Other useful references are the book by Economou (1983) on Green's functions, and the review by Elliot *et al.* (1974) of the early CPA work in disordered systems.

We wish to derive the Green's function that describes the coherent propagation of acoustic pulses in an effective medium. Our scattering medium, within the single coated-sphere approximation, has certain properties that need to be determined by some self-consistent condition. The means whereby these properties may be inferred is the subject of the next section. Our model, however, indicates the major steps that must be taken before this self-consistent condition may be applied. The first step is to calculate the

Green's function for the single scattering unit, and the second is to evaluate the net effect of the multiple scattering from the surrounding medium.

Let G_0 denote the Green's function for the *homogeneous* effective medium, and $G^{(s)}$ the exact Green's function for a *single* scattering unit embedded in the effective medium. It is convenient to consider the medium (i.e. the solid sphere, the fluid coating, and its surroundings) as consisting of minute volume elements identified in some unique fashion, such as sequentially by index number. Each volume element is assumed to wholly reside within either the solid sphere, the fluid, or the effective medium. Since any particular position vector $\boldsymbol{r}$ will locate one volume element or another, it may be associated with the volume element's unique identifier, or index. Then the Green's function $G_0(\omega, \boldsymbol{r}, \boldsymbol{r}')$ has two indices, one associated with $\boldsymbol{r}$ and the other with $\boldsymbol{r}'$. Thus G_0, and $G^{(s)}$, may be regarded as a matrix, or operator. To represent a single scattering, the scattering unit (*not* the infinitesimal volume element) located at $\boldsymbol{r}_j$ is described by a potential operator $U_j^{(s)}$. This is a diagonal operator representing the deviation of the wave vector from that of the homogeneous background. Then $G^{(s)}$ may be written as

$$G^{(s)} = G_0 + G_0 \, U_j^{(s)} \, G^{(s)} \tag{2.12}$$

(Sheng, 1995), where the superscript "s" is meant to emphasize that the operator refers to only a single scattering unit. Note that in the operator notation, equation (2.12) is valid regardless of whether the operators are still in real space or in the wave vector space representation.

An alternative way to express equation (2.12) is obtained by successively substituting $G^{(s)}$ into itself:

$$G^{(s)} = G_0 + G_0\, U_j^{(s)}\left[G_0 + G_0\, U_j^{(s)}\left(G_0 + G_0\, U_j^{(s)}\cdots\right]\right.$$

$$= G_0 + G_0\, U_j^{(s)} G_0 + G_0\, U_j^{(s)}\, G_0\, U_j^{(s)}\, G_0 + \cdots, \qquad (2.13)$$

which may be written as

$$G^{(s)} = G_0 + G_0\, T_j^{(s)}\, G_0, \qquad (2.14)$$

where $$T_j^{(s)} = U_j^{(s)} + U_j^{(s)}\, G_0\, U_j^{(s)} + U_j^{(s)}\, G_0\, U_j^{(s)}\, G_0\, U_j^{(s)} + \cdots \qquad (2.15a)$$

or $$T_j^{(s)} = U_j^{(s)}\left(1 - G_0\, U_j^{(s)}\right)^{-1}. \qquad (2.15b)$$

Equation (2.15a) shows that if each $U_j^{(s)}$ represents *one* scattering, then $T_j^{(s)}$ must denote the exact total scattering operator of the scattering unit and will include all the scattering inside the unit as well as the scattering *from* the medium outside. The operator $T_j^{(s)}$ may then be thought of as effectively including all the multiple scatterings.

For N identical scattering units centred at $\mathbf{r}_1, \mathbf{r}_2, \ldots, \mathbf{r}_N$, the *exact* Green's function of the *system*, denoted by G, satisfies equation (2.14), but with a total scattering operator for the whole system:

$$G = G_0 + G_0\, T\, G_0. \qquad (2.16)$$

We may also write G as

$$G = G_0 + G_0\, U\, G \qquad (2.17)$$

by defining a potential operator U for the system. From equation (2.15b), the relationship between the total scattering operator and the potential operator for the system is

$$T = U\left(1 - G_0\, U\right)^{-1} = \left(1 - U\, G_0\right)^{-1} U. \qquad (2.18)$$

Equation (2.18) allows us to reexpress this relationship as

$$U = T(1 + G_0 T)^{-1}. \tag{2.19}$$

It will prove useful to express equation (2.17) in a slightly different fashion. Writing it as $(1 - G_0 U)G = G_0$, taking the inverse of both sides, and then multiplying on the right by $(1 - G_0 U)$ yields

$$G^{-1} = G_0^{-1} - U. \tag{2.20}$$

The Green's function G describes the *local* character of the propagation. The statistical behaviour is provided by its configurational average. From equation (2.16), the relation between the configurationally averaged operators $\langle G \rangle$ and $\langle T \rangle$ is given by

$$\langle G \rangle = G_0 + G_0 \langle T \rangle G_0, \tag{2.21}$$

where G_0, being independent of the disorder, is not affected by the average. Using the configurationally averaged form of equation (2.20) then allows the definition of a *self-energy* operator Σ by what is known as the Dyson equation (Sheng, 1995):

$$\langle G \rangle^{-1} = G_0^{-1} - \frac{L^3}{N}\Sigma. \tag{2.22}$$

From equations (2.19), (2.20), and (2.22), the self-energy operator is related to the configurationally averaged total scattering operator for the system by

$$\Sigma = n_s \langle T \rangle (1 + G_0 \langle T \rangle)^{-1}, \tag{2.23}$$

where $n_s = N/L^3$ is the number density of the identical scattering units.

The glass beads used in this study are *elastic* solids, and thus support both compressional and transverse modes of vibration. The full elastic wave equation is thus needed to describe the wave excitation inside these solid spheres, and it may also be used to describe the propagation in the medium as a whole (cf. Sec. 2.1.7). Before proceeding

to a description of the formal Green's function solution of this equation [equation (2.39)], from which we may determine the propagation characteristics of the ballistic pulse, we will first illustrate the self-consistent condition that must be applied to give an effective medium. We show how such a condition is achieved within the coherent potential approximation (CPA), where, for simplicity, the scalar wave is used as an example. The inherent limitations of the CPA are overcome by extending it to the intermediate frequency regime through a reformulation of the approach.

2.1.6 The scalar wave equation

2.1.6.1 The effective medium

To efficiently illustrate the manner in which the effective medium must be treated in order to extract the desired information, we begin with the scalar wave equation:

$$\frac{\partial^2 \phi}{\partial t^2} - v^2(r)\nabla^2\phi = 0, \tag{2.24}$$

where ϕ denotes the wave amplitude function $\exp[-i(\omega t - k \cdot r)]$ and $v(r)$ is the local phase velocity, defined by the material parameters at position r. In a uniform isotropic medium, the propagation of both longitudinal and transverse acoustic waves can each be described by a scalar wave equation (with different velocities) because the different modes of vibration are decoupled from each other. This is not true in a disordered medium because the different modes are coupled at the scattering interfaces, implying that mode conversion may occur. Despite this, much of the basic characteristics of the propagation are still qualitatively captured by the scalar wave equation.

Removing the temporal dependence in equation (2.24) yields the time-independent scalar wave equation

$$\left(\nabla^2+\frac{\omega^2}{v^2(r)}\right)\phi=0, \tag{2.25}$$

as is given in equation (2.1), with $\kappa^2=\omega^2/v^2(r)$. This may be written in a slightly different form by defining the scattering relative to a uniform reference medium with velocity v_0. Adding and subtracting a constant term, equation (2.25) becomes

$$\left[\nabla^2+\frac{\omega^2}{v_0^2}-\left(\frac{\omega^2}{v_0^2}-\frac{\omega^2}{v^2(r)}\right)\right]\phi=0. \tag{2.26}$$

In equation (2.26), $\nabla^2+\omega^2/v_0^2$ may be regarded as the operator representing the uniform reference medium, and $\omega^2\left[v_0^{-2}-v^{-2}(r)\right]$ as a perturbation reflecting the presence of the inhomogeneities.

Taking the medium to be excited by a localized point source (cf. Sec. 2.1.2, 2.1.3), we may write the configurationally-averaged Green's function for equation (2.26), in the wave vector representation, as

$$\langle G(\omega,k)\rangle=\frac{1}{\kappa_0^2-k^2-\Sigma_{v_0}(\omega,k)}\ \frac{N}{L^3}, \tag{2.27}$$

which follows from equations (2.4) and (2.22) with $\kappa_0^2=\omega^2/v_0^2$. The self-energy $\Sigma_{v_0}(\omega,k)$ is calculated relative to the reference medium and represents all the effects of the multiple scattering caused by the inhomogeneities. Equation (2.27) clearly indicates that all non-trivial information about $\langle G\rangle$ is contained in $\Sigma_{v_0}(\omega,k)$. If Σ_{v_0} is

independent of k in some frequency regime, the effect of $\Sigma_{\nu_0}(\omega)$ is just to *renormalize* κ_0, the uniform medium wave vector. This renormalized medium is called the *effective medium*, and the new wave vector $\kappa_e^*(\omega)$ is then given by

$$\left[\kappa_e^*(\omega)\right]^2 = \kappa_0^2 - \Sigma_{\nu_0}(\omega). \tag{2.28}$$

2.1.6.2 The coherent potential approximation (CPA)

We now address the problem of determining the conditions under which this effective medium exists [i.e. for which $\Sigma_{\nu_0}(\omega, k) = \Sigma_{\nu_0}(\omega)$]. One approach that has met with much success is to apply the coherent potential approximation (CPA; Lax, 1951). The central idea behind the CPA is the requirement that, *relative* to the renormalized uniform medium with wave vector κ_e^*, $\langle G \rangle$ be just a uniform medium Green's function, that is

$$\langle G \rangle = G_0(\omega, \kappa_e^*). \tag{2.29}$$

Equation (2.22) then implies that $\Sigma_{\nu_0}(\omega)$ must vanish in the renormalized effective medium. Since the wave equation is invariant under the addition and subtraction of the constant term ω^2/ν_0^2 [cf. equation (2.26)], the requirement $\Sigma_{\nu_0}(\omega) = 0$ means that the self-energy is to be calculated with a particular choice of ν_0.

As equation (2.23) defines the self-energy in terms of the configurationally-averaged total scattering operator for the system, $\Sigma_{\nu_0}(\omega) = 0$ implies

$$\langle T \rangle = 0 \tag{2.30}$$

in the effective medium. This requirement is self-consistent because it is precisely in the limit as $\langle T \rangle \to 0$ that the problem becomes calculable, because $\langle T \rangle \to 0$ implies weak overall scattering. One means whereby this weak overall scattering may be achieved is for each *individual* scatterer to scatter weakly in the effective medium. The total scattering operator for the system may then be written as the sum of single scatterings from the individual scatterers:

$$T \cong \sum_j T_j^{(s)}. \tag{2.31}$$

Within this approximation, the particular choice of v_0 that satisfies the CPA requirement is found from

$$n_s \left\langle T^{(s)} \right\rangle = 0. \tag{2.32}$$

Hence, though the T matrix cannot, in general, be calculated for a disordered medium, under the CPA condition the problem is reduced to the determination of the matrix elements for the single-scatterer case. The phase velocity in the effective medium is then identified under the requirement that the scattering from the individual scattering units vanish on average — exactly what we would expect for a propagating mode.

2.1.6.3 Generalized CPA

The inherent limitation of the CPA is that it has been designed to describe wave propagation within the Rayleigh scattering regime (Lax, 1951), that is, under the condition that the wavelength λ be large compared to the length scale d of the inhomogeneities. In

this limit, not only can the wave not resolve the individual scattering elements, but the ω^4 frequency dependence in the Rayleigh regime ensures that the scattering remains weak. In the limit $d/\lambda \to 0$, the CPA condition [equation (2.30)] generally has a solution. As the self-energy $\Sigma_{\nu_0}(\omega)$ is in general a complex number [whose imaginary part must be negative since the DOS must be positive, cf. equation (2.11)], the choice of a particular ν_0 as the effective medium wave speed requires that the CPA condition be written as

$$\mathrm{Re}\,\Sigma_{\nu_0}(\omega) = 0. \tag{2.33}$$

When the CPA works, the Green's function may be taken for that of a uniform medium, since $\mathrm{Im}\,\Sigma_{\nu_0}(\omega)$ is generally of higher order in d/λ, and thus may be ignored:

$$\langle G(\omega,\boldsymbol{k})\rangle = \frac{1}{\kappa_0^{\,2} - k^2 - i\,\mathrm{Im}\,\Sigma_{\nu_0}(\omega)}\,\frac{N}{L^3} \cong \frac{1}{\kappa_0^{\,2} - k^2}\,\frac{N}{L^3}. \tag{2.34}$$

However, in the limit $d/\lambda \to 1$ (i.e. as the intermediate frequency regime is approached), the inhomogeneities begin to be resolved by the wave, and Σ_{ν_0} can become $\boldsymbol{k}$-dependent. With the increase in frequency, the solution to the CPA condition [equation (2.33)] may then abruptly vanish, implying the *sudden* disappearance of the propagating mode; this is unphysical. The solution may also vary discontinuously, or appear multiply, making suspect the identification of ν_0 with the effective medium wave speed (Sheng *et al.*, 1994). Physically, what we expect to happen, as the intermediate frequency regime is approached, is the gradual transformation of the propagating mode into a quasimode, that is, a mode with a short lifetime and mean free path. Thus, a new way of looking at the problem is required. An alternative approach has been demonstrated (Jing *et al.*, 1991, 1992) where the CPA requirement was abandoned and, instead, the peaks in the spectral function

$-\mathrm{Im}\langle G(\omega,k)\rangle$ monitored. The spectral function is just the wave vector representation of the real space DOS shown in equation (2.11).

The rational for monitoring the peaks in the spectral function may be illustrated by returning, for the moment, to the uniform medium [Sec. 2.1.3; see especially equation (2.5)]. The spectral function $-\mathrm{Im}G_0(\omega,k)$ is a *delta* function that picks out the dispersion relation of the medium. The same effect holds true in a random medium when the CPA requirement is satisfied, as equation (2.34) implies:

$$-\frac{L^3}{N}\mathrm{Im}\langle G(\omega,k)\rangle = \frac{-\mathrm{Im}\Sigma_{v_0}(\omega)}{\left(\kappa_0^2 - k^2\right)^2 + \left(\mathrm{Im}\Sigma_{v_0}(\omega)\right)^2} . \qquad (2.35)$$

Clearly, the peak in the spectral function occurs for $k = \kappa_0 = \omega/v_0$, and its width is given by $-\mathrm{Im}\Sigma_{v_0}(\omega)$ (a positive quantity). If $\mathrm{Im}\Sigma_{v_0}(\omega) = 0$ (as is the case for a true uniform medium), then the peak is just a delta function, as expected. The advantage of considering the spectral function is that even when $\mathrm{Re}\Sigma_{v_0}$ is no longer zero, the peaks of $-\mathrm{Im}\langle G(\omega,k)\rangle$ still exist. This means the CPA mode simply becomes a quasimode, as we would expect. This process is a continuous one as the frequency is increased.

To implement this approach, we recall that adding and subtracting a constant term did not change the wave equation [equation (2.26)]; that is, the value of v_0 is completely *arbitrary*. We thus have the freedom to *choose* to calculate $-\mathrm{Im}\langle G(\omega,k)\rangle$ with the condition that (Sheng *et al.*, 1994; Sheng, 1995)

$$v_0 = \omega/k , \qquad (2.36)$$

so that [from equation (2.27)]

$$-\frac{L^3}{N}\mathrm{Im}\langle G(\omega,k)\rangle = \mathrm{Im}\ \frac{1}{\Sigma_{\nu_0}(\omega,k)}$$
$$= \frac{-\mathrm{Im}\,\Sigma_{\nu_0}(\omega,k)}{\left(\mathrm{Re}\,\Sigma_{\nu_0}(\omega,k)\right)^2+\left(\mathrm{Im}\,\Sigma_{\nu_0}(\omega,k)\right)^2}. \tag{2.37}$$

Since $-\mathrm{Im}\langle G(\omega,k)\rangle$ depends on both ω and k, plotting a two-dimensional map of the intensity of the spectral function will allow the determination of the peaks in the (ω,k) plane. The physical significance of these peaks is described by their identification with the dispersion relation of the (quasi)modes of the system. Thus the spectral function not only reproduces the CPA results, but also extends its validity beyond the CPA regime. This approach has been denoted the generalized CPA (Sheng, 1995).

The means of determining $\Sigma_{\nu_0}(\omega,k)$, which is usually difficult to calculate exactly, is similar to that employed in the CPA. We use the equation (2.23) to first order in $\langle T\rangle$ (i.e. $\langle T\rangle \cong 0$) within the single-scatterer approximation [cf. equation (2.30) – (2.32)]:

$$\Sigma_{\nu_0}(\omega,k) \cong n_s\langle T^{(s)}\rangle. \tag{2.38}$$

This approximation is most accurate when $\Sigma_{\nu_0}(\omega,k)\cong 0$, which occurs near the peaks of the spectral function, equation (2.37), thus allowing the dispersion relation to be determined with confidence. The approximation is poor only in those regions in which we have no interest (i.e. far from the peaks).

2.1.7 Elastic wave equation: Green's function solution

This section summarizes the approach taken by Jing *et al.* (1992), to whom the reader is referred for additional details. Here, we concentrate on showing how the Green's function solution may be obtained for the elastic wave equation as applied to our single-scattering-unit model (Sec. 2.1.4) within the context of the effective medium approach (illustrated in the previous section, Sec. 2.1.6). In the discussions to follow, the solid phase (of the scattering unit) will be denoted as region I, the liquid phase as region II, and the effective medium as region III [see figure 2.1(b)]. The effective medium will be assumed to be fluid-like, since, macroscopically, the system can only support compressional waves.

The elastic wave equation, as applied to each of the three homogeneous regions, may be written as

$$\frac{\partial^2 \boldsymbol{u}}{\partial t^2} = v_t^2(\boldsymbol{r})\nabla^2 \boldsymbol{u} + \left[v_L^2 - v_t^2\right]\nabla(\nabla \cdot \boldsymbol{u}), \tag{2.39}$$

where $\boldsymbol{u}$ denotes the particle displacement, and the longitudinal and transverse velocities are $v_L(\boldsymbol{r})$ and $v_t(\boldsymbol{r})$, respectively, at position $\boldsymbol{r}$. Neither the fluid coating nor the effective medium support transverse waves so for regions II and III, $v_t = 0$.

It is possible, in general, to decompose the displacement $\boldsymbol{u}$ into a longitudinal part and a transverse part (Panofsky and Phillips, 1962), with each part being derived from a scalar potential ψ and a vector potential $\boldsymbol{A}$, respectively:

$$\boldsymbol{u} = \nabla\psi + \nabla \times \boldsymbol{A}. \tag{2.40}$$

As our model exhibits spherical symmetry, the vector potential A can be written in terms of a scalar potential ξ:

$$A = \nabla \times (r\xi). \tag{2.41}$$

Both ψ and ξ must then satisfy the scalar wave equations

$$\left(\nabla^2 + \frac{\omega^2}{v_L^2(r)}\right)\psi = 0 \tag{2.42a}$$

and

$$\left(\nabla^2 + \frac{\omega^2}{v_t^2(r)}\right)\xi = 0, \tag{2.42b}$$

respectively. The response of the scalar potential ψ (at r) to a compressional point source (at r') is described by the Green's function that satisfies

$$\left(\nabla^2 + \frac{\omega^2}{v_L^2(r)}\right)G_\psi^{(s)}(r,r') = \delta(r-r'), \tag{2.43}$$

where $v_L(r)$ represents the longitudinal wave speed in region I (the solid sphere), the compressional wave speed $v_l(r)$ in region II (the fluid), and the effective medium wave speed $v_0(r)$ in region III [cf. equation (2.2)]. For ξ we have

$$\left(\nabla^2 + \frac{\omega^2}{v_t^2(r)}\right)G_\xi^{(s)}(r,r') = 0 \quad \text{in region I,} \tag{2.44a}$$

and

$$G_\xi^{(s)}(r,r') = 0 \quad \text{in regions II and III,} \tag{2.44b}$$

due to the vanishing of the shear velocity in the fluid and the effective medium, respectively.

The Green's functions $G_\psi^{(s)}(r,r')$ and $G_\xi^{(s)}(r,r')$ are coupled by the boundary conditions imposed at the interfaces of the three regions. These conditions are the

continuity of the normal displacement and normal stress at both $r = a$ and $r = b$ [see figure 2.1(a)], and the vanishing of the tangential stress at the solid-liquid interface $r = a$. Here we assume the fluid to be inviscid. Numerical investigations by Jing *et al.* (1992) have determined the effect of viscosity to be negligible for all physically permissible values. The application of the generalized CPA is to $G_{\psi}^{(s)}(r,r')$, as it describes the compressional response of the system. This Green's function is obtained by solving three boundary-value problems where the source point r' is located in each of the three regions. The exact total scattering operator (matrix) for a single coated sphere may then be determined from equation (2.14). This is most easily accomplished if the Green's functions are first Fourier transformed to wave-vector-space,

$$G_{\psi}^{(s)}(r_1,r_2) \rightarrow G_{\psi}^{(s)}(k_1,k_2;\omega), \tag{2.45}$$

where k_1 is the wave vector of the incident wave, and k_2 is the wave vector of the scattered wave (and explicitly noting the dependence on the frequency ω), and then expanded in angular-momentum-space (wave-vector-space) as

$$G_{\psi}^{(s)}(k_1,k_2) = (4\pi)^2 \sum_{l,m} g_{\psi l}^{(s)}(k_1,k_2)\, Y_{l,m}(\hat{k}_1)\, Y_{l,m}^{*}(\hat{k}_2), \tag{2.46}$$

where $Y_{l,m}(\hat{k})$ represents the spherical harmonics, $\hat{k}$ a unit vector, and $g_{\psi l}^{(s)}$ the lth component of the Green's function in wave-vector-space space (which may be determined from $G_{\psi}^{(s)}$). Similarly, in wave-vector-space, the total scattering operator can be written as

$$T^{(s)}(k_1,k_2) = (4\pi)^2 \sum_{l,m} t_l^{(s)}(k_1,k_2)\, Y_{l,m}(\hat{k}_1)\, Y_{l,m}^{*}(\hat{k}_2). \tag{2.47}$$

The angular momentum components $t_l^{(s)}$ are then determined, using equation (2.14), from a knowledge of the angular momentum components of the Green's functions. Under the condition of elastic scattering, $k_1 = k_2 = k$, equation (2.47) reduces to just the diagonal components of the scattering $T^{(s)}$ matrix,

$$T^{(s)}(k,k') = 4\pi \sum_{l,m} t_l^{(s)}(k,k') = 4\pi \sum_{l} (2l+1) t_l^{(s)}(k,k'), \tag{2.48}$$

with the prime on the scattered wave vector implicitly indicating the dependence on scattering angle. The details of the calculation, and final form, are shown in Jing *et al.* (1992); please refer to their appendix A.

2.1.8 The density of states (DOS): phase and group velocities, and the scattering mean free path

The density of states (DOS) has been discussed in Sec. 2.1.3; there we showed, equation (2.11), that the local DOS could be written in terms of the imaginary part of the real-space Green's function. Recasting equation (2.11) into the wave vector representation:

$$DOS(\omega,k) = -\frac{2\omega}{v_0^2\pi} \operatorname{Im}\left\langle G_{\psi}^{(s)}(\omega,k)\right\rangle. \tag{2.49}$$

This can be written in terms of the imaginary part of the self-energy through equation (2.37) as

$$DOS(\omega,k) = \frac{2\omega}{v_0^2\pi} \operatorname{Im} \frac{n_s}{\Sigma_{v_0}(\omega,k)}. \tag{2.50}$$

The task that remains, then, is the determination of $\Sigma_{\nu_0}(\omega,k)$. The self-energy (within the GCPA) is related to the total scattering operator for the single scattering-unit by equation (2.38), as

$$\Sigma_{\nu_0}(\omega,k) = n_s\left\langle T^{(s)}(k,k)\right\rangle. \tag{2.51}$$

It is customary to define the *scattering amplitude* $f(k,k')$, in terms of the known quantity $T^{(s)}(k,k')$ [see equation (2.48)], as

$$f(k,k') = \frac{-1}{4\pi} T^{(s)}(k,k') \tag{2.52}$$

(Sheng, 1995), where k is the incident wave vector and k' the scattered wave vector. Comparing equation (2.51) and equation (2.52) reveals that the self-energy is related to the forward scattering amplitude. After averaging the scattering amplitude over all incident wave directions,

$$f(\omega,k) = \frac{1}{4\pi}\int f(k,k)d\Omega, \tag{2.53}$$

with the frequency dependence explicitly noted, the self-energy may then be written as

$$\Sigma_{\nu_0}(\omega,k) = -n_s f(\omega,k). \tag{2.54}$$

Hence the density of states, using equation (2.36), becomes

$$DOS(\omega,k) = -\frac{2k^2}{\omega\pi}\,\mathrm{Im}\,\frac{1}{f(\omega,k)}. \tag{2.55}$$

The density of states for a system of randomly close packed glass spheres immersed in water, based on the single coated sphere model (treated within the GCPA), is plotted in

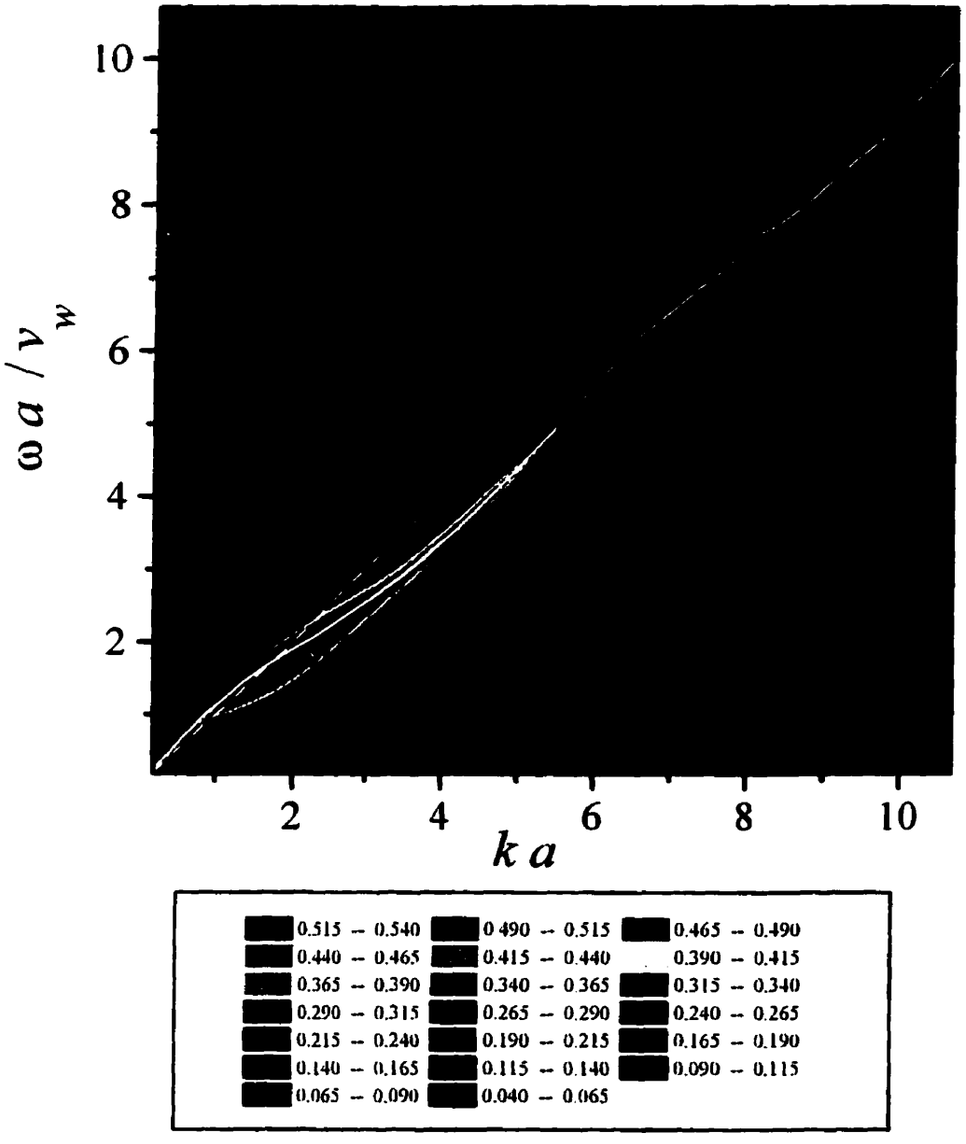

Figure 2.2 The density of states as a function of normalized frequency and wave vector. The solid white line is the dispersion curve for the renormalized medium; the dashed white line is that for water. The magnitude (red: high, blue: low) is in arbitrary units.

figure 2.2. The magnitude (given in arbitrary units) is indicated by the colours, with red being high and blue being low. It should be emphasized that there are no adjustable parameters, the calculation of the DOS requiring only those material parameters (densities and velocities) given in chapter 3.

It is clear from equation (2.55) that the maxima of the DOS (a function of both ω and k) correspond to minima in the scattering and so identify the propagating modes, and thus directly give the dispersion relation

$$\omega = v_p k, \tag{2.56}$$

where v_p, the *phase* velocity, is identified with the effective medium velocity v_0 at the position of the peaks in the DOS. The dispersion curve, shown by the solid white line in figure 2.2, has been accurately determined since the widths of the peaks are substantially less than their central frequencies. It is seen to fall below the dispersion curve for pure water (dashed white line) over most of the frequency range. The phase velocity is thus less than that of water over much of the frequency range.

Knowledge of the dispersion relation allows us to determine the *group* velocity v_g, which is the speed at which the envelope of a wave pulse travels, or the velocity of the coherent transport of energy. We have (Jackson, 1975)

$$v_g = \frac{d\omega}{dk}, \tag{2.57}$$

which may be obtained by differentiating the dispersion relation.

The real-space Green's function has the form of equation (2.6) for a uniform medium, but with κ_0 replaced by κ_e^*:

$$\langle G(\omega, r - r') \rangle = -\frac{\exp\left(i\kappa_e^* |r - r'|\right)}{4\pi |r - r'|}. \tag{2.58}$$

where κ_e^* is given by [cf. equation (2.28)]

$$\kappa_e^* = \sqrt{\kappa_e^2 - i \operatorname{Im} \Sigma_{\nu_0}(\omega, k)}, \tag{2.59}$$

with $\kappa_e^2 = \omega^2 / v_0^2 - \operatorname{Re} \Sigma_{\nu_0}(\omega, k)$. The self-energy $\Sigma_{\nu_0}(\omega, k)$ is in general a complex number, with a *negative* imaginary part [since the DOS must be positive, cf. equation (2.11)]. Since κ_e^* has a *positive* imaginary part, $\langle G(\omega, r - r') \rangle$ decays exponentially and hence defines the scattering mean free path (cf. Sec. 2.1.2) (Sheng, 1995)

$$l_s = \left(2 \operatorname{Im} \kappa_e^*\right)^{-1}. \tag{2.60}$$

Where the GCPA is valid, equation (2.60) may be approximated as

$$l_s \cong \frac{\kappa_e}{-\operatorname{Im} \Sigma_{\nu_0}(\omega, k)}. \tag{2.61}$$

The total scattering cross section σ (evaluated in the effective medium) may be written in terms of the forward scattering amplitude by applying the optical theorem, a statement of flux conservation, which relates the total scattering cross section to the imaginary part of the forward scattering amplitude (Jackson, 1975). An excellent review of the history of the application of the optical theorem to scattering problems, both quantum and classical, is given by Newton (1976). Hence

$$\sigma = \frac{-4\pi \operatorname{Im} f(\omega, k)}{\kappa_e}, \tag{2.62}$$

where $f(\omega,k)$ is evaluated, as described above, using equations (2.52) and (2.53). Applying equation (2.54), the scattering mean free path, equation (2.61), is then seen to be inversely proportional to the total scattering cross section of the coated elastic sphere:

$$l_s = \frac{1}{n_s \sigma}. \tag{2.63}$$

The theoretical description of the coherent transport, using a simple single coated-sphere model and a new effective medium approach that goes beyond the limitations of the CPA, will be tested against the experimentally determined parameters that characterize the ballistic propagation in the intermediate frequency regime. The comparison of theory and experiment will provide a framework for understanding the basic physics of the transport while identifying any inadequacies in the former.

2.2 Diffusive propagation

2.2.1 Introduction

In Sec. 2.1.2, the propagation of an acoustic wave in a disordered medium was discussed within the context of the Green's function for the wave equation. The information contained in the Green's function was illustrated by analogy with the classical random walker. It was noted that the coherent component of the propagation could be described by the configurationally averaged Green's function $\langle G \rangle$. We now wish to describe the transport dynamics *beyond* the scale of the mean free path. This, the incoherent part of the propagation, is what is known as the diffusive component, and its intensity transport behaviour is given by the second moment of the configurationally averaged Green's function, $\langle GG^* \rangle$. The Green's function approach will not, however, be employed here. Rather, the focus will be on using the conceptually simpler diffusion approximation to describe this propagation. The reason for this is historical. Much of the recent understanding of classical wave propagation has been due to the investigation of the propagation of *electromagnetic* waves through strongly scattering media (Sheng, 1990). This progress has, to a large extent, been based on the success of the diffusion approximation, which neglects all phase information and treats the propagation of the intensity as a diffusive process. Consequently, our initial investigations of the multiple scattering of *acoustic* waves were concerned with the critical testing of this approximation for sound propagation, and the Green's function approach was ignored.

The description of the propagation of the multiply scattered sound is given in this section. The nature of the diffusive propagation is first illustrated by analogy with the classical random walker (cf. Sec. 2.1.2). A more quantitative description of the wave transport, within which the diffusion approximation is discussed, then follows. The diffusion approximation is then used to develop the diffusion equation from the more general equation describing the wave transport. Realistic boundary conditions, incorporating partial reflection and partial transmission at the sample interfaces, are then derived, and the reflection coefficients given. The solutions to the diffusion equation, from which the diffusion parameters may be extracted, are then presented. Complementary information, acquired from the study of both time dependent and steady state (time independent) solutions, finds its synthesis in the discussion on the velocity of energy propagation (i.e. energy velocity) and its relation to the group velocity.

2.2.2 The random walk analogy

Physically, the diffusion approximation describes the propagation as a random walk of phonons through the scattering medium, as depicted in figure 2.3. Clearly, as in any random walk, there will be many different possible paths that could be traversed between two fixed points. In a three-dimensional medium of infinite extent, the probability $P(s)$ that a classical random walker of step length l will follow a path of length s between two points separated by a distance R is (Pine *et al.*, 1990)

$$P(s) = \left(3/4\pi sl\right)^{3/2} e^{-3R^2/4sl}. \qquad (2.64)$$

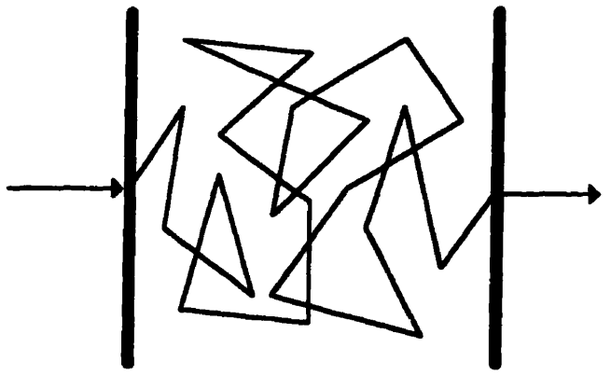

Figure 2.3 Classical random walk in two dimensions, with mean step size l, representing the multiple scattering in a sample of thickness L.

For an instantaneous point source located at the origin, the diffuse energy density $U(t)$ at R, which is proportional to the distribution of path lengths, is due to the evolution of the contributions from different path lengths with time t. The solution to the diffusion equation determines the average transport of energy, and hence the distribution of multiple scattering paths. Hence, for the conditions under which equation (2.64) is applicable, the diffuse energy density may be given by

$$U(t) = \left(1/4\pi Dt\right)^{3/2} e^{-R^2/4Dt}, \tag{2.65}$$

where the transformation from path length to time has been accomplished using $s = v_e t$. The distribution of scattering paths may then be characterized by the diffusion coefficient

$$D = \tfrac{1}{3} v_e l^*, \tag{2.66}$$

where v_e is the local velocity at which energy is transported, and l^*, the transport mean free path, is the distance traveled before the direction of propagation becomes

randomized. It should be noted that the *transport* mean free path l^* is not necessarily the same as the *scattering* mean free path l_s; they are only equal if the scattering is isotropic. For anisotropic scatterers, the single particle scattering is peaked in the forward direction so that the effective random walk step size is lengthened by an amount corresponding to the mean forward scattering; hence we define, in the absence of absorption, the relation

$$l^* = \frac{l_s}{1-\langle\cos\theta\rangle}, \tag{2.67}$$

where θ is the scattering angle. Thus, if l_s describes the distance between scattering events, then l^* represents the mean distance required before the direction of propagation becomes randomized. It should also be pointed out that the configurationally-averaged cosine of the scattering angle is to be calculated within the single coated-sphere model under the conditions imposed by the GCPA (see Sec. 2.2.8). Figure 2.4(a) illustrates the propagation of a delta-function pulse in a strongly scattering medium. Path 1 shows the shortest possible path through the sample, namely the ballistic path (ballistic propagation has been discussed in detail in Sec. 2.1). Path 2 indicates a wave that has undergone only a single scattering and is thus still quite short, while path 3 illustrates the path length of a wave that has undergone many scatterings and so is very long. The temporal positions of the contributions of these various path lengths to the diffuse intensity, as modeled by equation (2.65), are shown in figure 2.4(b). It should, of course, be remembered that the ballistic component (i.e. path 1) is not part of the *diffuse* intensity. The temporal position of path 1 thus indicates where the ballistic component, should its intensity also be plotted, would appear if a fraction of the incident signal remained unscattered (or forward scattered).

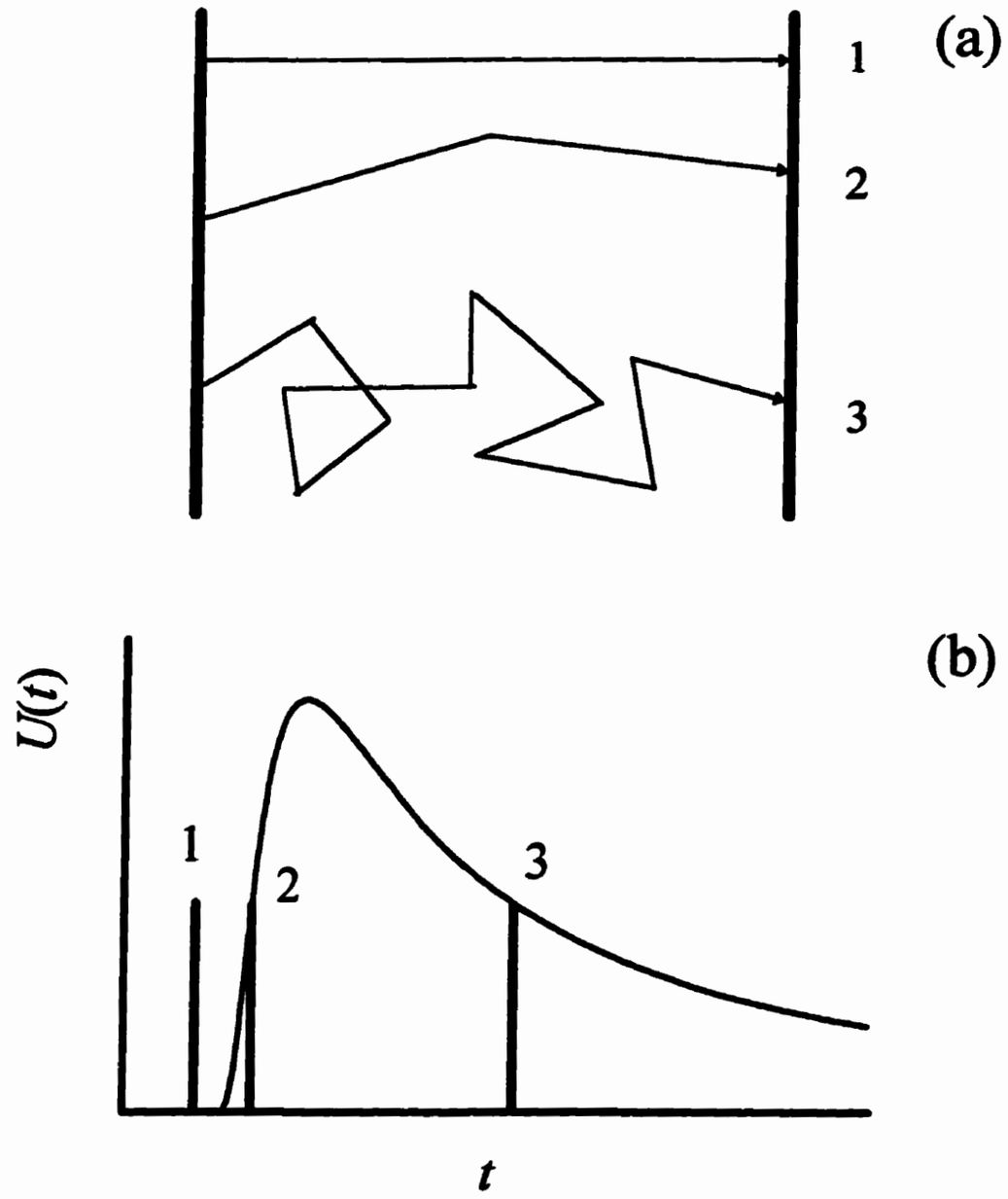

Figure 2.4 (a) The ballistic path (1), a short path (2), and a long path (3) traversed by a delta function pulse. (b) The temporal positions of their contributions to the diffuse energy density. Note that the ballistic contribution is zero within the diffusion approximation.

2.2.3 The transfer equation

A full description of the wave transport is now given, in the Ishimaru formalism (Ishimaru, 1978), where for simplicity, our consideration is initially restricted to the time-independent (steady state) behaviour. The physical basis for the equations governing the transport of the specific intensity are explained, and the transfer equation governing the behaviour of the scattered waves is decoupled from the full transfer equation.

We consider wave propagation in a scattering medium in terms of the specific intensity I at a position r in the direction s (a unit vector); $I(r,s)$ is defined as the average power within a unit solid angle. Let us consider the *change* in the specific intensity dI in a cylindrical volume element, of unit cross section and length ds, containing $n\,ds$ particles, where n is the number density. Three terms may contribute to the change dI. The first term is due to the fact that each particle absorbs a power $\sigma_a I$ and scatters a power $\sigma_s I$. The decrease in the specific intensity for the volume element ds is then

$$n\,ds\,\sigma_t I,$$

where $\sigma_t = \sigma_a + \sigma_s$ is the total cross section. The second term yields an increase in the specific intensity since a portion of the intensity incident on the volume element from other directions s' becomes scattered into the direction s (figure 2.5). This increase in intensity is described by (Ishimaru, 1978)

$$\frac{n\,ds\sigma_t}{4\pi}\int_{4\pi} p(s,s')I(r,s')d\Omega',$$

where $p(s,s')$, denoted the phase function, is proportional to the square of the angular dependent scattering amplitude, and the integration is over all solid angles. The final term

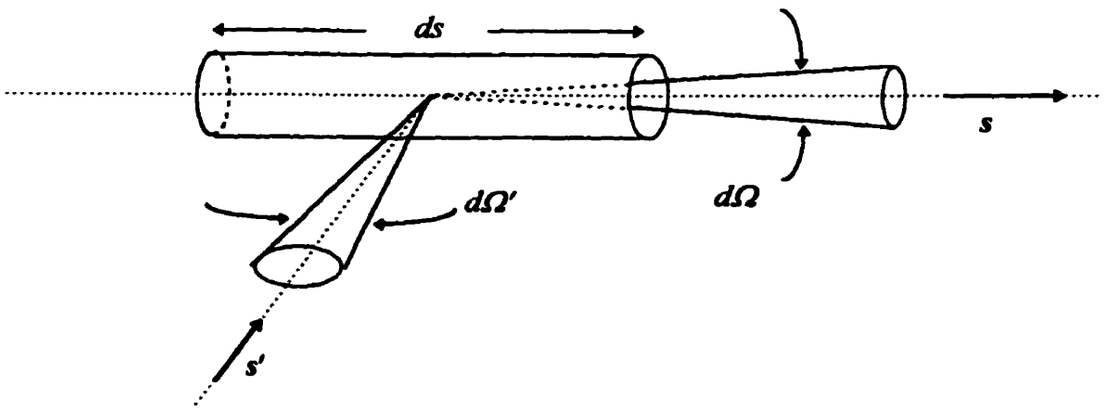

Figure 2.5 Scattering of specific intensity incident upon the volume ds from the direction s' into the direction s (Ishimaru, 1978).

gives the increase in the specific intensity due to any sources of emission within the volume element. If we define $\varepsilon(r,s)$ as the power radiated per unit volume per unit solid angle, then the increase is

$$ds\varepsilon(r,s).$$

The transfer equation is the result of the sum of all these changes. Hence

$$\frac{dI(r,s)}{ds} = -n\sigma_t I(r,s) + \frac{n\sigma_t}{4\pi}\int_{4\pi} p(s,s')I(r,s')d\Omega' + \varepsilon(r,s). \qquad (2.68)$$

To decouple the contribution of the scattered waves, we may write the specific intensity as the sum of a reduced incident intensity I_{ri} and a diffuse intensity I_d:

$$I(r,s) = I_{ri}(r,s) + I_d(r,s) \qquad (2.69)$$

The first part results from that portion of the flux incident upon the medium which has not yet been scattered (nor absorbed), and the second part is that portion created in the

medium due to the scattering (or other internal sources). Substituting equation (2.69) into equation (2.68), and decoupling the equation describing the behaviour of the reduced intensity, yields the diffusive transfer equation

$$\frac{dI_d(\boldsymbol{r},\boldsymbol{s})}{ds} = -n\sigma_t I_d(\boldsymbol{r},\boldsymbol{s}) + \frac{n\sigma_t}{4\pi}\int_{4\pi} p(\boldsymbol{s},\boldsymbol{s}')I_d(\boldsymbol{r},\boldsymbol{s}')d\Omega' + \varepsilon_{ri}(\boldsymbol{r},\boldsymbol{s}) + \varepsilon(\boldsymbol{r},\boldsymbol{s}), \quad (2.70)$$

where ε_{ri}, being generated by the reduced incident intensity, is the equivalent source function given by

$$\varepsilon_{ri}(\boldsymbol{r},\boldsymbol{s}) = \frac{n\sigma_t}{4\pi}\int_{4\pi} p(\boldsymbol{s},\boldsymbol{s}')I_{ri}(\boldsymbol{r},\boldsymbol{s}')d\Omega', \quad (2.71)$$

and $\varepsilon(\boldsymbol{r},\boldsymbol{s})$ represents all other internal sources (or sinks).

2.2.4 The diffusion approximation

Under the assumption that the diffuse intensity sees many particles and is thus scattered *almost* uniformly, its angular distribution is then too almost uniform. Since the distribution cannot be constant (because if it were, the diffusive flux $\boldsymbol{J}_d(\boldsymbol{r})$ would be zero and there would be no net transport of energy), we will require the diffuse intensity to have *slightly* more magnitude in the direction of net flux flow than in the reverse direction. Since the diffusive flux $\boldsymbol{J}_d(\boldsymbol{r})$, and the diffusive energy density $U_d(\boldsymbol{r})$, are related to the diffuse intensity by

$$\boldsymbol{J}_d(\boldsymbol{r}) = \int_{4\pi} I_d(\boldsymbol{r},\boldsymbol{s})\,\boldsymbol{s}\,d\Omega, \quad (2.72)$$

and

$$U_d(\boldsymbol{r}) = \frac{1}{v_e}\int_{4\pi} I_d(\boldsymbol{r},\boldsymbol{s})d\Omega, \quad (2.73)$$

respectively, we may, to first order, approximate the diffuse (specific) intensity in the s direction (at some point r) as the sum of the average diffuse intensity at r and that component of the diffusive flux at r in the s direction. Hence,

$$I_d(r,s) \cong \frac{v_e}{4\pi} U_d(r) + \frac{3}{4\pi} J_d(r) \cdot s, \tag{2.74}$$

where the coefficient of the second term results from the normalization imposed by equation (2.72) upon substitution of equation (2.74). The second term is much smaller than the first due to the requirement that the scattering be almost uniform. Figure 2.6 illustrates the essence of the diffusion approximation. The dashed circle represents the average diffuse intensity in the neighbourhood of r. The direction of the (net) diffusive flux vector at r is indicated by s_f (the magnitude of the flux vector is exaggerated, for clarity). Taking s to be the mean direction of power flow in the scattering medium, the approximate diffuse intensity at r may be represented by the solid circle. The slight displacement of the two circles is meant to indicate the rate at which the power flows in the s direction.

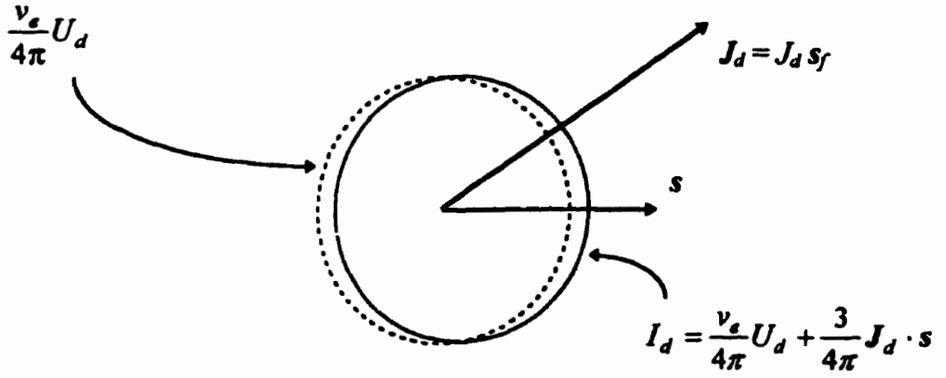

Figure 2.6 The diffuse intensity $I_d(r,s)$ for the diffusion approximation (Ishimaru, 1978).

2.2.5 The diffusion equation

The derivation of the diffusion equation begins with the evaluation of the diffusive transfer equation, equation (2.70), within the diffusion approximation, equation (2.74). Multiplying the result by s and integrating over all solid angles yields

$$\nabla U_d(\boldsymbol{r}) = -\frac{3n(\sigma_{tr}+\sigma_a)}{v_e} J_d(\boldsymbol{r}) + \frac{3}{v_e}\int_{4\pi} \varepsilon_{ri}(\boldsymbol{r},\boldsymbol{s})\boldsymbol{s}\,d\Omega + \frac{3}{v_e}\int_{4\pi} \varepsilon(\boldsymbol{r},\boldsymbol{s})\boldsymbol{s}\,d\Omega, \quad (2.75)$$

where $\sigma_{tr} = \sigma_s\left(1-\langle\cos\theta\rangle\right)$ is the transport cross section. Invoking conservation of energy, the flux must be equal to the power flow generated (from all sources) less the power flow absorbed, so the diffusive flux must satisfy

$$\nabla\cdot J_d(\boldsymbol{r}) = -n\sigma_a v_e U_d(\boldsymbol{r}) + n\sigma_s v_e U_{ri}(\boldsymbol{r}) + E(\boldsymbol{r}), \quad (2.76)$$

where $U_{ri}(\boldsymbol{r})$ is the energy density of the reduced incident wave, and

$$E(\boldsymbol{r}) = \int_{4\pi} \varepsilon(\boldsymbol{r},\boldsymbol{s})\,d\Omega \quad (2.77)$$

represents all internal sources. We now identify the scattering and transport mean free paths in the medium as $l_s = (n\sigma_s)^{-1}$ and $l^* = (n\sigma_{tr})^{-1}$ respectively, and, under the assumption that all absorption occurs in the scattering particles, the absorption length as $l_a = (n\sigma_a)^{-1}$. Solving equation (2.75) for $J_d(\boldsymbol{r})$ and substituting it into equation (2.76) yields the steady state diffusion equation

$$D\nabla^2 U_d(\boldsymbol{r}) - \tau_a^{-1} U_d(\boldsymbol{r}) = -E(\boldsymbol{r}) - \frac{v_e}{l_s} U_{ri}(\boldsymbol{r}) + l^*\nabla\cdot\int_{4\pi} \varepsilon_{ri}(\boldsymbol{r},\boldsymbol{s})\boldsymbol{s}\,d\Omega + l^*\nabla\cdot\int_{4\pi} \varepsilon(\boldsymbol{r},\boldsymbol{s})\boldsymbol{s}\,d\Omega, \quad (2.78)$$

where $\tau_a = l_a/v_e$ is the absorption time. Up to this point we have implicitly assumed that the diffuse energy density is time independent (i.e. the incident wave is a continuous wave). Assuming now the diffuse energy density to change over time (e.g. a delta function, or narrow pulse incident wave packet), the time varying diffusion equation may be constructed by moving all terms from the right hand side of the equals sign in equation (2.78) to the left hand side and then equating the result to $\partial U_d(r,t)/\partial t$. This may then be rewritten in the more familiar form

$$\frac{\partial U_d(r,t)}{\partial t} - D\nabla^2 U_d(r,t) + \tau_a^{-1} U_d(r,t) = Q(r,t), \tag{2.79}$$

where

$$Q(r,t) = E(r,t) + \frac{v_e}{l_s} U_n(r,t) - l^* \nabla \cdot \int_{4\pi} \varepsilon_n(r,t;s)\, s\, d\Omega - l^* \nabla \cdot \int_{4\pi} \varepsilon\,(r,t;s)\, s\, d\Omega, \tag{2.80}$$

is the full source term, assumed to also be time dependent.

2.2.6 The boundary conditions

The boundary conditions to be imposed on equation (2.79) must model the physical reality imposed by the particular experiment being performed. For the series of experiments conducted, the sample was of slab geometry. Since the effective transverse dimensions (i.e. the diameters) of the samples were at least an order of magnitude larger than their thickness (Sec. 3.1), it is then not unreasonable to apply boundary conditions in the x and y directions equivalent to those for a sample of infinite transverse extent. This means that the diffuse energy density must effectively vanish at large transverse

separations (i.e. x and/or y) from the source point. The boundary condition in the z (thickness) direction, however, requires more careful consideration.

The sample is immersed in water, which serves to couple the sound from the wave generator to the sample and thence to the detector (Sec. 4.1). Because the acoustic impedances of the sample and the coupling medium are not in general the same, there will be *internal* reflections at the sample interfaces. This means that a wave incident upon the exit face of the sample (in general, at any angle) will be partially reflected *back into* the sample. This effectively alters the diffuse energy density by shifting the distribution of path lengths towards longer path lengths since reflections cause the sound to remain longer in the sample. For thin samples, the increase in path length is generally a significant fraction of the total path length, while for thick samples (where all paths are long), the increase is usually only a small fraction of the total path length (Lagendijk *et al.*, 1989; Zhu *et al.*, 1991). The reflectivity of the interfaces must then be incorporated in the boundary conditions imposed on the diffusion equation.

Lagendijk *et al.* (1989), within the context of the coherent backscattering and diffusive transport of light, were first to realize that internal reflection could seriously modify the outcome. The following years were to see rigorous testing of the effect of the inclusion of the internal reflection on the agreement between theory and experiment, as well as the consistency of the diffusive parameters obtained by complementary methods (Zhu *et al.*, 1991; ref. 3-7, especially). The determination of the appropriate boundary conditions for the diffusion equation, incorporating the angular dependent reflectivity, was done by Zhu *et al.* (1991). Their approach equates the flux of the waves internally reflected from a boundary with a fictitious flux entering the sample from outside. Their

arguments are reproduced below to justify the particular form of the boundary condition, and its dependence on the reflection coefficient.

The acoustic diffusive flux through an arbitrarily small area dS inside the sample is just the flow of the acoustic diffuse energy through this area within some characteristic time (i.e. a *power*). Assuming the scattering to be isotropic, this characteristic time may be taken as that required for the wave to move one mean free path, namely l_s/v_e, where l_s is the scattering mean free path and v_e is the velocity of energy transport. We begin by considering the diffuse energy contained in an infinitesimal volume element dV, *vis.* $U_d(\mathbf{r})dV$. If dS is placed at the origin and normal to the z axis (for convenience), and the volume element is put a distance r away, as shown in figure 2.7, then dS subtends a certain solid angle $d\Omega = \frac{dS\cos\theta}{r^2}$ with respect to dV. The fraction of the diffuse energy from dV that initially flows in the direction of dS is $d\Omega/4\pi$. Neglecting absorption, the proportion of this energy that actually passes through dS is e^{-r/l_s}, as some will have been scattered out of the path. Omitting the subscript "d" on the diffuse energy density for convenience (from this point on), the flux through the small area from this infinitesimal volume element may be presented as

$$\frac{[U(r,\theta,\phi)dV]\left[\frac{1}{4\pi}\frac{dS\cos\theta}{r^2}\right]\left[e^{-r/l_s}\right]}{l_s/v_e}. \qquad (2.81)$$

The total flux through dS in the negative z direction, $J^- dS$, is found by integrating equation (2.81) over the entire positive half-space:

$$J^{-}\,dS = \frac{v_e\,dS}{4\pi\,l_s}\int_0^{\pi/2} d\theta \int_0^{2\pi} d\phi \int_0^{\infty} dr\,U(r,\theta,\phi)\cos\theta\,\sin\theta\,e^{-r/l_s}\,. \qquad (2.82)$$

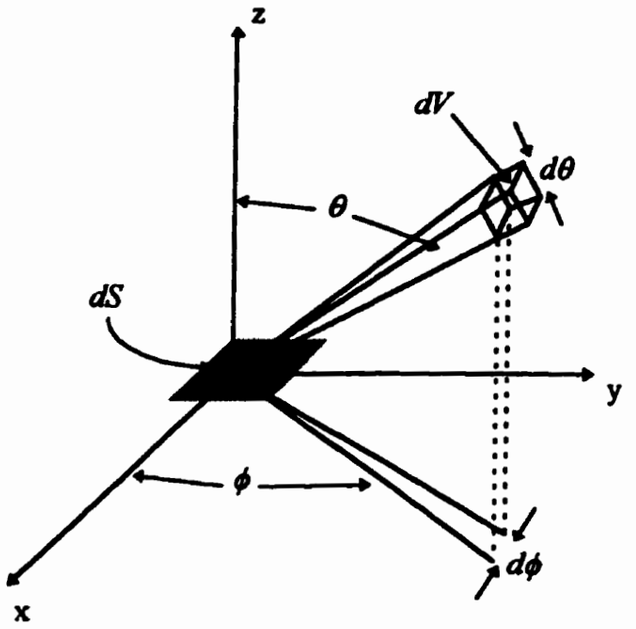

Figure 2.7 Scattering geometry for the calculation of the diffusive flux.

Since the primary contribution to the acoustic flux through dS is from a neighbourhood of a few mean paths, to evaluate equation (2.82) we expand $U(r,\theta,\phi)$ in a first-order Taylor series about the origin:

$$U(r,\theta,\phi) = U_0 + x\left(\frac{\partial U}{\partial x}\right)_0 + y\left(\frac{\partial U}{\partial y}\right)_0 + z\left(\frac{\partial U}{\partial z}\right)_0, \qquad (2.83)$$

where the subscripts denote evaluation at the origin. The independent variables x, y, and z are then expressed in spherical coordinates as $x = r\sin\theta\cos\phi$, $y = r\sin\theta\sin\phi$, and

$z = r\cos\theta$, and equation (2.82) evaluated. Since the integrals over $\sin\phi$ and $\cos\phi$ vanish in equation (2.82), the only contribution is from the z component. The flux through dS in the negative z direction [using equation (2.66)] is then

$$J^- dS = dS\left\{\tfrac{1}{4}Uv_e + \tfrac{1}{6}v_e l_s \frac{\partial U}{\partial z}\right\}, \tag{2.84}$$

where we have neglected the subscript, for convenience.

The expansion of U to first order in equation (2.83) may be further justified by comparison with the results of the so-called P_N approximation (with $N = 1$) used in neutron scattering theory. It has been shown (Bell and Glasstone, 1970) that the P_1 approximation, which is identical to diffusion theory, also yields equation (2.84). Furthermore, they show that the P_1 approximation is also valid for anisotropic systems, provided that l^* replaces l_s in equation (2.84). The flux through dS in the negative z direction is then

$$J^- = \tfrac{1}{4}Uv_e + \tfrac{1}{2}D\frac{\partial U}{\partial z}. \tag{2.85}$$

Similarly, the flux through dS in the positive z direction is found as

$$J^+ = \tfrac{1}{4}Uv_e - \tfrac{1}{2}D\frac{\partial U}{\partial z}. \tag{2.86}$$

Now consider the flux at the boundaries of a slab of infinite transverse extent positioned perpendicularly to the z axis between $0 < z < L$. The flux of the waves internally reflected from a boundary may be thought of as due to a fictitious flux entering the sample from outside. In the absence of internal reflections, as is the case for a sample impedance matched to its surroundings, there is no flux that may be considered as originating outside the sample. The boundary conditions may then be determined from

$J^+ = 0$ at $z = 0$, and $J^- = 0$ at $z = L$. However, internal reflections *do* produce some "incoming flux" due to reflections at the boundaries. One may define a mean reflection coefficient R as the ratio of the incoming flux to the outgoing flux at the boundaries. Thus the boundary conditions are $J^+ = RJ^-$ for $z = 0$, and $J^- = RJ^+$ for $z = L$. These may be rewritten, using equations (2.85) and (2.86), as

$$U - h\frac{\partial U}{\partial z} = 0 \qquad \text{at } z = 0, \tag{2.87}$$

and

$$U + h\frac{\partial U}{\partial z} = 0 \qquad \text{at } z = L, \tag{2.88}$$

where

$$h \equiv \frac{2l^*}{3}\frac{1+R}{1-R} \tag{2.89}$$

is denoted the extrapolation length, as equations (2.87) and (2.88) are equivalent to extrapolating U to zero at a distance h on either side of the boundaries (see Sec. 2.2.7.2, figure 2.8). Appendix A describes how the reflection coefficient may be determined from a knowledge of the material parameters of the system.

2.2.7 Solutions to the diffusion equation

2.2.7.1 Time varying case: the diffusion coefficient and the absorption time

To determine an explicit expression for the spatial and temporal dependence of the diffuse energy density in a slab of infinite transverse extent and thickness L due to the multiple scattering of a short acoustic pulse, consideration must be given as to what

should constitute the source function, equation (2.80). If we assume a *diffusive* point source at position $r_0 = (x_0, y_0, z_0)$ to deposit a total energy P_0 instantaneously, then

$$\varepsilon(r,t;s) = \frac{P_0}{4\pi}\delta(r-r_0)\delta(t), \tag{2.90}$$

whence, using equation (2.77), the first term in the source function, equation (2.80), yields $E(r,t) = P_0\delta(r-r_0)\delta(t)$. The last term in the source function clearly vanishes, and the second and third terms can be neglected as they represent reduced *incident* intensity sources, and not diffusive ones. Hence,

$$Q(r,t) = P_0\delta(r-r_0)\delta(t). \tag{2.91}$$

The effects of absorption may be decoupled by making the transformation of variables $U \rightarrow Ue^{-t/\tau_a}$ whence equation (2.79) reduces to

$$\frac{\partial U}{\partial t} - D\nabla^2 U = P_0\delta(r-r_0)\delta(t), \tag{2.92}$$

the temporal delta function having subsumed a term e^{-t/τ_a}. The solution to equation (2.92), given the boundary conditions expressed by equations (2.87) and (2.88), has been determined by Carslaw and Jaeger (1959) for the purpose of describing the conduction of heat. In our notation, explicitly including the absorption term, and assuming a unit energy source $P_0 = 1$, the diffuse intensity may thus be described by

$$U(x,y,z) = \frac{e^{-r^2/4Dt}e^{-t/\tau_a}}{2\pi DLt}\sum_{n=1}^{\infty} C_n(z)\, e^{-D\beta_n^2\, t/L^2}, \tag{2.93}$$

with

$$C_n(z) = \frac{\left[\beta_n K\cos(\beta_n z/L) + \sin(\beta_n z/L)\right]\left[\beta_n K\cos(\beta_n z_0/L) + \sin(\beta_n z_0/L)\right]}{\beta_n^2 K^2 + 1 + 2K}, \tag{2.94}$$

and $r^2 = (x - x_0)^2 + (y - y_0)^2$, the transverse distance (i.e. the distance in the direction of infinite extent) from the source position (x_0, y_0, z_0). The values of β_n are given by the positive zeros of the transcendental equation

$$\tan\beta = \frac{2\beta K}{\beta^2 K^2 - 1}, \tag{2.95}$$

and the dimensionless constant K is given by

$$K = h/L, \tag{2.96}$$

where h is determined by equation (2.89) to account for the reflectivity of the boundaries.

The experimentally determined quantity is the transmitted flux normal to the slab (i.e. the acoustic *intensity*, which is proportional to the square of the detected pressure) which is related to the energy density via Fick's law:

$$J(t) = -D\frac{\partial U}{\partial z}. \tag{2.97}$$

The transmitted flux (i.e. the flux evaluated at the boundary $z = L$) for a point source is thus described by

$$J(t) = \frac{e^{-r^2/4Dt} e^{-t/\tau_a}}{2\pi L^2 t} \sum_{n=1}^{\infty} A_n \, e^{-D\beta_n^2 t/L^2}, \tag{2.98}$$

with

$$A_n = \frac{\beta_n \left[\beta_n K \sin\beta_n - \cos\beta_n\right]\left[\beta_n K \cos(\beta_n z_0/L) + \sin(\beta_n z_0/L)\right]}{\beta_n^2 K^2 + 1 + 2K}. \tag{2.99}$$

The transmitted flux due to an incident plane wave, under the assumption that it may be thought to constitute an array of diffusive point sources within the plane $z = z_0$, is found by integrating equation (2.98) over all (x_0, y_0), and is given by

$$J(t) = \frac{2D\, e^{-t/\tau_a}}{L^2} \sum_{n=1}^{\infty} A_n\, e^{-D\beta_n^2\, t/L^2} . \qquad (2.100)$$

Under actual experimental conditions, the incident flux (i.e. the source) is not, of course, a delta function in time, but is rather a function with finite (nonzero) width. To represent the transmitted flux J_{trans} then, requires that the transmitted flux due to an instantaneous source J_{delta} be convoluted with the incident flux distribution J_{in}. Hence

$$J_{trans}(t) = \int_{t_1}^{t_2} J_{in}(t')\, J_{delta}(t - t')\, dt' , \qquad (2.101)$$

where the nonzero extent of the incident pulse is delimited by t_1 and t_2.

2.2.7.2 Steady state case: the transport mean free path

The diffuse energy density under steady state conditions (i.e. when the incident pulse is very long) obeys equation (2.78), the time independent diffusion equation. The appropriate boundary conditions, usually given by equations (2.87) and (2.88), may also be derived *explicitly* for arbitrary scattering anisotropy (i.e. without letting l^* replace l_s, as has been done in the above derivation of the boundary equations) yielding a nonzero term to the right hand sides. Durian (1994) has solved equation (2.78), within the Ishimaru formalism, for a slab of arbitrary thickness and scattering anisotropy; he has neglected the absorption and taken as the source function [see equation (2.78), or equation (2.80) ignoring the time dependence] those terms arising from the reduced incident intensity. The energy density, normalized by the value at the incident wall, was found to be

$$\frac{U(z)}{U(0)} = 1 + \frac{1 - e^{-z/l_s} - zT/l^*}{z_e(1-T)}, \tag{2.102}$$

where T is the total transmission, or fraction of incident flux transmitted through the sample, and z_e is the dimensionless extrapolation length ratio

$$z_e = \frac{2}{3}\frac{1+R}{1-R} = \frac{h}{l^*}, \tag{2.103}$$

as seen from equation (2.89).

Equation (2.102) may be rewritten, with $z = L$, as

$$\frac{U(L)}{U(0)} = 1 - \frac{1}{z_e}\left(\frac{T}{1-T}\right)\frac{L}{l^*} + \frac{1}{z_e}\left(\frac{T}{1-T}\right)\left(1 - e^{-L/l_s}\right), \tag{2.104}$$

in order to more conveniently indicate the physical origin of each factor. The three terms in equation (2.104) correspond, respectively, to the incident energy (normalized to unity), the reduction in energy due to diffusion within and subsequent transmission out of the region $0 < z < L$, and the increase in energy due to that component of the diffusive (scattered) waves that remain in the region. The $(1-T)$ factors normalize the second and third terms to the energy remaining within the region. The z_e factor accounts for the reduction in energy density due to an effective increase in the sample volume caused by the extrapolation of U to zero at a distance h past the boundaries. The L/l^* factor in the second term is the dimensionless actual volume within which the waves propagate (as the volume increases, the energy density decreases). Finally, the $\left(1 - e^{-L/l_s}\right)$ factor in the third term indicates the total diffusive component, only a portion of which remains in the region.

The total transmission T can be thought of as the sum of a ballistic contribution T_b, given by Durian (1994) as e^{-L/l_s} (where he ignores the reflection of the incident wave at the boundary $z = 0$), and a diffuse contribution T_d. The diffusive term has been determined to be (Durian, 1994)

$$T_d = \frac{(1+z_e) - \left(1 + z_e + L/l^*\right) e^{-L/l_s}}{L/l^* + 2z_e}, \tag{2.105}$$

which, for samples sufficiently thick that the exponential term is small, reduces to

$$T_d = \frac{1+z_e}{L/l^* + 2z_e}. \tag{2.106}$$

It is clear that, if the extrapolation length ratio is small, the transmission of multiply scattered waves depends primarily on the sample thickness and on the transport mean free path. However, it is possible for z_e to be quite large if internal reflections are significant, as may be seen from equation (2.89). Since an increase in z_e causes the denominator in equation (2.106) to increase faster than the numerator, the effect of ignoring internal reflections is to *overestimate* the diffuse transmission (Zhu *et al.*, 1991). This indicates quite explicitly the necessity of incorporating the effects of internal reflections into the boundary conditions.

The energy density, equation (2.104), was derived without recourse to the oversimplification of assuming of a diffusive source located a distance z_0 into the sample (as was done in the time dependent case), having properly treated the reduced intensity as the source function. In order to verify the equivalence of these two treatments, we now

derive the transmission under the assumption that the source is strictly diffusive, and located a distance $z = z_0$ into the sample; for convenience, we take $z_0 = l^*$.

Neglecting absorption, the diffuse energy density far from the source position is the solution of the Laplace equation [cf. equation (2.78)]

$$\frac{\partial^2 U}{\partial z^2} = 0. \tag{2.107}$$

Hence, solutions are of the form $U = mz + b$ near the boundaries, where m and b are constants determined by the boundary conditions. Assuming that the diffuse energy density extrapolates to zero a distance $h = z_e l^*$ past the boundaries (as shown previously), and that the diffuse energy density is a maximum C at $z = l^*$, we have $U(-h) = 0$, $U(h + L) = 0$, and $U(l^*) = C$. We thus find

$$m_{z<l^*} = \frac{C}{h + l^*} \tag{2.108}$$

near the boundary $z = 0$, and

$$m_{z>l^*} = \frac{-C}{L + h - l^*} \tag{2.109}$$

near the boundary $z = L$. As the flux is proportional to $\partial U/\partial z$ [cf. equation (2.97)], it is thus determined, near the boundaries, by the constant m. If we denote the magnitude of the transmitted flux by J_T and the magnitude of the backscattered flux by J_B, then the sum $J_T + J_B$ is obviously just the incident flux. The diffuse transmission T_d, which is the fraction of the incident flux transmitted through the sample, is thus

$$T_d = \frac{J_T}{J_T + J_B} = \frac{1 + z_e}{L/l^* + 2z_e}, \tag{2.110}$$

which reproduces equation (2.106) exactly. Equation (2.110) was derived under the assumption that the "conversion" to a diffusive source was complete, which is equivalent to assuming that the sample is sufficiently thick that no ballistic signal remains. If a ballistic signal *does* remain, T_d is no longer equal to the total transmission T, which must now contain a contribution from the reduced incident flux. Furthermore, the magnitude of the diffusive source is reduced by the fraction of the incident signal that is *not* diffusive. Assuming these changes to be proportional to e^{-L/l_s}, the total transmission, valid for all sample thicknesses, is

$$T = \frac{(1+z_e)-(1-z_e)e^{-L/l_s}}{L/l^* + 2z_e}, \tag{2.111}$$

where the prefactor of the exponential arises from the normalization condition that the transmission approach unity in the limit of very small L. The diffuse component T_d is obtained from the above upon subtraction of the ballistic component T_b and reproduces equation (2.105) exactly.

To summarize, in figure 2.8 we illustrate the diffuse energy density, under the assumption of zero boundary reflectivity and isotropic scattering, for a sample ten mean free paths thick. The existence of an extrapolation length is clearly demonstrated by the tangents to the energy density at the boundaries. The intersection of the tangent lines at $z = l^*$ demonstrates the equivalence of the diffusive source at this position with the more rigorous reduced intensity source.

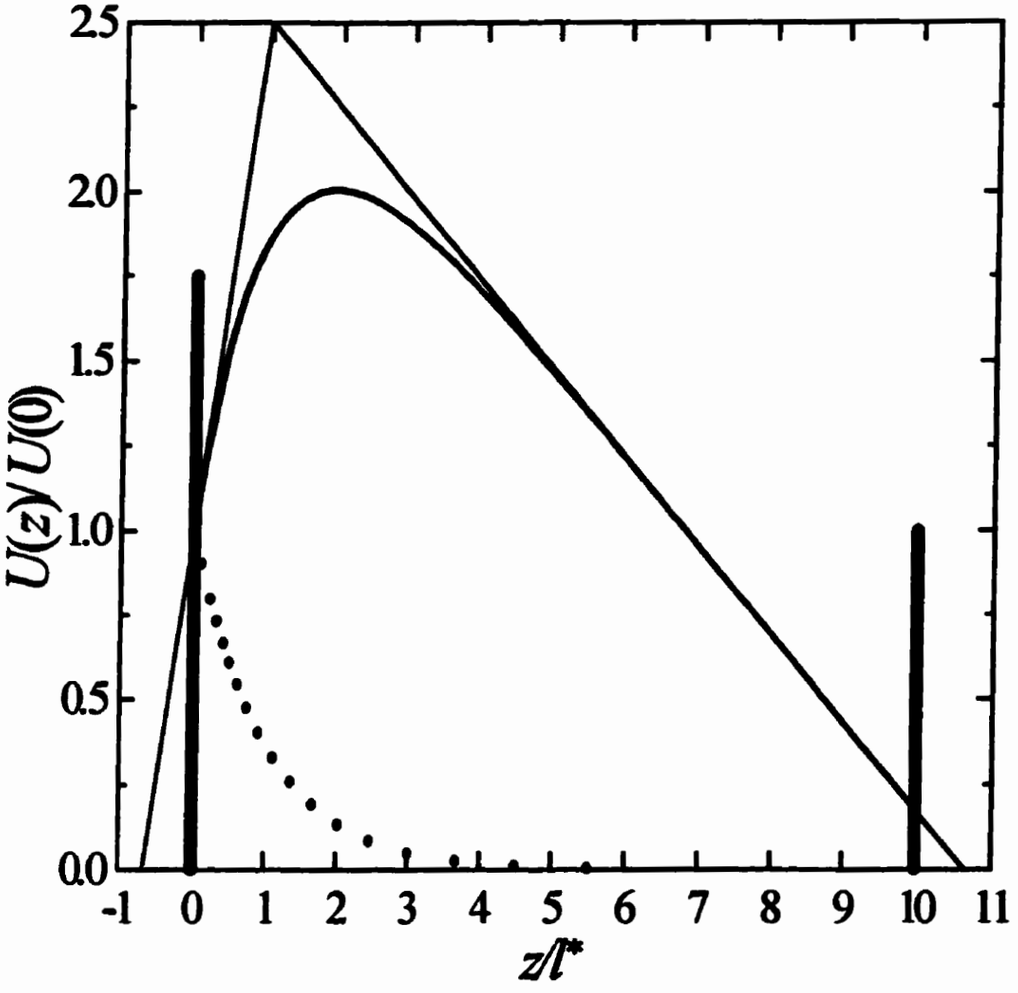

Figure 2.8 Diffuse (bold) and ballistic (dotted) energy densities versus transverse distance through a slab ten mean free paths thick, for the case of isotropic scattering and zero boundary reflectivity. The lines tangent to the energy density at the boundaries $z = 0$ and $z = L$ intersect at $z = l^*$ and go to zero a distance $h = z_e l^*$ past the boundaries, where $z_e = \frac{2}{3}$ is called the extrapolation length (Durian, 1994).

It is clear from equation (2.105) that measurements of the diffuse transmission allow one to determine the transport mean free path l^*, and hence the energy velocity v_e (provided the diffusion coefficient D is known from pulse measurements). However, the above derivation does not consider the effect of absorption on the transmission. As the determination of l^* requires the measurement of the *absolute* transmission, it is most critical that absorption be included, especially since it is *not* negligible in typical experiments. This inclusion can be accomplished most directly by using the angular correlation function calculated (for an equivalent geometry and identical boundary conditions) for diffusing *light* in the presence of absorption (Zhu *et al.*, 1991). Evaluating their expression at zero wave vector, we obtain

$$g_1(\tau_a) = \frac{\left(\frac{L+2h}{z_0+h}\right)\left[\sinh(z_0\alpha)+z_e\alpha\cosh(z_0\alpha)\right]}{\left(1+h^2\alpha^2\right)\sinh(L\alpha)+2z_e\alpha\cosh(L\alpha)}, \tag{2.112}$$

where

$$\alpha = (D\tau_a)^{-1/2}. \tag{2.113}$$

Incorporating absorption, the total transmission should thus be the product of equations (2.111) and (2.112), *vis.*

$$T = g_1(\tau_a)\frac{(1+z_e)-(1-z_e)e^{-L/l_s}}{L/l^*+2z_e}. \tag{2.114}$$

That equation (2.114) does indeed properly express the absolute transmission in the presence of absorption may be verified by returning to the pulse geometry. If equation (2.100), which gives the transmitted flux resulting from an incident delta-function plane

wave, is convolved with the incident flux for a "pulse" of infinite temporal extent [cf. equation (2.101)], then the resultant flux, or transmitted intensity, is given by

$$T = 2\sum_{n=1}^{\infty} \frac{A_n}{(L\alpha)^2 + \beta_n^2} , \tag{2.115}$$

with β_n, A_n, and α, as defined in equations (2.95), (2.99), and (2.113), respectively. Equations (2.114) and (2.115) have been evaluated, using as parameters typical values for the sample thickness, mean reflection coefficient, diffusion coefficient, absorption time, and scattering and transport mean free paths. There was agreement within 0.1%, the slight difference arising from the roundoff error inherent in solving the transcendental equation for β_n, and the truncation of the summation in equation (2.115) after 50 terms. The analytic form for the absolute transmission, equation (2.114), is preferred over the series solution, equation (2.115), not only for the clarity with which it illuminates the physics (the effect on the transmission by the variation in the physical parameters is more readily apparent), but also for aesthetic reasons.

2.2.8 Predicting the transport mean free path, the energy velocity, and the diffusion coefficient, using the GCPA

The three parameters that characterize the wave transport in the diffusive regime, the transport mean free path l^*, the energy velocity v_e, and the diffusion coefficient D, are related through equation (2.66), to wit: $D = \frac{1}{3} v_e l^*$. The effective medium model, originally developed for ballistic propagation (Sec. 2.1), is extended to account for the

angular dependence of the scattering delay experienced by a wave *pulse*, thus relating the two transport processes.

The characteristic length scale for diffusive transport is the transport mean free path, whereas for ballistic transport it is the scattering mean free path; the relation between these two quantities is given by equation (2.67). To evaluate the configurationally-averaged cosine of the scattering angle, we return to the scattering cross section σ, which was previously written in terms of the forward scattering amplitude via the optical theorem [equation (2.62)]. We consider instead the complex scattering amplitude $f(\omega,\boldsymbol{k},\boldsymbol{k}') \equiv f(\omega,\theta)$ at *all* angles, where θ is the scattering angle (i.e. the angle between the incident wave vector $\boldsymbol{k}$ and the scattered wave vector $\boldsymbol{k}'$) [equation (2.52)]. The scattering cross section may thus be written as the integral of the square of $f(\omega,\theta)$ over all solid angles, and l_s then calculated from equation (2.63). The lengthening of the effective random walk step size due to the scattering anisotropy is accomplished by including the $1-\cos(\theta)$ term in the integral. The transport mean free path is then given by

$$l^* = \left\{ n_s \int (1-\cos(\theta)) \left| f(\theta) \right|^2 d\Omega \right\}^{-1} . \qquad (2.116)$$

The scattering mean free path may, of course, be given by the same expression without the $1-\cos(\theta)$ factor.

In addition to the scattering mean free path, the propagation of the ballistic pulse was described by both the phase and group velocities, which were shown to depend on the scattering in the medium (Sec. 2.1.8). The Amsterdam group has suggested (van Albada *et al.*, 1991) that very strong resonant scattering can so modify the values of these

velocities, which rely on the coherence of the incident wave, that they no longer retain physical significance. Their calculations have demonstrated an anomalous dispersion in the group velocity (i.e. velocities greater than the speed of light), thus implying that v_g loses its meaning as a velocity of energy transport. It then becomes imperative that a meaningful propagation velocity be defined for the diffusive transport.

The Amsterdam group was the first to correctly point out that the velocity appearing in the diffusion coefficient [equation (2.66)] is neither the phase velocity nor the group velocity but instead a *transport* velocity. In order to explain the observed low value of v_e (van Albada *et al.*, 1991), they derived a microscopic theory based on the generalized Boltzmann equation and evaluated in the low concentration limit (van Albada *et al.*, 1991; van Tiggelen *et al.*, 1992). This allowed v_e to be determined by the energy flux approach proposed by Brillouin (1953, 1960). Their expression for the energy velocity may be written as

$$v_e = \frac{v_0^2}{v_p(1+\delta)}, \tag{2.117}$$

where v_0 is the phase velocity in some homogeneous reference medium, v_p the phase velocity in the effective medium, and δ a propagation delay induced by the strong resonant scattering (van Albada *et al.*, 1991; van Tiggelen *et al.*, 1992; see also Sheng, 1995). Calculations by this group at low volume fractions Φ of scatterers have correctly accounted for the extremely low value of v_e found in their light scattering experiments. In addition, they have predicted a strong frequency dependence to the energy velocity in the neighbourhood of Mie resonances. This strong slowing down at frequencies associated

with the internal scatterer resonances is associated with the temporary storage of wave energy in the scatterer (van Tiggelen, 1992; van Tiggelen *et al.*, 1992; Cwilich and Fu, 1992; Kogan and Kaveh, 1992; van Tiggelen and Lagendijk, 1993; Livdan and Lisyansky, 1996), and, in their theory, results in propagation delays $\delta >> 1$. However, these predictions begin to lose their validity with increasing Φ (Soukoulis *et al.*, 1994), as expected for low concentration theories.

Recent efforts involving CPA calculations to resolve this deficiency at the higher volume fractions, based on earlier suggestions by Sheng (Sheng, 1995), have implied that the large frequency variations in v_e are actually washed out with increasing Φ (Busch and Soukoulis, 1995, 1996; Kafesaki and Economou, 1997). These results are alleged to be in excellent agreement with the limited experimental data for v_e published to date (Genack *et al.*,1993; Page *et al.*, 1995). However, the inherent limitations of the CPA have not been overcome in these calculations, and their conclusions are thus suspect. Recall that the CPA is essentially a long wavelength theory so not only is the scattering weak, but the wave cannot resolve the individual scatterers. The self-energy is then dependent purely on frequency, and the CPA condition [equation (2.33)] may be confidently applied. In the intermediate frequency regime, the wavelength is comparable to the size of the scatterers and strong resonant scattering can occur. The self-energy can then acquire a wave vector dependence (Sec. 2.1.6.3), and the CPA renormalization of the self-energy into a purely frequency dependent velocity is no longer valid.

To quantitatively calculate v_e in the intermediate frequency regime, the GCPA is employed to calculate the delay of the wave pulse scattering from the coated sphere.

While the GCPA calculations of v_g capture this delay in the forward direction, it is the angular dependence of the scattering delay that causes v_e to differ from v_g. The complex scattering amplitude for a single coated-sphere is first found for each scattering angle and frequency. A reference pulse $r(t)$, chosen to have a Gaussian envelope containing the frequency spectrum of interest, is constructed, and $R(\omega)$, the complex FFT of the pulse, then determined. At each angle θ, the scattered wave pulse $s_\theta(t)$ is found from the inverse FFT of the product of $R(\omega)$ and $f(\omega,\theta)$ as

$$s_\theta(t) = \frac{1}{\sqrt{2\pi}} \int_0^\infty e^{-i\omega t} R(\omega) f(\omega,\theta)\, d\omega . \tag{2.118}$$

At each angle, the scattering delay $\Delta t(\theta)$, with respect to the forward scattered component, is determined from the difference between the temporal positions of the maxima of the wave form envelopes. The intensity-weighted angular averages of these delays are then calculated as

$$\Delta t_{ave} = \frac{\int_0^{\pi/2} \Delta t(\theta)\, I(\omega,\theta) \sin(\theta)\, d\theta}{\int_0^{\pi/2} I(\omega,\theta) \sin(\theta)\, d\theta}, \tag{2.119}$$

where I is the intensity of the scattering amplitude. Equation (2.119) gives the retardation (or advancement, if negative) of the scattered pulse envelope relative to the forward direction. As v_e is the average velocity of waves whose direction of propagation has been altered many times by the scattering, the energy velocity may be expressed, to a good approximation, as

$$v_e = \frac{l^*}{l^*/v_g + \Delta t_{ave}}. \tag{2.120}$$

Equation (2.120) may be rewritten as

$$v_e = \frac{v_g}{1+\delta_m}, \tag{2.121}$$

with

$$\delta_m = \frac{\Delta t_{ave}\, v_g}{l^*}, \tag{2.122}$$

in principle, also frequency dependent. Equation (2.121) is similar in form to the expression first proposed by the Amsterdam group [equation (2.117)], although in our case δ_m is *small*, as v_g and Δt_{ave} are calculated in a renormalized effective medium to properly account for the effects of multiple scattering. Having predicted l^* and v_e, the frequency dependence of the diffusion coefficient follows from $D = \frac{1}{3} v_e l^*$ [equation (2.66)].

The theoretical description of the transport of the multiply scattered sound within the diffusion approximation will allow critical experimental tests to be performed regarding its validity. The experimental determination of the parameters that characterize this transport may then be compared to predictions arising from an extension of the new effective medium approach that describes the *ballistic* transport. From this will emerge a comprehensive physical picture of the ballistic and diffusive propagation, in the intermediate frequency regime, of acoustic waves through random media .

3 The scattering medium

3.1 Sample preparation

In order to study the propagation of sound in the intermediate frequency regime, samples consisting of glass beads immersed in water were prepared. Strong scattering was thereby ensured as the acoustic impedance ratio is approximately 10. The scattering was further enhanced by choosing the glass bead diameter to be the same order of magnitude as the acoustic wavelength in water. To cover a larger frequency range, two different bead sizes , with nominal radii of 0.25 mm and 0.5 mm, were used. The bulk of the measurements were, however, made on the 0.5 mm radius beads. The glass beads were contained in disk-shaped cells having parallel walls glued to a uniform spacer ring; this ring formed the outer circumference of the disk and had a diameter that was at least ten times larger than the cell thickness, which varied from about 2 mm to 25 mm (see figure 3.1). The cell walls usually consisted of 1.5 mm or 3 mm polystyrene plates (depending on the sample diameter), but 25 mm thick acrylite walls were found to be necessary for some of the group velocity measurements so as to preclude any possibility of interference from round-trip echoes in the wall. The beads were carefully packed into the water-filled sample cells so as to avoid trapped air bubbles, which would have caused significant additional absorption, obscuring the propagation of the multiply scattered sound. The beads were packed near the limit of random close packing, or about 63%, though for the thinnest samples with the rigid acrylite walls, occupied volume fractions as low as 55% were measured.

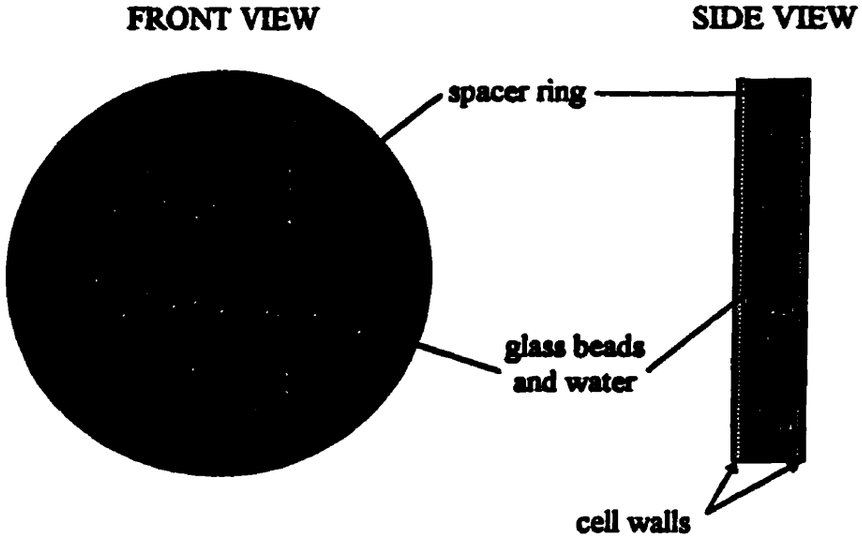

Figure 3.1 Interior views of a typical sample cell.

Range of bead radii (mm)	Fraction
0.350–0.425	0.117
0.425–0.450	0.542
0.450–0.500	0.311
0.500–0.590	0.030

Table 3.1 Glass bead distribution

3.2 Glass bead polydispersity

Two different sample sets were prepared in order to investigate the effects of the glass bead polydispersity upon the sound propagation. The nominally 0.5 mm radius glass beads ranged from a minimum radius of 0.35 mm to a maximum radius of 0.59 mm. These beads were sieved in order to determine their size distribution, shown in table 3.1. The bead distribution was found to be reasonably well described by a Gaussian distribution of width 0.07 and centre 0.45 (figure 3.2), implying a polydispersity of about 15%. The smaller beads had a similar variation in size. The sieved bead samples were made using beads from the flattest part of the distribution, namely the 0.45–0.5 mm range. The mean radius of the beads in this range was taken to be 0.47 mm, and the polydispersity was estimated at about 5%.. The smaller beads were not sieved.

3.3 Gelled bead samples

It is necessary to know the effect of the cell walls on the absolute transmitted intensity of sound through the sample, as the walls were merely used to define the sample geometry. In order to maintain the sample geometry in the absence of walls, the water in the sample was replaced by a polyacrylamide gel, and the ratio of the transmissions, with and without walls, determined. Due to the dilute concentrations of the gels used, this procedure was limited to samples of thickness greater than about 7 mm in order to avoid bowing and catastrophic structural failure.

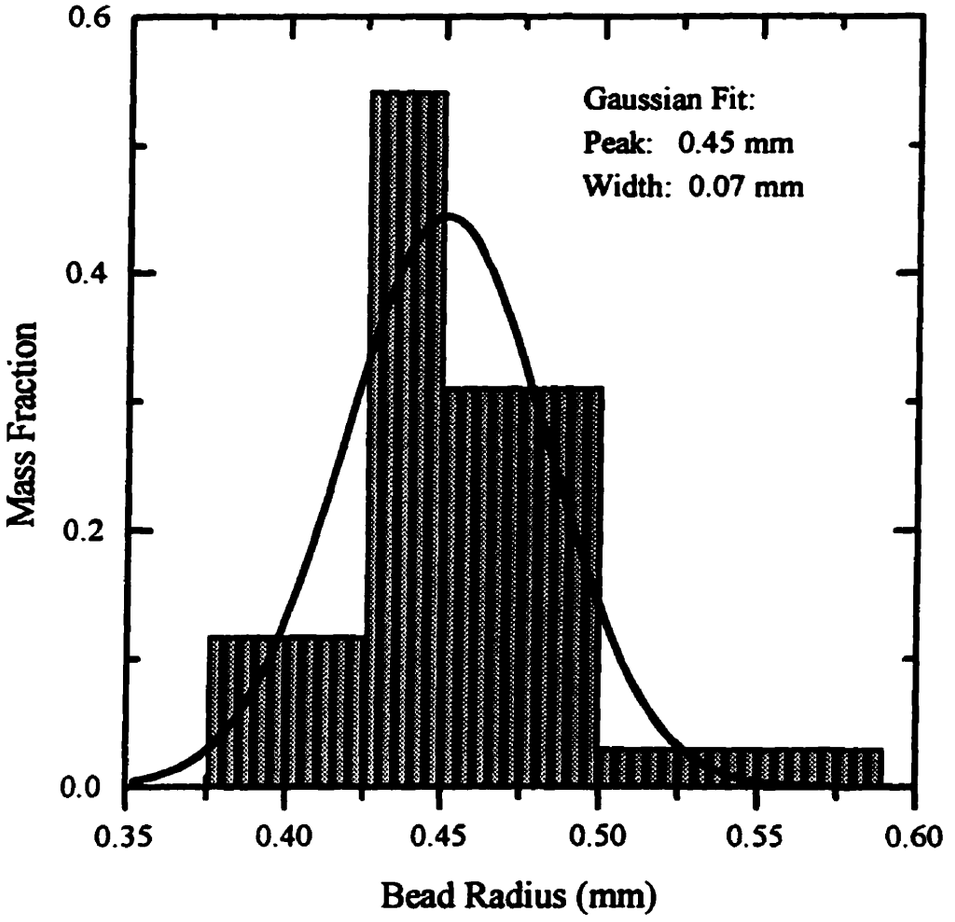

Figure 3.2 Glass bead size distribution. The histogram has been fitted to a Gaussian of centre 0.45 and width 0.07.

Gels of acrylamide (the monomer) and N,N'-methylenebisacrylamide (the cross-linking monomer) were made with a total monomer concentration of 5 g/100 mℓ and a cross-linker density of 2.6% by free radical polymerization in water (Bansil and Gupta,

1980) using 30 mg/100 mℓ of ammonium persulfate as an initiator and 120 μℓ/100mℓ of N,N,N′,N′-tetramethylethylenediamine (TEMED) as a catalyst. Polymerization was essentially complete after about 20 minutes, producing a clear gel. The samples were usually cured for an additional day, to ensure that the reaction had proceeded to completion, before measurements were performed.

3.4 Material parameters

The longitudinal and shear velocities of the glass spheres, acquired from Potters Industries Inc. (NJ)., were needed in order to theoretically describe the sound propagation. These values were determined from the technical specifications supplied by the manufacturer, namely, a density of 2.5 g/cm^3, a Poisson's ratio of 0.21, a Young's modulus of 6.89x10^{10} N/m^2, and a shear modulus of 2.96x10^{10} N/m^2. The longitudinal and shear velocities were then calculated to be 5600 m/s and 3400 m/s, respectively.

Timing corrections to the measured sound required knowledge of the transit time through the cell walls and the water. The polystyrene and acrylite used to construct the walls were found to have longitudinal velocities of 2120 m/s and 2740 m/s, respectively. The accepted value for the sound velocity in pure water at a room temperature of 20 °C is 1490 m/s.

4 Experimental

4.1 Introduction

The description of the propagation of ultrasonic waves in the strongly scattering glass-bead samples required the measurement of both the scattered and the unscattered sound intensity. These were acquired by placing a generating transducer near one face of the sample and measuring the transmitted sound with a second transducer at the opposite face. The experiments were performed in a tank of water, which provided a convenient coupling medium between the transducers and the sample cell and allowed their relative positions to be readily varied. The dimensions of the water tank were large enough to eliminate interference problems due to stray scattered signals such as side-wall reflections. Measurements of the scattered sound were accomplished with the use of a miniature hydrophone as the detecting transducer, thus ensuring that the sound was detected over a single coherence area, or speckle spot; this was essential to avoid phase cancellation of the detected scattered wave across the face of the hydrophone which would greatly reduce the signal (see Sec. 4.2.5 and Appendix B.2.2). Measurements of the unscattered, or ballistic, sound were accomplished with large element diameter planar wave transducers.

The experiments were performed in both point source and planar wave source geometries to verify the consistency of the description of the ensemble-averaged transmitted sound pulse. For the point source geometry, the incident sound pulse was generated by a focusing transducer arranged so that its focal plane was coincident with the input face of the sample. The detecting hydrophone was placed close to the opposite face of the sample, on-axis with the generating transducer. Signals from statistically

independent ensembles of the glass-bead disorder were then collected by translating the sample. For the planar wave geometry, a good approximation to a planar wave source was achieved by placing the sample deep in the far field of a planar wave generating transducer (see Sec. 4.2.2, 4.2.3). Here, the sample remained fixed and the hydrophone was scanned over the central portion of the back face to collect the transmitted sound in many speckles. The same planar wave geometry was used in the measurements of the absolute transmission of the sound in a quasi-continuous-wave configuration.

4.2 Ultrasonic wave generation and detection

4.2.1 Piezoelectric effect

The sound incident on the sample was generated with an ultrasonic transducer. These transducers employed the piezoelectric effect to convert the electrical energy of an electromagnetic excitation into the mechanical energy of an ultrasonic vibration. When subjected to an electric field, piezoelectric materials exhibit a linear property manifested by the onset of deformation. The electric field causes an asymmetry in the ionic polarization, the piezoelectric effect arising due to an interaction between the Coulomb forces and the elastic restoring forces in the material. The inverse behaviour also holds true, namely, that the application of a mechanical stress is manifested by the onset of electrical polarization, resulting in the generation of an electric field. Transducers may thus be used to both generate *and* detect sound waves.

4.2.2 Disk radiator

Let us consider an idealized transducer, comprised of a circular thin planar piezoelectric body of radius R, whose circumference is constrained to be rigidly fixed. The application of a sinusoidally-varying current on the piezoelectric body results in a matching variation in its particle velocities v_0, which we take to be uniform across the surface of the disk. We assume this disk radiator to be immersed in a fluid of mass density ρ_m, and having a phase velocity v_l. The sinusoidally-varying velocity of the radiator launches a hydrostatic pressure wave of amplitude p into the fluid. The intensity I of this wave exhibits maxima and minima (radially outwards from the disk) as a consequence of

the interference effects between waves originating along the continuum from the edge of the disk to its centre.

The intensity may be determined from a knowledge of the complex Poynting vector $\tilde{\Pi}$ (derivable on the basis of conservation of energy principles), which here describes the energy propagation in a fluid medium in terms of the complex velocity $\tilde{v}$ and the complex pressure $\tilde{p}$:

$$I = \mathrm{Re}\left(\tilde{\Pi}\right) = \frac{1}{2}\mathrm{Re}\left(\tilde{p}\cdot\tilde{v}\right), \tag{4.1}$$

where Re implies that the real part of the complex quantity is to be taken. The quantities involved are complex as a result of assuming time-harmonic excitations of the form $e^{i\omega t}$, where ω is the angular frequency of the excitation. Along the longitudinal axis z of the disk, the normalized intensity is given by (Ristic, 1983)

$$\frac{I_z}{I_{max}} = \left(1 + \frac{z}{\sqrt{z^2 + R^2}}\right)\sin^2\left\{\frac{\pi}{\lambda}\left[\sqrt{z^2 + R^2} - z\right]\right\}, \tag{4.2}$$

where λ is the wavelength of the excitation in the fluid. Recall that $k = \omega/v_l = 2\pi/\lambda$ defines the wave vector of the excitation. Defining the acoustic impedance of the fluid as $Z_l = \rho_m v_l$, the maximum intensity may be written as $I_{\max} = Z_l v_0^2$.

The maxima in equation (4.2) occur for values of z given by

$$z_{max} = \frac{4R^2 - \lambda^2(2n+1)^2}{4\lambda\,(2n+1)}, \tag{4.3}$$

where $n = 0, 1, 2, \ldots$; the last axial maxima occurs for $n = 0$ and is given by

$$z_F = \frac{4R^2 - \lambda^2}{4\lambda}, \tag{4.4}$$

which, for disk diameters significantly greater than the wavelength, may be approximated by

$$z_F = \frac{R^2}{\lambda}. \tag{4.5}$$

The quantity z_F defines the transition between the near field, or Fresnel zone ($z < z_F$), and the far field, or Fraunhofer zone ($z > z_F$). As is seen in figure 4.1, the axial intensity in the Fresnel zone exhibits many maxima and minima, while in the Fraunhofer zone, the axial intensity is slowly decreasing, due to spherical beam divergence.

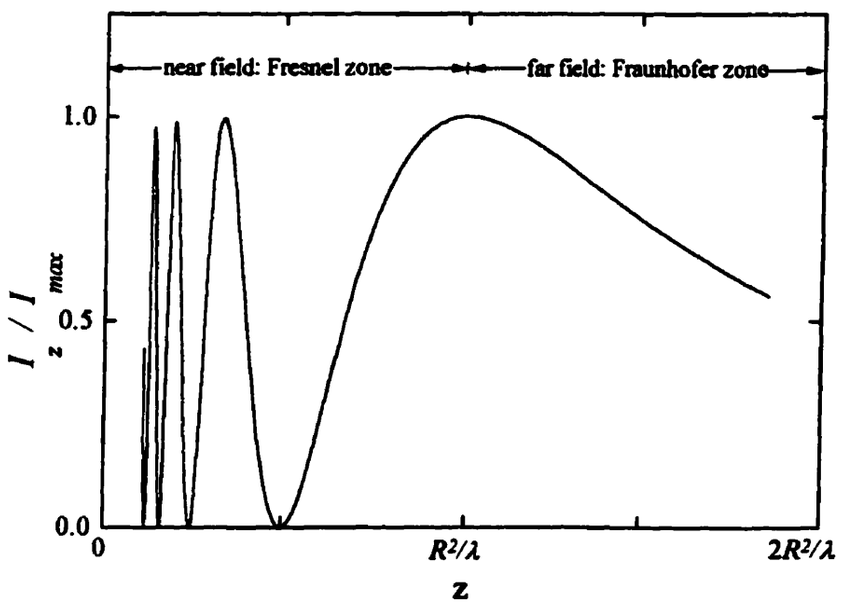

Figure 4.1 The axial intensity of an idealized transducer.

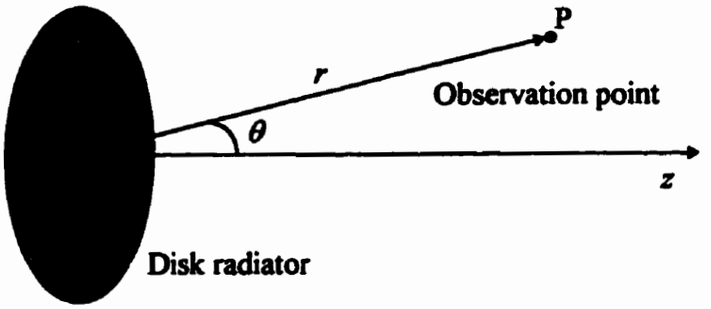

Figure 4.2 Geometry used in the description of the radial variation in the sound intensity for an ideal transducer.

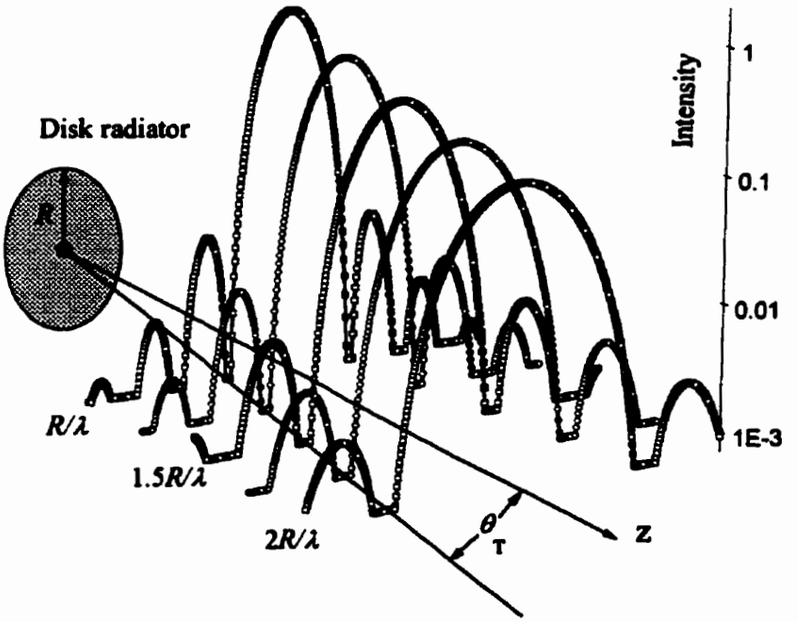

Figure 4.3 Log plot of the far field intensity at positions normal to the axis of propagation. The spherical beam divergence semi-angle θ_T is as shown. The flat regions around the zeros are an artifact of the logarithmic plot.

The variation in the far field intensity for off-axis positions $r = r(\rho, \theta, z)$, where r is the distance from the centre of the disk to the observation point P, ρ the radial distance normal to the z axis, and θ the polar angle (see figure 4.2), has been given as

$$\frac{I_r}{I_{max}} = \left(\frac{kR^2}{2r}\right)^2 \left[\frac{J_1(kR\sin\theta)}{kR\sin\theta}\right]^2, \tag{4.6}$$

where J_1 is the first order Bessel function (Ristic, 1983). This variation is shown in figure 4.3, for axial positions $1 < z_F < 2$. The logarithmically plotted intensity initially decreases with increasing polar angle θ, the first zero occurring at $kR\sin\theta_T = 3.83$ (i.e. at $\sin\theta_T = 0.61\lambda/R$), where θ_T is the theoretical beam divergence semi-angle. Equation (4.6) is not valid in the near field due to certain approximations made in developing a closed algebraic expression for the pressure, from which the intensity is derived. A description of the variation in the near field intensity for a disk radiator (off axis positions) requires some fairly involved numerical integration and differentiation (see Ristic, 1983).

4.2.3 Planar transducers

The transducers used in the experiments employed piezoelectric elements made from PZT (lead zirconium titanate) to generate clearly defined longitudinal acoustic waves that faithfully reproduced the driving electromagnetic waves. To see how this was accomplished, consider the pulsed excitation of a planar piezoelectric element placed between materials with differing acoustic impedances. The piezoelectric element generates a vibration that propagates in both the forward and reverse directions. The element has an acoustic impedance mismatch with its surroundings so reflections occur at

the interfaces, causing interference with the desired waveform and increasing the temporal extent of the pulse. As PZT is not highly attenuating, the problem is exacerbated by round-trip echoes (due to multiple reflections) in the element. However, as long as the thickness of the piezoelectric element is an integer multiple of half wavelengths (for the transducers used, the element thickness was nominally one-half the wavelength at the transducer's central frequency), the interference will be constructive and the transmitted intensity will be a maximum. The increase in the temporal extent of the pulse, due to the extra time required for the reflected pulse(s) to traverse the element before combining with the initial pulse, describes the phenomena of transducer *ringing* and has been mitigated by *backing* the piezoelectric element (figure 4.4). The backing is a highly attenuative material whose acoustic impedance is comparable to that of the piezoelectric element. The backing absorbs the acoustic energy radiating from both the back face (directly) and the front face (upon reflection) of the element, thus minimizing ringing.

If the piezoelectric element were immersed in water, then the front face of the PZT would see a substance much lower in acoustic impedance. Most of the acoustic energy would then be reflected back into the transducer and the sound field in the water would then of greatly reduced intensity. To avoid this reduction in signal, an acoustic transformer (i.e. a matching layer) is inserted between the piezoelectric element and the water. The matching layer, which also serves as a wear plate (thus protecting the piezoelectric element), has a thickness of one-quarter wavelength and an impedance intermediate between that of the PZT and the water. The choice of thickness is dictated

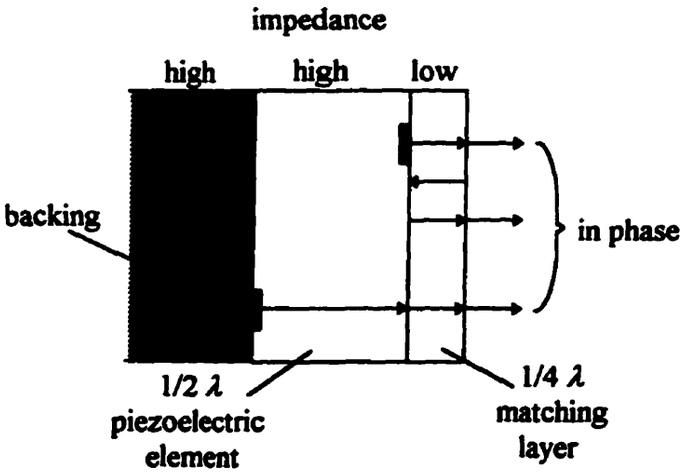

Figure 4.4 The matching layer on the generating face of the piezoelectric element employs the principle of constructive interference to increase the transmission of sound into the fluid medium (of lower impedance). The backing is also shown.

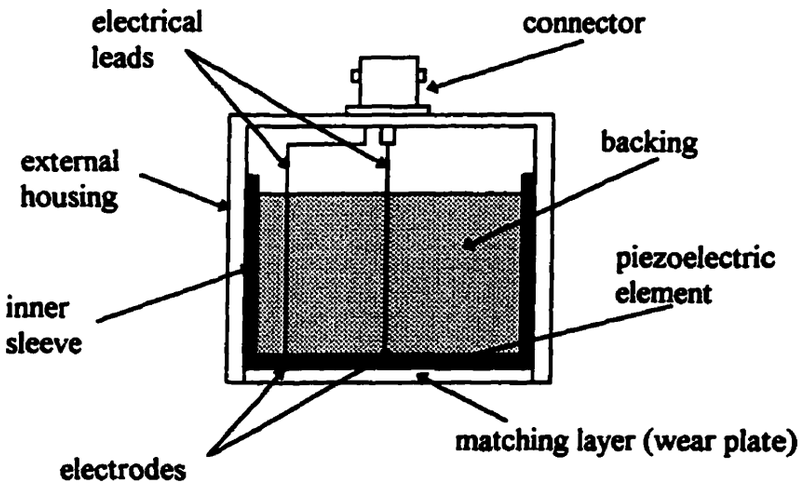

Figure 4.5 Simplified schematic of the planar transducers used in the experiments.

by the requirement that waves generated by the piezoelectric element interfere constructively with waves reverberating in the matching layer, as shown in figure 4.4. A simplified schematic of the planar transducers used is shown in figure 4.5.

4.2.4 Focusing transducers

The near field point z_F may be thought of as the natural *focus* of a planar transducer, as it is at this point that the intensity is a maximum and that the wave front may begin to be considered spherical. It is, of course, an extremely *poor* focus – by no stretch of the imagination may the sound waves be thought of as originating from a point source at this position (cf. figure 4.3). A spherical point source of acoustic waves is, however, a very desirable thing to have. Such a source may be achieved by combining a planar transducer and an acoustic lens. The effect of the lens is to effectively shift the location of the near field point closer to the transducer, and to increase the pressure (and hence the intensity) at that point.

In order to minimize energy losses, the acoustic impedance of the lens, $Z_L = \rho_L v_L$, was comparable to the acoustic impedance of the surrounding water, $Z_W = \rho_W v_W$, where ρ_L and ρ_W are the mass densities, and v_L and v_W the (longitudinal) acoustic velocities, of the lens and water respectively. From Snell's law, the focusing process requires $v_L \neq v_W$. The acoustic converging lenses associated with the focusing transducers used were concave since the acoustic velocity of the lens is greater than that of the water.

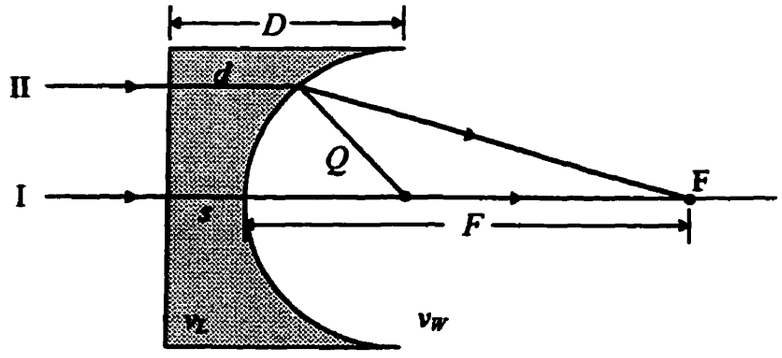

Figure 4.6 Plano-concave lens with spherical surface of radius Q (Ristic, 1983).

The plano-concave lens, with the concavity defined by a spherical surface of radius Q, replaces the wear plate on a planar transducer. Only spherical surfaces are considered because there are economical restrictions on manufacturing the more appropriate parabolic surfaces. Consider such a lens, shown in figure 4.6. For plane acoustic waves incident normally from the left, the focal distance is determined by the requirement that all waves be of equal phase at the focal point. Employing the ray technique of geometrical acoustics, and requiring that rays I and II have zero phase difference at F, it follows that

$$\frac{F}{v_W} = \frac{d-s}{v_L} + \frac{1}{v_W}\left[(f-d+s)^2 + 2Q(d-s) + (d-s)^2\right]^{1/2}, \tag{4.7}$$

or

$$F = \frac{Q}{1-v_W/v_L} - \frac{(d-s)(v_W/v_L)^2}{2(1-v_W/v_L)}. \tag{4.8}$$

In figure 4.6, ray II traversed a distance d in the lens. Since ray II was chosen arbitrarily, d may vary anywhere from a minimum of s to a maximum of D. Equation (4.8) thus implies that one does not actually have a focal *point*, but rather a focal *line*. This line,

even for ideal lenses, is actually of finite width due to the limitations imposed by diffraction, thus implying that it is more appropriate to speak about a focal *zone*.

For the spherically-focused immersion transducers employed in these experiments, the length F_Z of the effective focal zone (as measured from the positions where the on-axis sound *amplitude* is 6 dB down from its maximum) is (Panametrics, 1993)

$$F_Z \cong \frac{4F^2}{F + 2z_F}, \tag{4.9}$$

where F is the *nominal* focal point placed at the position of the on axis maximum. The 6 dB beam diameter D_B at the nominal focus has likewise been determined as

$$D_B \approx \frac{RF}{2z_F}. \tag{4.10}$$

Typical values for these parameters are on the order of centimeters for the length of the focal zone, and on the order of millimeters for the beam diameter. These parameters are illustrated in figure 4.7.

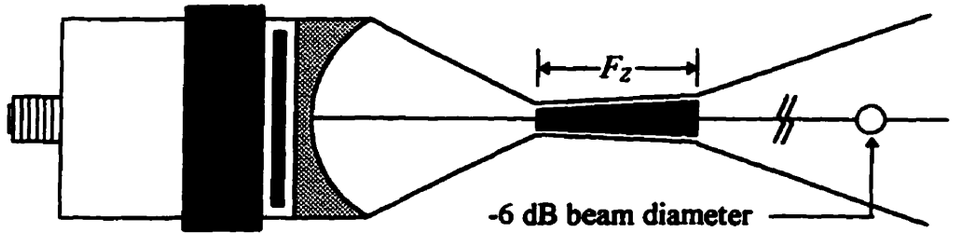

Figure 4.7 Practical spherical focused immersion transducer with the focal zone and beam diameter indicated (Panametrics, 1993).

4.2.5 Hydrophones

The hydrophones used in the experiments are a particular class of highly sensitive small-element-diameter transducers designed to provide good spatial resolution when detecting acoustic waves in fluids. Since only longitudinal waves propagate in fluids, the piezoelectric material used in these hydrophones must have negligible coupling to transverse modes. This minimizes problems with mode conversion that can seriously interfere with the desired signal. The choice of PZT as the piezoelectric material proved ideal. The piezoelectric element was heavily backed (i.e. placed in contact with a long, highly attenuating, substance) with a matched acoustic impedance material to avoid problems with multiple round trips and ringing. By keeping the piezoelectric element very thin, the hydrophone operated in the subresonant mode thus providing a large frequency bandwidth with a flat sensitivity. For the frequency range from 1 to 20 MHz, hydrophones with piezoelectric elements having diameters as small as 200 μm and thicknesses as low as 70 μm are the current state-of-the-art. Their angular response tends to be excellent (see Sec. 4.3.3.2.2 and Appendix B.2.1). Figure 4.8 gives a simple schematic of such a hydrophone, which is usually covered with a fine gold film for electrical isolation, followed by a thin water resistant coating.

The necessity of employing a small-element-diameter hydrophone results from the rapid spatial variations in the phase and amplitude of the scattered sound caused by interference between ultrasonic waves that have traveled different paths through the sample. This variation produces the familiar phenomena of speckle (see Sec. 5.3). The speckle size, or coherence area, is the region over which the ultrasonic signal remains relatively constant; this is approximately λ^2, where λ is the ultrasonic wavelength (Jones,

1996; see also Sec. 5.3). Since piezoelectric transducers measure the ultrasonic *field* (i.e. the pressure wave), it is necessary to detect the scattered sound within a single coherence area in order to avoid spurious phase cancellation effects due to these rapid spatial fluctuations. In water, for frequencies ranging from 1 to 5 MHz, the wavelength varies between 1.5 mm and 0.3 mm. Thus, hydrophones with element diameters less than 0.3 mm are necessary to accurately measure the scattered sound within this frequency range (see, however, Sec. 4.3.3.2.3 and Appendix B.2.2).

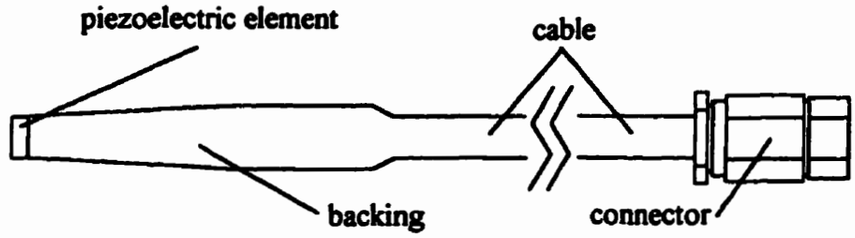

Figure 4.8 Schematic of the type of hydrophone used in the experiments.

4.3 Measurement technique and geometries

4.3.1 Determining the phase and group velocities, and the scattering mean free path. Ballistic pulse mode: planar source geometry

Experiments were performed to measure the phase and group velocities, and the scattering mean free path, of ballistic pulses propagating in the resonantly scattering glass-bead medium. The frequency of the sound, generated by large-element-diameter planar transducers, was varied between 1 and 5 MHz. The samples consisted of both the sieved and unsieved beads, where for the unsieved beads both sizes were used to increase the effective frequency range. The velocities of ballistic propagation were measured using a square input pulse consisting of about 10 oscillations thus giving a well-defined central frequency. The scattering mean free path was determined, using an input pulse consisting of only one or two oscillations so as to increase its frequency content, from the attenuation of the frequency components of the ballistic pulse. The detectors used were also large-element-diameter planar transducers, arranged so as to be coplanar with the generator. The sample was placed between the two transducers, parallel to their faces. Figure 4.9 shows the experimental setup for the ballistic pulse measurements in the plane wave geometry.

The distance from a transducer face to the nearest sample wall was usually within the transducer's near field, though not so close that round trip echoes between the two would interfere with the ballistic signal. Recall that within the near field, the intensity of

the wavefront incident on the sample face may then vary extensively (cf. figure 4.1). However, as the concern is with the *unscattered* transmission through a *macroscopically* homogeneous medium, these intensity variations will be preserved in the signal ballistically transmitted through the sample. A similar large-element-diameter planar transducer, correspondingly positioned, acted as a detector and averaged these variations in the ballistically transmitted signal in the same manner as it did for the reference pulse (i.e. the sound pulse incident on the sample face). Thus, an accurate measure of the ballistic attenuation could be made to determine the scattering mean free path. Operating the detector close to the sample face had the further advantage of minimizing the amount of scattered sound, obliquely incident on the detector, arising from regions of the sample not directly illuminated by the incident wave. Of course, the scattered sound arising from the region directly in front of the detection face cannot be minimized, and many individual speckles thus impinge on the detector. These, however, effectively canceled (due to the random fluctuations of their phase – recall that a transducer measures the total pressure *field*) if the surface area of the detector was sufficiently large. To ensure that the background contribution from scattered sound was effectively eliminated from the ballistic pulse, the phase cancellation of the scattered sound was further improved by translating the sample and averaging the transmitted field from completely new ensembles of the scatterers. This left only the unscattered ballistic wave, which was spatially and temporally coherent across the whole surface of the detector.

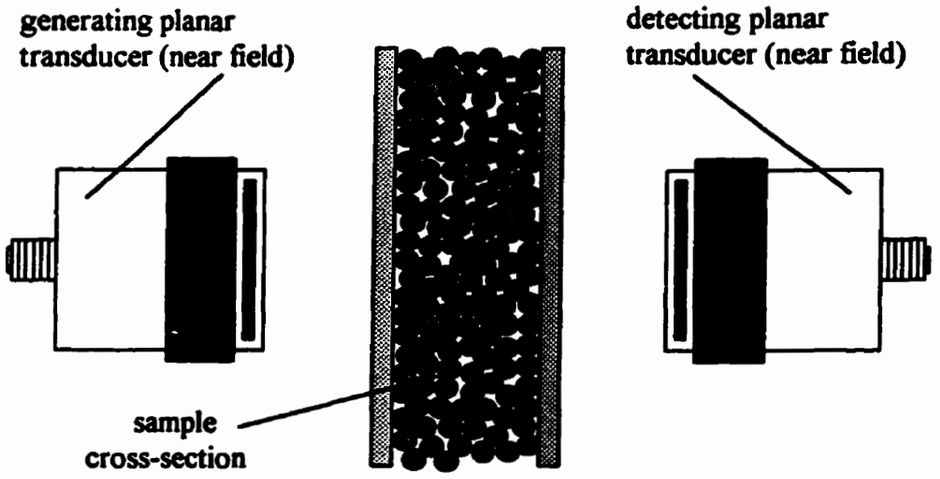

Figure 4.9 Ballistic pulse mode: planar source geometry. The transducers are fixed but the sample may be translated.

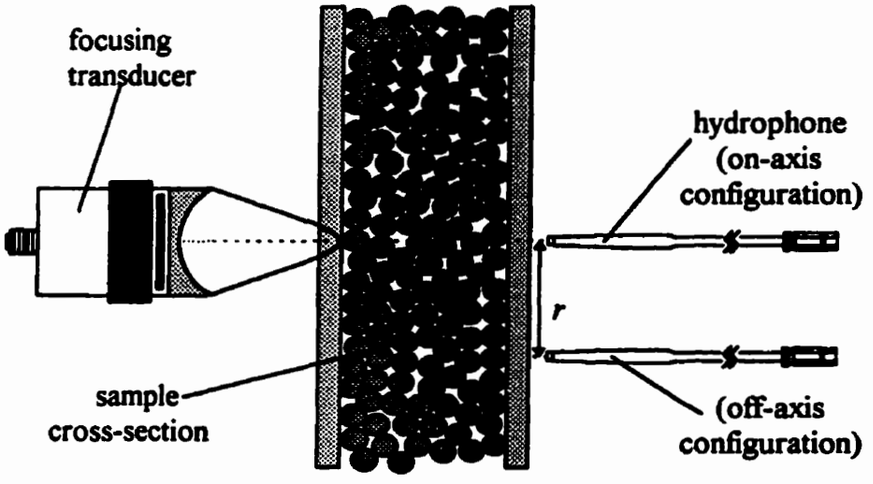

Figure 4.10 Diffusive pulse mode: point source geometry. Note that the focusing transducer and the hydrophone remain fixed, while the *sample* is translated.

4.3.2 Determining the diffusion coefficient and the absorption time

4.3.2.1 Diffusive pulse mode: point source geometry

Experiments in the point source geometry were performed to test the applicability of the diffusion approximation in the description of the propagation of strongly scattered ultrasound pulses in the medium, and to subsequently understand the behaviour of the diffusion and absorption coefficients Only unsieved glass-bead samples were studied in this geometry, though both sizes of beads were used. Short acoustic pulses, of about 10 oscillations (in the frequency range from 1 to 5 MHz), were generated by a focusing transducer arranged so that its focal plane was coincident with the input face of the sample. The detecting hydrophone was placed close to the opposite face of the sample, and signals from statistically independent ensembles of the glass-bead disorder were then collected by translating the sample. This allowed the pulse shape of the average multiply scattered intensity that was transmitted through the medium to be determined from the scattered intensities in a large number of speckles. This pulse shape was then compared to the shape predicted by the diffusion equation for this particular geometry, allowing the determination of the diffusion coefficient and the absorption time.

Figure 4.10 shows the experimental setup for the point source geometry. Most of the measurements were taken with the hydrophone on-axis with the focusing transducer to simplify the comparison with the predicted diffusive pulse shape [cf. equation (2.98) — the factor $e^{-r^2/4Dt}$ equals unity, as $r = 0$ for on-axis measurements]. Several data runs

were, however, performed for both on-axis and off-axis hydrophone positions. This allowed D to be obtained independently of the complications due to absorption and boundary conditions (see Sec. 5.5.1.3.5).

4.3.2.2 Diffusive pulse mode: planar source geometry

Experiments in the plane wave source geometry were performed to determine the diffusion coefficient and the absorption time, and to test the consistency of the diffusion approximation in the description of the propagation of strongly scattered ultrasound pulses in the medium. Only the sieved glass-bead samples were studied in this geometry. As before, short acoustic pulses, of about 10 oscillations (in the frequency range from 1 to 5 MHz), were generated, though now by a planar transducer operating deep in its far field (~ 0.75 m). This meant that the wave front incident on the sample surface was as good an approximation to a planar wave as possible. The detecting hydrophone was placed close to the opposite face of the sample, and the average transmitted intensity determined by translating the *hydrophone* over the central region of the sample face. This region was small enough that the incident wave across this portion of the sample was a very good approximation to a planar wave, and that there was no possibility of interference due to sidewall reflections from the spacer ring. It was, however, large enough to contain a sufficient number of speckles to ensure that the average transmission in the region was equivalent to that of a sample of infinite transverse extent. This allowed the pulse shape of the average multiply scattered intensity that was transmitted through the medium to be determined from the individual scattered intensities. This pulse shape was then compared

to the shape predicted by the diffusion equation for this particular geometry. Figure 4.11 shows the experimental setup for the planar wave source geometry in the far field configuration.

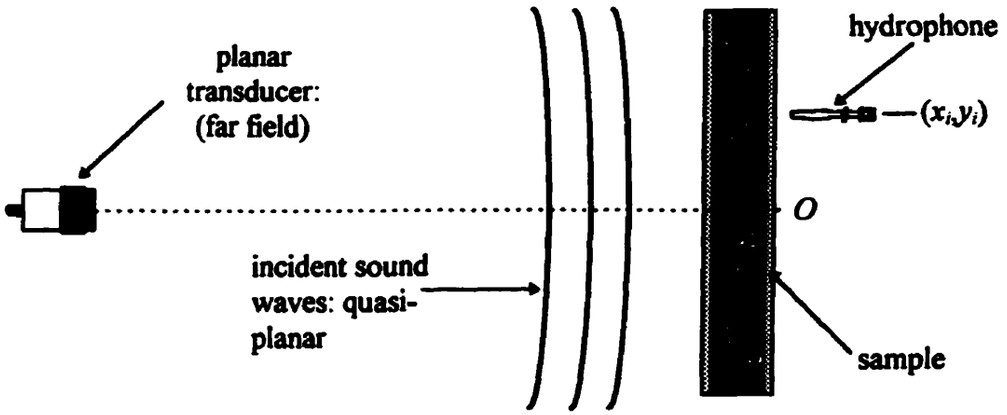

Figure 4.11 Planar source geometry: far field configuration. Here the generator and sample are fixed and the hydrophone is moved.

4.3.3 Absolute transmission measurements: determining the transport mean free paths, and hence, the energy velocities.

4.3.3.1 Quasi-continuous wave mode: planar source geometry

The absolute transmission of the average sound intensity through the scattering medium was undertaken to provide an accurate determination of the transport mean free

path l^*. It also afforded an independent measurement of the diffusion parameters D and τ_a [through their product; see equations (2.112) – (2.114)], thus acting, in part, as a consistency check on those values as determined via pulse measurements. Again, both sieved and unsieved glass-bead samples were studied, though most of the data were acquired with the former. The experimental geometry, identical to that described in the previous section (Sec. 4.3.2.2), is illustrated in figure 4.11. The sound waves, generated by a small-element-diameter planar transducer deep in its far field (and thus a close approximation to a plane wave), were normally incident upon the sample and ranged in frequency from 1 to 3.5 MHz. The hydrophone was placed close to the opposite sample face (about 0.5 to 1 mm away), and the ultrasonic fields at many positions, within a limited region of the sample face, were acquired. Typically, 121 spectra (corresponding to an 11 by 11 square grid) were acquired within a 4 cm^2 region. The sampling region was sufficiently large to contain a statistically significant number of coherence areas ("speckles": see Sec. 5.3), yet small enough to avoid all possible edge effects. The positions of the speckles being apparently random (see Sec. 5.3), the regular sampling was sufficiently dense to ensure equal representation over the continuum of speckle "highs" and "lows." The transmitted intensities at all detection points were normalized by the intensity of the incident wave at those points, and then averaged to acquire the total transmission per unit area. The calculation of the total transmission did require the incorporation of several correction factors to ensure that it was accurately determined. These are discussed in Sec. 4.3.3..2 and Appendix B.

As has been shown in chapter 2 (Sec. 2.2.7.2), if the incident planar wave is *continuous*, than a determination of the fraction of the incident flux transmitted through

the sample (i.e. the absolute transmission) quite plainly yields the transport mean free path. This is seen most clearly in equation (2.106). In practice, a truly continuous wave is not really necessary. What is needed may be described as a *quasi-continuous* wave, that is, a *very long* sound pulse. The temporal extent of this pulse should be sufficient to cause a *constant* signal level to be detected, for a suitable length of time, within the total transmission from each speckle. Physically, the constant signal level is indicative of having maximally filled all scattering paths (i.e. paths of all lengths) that impinge at a common point at the exit face of the sample. That a finite pulse is able to accomplish this is due to the fact that the proportion of path lengths (arising from the excitation at some specific time within the incident pulse) contributing decreases markedly after long times [see equation (2.65) and figure 2.4(b)]. The presence of absorption also provides a second exponential damping mechanism that preferentially selects against longer path lengths. Thus, the incident pulse length need only be longer than the time required to traverse the longest paths through the sample (arising from a delta-function input pulse) that measurably contribute to the ensemble average. In practice, the incident pulse lengths necessary to mimic a continuous wave range from about 70 to 250 μs, depending on the sample thickness and the frequency of the incident wave.

The determination of the transport mean free path required the *absolute* measurement of the total transmission under the conditions set forth in the theory. The primary concern, experimentally, was then to ensure that the intensity of the incident wave remained constant, or if not, that its variation could be recorded concurrently with the acquisition of the transmission data. Initial measurements of the absolute transmission included the concurrent monitoring of the incident wave. It was discovered that the

variation in the incident wave intensity was negligible over a period of several hours, provided one avoided times when the supply voltage from the mains was adjusted to account for periods of increased domestic consumption. Subsequent measurements determined the acoustic field of the incident wave just before, and usually just after, the data run, dramatically speeding up the rate at which data could be acquired.

4.3.3.2 Ensuring an accurate determination of the transmission

Under the conditions set forth in the theory, a continuous planar wave must arrive at normal incidence upon a slab of randomly close-packed spherical scatterers immersed in water. The entire transmitted field, over all 2π steradians, must then be detected at each point on the exit face of the sample. An accurate determination of the transport mean free path required understanding the effect of all departures from such conditions upon the theoretical total transmission. In other words, before the data could be reliably fit for l^*, correction factors were necessary to adjust the experimentally determined total transmission for every point of departure from the theory. In decreasing order of importance, the subjects that necessitate these corrections are as follows: (1) the presence of the sample walls, (2) the angular response of the hydrophone, (3) interference across the hydrophone, (4) the initial reflective loss, and (5) nonplanar incident waves. The nature and origin of these correction factors are addressed below. Specific details regarding their measurement or calculation may be found in Appendix B, including a summary of the numerical results.

4.3.3.2.1 The wall correction

The most significant departure from the conditions set forth in the theory involved the nature of the sample itself. Since the glass beads do not adhere to one another, it was necessary to confine them between walls to maintain the slab geometry. The theory makes no provision for the effect of walls upon the total transmission. The plastic walls have acoustic impedances different from that of water and thus change the nature of the interface between the sample and the coupling medium. It is known, however (Sec. 2.2.6), that changing the reflectivity at the interfaces modifies the distribution of path lengths in the sample, and hence both the magnitude and angular distribution of the transmission. Moreover, the walls, being a solid, also support shear waves, and thus allow mode conversion at the interfaces. These shear wave excitations in the walls may subsequently be reconverted and travel back into the sample (thus further modifying the path length distribution), or may possibly be dissipated in the form of an evanescent wave along the wall/water interface.

The question of the effect of the walls on the total transmission can, of course, be avoided completely if there is some means whereby the sample geometry can be maintained *without* walls. This may be achieved by replacing the water in the sample by a polyacrylamide gel (see Sec. 3.3). For the gel to have the same fluid properties as water (e.g. no shear modes), it must be fairly dilute (~5%). The low structural rigidity of such samples permits only relatively thick samples (>7 mm) to be made. Consequently, the restriction in the range of sample thickness' for which total transmission data may be obtained then limits the precision with which l^* can be determined. In addition, the gelled samples also have a finite lifetime (less than a day), due to the absorption of water from

the coupling medium and the ensuing swelling and distortion. Gelled samples thus cannot be used directly to determine the absolute transmission. However, if a gelled sample is sealed between plastic walls and the absolute transmission subsequently determined *without* and *with* the walls, the ratio of the transmissions provides the effect of the walls on the transmission. Using gelled samples approximately 10 mm thick, it was found that these ratios (or "wall correction factors") ranged from about 2.5 to 5, depending on the frequency.

4.3.3.2.2 The hydrophone angular response correction

Absolute measurements of the total transmission require not only the intensity of the incident waves to be confidently known but also that the conditions for the detection of both the incident and transmitted waves be the same. One significant difference between the detection of the incident and transmitted waves is as regards their angular distribution. The incident waves are planar waves and arrive at normal incidence to the hydrophone, whereas the transmitted waves have a 2π steradian angular distribution. This means that the angular response of the hydrophone needs to be considered. The geometrical cross section of the hydrophone, as seen by the waves transmitted from a point in the sample , decreases as the cosine of the azimuthal angle is increased (cf. figure 2.7). If one considers the "region" on the sample face over which transmitted waves are detected, then provided the hydrophone is sufficiently close to this point, it will subtend practically the entire solid angle. This corresponds to the circumstances under which the boundary conditions have been determined (Sec. 2.2.6). The boundary conditions, which can be used in the determination of a theoretical expression for the total transmission [Sec.

2.2.7.2; equations (2.107) – (2.110)], incorporate this cosine factor [Sec. 2.2.6; equations (2.81) – (2.88)]. Any correction factor involving the angular response of the hydrophone will then be due to departures from the expected cosine behaviour.

Given a beam of incident planar waves, the angular response of the hydrophone may be experimentally determined by rotating it through 90°, beginning at normal incidence. The effect of the angular response on the detection of the waves transmitted through a gelled sample (as the result of the wall correction) is then investigated. The relative number of transmitted phonons (per unit area, per unit exit angle) is integrated over all exit angles to provide the expected transmission (see Appendix B.2.1 for details). Dividing the angular response of the hydrophone by the cosine of the azimuthal angle and multiplying the result by the relative number of transmitted phonons, yields, after integration over all angles, the detected transmission. The correction factor is then found by calculating the ratio of the expected transmission over that of the detected transmission. The hydrophone angular response correction factors were found to be strongly frequency dependent, ranging from about 0.75 to 1.2.

4.3.3.2.3 The hydrophone interference correction

One further difference between the detection of the incident and transmitted waves lies in the phase of the waves being detected. The wave front incident on the face of the hydrophone is a plane of constant phase as the result of the normal incidence of the planar wave on the detector. The acoustic fields will thus add constructively. The transmitted waves vary in phase and amplitude across the sample face, producing the familiar phenomena of speckle (Sec. 5.3). At worst, the amplitude and phase *within* a speckle will

vary slowly (otherwise, there would not be a speckle). The ability to measure the transmitted acoustic field of multiply scattered sound requires the area of the detector to be "smaller" than that of the speckle. Precisely how much smaller depends on the accuracy required and the degree of variation within the speckle.

The variation in the phase and amplitude has been measured at 1.5 MHz using a hydrophone with a diameter nominally one-fifth that of the speckles (Appendix B.2.2). Within the regions of high amplitude ("bright" speckle), the variation in the phase ranged from nil to, at worst, 120°. Since this variation occurred smoothly across the speckle, the interference was almost entirely constructive over the detector. In the regions of low amplitude ("dark" speckle) however, the variation in phase was extremely rapid, approximately 180° as a rule. This implies a significant amount of destructive interference over the detector. As a proportion of the total transmitted intensity though, the effect of all the destructive interference is minimal as the major component arises from regions where the intensity is very low. The measured transmission has been estimated as about 5% less than the "true" transmission.

The speckle size being inversely proportional to the frequency of the incident sound, the destructive interference increases with increasing frequency. To reliably ascertain the degree of interference at each frequency of interest, the spatial dimensions for the variation in the phase and amplitude data discussed above were scaled by the ratio of the wavelength to the hydrophone diameter. Alternatively, this may be understood as an increase in the relative area of the detector as compared to the speckle size. The average ultrasonic fields were then calculated across these "enlarged" detectors, for each detection position, and the total transmission then determined. The ratio of the total

transmission calculated without interference to that calculated with interference gives the effect of the decrease in speckle size on the total transmission. Adding 5% to this value (to account for the initial underestimation of the transmission at the reference frequency) then yields the hydrophone interference correction. For the small element diameter hydrophone, the correction varies from about unity (at 1 MHz) to 1.2 (at 3.5 MHz). Specific details are provided in Appendix B.2.2.

4.3.3.2.4 The initial reflective loss correction

The intensity of the incident wave provides the absolute reference for the total transmission measurements. However, due to the difference between the acoustic impedances of the coupling medium and the sample (i.e. the gelled sample, as the wall correction has made it the effective sample), only a part of this is transmitted into the sample, the remainder being reflected from the sample interface. Using the two fluid model (Appendix A.1), the transmission into the sample was calculated for the frequencies of interest and found to vary from about 0.92 to 0.94 times the incident intensity. The initial reflective loss corrections thus range from about 1.06 to 1.09. Specific details are provided in Appendix B.2.1.

4.3.3.2.5 The input beam distribution correction

The generating transducer, operating deep in its far field, produced a good approximation to a planar wave when incident on the sample face. The fact that there was an actual input beam *distribution* (i.e. a variation in the intensity of the incident wave as a

function of position) complicated the question of the appropriate normalization for the total transmission. The normalization undertaken, whereby the transmission at each point was normalized by the intensity of the incident wave at that point, was found to slightly underestimate the transmission as compared to that for a true planar wave. To determine this, the point source expression for the transmitted flux [equation (2.98)] was numerically integrated over the input beam distribution (treated as an array of point sources), thus yielding the total transmission. This was done both for a true planar wave and for the measured input beam distribution, using as diffusion parameters the best known values at each frequency of interest. The effect of the actual beam distribution not accounted for in the initial point-by-point normalization was then found by taking the ratio of these two transmissions. The input beam distribution correction factors varied from a low of 1.02 to a high of 1.07, depending on the frequency of the incident wave, and on the diameter of the generating transducer. Additional details are provided in Appendix B.3.

4.4 Setup and apparatus

4.4.1 Introduction: the experimental configuration

The interrelation between the various pieces of equipment necessary to carry out the measurements of both the ballistic and scattered sound is illustrated by the block diagram provided in figure 4.12. The positioning of the sample and transducers (hydrophone) was controlled using either automated or manual translation stages, depending on the particular experiment being performed. The main body of the block diagram (the primary configuration) indicates the setup for the ballistic and the diffusive pulse experiments, whereas the inclusion of the dashed box (the secondary configuration) indicates the arrangement of the components necessary to do absolute transmission measurements (though it was also employed in the planar source diffusive measurements). In the latter case, the electrical connections indicated by the diagonally lined arrows should be omitted. The difference between the two setups involves the generation of the RF pulse used to drive the transducer. The overall setup will be discussed in more detail within the context of describing the apparatus (Sec. 4.4.2 to Sec. 4.4.12). Further details regarding the measurements are provided in the discussion on the data acquisition system, which deals with the computer control of the stepper-motor translation stages and the digital oscilloscope.

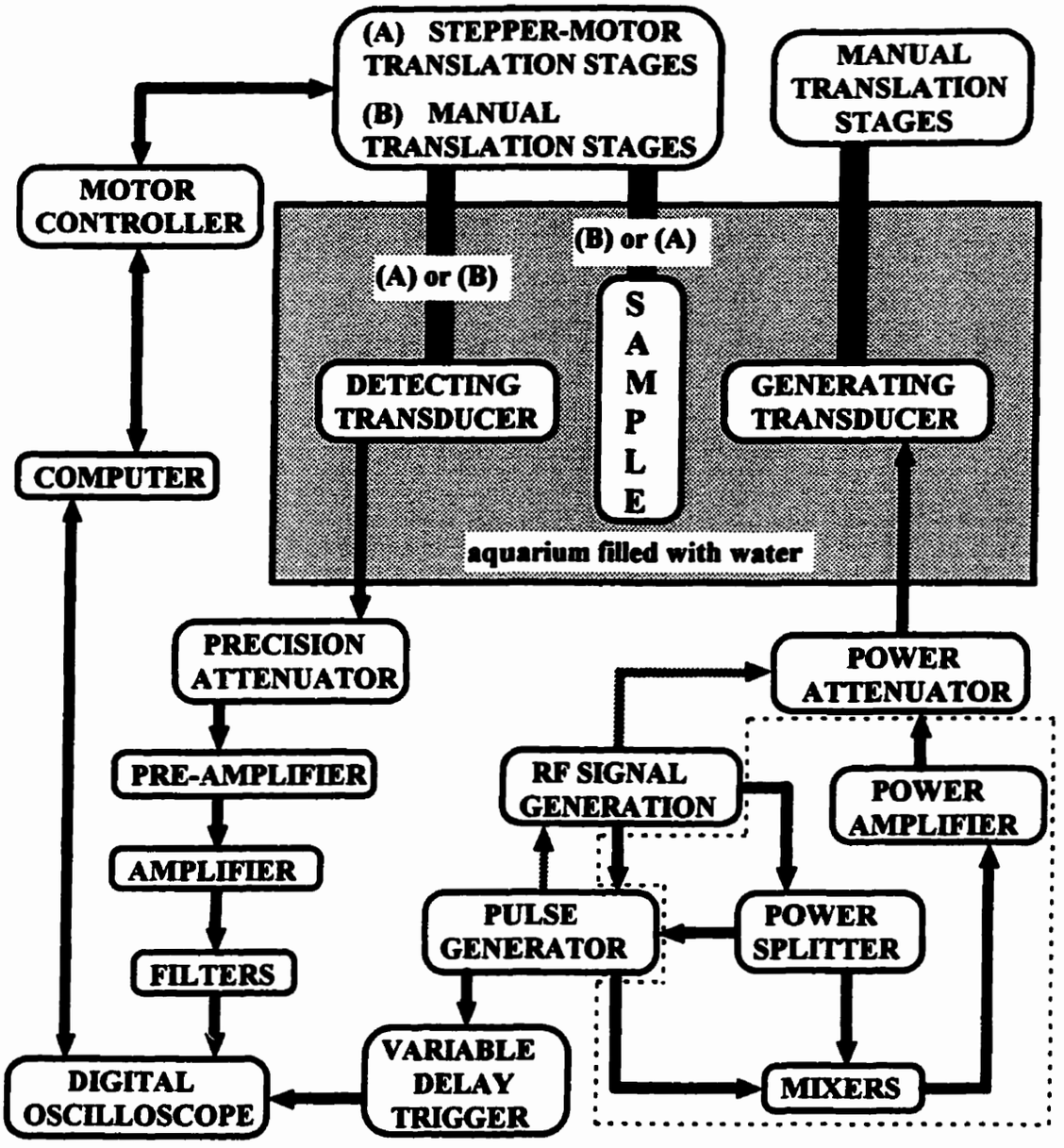

Figure 4.12 Block diagram of experimental setup. Arrows indicate electrical connections; arrows at both ends imply control systems and denote information transfer in both directions. The diagonally-lined bars indicate mechanical supports. For the absolute transmission measurements, the diagonally lined arrows are omitted, and the components in the dashed box (otherwise ignored) are inserted. If the sample is moved remotely (A), then the detecting transducer is manually aligned (B), and vice-versa.

4.4.2 The aquariums

As has been mentioned before, the sample was immersed in an aquarium filled with water. The ballistic measurements and the point source diffusive measurements, being in the near field geometry, were customarily performed in an 80 litre aquarium. Here, a small aquarium sufficed as the sample occulted the entire incident wave, and the width of the sound pulse was sufficiently short (or, the tank was sufficiently large) that reflections off the back wall of the aquarium (arising from the sound transmitted from the exit face of the sample) did not interfere with the desired signal. Measurements performed in the far field geometry, however, necessitated the use of a 425 litre aquarium since the generating transducer needed to be about 0.75 m away from the sample. This, of course, meant that the spatial extent of the incident wave (being effectively a planar wave across the sample surface) was far larger than that of the sample. As transmission losses in water are negligible, this meant that a great deal of sound was left to bounce off the glass walls (whose reflection coefficient with respect to water is quite large). Some of this sound acted as a secondary input source, and some was reflected directly into the hydrophone, measurably interfering with the transmitted sound arising from the initial input wave. For the absolute transmission measurements especially, this was of great concern. The larger aquarium (including the water surface) was therefore lined with expanded polystyrene foam into which rigid baffles were inserted, and the reflected sound was thus redirected and/or absorbed. This mitigated the problem, but did not entirely eliminate it (the acoustic impedance of the foam, though lower than that of glass, is still higher than that of water). Consequently, the aquarium was partitioned by a thick foam baffle into which the sample was inserted. The baffle was sufficiently thick that no measurable signal was transmitted

through to the detection side. The dimensions of the region on the generation side of the baffle were large enough that no remnant waves in that region could interfere with the initial incident wave, even for the longest of quasi-cw pulses.

4.4.3 The translation stages

The water provided a coupling medium for the sound to travel from the generating transducer to the sample, and from thence to the detecting transducer (usually the hydrophone). The generating transducer was mounted on a shaft connected to a set of manual translation stages so as to properly align it with respect to the sample and detecting transducer. In the near field configuration, the detecting transducer (hydrophone) was also connected to a set of manual translation stages, while the sample, which was required to move in the vertical plane for data taking, was connected to the stepper-motor translation stages. In the far field configuration, this order was reversed, as the sample needed to remain fixed while the hydrophone traversed the vertical plane collecting data.

The stepper-motor translation stages were Unislide™ motor driven positioning systems manufactured by Velmex, Inc. (East Bloomfield, NY). The stepper-motors could move the stages, in increments of 3.175 μm, over a 30 cm range. They were arranged with one stage oriented horizontally and the other mounted vertically upon the first so as to independently provide movement in both directions. All the translation stages were mounted on a supporting cradle which incorporated two optical tracks (see figure 4.13), thus allowing precise adjustment of their longitudinal position.

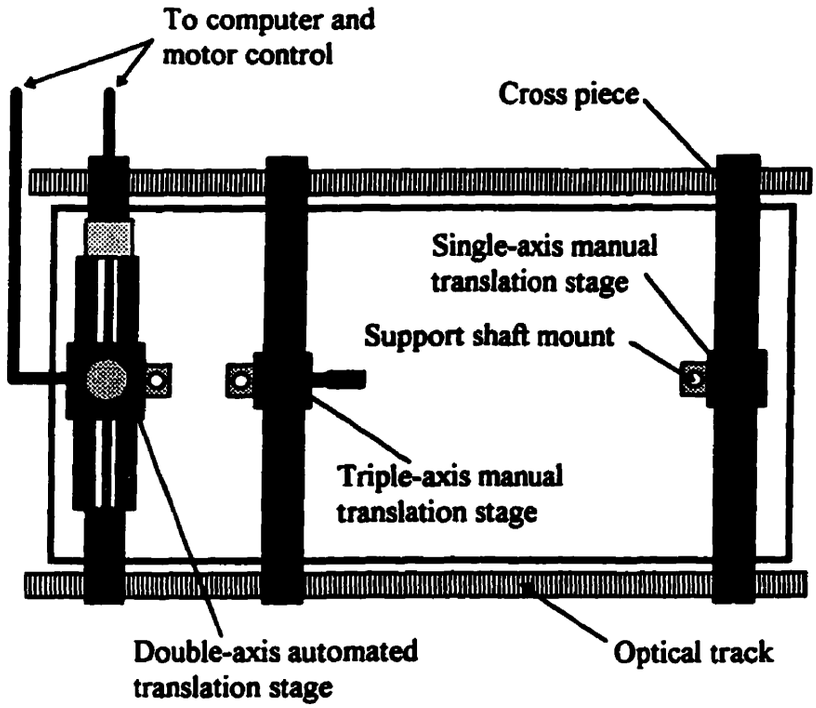

Figure 4.13 Translation stage arrangement; top view.

4.4.4 The transducers

The plane wave and focusing transducers used in these experiments were Accuscan-V series immersion transducers from Panametrics, Inc. (Waltham, MA). Transducers with central frequencies of 1.0, 2.25, 3.5, and 5.0 MHz, were used. Their bandwidths were sufficiently broad to collectively span the entire frequency range from 1 to 5 MHz. The focusing transducers had focal lengths ranging from about 5 cm to 15 cm, with most of the point source data being generated with the 5 cm focal length transducers.

Since the near field distance increases as the square of the transducer diameter, and linearly with the frequency (equation (4.5)), relatively large diameter transducers (both flat and focused) could be used for near field geometries. In the near field configuration, 2.5 cm diameter transducers were used, and in the far field 0.625 cm and 1.25 cm diameter ones. Actual descriptions of the transducers (including hydrophones) are provided in Sec. 4.2, as well as their basic operating principles.

4.4.5 The hydrophones

The hydrophones used in these experiments were model PZTZ44 ceramic hydrophones purchased from Specialty Engineering Associates (Milpitas, CA). Hydrophones with element diameters of 200 μm and 400 μm were used. Both were broadband devices operating in the subresonant mode, allowing frequencies from 1 MHz to 20 MHz (3 dB points) to be measured. Details of the construction and operating principles of hydrophones may be found in section 4.2.5. The angular response of the hydrophones is discussed in Sec. 4.3.3.2.2 and Appendix B.2.1. The consequences of element areas greater than the coherence areas of the scattered sound are discussed in Sec. 4.3.3.2.3 and quantified in Appendix B.2.2.

The hydrophone operated in conjunction with a broadband, high input impedance, preamplifier (model A17DB, Specialty) carefully designed for low noise. The 3 dB passband extended from 8 kHz to 25 MHz, for a gain of typically 16 dB, when loaded at 50 Ω. To minimize line losses, the preamplifier was connected within a few centimeters of the hydrophone, and then water proofed.

4.4.6 RF signal generation and pulse production

Two different radio-frequency (RF) signal generation systems were used to excite the transducers, depending on the particular experiment. The first system was a high output power pulsed RF source used primarily for the ballistic and diffusive point source experiments. The second system used a continuous wave RF source and external signal modulation to produce lower output power square pulses and quasi-continuous waves for the planar wave source measurements and the absolute transmission measurements, respectively.

The first system generated RF pulses of approximately 1000 W peak output power (see, however, Sec. 4.4.8), with pulse widths usually between 0.5 μs and 10 μs. This was done using a model 6600 Matec (Warwick, Rhode Island) RF generator and receiver in conjunction with a model 755 RF plug in. The Matec was externally modulated by a pulse generator to produce pulses with smooth rise and fall times at repetition rates of up to 300 Hz. The Matec receiver was not used.

The second system used a model 6060B synthesized RF signal generator from Fluke (John Fluke Mfg. Co., Everett, Washington). This frequency synthesizer is a fully programmable source of continuous waves in the frequency range from 0.01 MHz to 1050 MHz, and in the amplitude range from -127 dBm to +13 dBm (equivalent to 50 Ω-terminated voltages of 0.1 μV to 1 V). It is extremely stable in frequency and amplitude, making it particularly useful for the absolute transmission experiments. Operating at 10 dBm, the continuous wave (cw) was mixed (i.e. *multiplied*) with a rectangular pulse

produced by a pulse generator (see next section). This was done by triple-cascading (to overcome leakage of the continuous RF oscillations into the zero-volt baseline region from the rectangular pulse) MiniCircuits model 15542 ZAY-3 mixers. Synchronization was achieved by using the 10 MHz internal reference oscillator in the signal generator as the external reference clock for the pulse generator. A Merrimac model PDM-20-250 power splitter was placed on the output of the signal generator with one component externally triggering the pulse generator and the other being modulated by the mixers. The resulting low power rectangular RF pulse was then fed through an Amplifier Research (Souderton, PA) power amplifier, which was capable of 50 W peak output power.

4.4.7 The variable delay trigger and pulse generator

A Stanford Research Systems, Inc. (Sunnyvale, CA), model DG535 digital delay/pulse generator was used to provide precisely timed logic transitions which were used to trigger the external modulation for the Matec RF signal generation system. Its low jitter (50 ps RMS) made it ideal for synchronizing the averaging of the digitizing oscilloscope with the repetition rate of the signal generator. It could also produce precisely timed logic pulses, thus operating as a pulse generator. The resulting square envelopes were mixed with the cw output of the Fluke signal generator, as mentioned above (Sec. 4.4.6). For the planar wave diffusive measurements, pulse widths varied from 3 to 8 μs, whereas for the absolute transmission measurements, quasi-cw pulses ranging from 70 to 250 μs were generated. Delays and pulse widths could be varied independently

to a precision of 5 ps and to an accuracy of 1 ppm. The pulse repetition rate was about 330 Hz.

4.4.8 The attenuators

The power output of the Matec RF pulse generation system was too large to directly drive the generating transducers without causing severe waveform distortion. Consequently, a fixed 3 dB Weinschel attenuator and a variable 0–42 dB Alan attenuator were used to limit the input signal amplitude to tolerable levels. This required a minimum of 15 dB. The output power of the Fluke signal generator via the power amplifier, being about 25 dB less than that of the Matec, did not require any attenuation.

In order to avoid saturating the detecting amplifiers (in particular, for the reference signals), the signal from the detecting transducer was attenuated using precision attenuators from Telonic, Inc. This allowed precision amplitude measurements to be made (in conjunction with the digitizing oscilloscope).

4.4.9 The preamplifier

Two different preamplifiers were used over the course of the experiments. The first was an Anzac amplifier which provided 30 dB of gain. After this unit became inoperable, the vertical amplifier of a Hitachi model V-222 analogue oscilloscope was employed to provide 26 dB of gain.

4.4.10 The amplifier

The primary detecting amplifier used in the experiments was a Keithley Instruments, Inc. (Cleveland, Ohio), model 107 pulse amplifier. The Keithley is a low noise wideband (flat response from 2.5 kHz to 150 MHz) amplifier specifically designed to maintain pulse fidelity. It contains three separate x10 gain amplifiers which may be cascaded to provide greater amplification. It was operated in the double cascade mode, thus providing a gain of 40 dB.

4.4.11 The filters

Filters were employed on the input to the digitizing oscilloscope to limit the noise component of the signal. This was especially necessary when using the Hitachi preamplifier. Both high and low pass multipole Butterworth filters were used. Frequently, they were used simultaneously, thus forming simple bandpass filters.

4.4.12 The data acquisition system

The data acquisition system consisted of the computer-controlled digitizing oscilloscope and the motor controllers for the stepper-motor translation stages. A Tektronix 544A digitizing oscilloscope in averaging mode was used to acquire the data. The averaging, which was on the order of 1000 sweeps, greatly improved the signal-to-noise ratio. The triggering of the sweeps was performed, by the Stanford delay generator, to synchronize the data acquisition with the repetition rate of the signal generator. The

oscilloscope was capable of a maximum digitization rate of 1 GigaSample/s, and could acquire record lengths of up to 50000 points. A general purpose interface bus (GPIB) connection between the scope and the computer allowed direct computer control of the data acquisition and enabled the acquired waveforms to be transmitted directly to disk. There was also a GPIB connection between the computer and the stepping motor controllers (model MCB-1, Advanced Control Systems Corp., Hingham, MA) for the automated translation stages. The computer was then able to send one message telling the motor controllers to move the detecting transducer (or sample) to a specified location, and then another to the scope telling it to acquire and transmit the data to the computer. This whole procedure was automated so that large amounts of data could be collected swiftly (~ 1 hr for a typical data run) without the constant attention of the experimenter.

5 Results and discussion

5.1 Introduction

In this chapter, the presentation of experimental data and their analysis is discussed in light of theoretical predictions. The first portion of the chapter deals with the transport of the ballistic pulse (Sec. 5.2), and the second portion with the transmission of multiply scattered sound (Sec. 5.3 through Sec. 5.5). The former first considers how the coherent pulse is extracted from the total transmitted signal (Sec. 5.2.1). The frequency dependence of the scattering mean free path, both experimentally measured and theoretically determined, is then presented (Sec. 5.2.2). This is followed by an explanation of how the phase and group velocities are found, what their behaviours are, and how they compare with expectations (Sec. 5.2.3). The treatment of the ballistic propagation is concluded by a discussion of the nature of the transport through the medium (Sec. 5.2.4).

The propagation of the multiply scattered sound is introduced by considering the statistical character of the observed ultrasonic speckle (Sec. 5.3), and the nature of the temporal fluctuations within individual coherence areas (Sec. 5.4). The transmission is then described (Sec. 5.5), beginning with critical tests of the diffusion approximation using dynamic (pulse) measurements (Sec. 5.5.1). Here, the construction of the ensemble-averaged diffusive pulse is explained, and the fitting procedure illustrated with data arising from various detection geometries; typical results (i.e. D and τ_a) are presented. The experimental determination of the transport mean free path l^*, from static (quasi-continuous wave) measurements of the absolute transmission, is then described (Sec.

5.5.2), with the details of the principle concerns relegated to Appendix B. Combining measurements of D and l^* allows an experimental determination of the energy velocity. Finally, the frequency dependencies of the measured diffusion parameters are summarized, and compared with theoretical predictions. A unified physical picture of the energy transport by ballistic and diffusive waves thus emerges and is discussed (Sec. 5.5.3).

5.2 Coherent transmission

5.2.1 Determination of the coherent pulse

Ultrasonic waves propagating through a disordered medium in which the inhomogeneities are on the order of the wavelength do, in principle, consist of both coherent and incoherent components. The difficulty in determining the behaviour of the coherent component arises when the sample is sufficiently thick that the ballistic pulse has become immeasurably small. The obvious solution to such a dilemma is to make measurements on thinner samples. There is, however, a constraint that must be imposed on such a treatment. The samples must remain sufficiently thick that the macroscopic homogeneity is maintained, and that the random close-packing is not significantly perturbed by the sample walls. In practice, for slabs of slightly polydisperse randomly close-packed glass beads immersed in water, the minimum thickness appears to be 2 or 3 bead diameters. As a consequence, the ballistic component may still be extremely small, and thus difficult to measure. Two things make possible the reliable identification of the ballistic pulse, even if only a vanishingly small coherent component is left. The first is a technological consideration regarding the fact that signal averaging is capable of recovering quite small signals hitherto buried in the noise. There remains, however, the task of distinguishing between the coherent and incoherent components of the transmission. The second consideration thus concerns the fundamental difference between the two components.

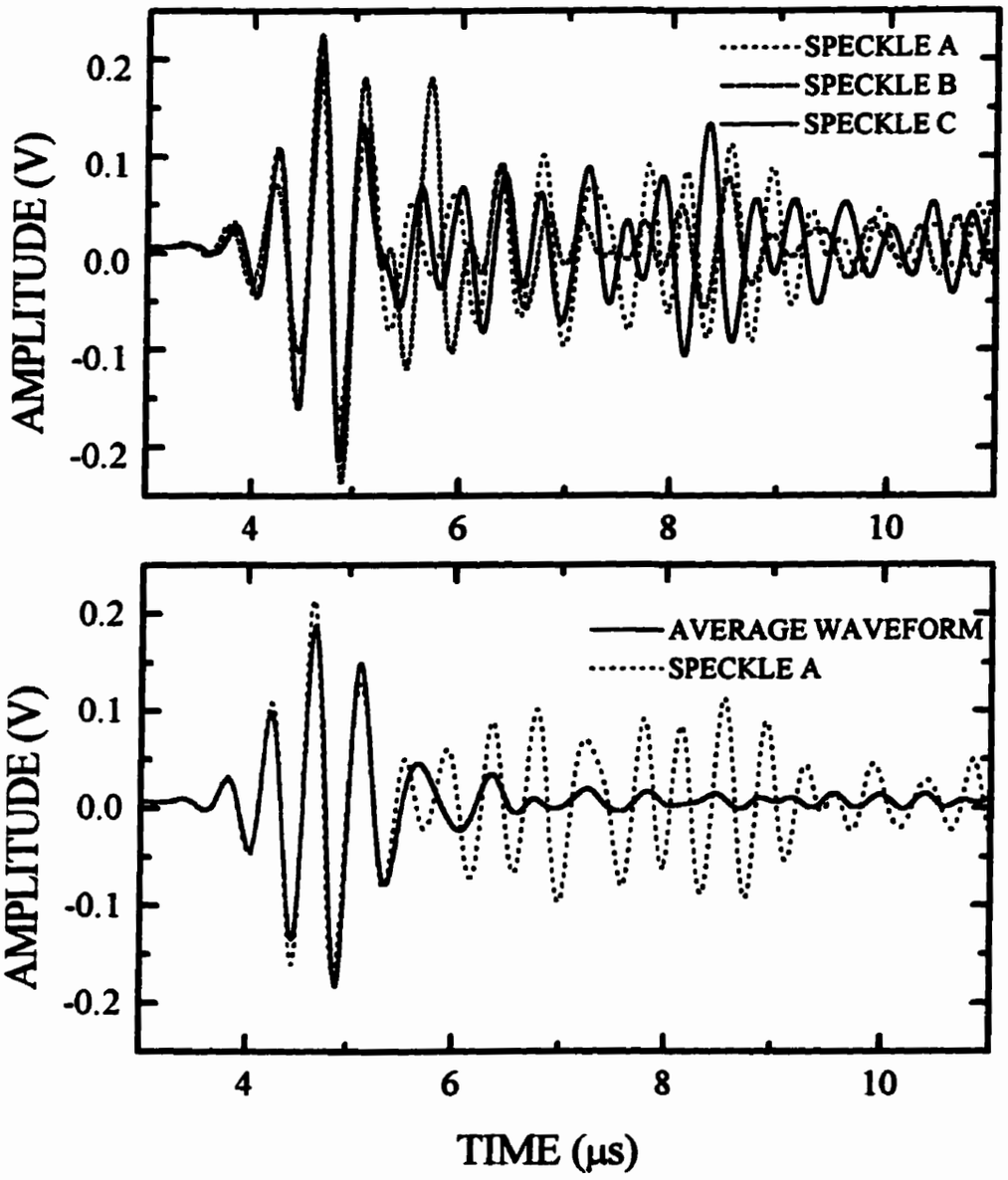

Figure 5.1 Transmission speckles for a thin sample (L = 3.4 mm), containing 0.5 mm radius glass beads, showing coherent and incoherent components. The coherent component is the result of averaging the field over 121 speckles.

As has been pointed out in Sec. 2.1.1, the coherent pulse has a definite phase relation to the incident pulse. Thus, if the temporal variations within a number of different speckles are compared, the ballistic portions of the signals will exhibit the same phase dependence, whereas the scattered components will have phases which are randomly distributed (see Sec 5.3). Such behaviour is illustrated in the upper panel of figure 5.1 where the temporal variation in three different speckles (resulting from the transmission through a 3.4 mm sample containing 0.5 mm glass beads, and acquired using the hydrophone) is compared. From the beginning of the waveforms until about 5.5 μs, the signals appear remarkably similar in phase (and amplitude). In contrast, there does not seem to be any relation between the phases of the signals in different speckles for times beyond this point. Since the ballistic pulse is that portion of the signal that remains unscattered (or is forward scattered), it arrives earlier in time than the scattered signals which traverse longer and longer path lengths. The initial ~2 μs of the temporal variations is then identified, by their position and phase coherence, as being primarily the ballistic signal, and the remainder as the scattered signal. The bottom panel of figure 5.1 shows the effect of averaging the ultrasonic *fields* of a large number (121) of different speckles; the resulting average waveform is given by the solid line. The coherent components of the waveforms add constructively while the incoherent components, being of random phase, tend to add destructively. The dotted line gives the temporal variations in a typical speckle for comparison. To take advantage of this effect, a large-element-diameter planar transducer was used to average the ultrasonic field over a large number of speckles. Further reduction of the scattered component was achieved by translating the sample, increasing the number of speckles that were averaged, to ensure cancellation of the

scattered fields. The resulting ballistic pulses were analyzed to determine the frequency dependence of the scattering mean free path (Sec. 5.2.2), and of the phase and group velocities (Sec. 5.2.3).

5.2.2 The scattering mean free path

A sound pulse of incident intensity I_0 propagating through a sample of thickness L becomes progressively attenuated as more and more of the incident beam is scattered out of the original direction of propagation. The transmitted intensity I of the unscattered component is described by the attenuation of the ballistic pulse as

$$I = I_0 \exp(-L/l_s), \tag{5.1}$$

thus defining the scattering mean free path l_s. The diffusely propagating component of the transmitted sound shows that the absorption length is at least 20 times larger than l_s (Sec. 5.5.3.1), confirming that the observed attenuation of the ballistic pulse is the result of scattering, not absorption. Equation (5.1) may be rewritten to present the frequency dependence of l_s in terms of $A_0(\omega)$ and $A(\omega)$, the incident and transmitted ballistic amplitudes, respectively:

$$l_s(\omega) = \frac{-L}{2\ln[A(\omega)/A_0(\omega)]}. \tag{5.2}$$

The scattering mean free path for the unsieved bead samples was determined experimentally by choosing as incident pulse a waveform containing only one or two oscillations. Such a pulse thus consisted of a wide spread of frequency components. After correcting for losses due to the effect of the sample walls (see Appendix B.1), the

fast Fourier transforms (FFT) of the incident and transmitted ultrasonic fields were then calculated, and their ratio determined. This is illustrated in figure 5.2, which shows the result of normalizing the FFT of the averaged ultrasonic field (transmitted through a 5.28 mm sample containing 0.25 mm radius glass beads) by that of the incident pulse, generated by a transducer with a bandwidth from 1 MHz to 3.5 MHz. The thick curve shown indicates the ω^{-4} behaviour of the Rayleigh scattering regime, which for this sample is seen to be for frequencies less than about 1.7 MHz. Data were acquired using transducers with different central frequencies, allowing the entire frequency range of interest to be explored. Thin samples composed of 0.5 mm radius glass beads were also used to increase the available frequency range (doubling the bead size allows one to effectively double the frequency range). Ignoring regions of the FFTs outside the effective bandwidths of the incident pulses, and accounting for losses in the sample walls, the scattering mean free path was then calculated from equation (5.2). For some of the sieved bead samples, wide pulses centred at many different frequencies were used, and l_s calculated directly from the attenuation of the incident pulse [using equation (5.1), and correcting for the losses in the sample walls]. Many sets of mean free path data were then combined to indicate the ensemble variation from sample to sample.

The scattering mean free path for the unsieved beads samples is plotted, in figure 5.3, as a function of the normalized wave vector in water ($\propto$ frequency). The mean free path and the wave vector were both scaled by the bead radius to account for the fact that samples with different bead sizes were studied. The solid circles indicate data taken with the 0.5-mm-radius glass beads, while solid triangles indicate data taken with the 0.25-mm-

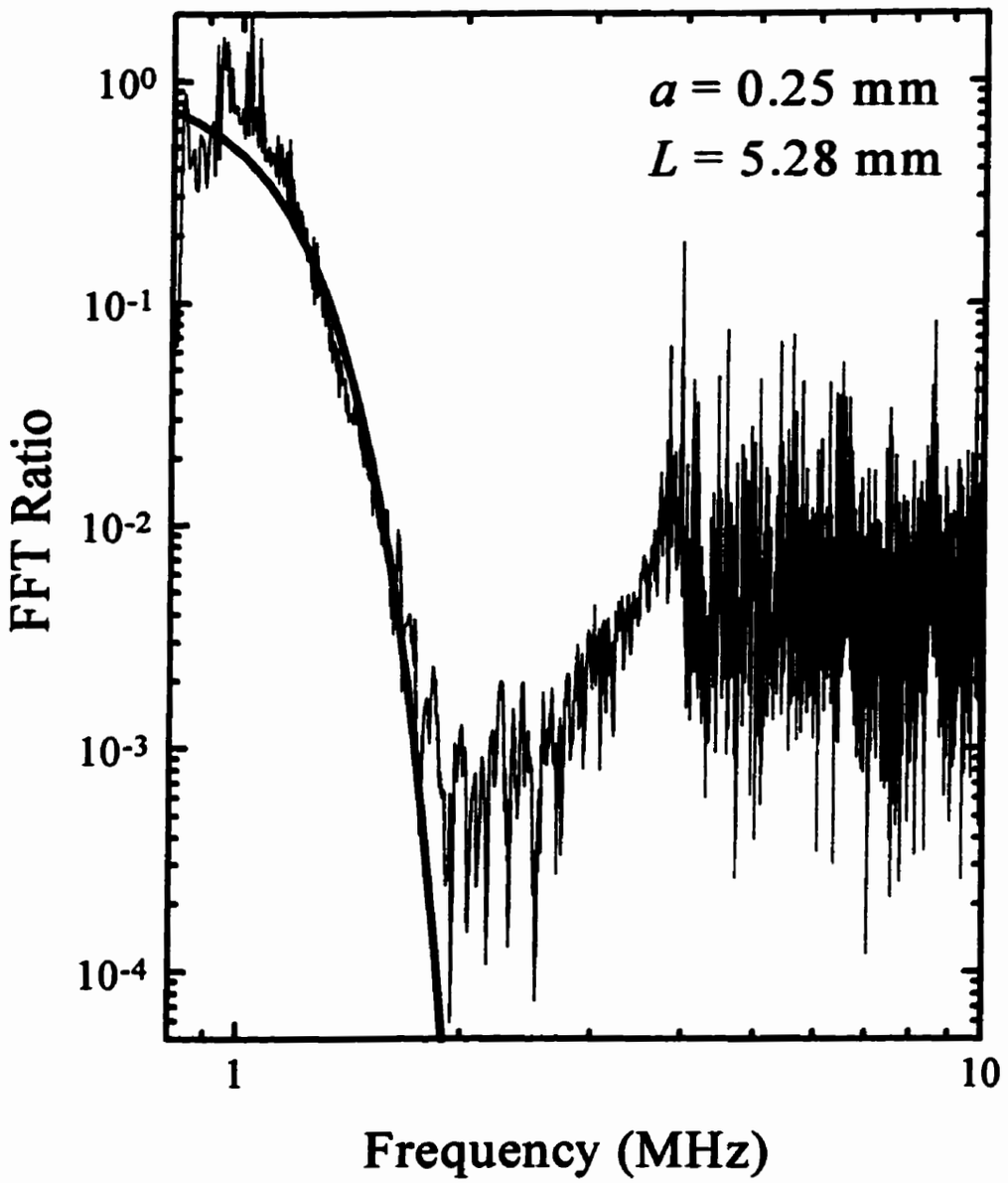

Figure 5.2 FFT of the average transmitted ultrasonic field normalized by the FFT of the input pulse (input pulse bandwidth: 1 to 3.5 MHz). The thick curve shows the ω^{-4} behaviour indicative of Rayleigh scattering.

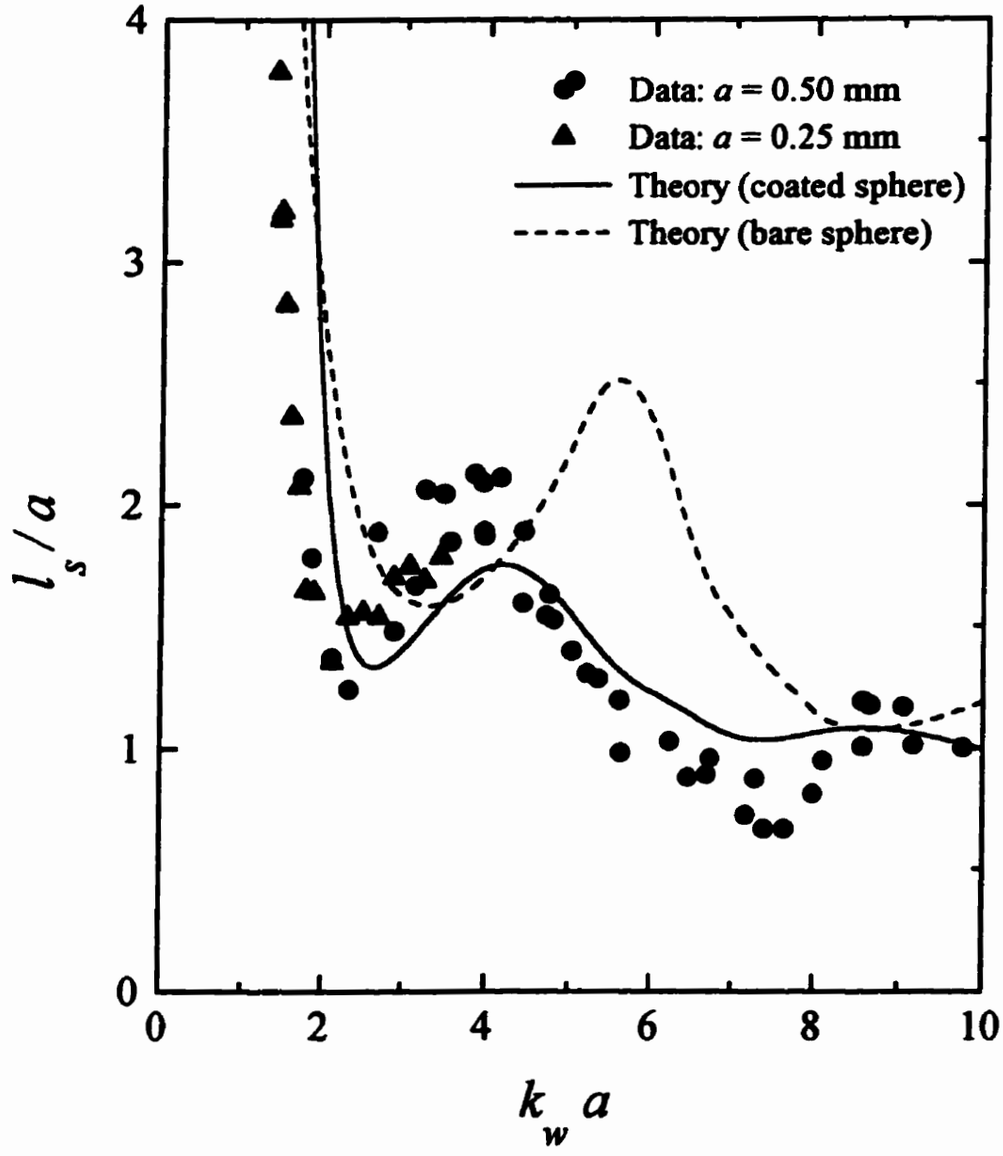

Figure 5.3 The scattering mean free path for the unsieved glass beads, normalized to the bead size, plotted as a function of the normalized wave vector in water. The theoretical predictions for both the bare and the coated spheres are as shown.

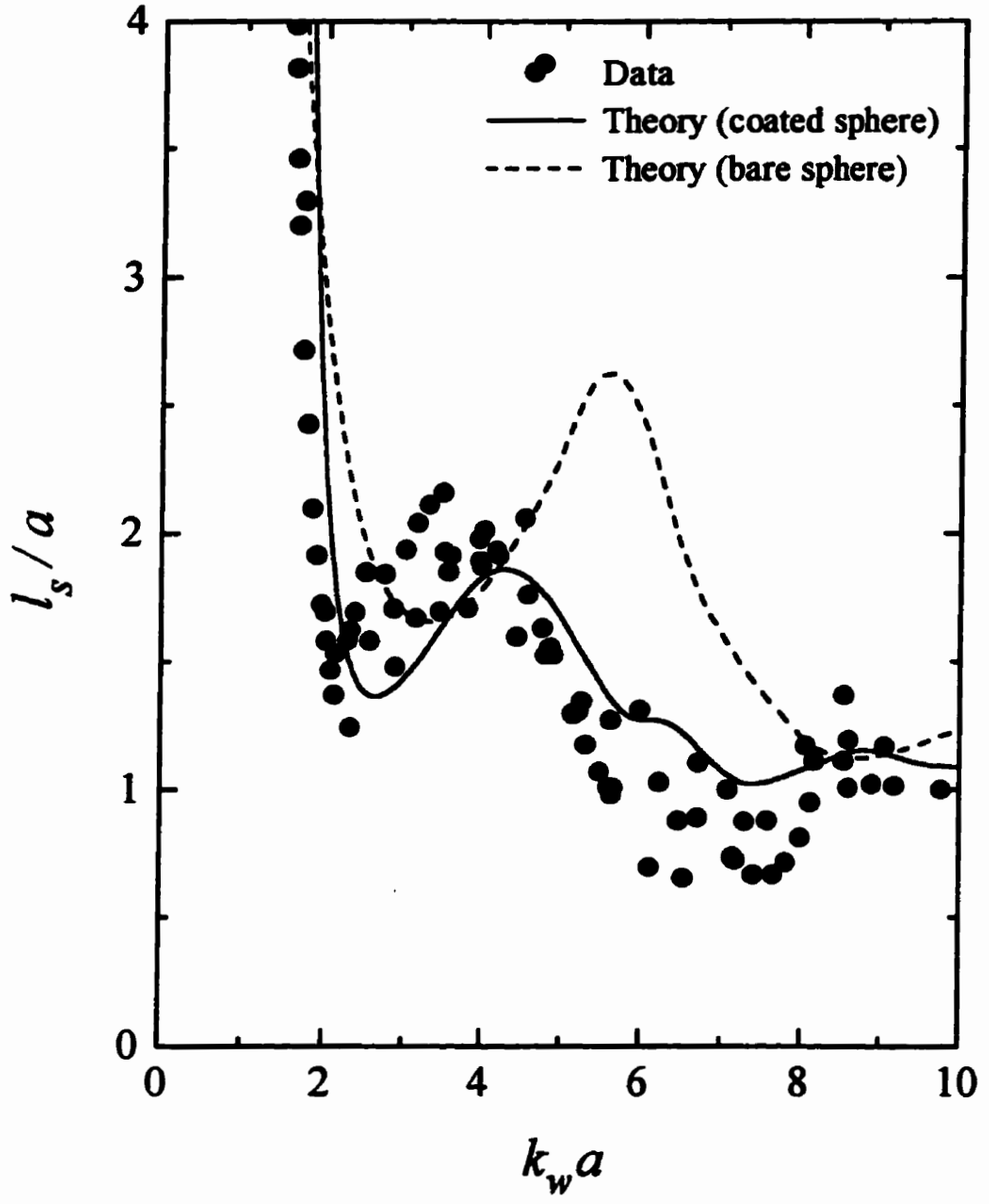

Figure 5.4 The scattering mean free path for the sieved glass beads, normalized to the bead size, plotted as a function of the normalized wave vector in water. The theoretical predictions for both the bare and the coated spheres are as shown.

radius glass beads. As data from eight different samples were combined to form this composite plot, only a representative selection of the data is shown so that the symbols may be identified more clearly. Samples of similar thickness and glass-bead packing fraction, but statistically independent ensembles of the glass-bead disorder, give rise to the scatter in the data. The scattering mean free path for the sieved beads samples is similarly plotted in figure 5.4. Inspection of figure 5.3 and figure 5.4 reveals a strong similarity in the frequency behaviour between the two scattering mean free paths. The behaviour of both data sets for $k_w a$ less than about 1.7 is indicative of the Rayleigh scattering regime, mentioned above. Of much greater interest are the pronounced dips exhibited in both plots, where the scattering mean free paths reach values comparable to the bead radii. For both the unsieved and sieved bead samples, the first minimum in the scattering mean free path is observed at $k_w a \approx 2$, where is $l_s/a \approx 1.5$. The second dip (again, in both cases) is quite broad, with an ill-defined minimum at roughly $k_w a \approx 7$, where $l_s/a \approx 0.8$. The comparison of these two plots will be more fully discussed within the context of the group velocity of the ballistic pulse (Sec. 5.2.3.3).

To determine the origin of these dips, the total scattering cross section, which is related to the scattering mean free path by equation (2.63), has been calculated, using two different models for comparison. The first model assumed non-interacting, randomly close-packed, glass beads in water – in essence, calculating the scattering from an isolated (or *bare*) elastic sphere in water, a problem first solved by Faran (1951). The second model was the coated sphere model (Sec. 2.1.4), for which the calculation of the total scattering cross section [equation (2.62)] is described in Sec. 2.1.8. Both models involved

no adjustable parameters, depending only on the material parameters, and in calculating l_s from the scattering cross section, the glass bead number density.

The predicted mean free path, based on the bare sphere model, is shown by the dashed curve in both figure 5.3 and figure 5.4. Not only does this simple calculation predict slightly weaker scattering than is observed experimentally, but the positions of the predicted extrema are not in agreement with those observed experimentally. This is not surprising, as this single-sphere calculation neglects the multiple scattering entirely. The coated sphere prediction, shown by the solid curve in these two figures, correctly accounts for the strong frequency dependence of l_s. However, the magnitude has been empirically adjusted by a phenomenological, frequency independent, scaling parameter p_σ, determined through a fit to the data as $p_\sigma = 1.5$. There is physical justification for applying such a scaling parameter. As in the simple bare sphere calculation, the magnitude of the scattering has been underestimated. Although the coated sphere model does incorporate scattering from the surroundings, it does so by an effective medium approach, using the GCPA. The neighbourhood of a single sphere is, however, far from uniform, so the single coated-sphere approach does not adequately account for the additional random scattering between spheres (Jing *et al.*, 1991, 1992). For the coated sphere model, the case may be considered where there are $N > 1$ spheres in the scattering unit. The multiple scattering between the spheres of the scattering unit may then be treated exactly, the effective medium properties again being calculated within the GCPA. This has been done by Jing *et al.* (1992) for PMMA (polymethylmethacrylate) spheres dispersed in water. They showed that the peaks in the density of states are then considerably broadened, which implies a reduction in the mean free path over that calculated for models with

smaller N. The value determined for our scaling factor is consistent with these multiple sphere calculations.

The variation in the mean free path with normalized frequency, predicted by the single coated-sphere model, exhibits the same behaviour as that of the data (figure 5.3 and figure 5.4), correctly predicting the positions of the extrema. This means that the treatment of this model retained the essential physics necessary to describe the propagation of the multiply scattered sound. Hence the dips in l_s may be identified with resonances (i.e. "peaks") in the total scattering cross section of a single coated sphere in the renormalized effective medium. In other words, the very short mean free paths shown by these dips are indicative of the excitation of internal vibrational modes within the scatterering unit. Further discussions of the effect of the resonances upon the coherent transport, as well as the diffusive transport, of ultrasonic waves are found in Sec. 5.2.4 and Sec. 5.3.2, respectively.

5.2.3 The phase and group velocities

5.2.3.1 Some preliminaries

To determine the phase and group velocities, the ability of ultrasonic techniques to measure directly both the amplitude and phase of the detected signal was exploited. The group velocity was experimentally determined from the propagation of the ballistic pulse envelope, while the phase velocity was determined from the propagation of a particular oscillation within the envelope. Since a pulse is, of necessity, constructed from a continuum of frequency components, in a dispersive medium the peak of the pulse shape

(its "envelope") will travel at a different speed than the individual oscillations. Hence, the group velocity will differ from the phase velocity. Figure 5.5 shows the propagation of a narrow (~1 μs) pulse, of central frequency $f = 2.5$ MHz, through 0.5 mm radius glass bead samples of increasing thickness, with the incident pulse shown in figure 5.5(a). The positions of the envelopes (dashed lines) with respect to the peaks of the oscillations are seen to vary with the sample thickness, thus illustrating the difference in the velocities. It is further expected, however, that with increasing sample thickness the ballistic pulse should continue to broaden, as the different frequency components take different times to travel through the sample. Though this effect is seen for the thinnest sample [figure 5.5(b)], further broadening is not noted for the two thicker samples [figure 5.5(b) and figure 5.5(c)]. This is a consequence of the frequency dependence of the scattering. As seen in figure 5.3, the scattering mean free path decreases markedly for values of $k_w a$ between 4 and 8, corresponding to frequencies ranging from 2 MHz to 4 MHz for this bead size. Since the intensity of a particular frequency component of the ballistic pulse varies as $\exp(-L/l_s)$ [equation (5.1)], the higher frequency components (having smaller mean free paths in this bandwidth) suffer more attenuation than the lower frequency ones. This effect becomes more pronounced as the sample thickness increases, leading to a dominance in the low frequency components of the pulse and thus obscuring the broadening due to velocity dispersion.

The velocities were determined from the difference in transit time between the ballistic pulse and a reference pulse equivalent to the pulse incident on the sample. To

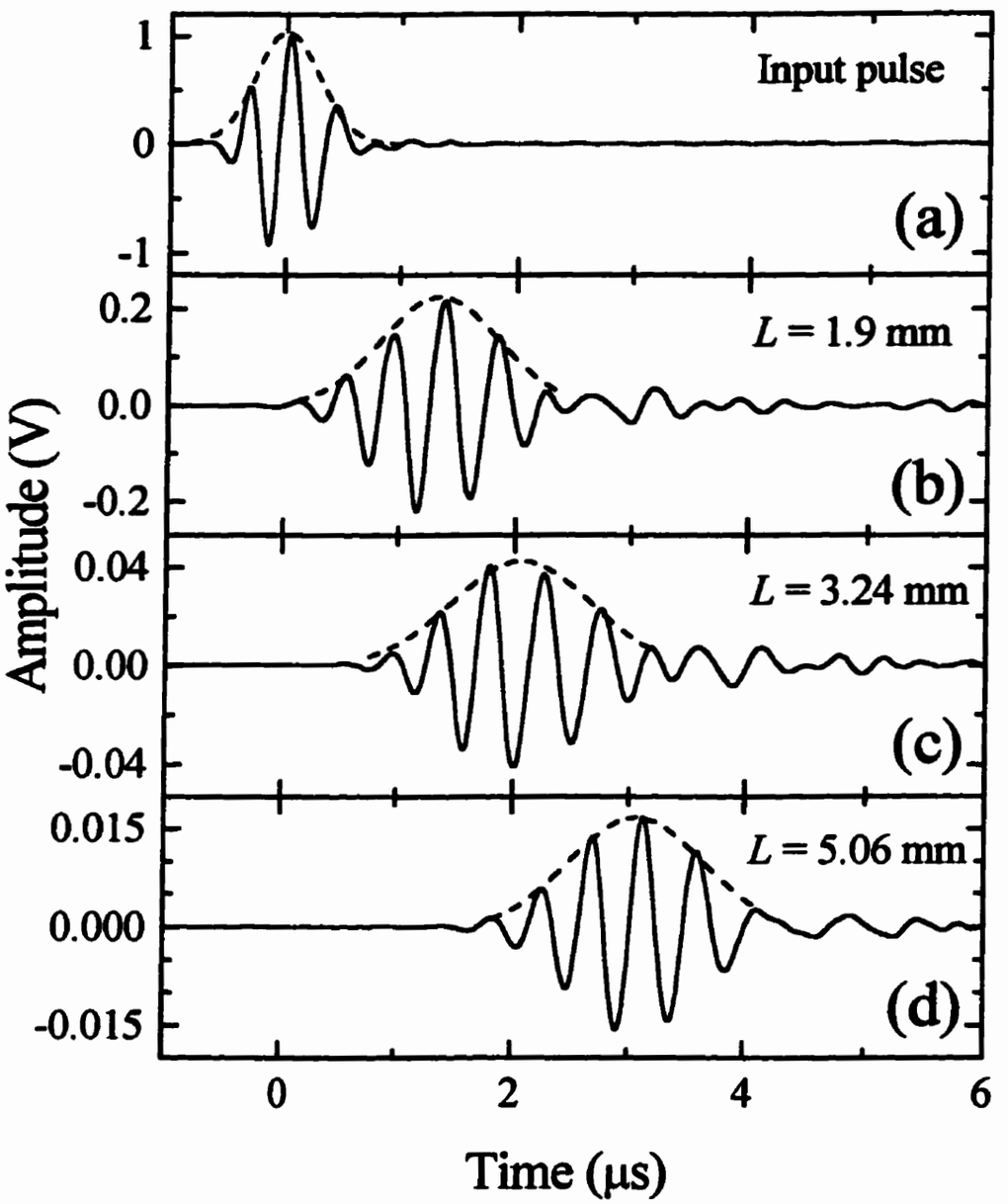

Figure 5.5 The propagation of a narrow pulse, with central frequency f = 2.5 MHz, through samples of increasing thickness, showing the effect of dispersion on the position of the envelope peak in comparison to the phase of the oscillations.

acquire this reference pulse, the sample was removed from between the two transducers, allowing the incident pulse to traverse the same water path as the ballistic pulse as well as a water path equal to the sample thickness (with walls). The difference in transit time Δt between the reference and transmitted pulse is then due entirely to the effect of the sample and sample walls on the propagation time, having no dependence on the distance between the generating and detecting transducers. Both phase and group velocities may then be determined using the relation

$$v = \frac{L}{\frac{d}{v_{H_2O}} - \frac{(d-L)}{v_{wall}} - \Delta t}, \tag{5.3}$$

where L is the thickness of the sample without walls, d the thickness of the sample with walls, v_{H_2O} the water velocity, and v_{wall} the velocity of the wall material. For the phase velocity, Δt was determined from the propagation time of the individual oscillations near the center of the pulse, where the carrier frequency is best defined. For the group velocity, Δt was determined by matching the centres of the transmitted and reference pulse envelopes and then measuring the propagation time.

The typical analysis undertaken to experimentally determine the phase and group velocities may now be illustrated. An incident (reference) pulse containing about 10 oscillations, at a central frequency of $f = 2.58$ MHz ($k_w a = 5.1$), is shown in figure 5.6(a). The resulting ballistic pulse transmitted through an $L = 2.9$ mm thick sample (with acrylite walls about 12 mm thick) containing sieved 0.5 mm radius glass beads is shown in figure 5.6(b). The temporal origins of the pulses are arbitrary. The very small ballistic pulse (in

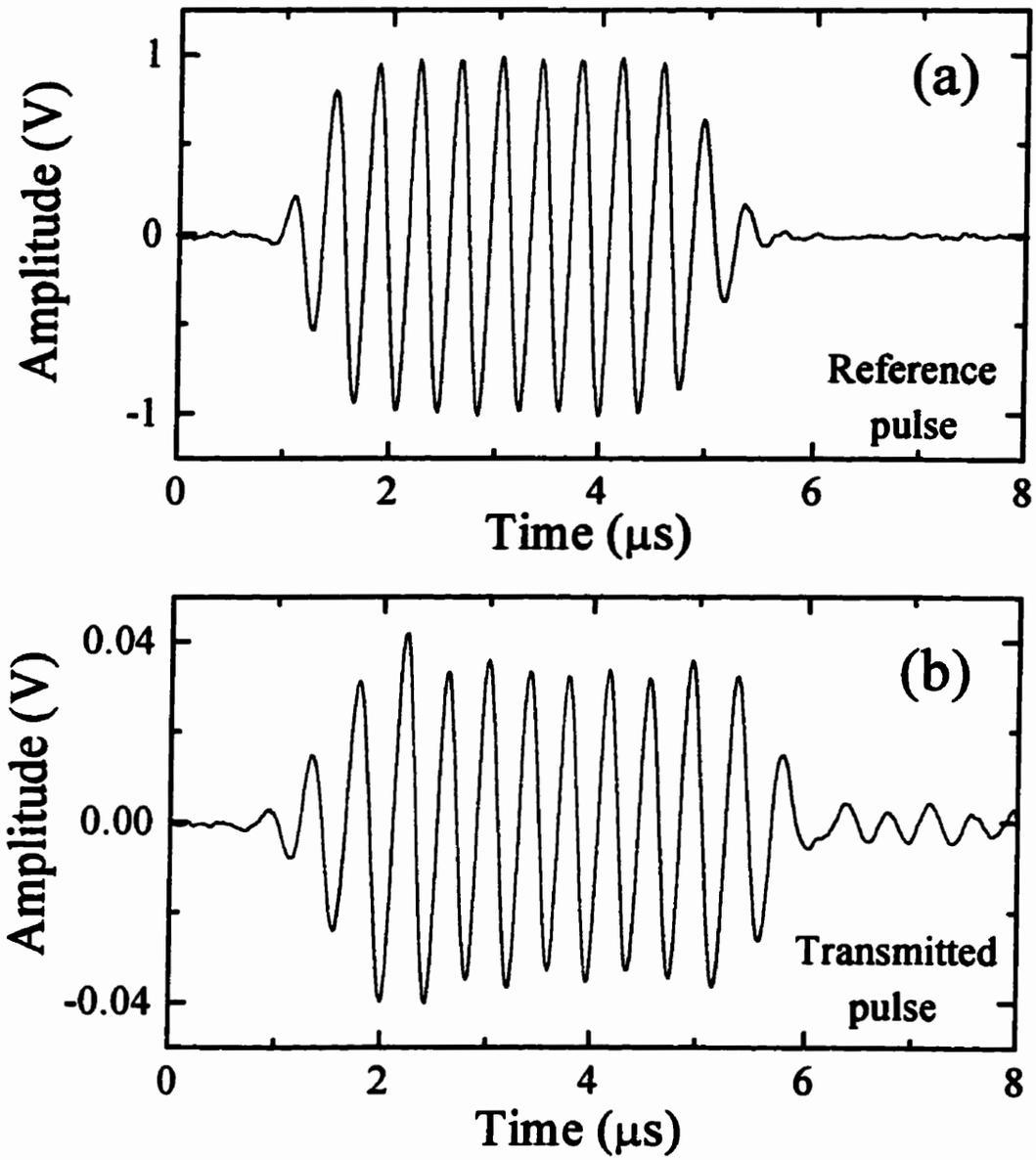

Figure 5.6 Ballistic pulse propagation, at a frequency $f = 2.58$ MHz, through a 2.9 mm sample (with 12 mm thick acrylite walls) containing sieved glass beads (radius, $a = 0.47$ mm). (a) Reference pulse, and (b) transmitted pulse.

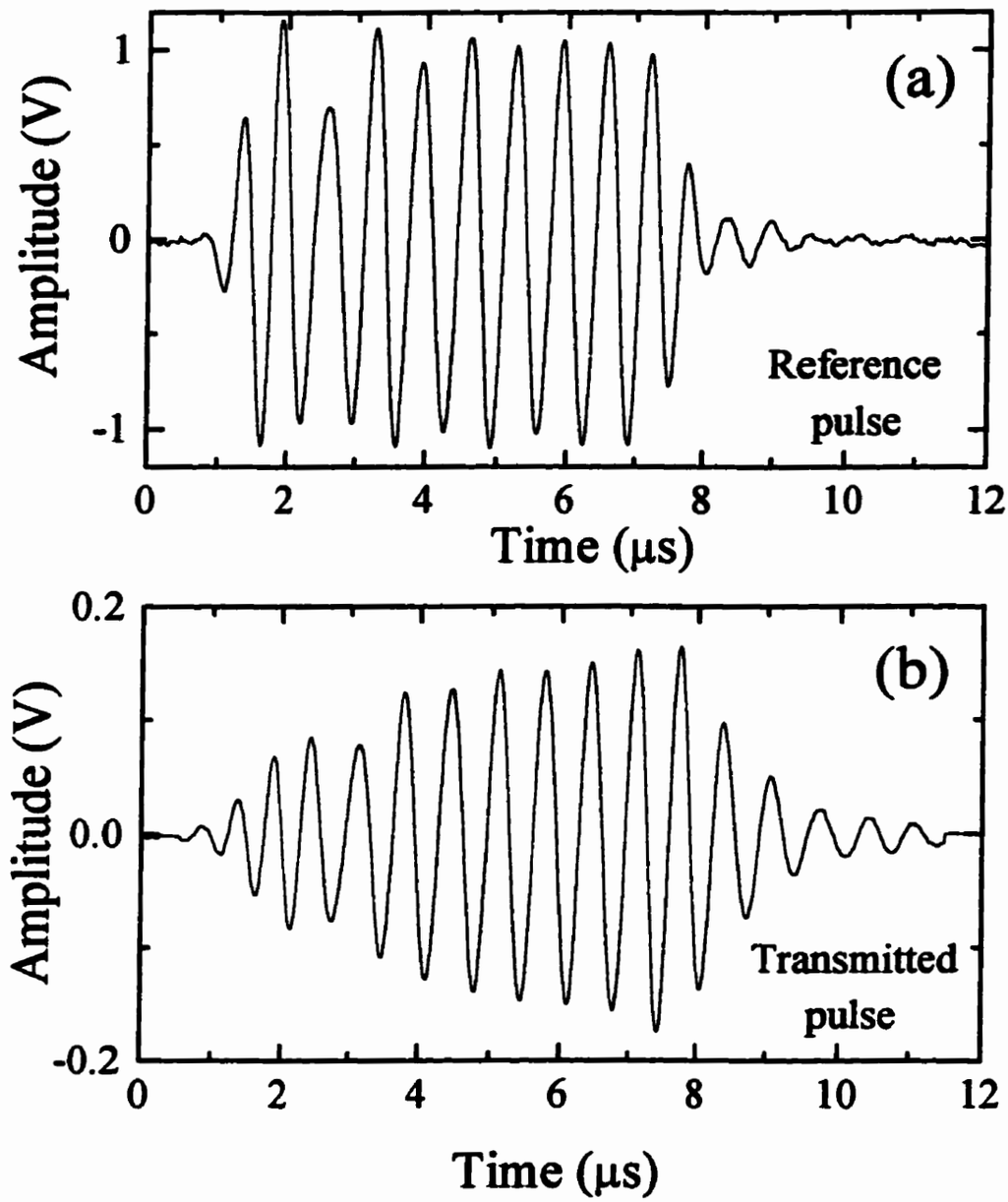

Figure 5.7 Ballistic pulse propagation, at a frequency f = 1.52 MHz, through a 2.9 mm sample (with 12 mm thick acrylite walls) containing sieved glass beads (radius, a = 0.47 mm). (a) Reference pulse, and (b) transmitted pulse.

this case, about 30 dB smaller than the incident pulse) was acquired by averaging the total transmitted signal over an area of about 35 cm^2. The transmitted pulse is seen to be no more than 10% wider than the reference pulse, indicating that the dispersion in the neighbourhood of 2.58 MHz is quite low. At a central frequency of f = 1.52 MHz ($k_w a = 3.0$) however, if the reference pulse incident on this sample [figure 5.7(a)] is compared with its resulting transmitted pulse [figure 5.7(b)], the 25% increase in the pulse width clearly demonstrates the effect of significant dispersion. That this pulse broadening is due to dispersion and not to significant remnants of the scattered signal (i.e. averaging the ultrasonic field over too small an area) was borne out by an independent assessment of the contributions of the four 5 cm^2 averaging regions to the final waveform. These waveforms, acquired from different ensembles of the glass-bead disorder, were found to be almost identical in both phase and amplitude throughout the entire pulse.

The pulse shapes may also be compared, as these are what are used to determine the group velocity. The smooth shape of the reference pulse in figure 5.6(a) is fairly well matched by that of the transmitted pulse [figure 5.6(b)], thus making possible a precise determination of the group velocity at $k_w a = 5.1$. At $k_w a = 3.0$, the determination is less precise due to dispersion and the strong frequency dependence of the attenuation near this frequency (figure 5.3). The distortion in the pulse shape of the rising edge of the reference pulse [figure 5.7(a)], which was a consequence of operating the generating transducer at the bottom of its bandwidth, exacerbated these effects. The effects of this distortion are preserved in the transmitted pulse [figure (5.7(b)], though considerably smoothed out by the interference arising from the dispersion (which dominates on the rising and falling edges of the pulse). The greater attenuation of the low frequency Fourier components on

the rising and falling edges of the transmitted pulse (which scattered more strongly than the higher frequency central region – cf. figure 5.3) also cause significant departures from the initial pulse shape.

To determine the centres of the reference and transmitted pulses to a higher precision, they were both digitally filtered to limit the signal to a Gaussian pulse with a relatively narrow bandwidth. This was done by first Fourier transforming the waveforms [using a fast Fourier transform (FFT) algorithm] to the frequency domain. The results were then convolved with a Gaussian pulse shape, normalized to unit amplitude at the central frequency $\overline{f}$, described by

$$\exp\left[-2\left(\frac{f-\overline{f}}{w}\right)^2\right], \tag{5.4}$$

where w was the specified bandwidth. Finally, the waveforms were transformed back into the time domain. Since a narrow pulse in the frequency domain is a wide pulse in the time domain, bandwidths of 0.1 MHz were used for frequencies of less than about 1.5 MHz, while for higher frequencies, bandwidths ranging from 0.15 to 0.2 MHz were employed so as not to unduly broaden the final waveforms. Thus the precision of the measurements were improved, particularly in cases where there was strong frequency dependence to the scattering; however, both techniques yielded essentially the same results.

The results of FFT filtering the 2.58 MHz data originally presented in figure 5.6, with a Gaussian pulse shape of central frequency $\overline{f}$ = 2.58 MHz and bandwidth of w = 0.2 MHz, are plotted in figure 5.8. As little dispersion was observed at this

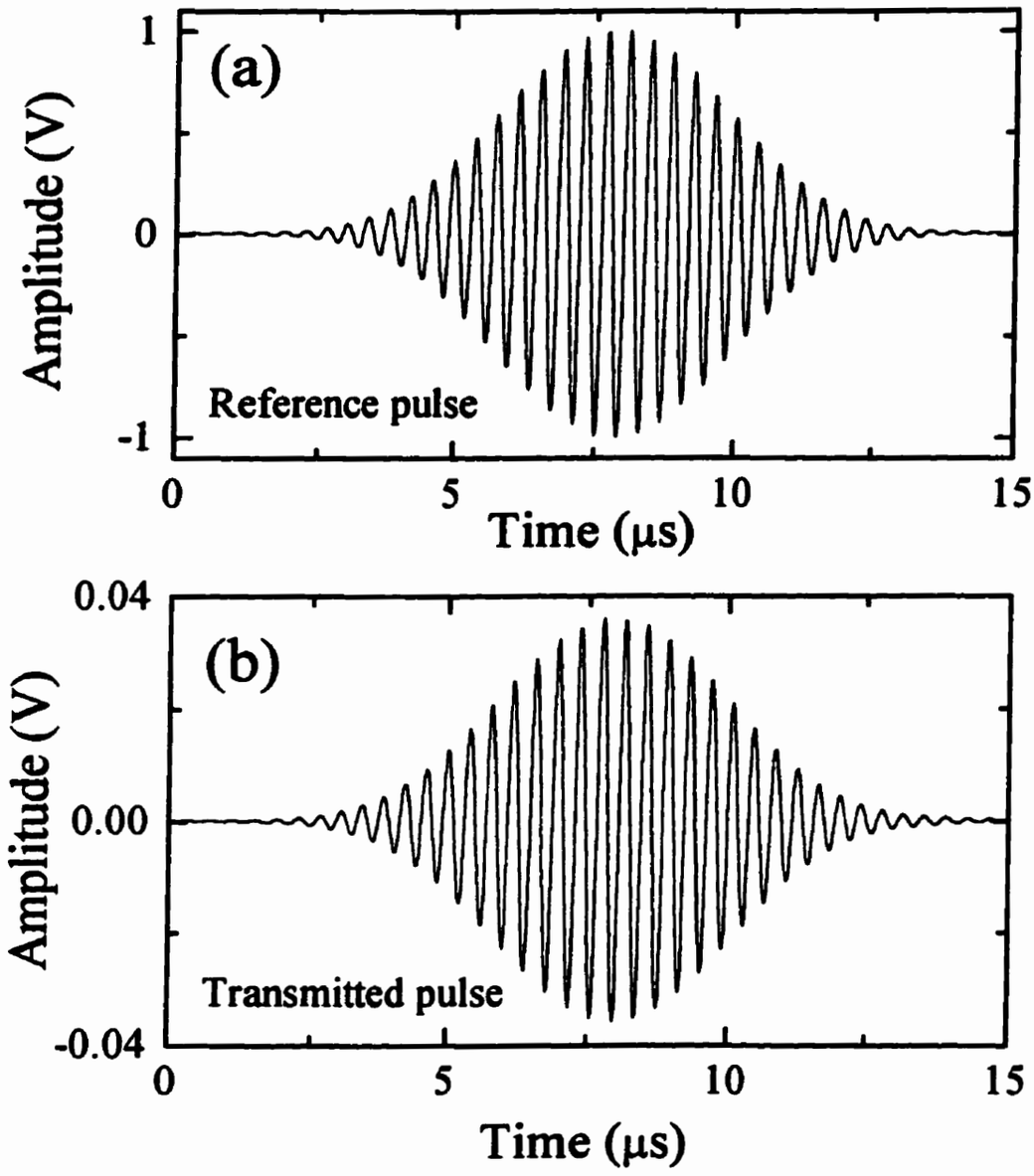

Figure 5.8 The result of Gaussian FFT filtering, with a bandwidth of 0.2 MHz and at a central frequency of 2.58 MHz, the reference and transmitted pulses shown in figure 5.6. (a) The reference pulse, and (b) the transmitted pulse.

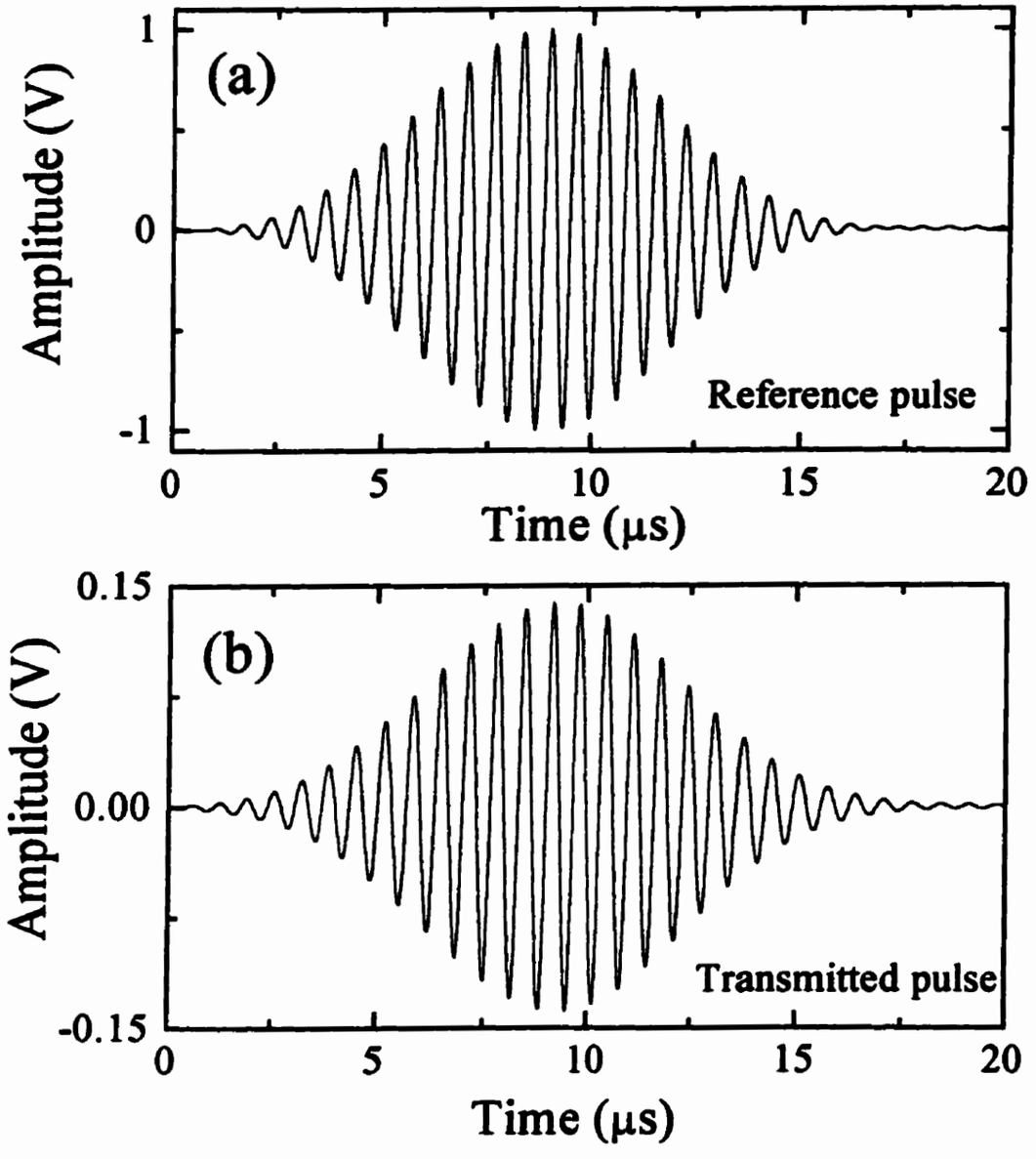

Figure 5.9 The result of Gaussian FFT filtering, with a bandwidth of 0.15 MHz and at a central frequency of 1.52 MHz, the reference and transmitted pulses shown in figure 5.7. (a) The reference pulse, and (b) the transmitted pulse.

frequency, the filtering only slightly increased the precision with which the group velocity was determined. The gain in defining the pulse centre was bought at the price of doubling the pulse width. The results of FFT filtering the 1.52 MHz data originally presented in figure 5.7, with a Gaussian pulse shape of central frequency $\overline{f}$ = 1.52 MHz and bandwidth of w = 0.15 MHz, are plotted in figure 5.9. Comparison of the reflected and transmitted pulse widths for the filtered pulses show them to be essentially the same, this despite the strong dispersion evidenced by the unfiltered ballistic pulse. Furthermore, the asymmetries in the pulse shapes, occurring as they did on the rising and falling edges of the pulses, are now gone. Confident matching of the pulse shapes, and thus an improved accuracy and precision in the determination of the difference in transit times, has resulted from filtering the data.

5.2.3.2 The phase velocity

The experimental determination of the phase velocity required ascertaining oscillations of equal phase in the reference and transmitted pulse. To accomplish this, the peak position of an oscillation near the centre of the reference pulse (where the frequency was best defined) was chosen as the reference time. The matching oscillation in the transmitted pulse then needed to be unambiguously identified. The procedure that was followed was to "guess" the most likely oscillation and determine its peak position, as well as the peak positions of oscillations on either side of the chosen one. The timing differences between the reference oscillation and the members of this set of transmitted oscillations were then determined, ensuring that one of these differences would be the

appropriate transit time. A set of "velocities" was then determined from these differences, using equation (5.3). This procedure was then repeated for several samples of different thicknesses, and the sets of "velocities" then compared. The correct correspondences between the oscillations of the reference and transmitted pulses were identified by ensuring the consistency of the phase velocity between these samples of different thicknesses, as only the phase velocity was common to all sets. Figure 5.10 shows the phase velocity of the acoustic waves in samples consisting of the unsieved glass beads in water, where both bead sizes were used. Significant dispersion can be seen, with the phase velocity dropping by about 50% to a minimum value of 1.25 km/s at $k_w a \approx 3$, where k_w is the acoustic wave vector in water. Furthermore, over most of the frequency range investigated, the phase velocities are significantly less than the sound speeds in either the water (v = 1.5 km/s) or the glass (longitudinal: v_L = 5.6 km/s; transverse: v_T = 3.4 km/s).

To compare with the experimental data, the peaks in the density of states (DOS), shown in figure 2.2 (Sec. 2.1.8) were first used to identify the dispersion curve, shown by the solid white line in figure 2.2. The phase velocity was then calculated from the ratio of the angular frequency ω to the effective medium wave vector k [equation (2.56)]. To properly compare with the experimental data, these calculations were averaged over the variation in bead size, assuming a Gaussian distribution of sizes (figure 3.2). The result is represented by the solid curve in figure 5.10, where excellent agreement with the experimental data is seen.

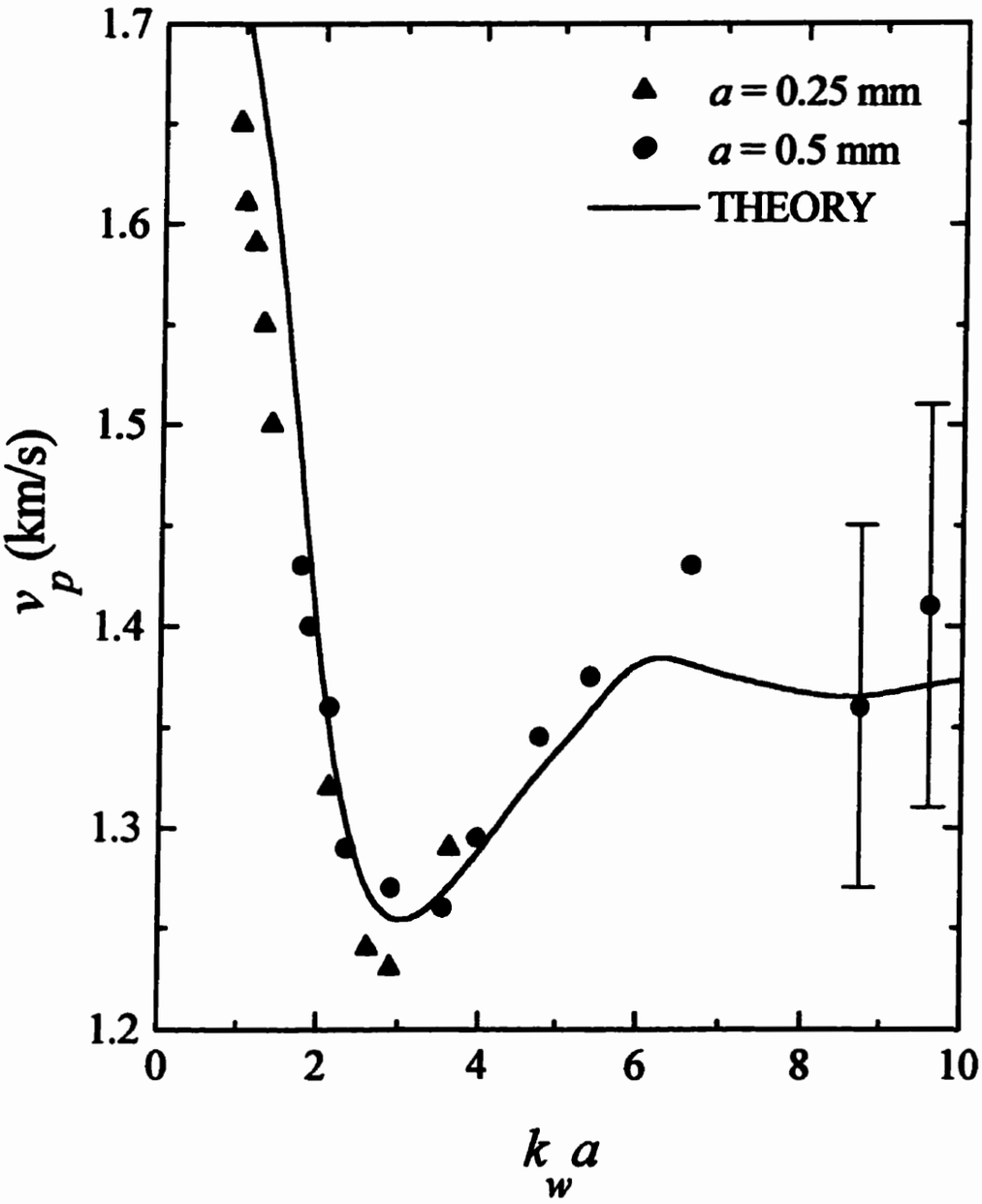

Figure 5.10 Phase velocities of acoustic waves in a strongly scattering medium consisting of the unsieved glass beads in water. The data (symbols) are compared with the predictions of the effective medium theory (line).

5.2.3.3 The group velocity

To determine the group velocity from the pulse data, the envelopes of the reference and transmitted pulses were established. Any dc offset to the baseline of the waveform was first corrected, so that the pulse shape was symmetric about zero amplitude. For the unfiltered data, the average value of the offset outside the pulse region was found and the result then subtracted from the waveform. For the filtered data, this did not need to be done since a constant offset merely provides a peak at zero frequency, the offset then vanishing upon transformation back to the time domain after multiplication by the Gaussian filter. The pulse envelope was then determined from the absolute value of the amplitudes of the positions of *both* the maxima and the minima of the oscillations of the ultrasonic pulse, effectively doubling the resolution. The results of the determination of the pulse envelopes are illustrated in figure 5.11 and figure 5.12, where the upper panel in each figure shows the reference pulse envelope (a), and the lower panel the transmitted pulse envelope (b). These two plots correspond, respectively, to those wave forms shown in figure 5.8 (filtered minimal dispersion example: $k_w a = 5.1$) and figure 5.9 (filtered pronounced dispersion example: $k_w a = 3.0$). The open circles denote the positions of the extrema of the ultrasonic field.

The difference between central positions was used to determine the transit time Δt between the reference pulse envelope and transmitted pulse envelope. For the unfiltered wave forms, this was accomplished by inspection. An improvement in the accuracy of the measurement was obtained by filtering the wave forms (as described

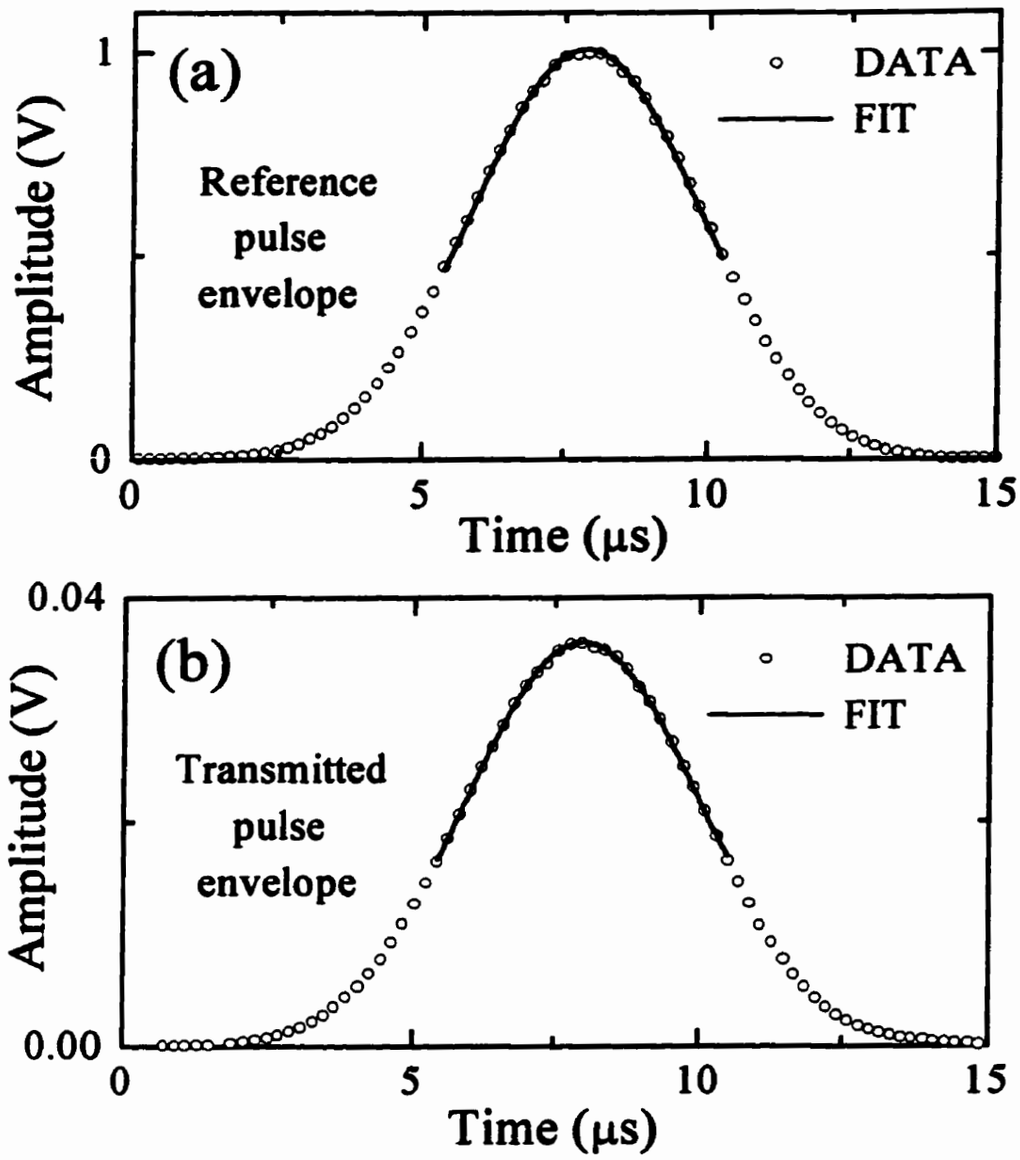

Figure 5.11 (a) Reference pulse envelope, and (b) transmitted pulse envelope, of those Gaussian-filtered waveforms shown in figure 5.8, at a frequency evidencing minimal dispersion ($k_w a = 5.1$, or 2.58 MHz). The open circles are the positions of the extrema of the ultrasonic field, and the solid lines are the best Gaussian fits to the coherent pulses.

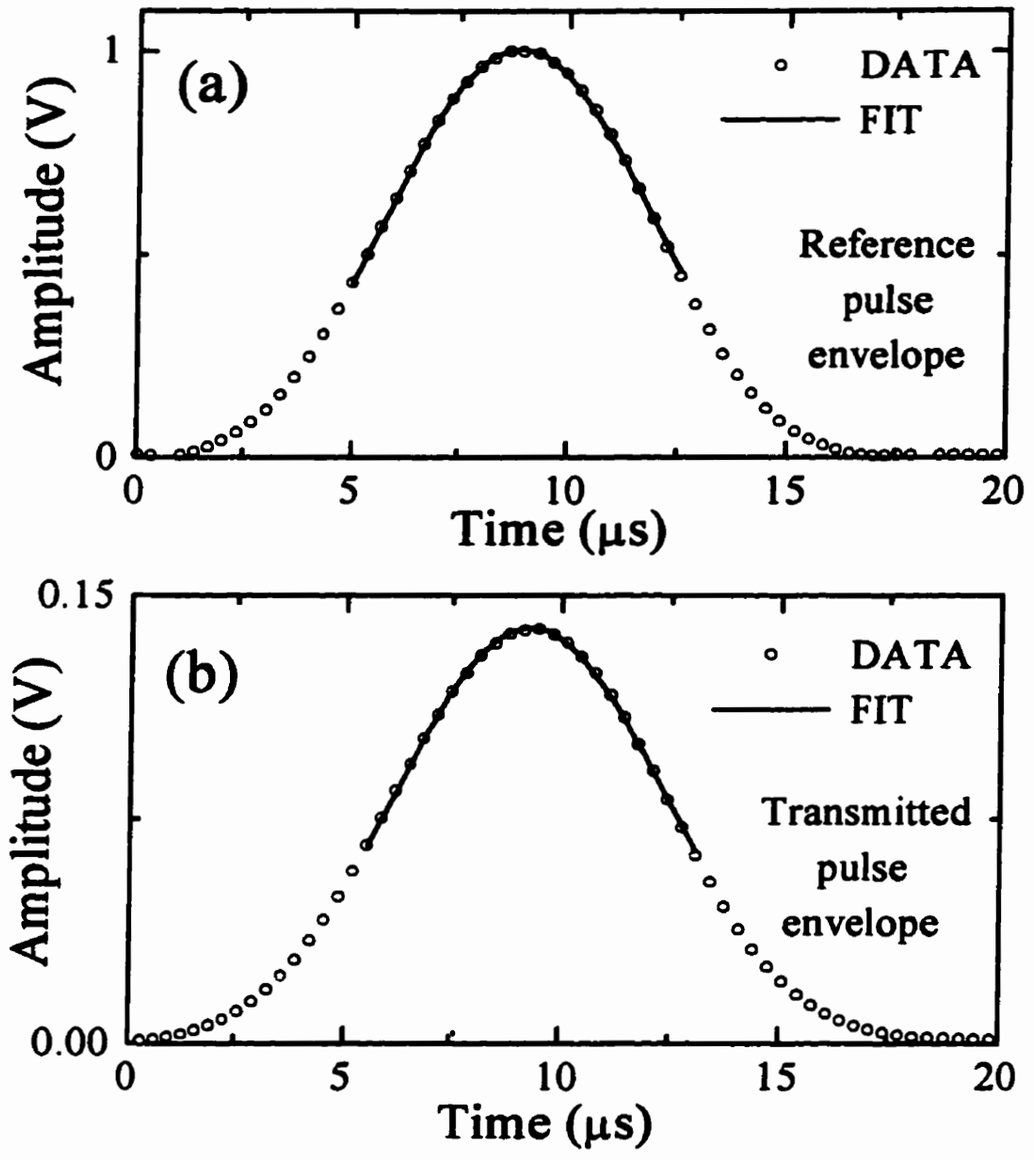

Figure 5.12 (a) Reference pulse envelope, and (b) transmitted pulse envelope, of those Gaussian-filtered wave forms shown in figure 5.9, at a frequency evidencing pronounced dispersion ($k_w a = 3.0$, or 1.52 MHz). The open circles are the positions of the extrema of the ultrasonic field, and the solid lines are the best Gaussian fits to the coherent pulses.

above). For the filtered wave forms, the centres of the envelopes were determined by fitting a Gaussian pulse shape to the envelopes. In general, the most accurate fit was obtained by fitting only the top half of the pulse (figure 5.11, and figure 5.12). Since the uncertainty in the fits were usually on the order of nanoseconds, the uncertainty in the transit time Δt was taken from the difference between the pulse widths of the fits. This difference provides an indication of the dispersion in the ballistic pulse and, in some qualitative sense, shows how much the peak may have been shifted. This was generally the largest contribution to the uncertainty in the group velocity.

The experimentally determined group velocities of acoustic waves propagating through the unsieved glass beads in water are presented in figure 5.13, and those for the sieved glass beads in water in figure 5.14. The group velocity is seen to exhibit a strong frequency dependence, being observed to vary in both cases by about a factor of two. Comparison of these group velocities show their behaviour to be similar, especially at low frequencies, with both the unsieved and the sieved data exhibiting a minimum of about 0.9 km/s near $k_w a \approx 2$, which is the same position as found for the first dip in the scattering mean free (figure 5.3 and figure 5.4, respectively). The second, fairly broad, dip in the unsieved bead group velocity is apparent between $k_w a \approx 7$ and $k_w a \approx 8$, which corresponds to the second dip observed in the scattering mean free path data for the unsieved bead samples (figure 5.3). The positions of the deep minima in the sieved bead group velocity ($k_w a \approx 7 \text{and} 8$) bracket the rather ill-defined minimum in the scattering mean free path data for the sieved bead samples (figure 5.4). The sieved bead group velocity also shows a sharp maximum at $k_w a \approx 7.5$, which is completely washed out for

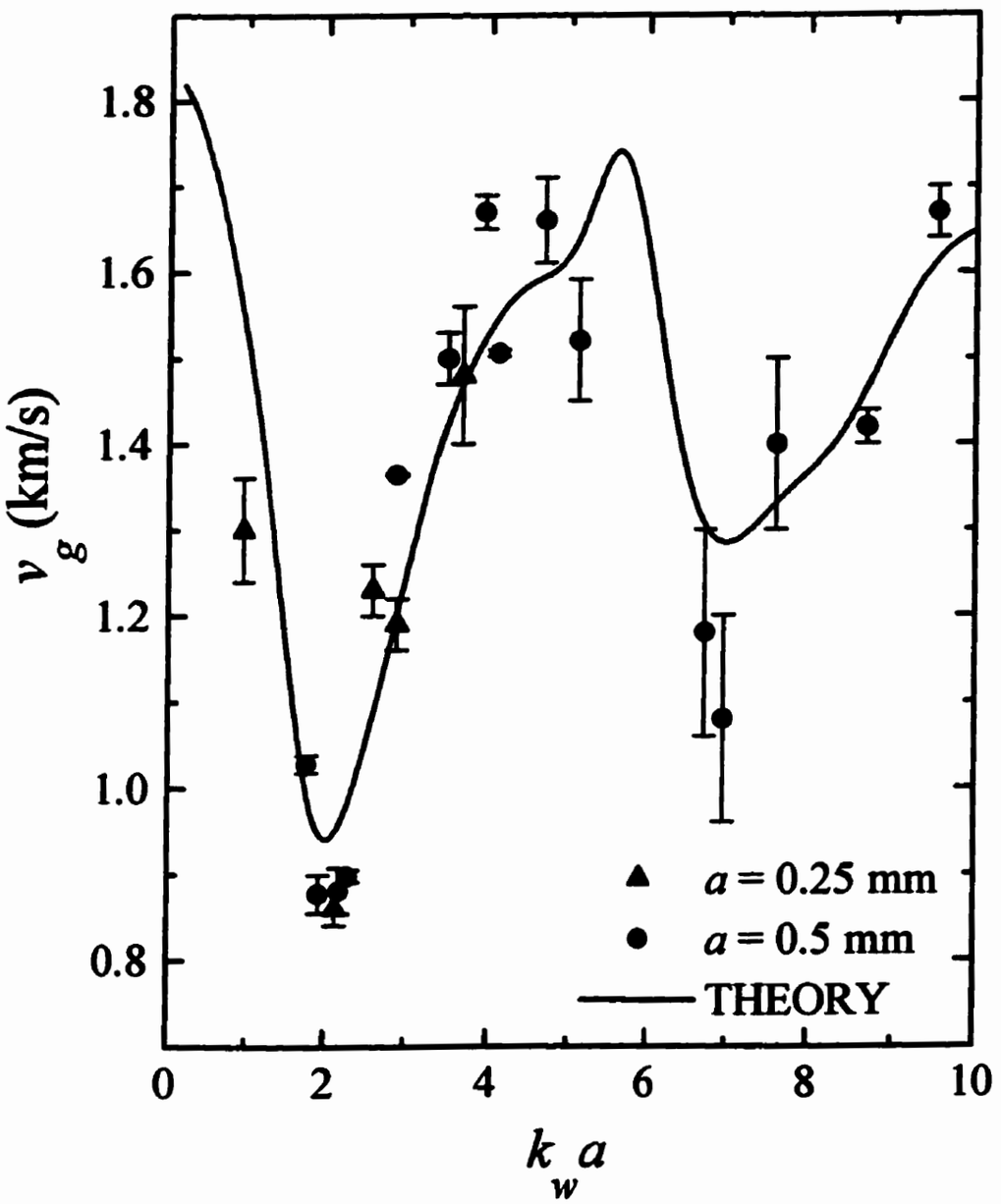

Figure 5.13 Group velocities of acoustic waves in a strongly scattering medium consisting of the unsieved glass beads in water. The data (symbols) are compared with the predictions of the effective medium theory (line).

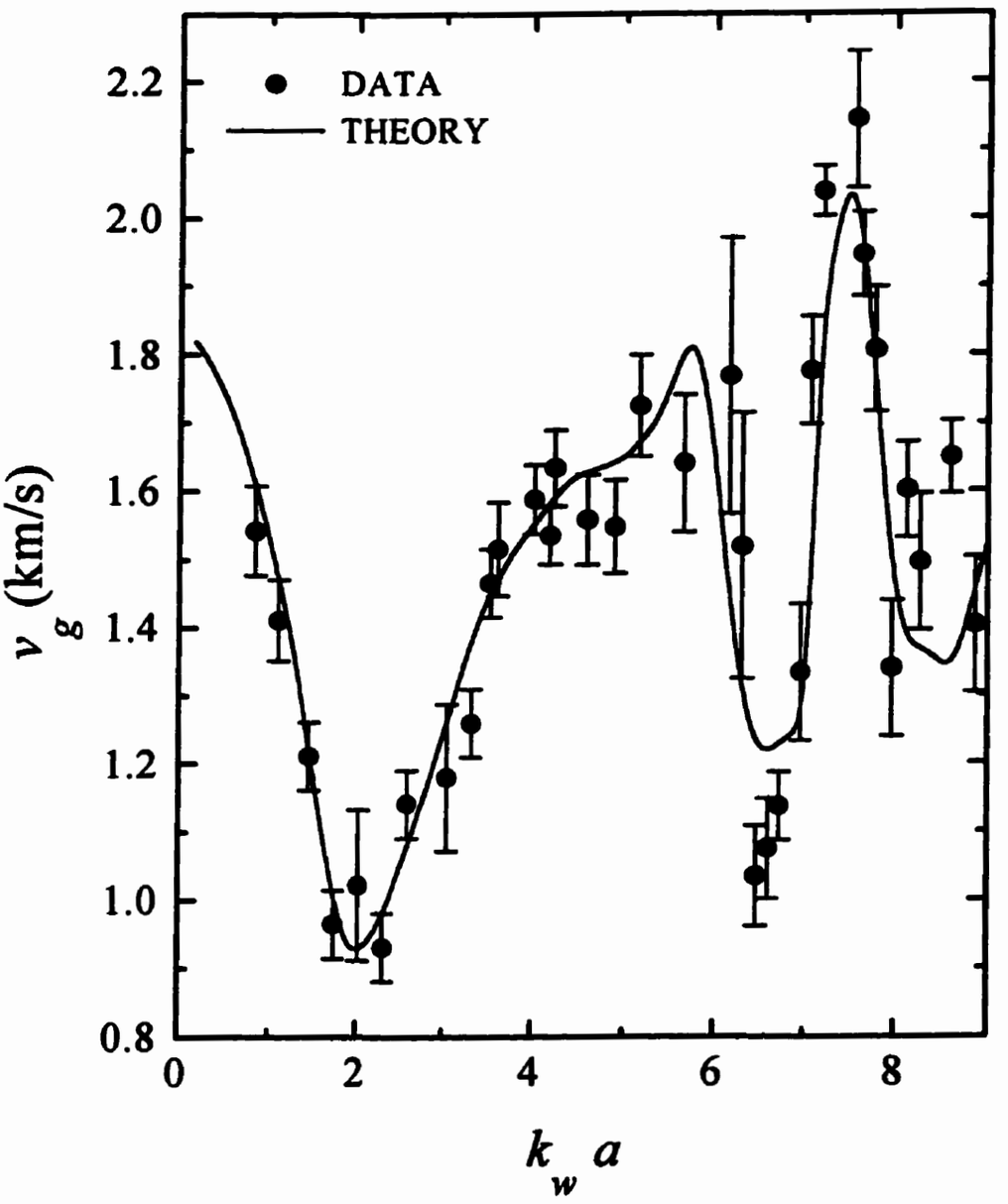

Figure 5.14 Group velocities of acoustic waves in a strongly scattering medium consisting of the sieved glass beads in water. The data (symbols) are compared with the predictions of the effective medium theory (line).

the unsieved beads due to the increased range of bead sizes, thus illustrating the greatly improved spectral resolution of resonant scattering features that can be achieved by significantly narrowing the bead size distribution.

The theoretical determination of the group velocity begins with the calculation of the DOS, as has been discussed in Sec. 2.1.8. The DOS was found from the Green's function solution to the elastic wave equation (Sec. 2.1.7) by embedding a single coated sphere in an effective medium (Sec. 2.1.4), whose properties were determined through the application of the GCPA (Sec. 2.1.6.3). From the peaks in the DOS, the dispersion curve (shown by the solid white line in figure 2.2), was thence obtained. Numerical differentiation [equation (2.57)] of the dispersion curve, and the subsequent convolution over the bead size distribution (cf. figure 3.2), yielded the predicted group velocities. These theoretical predictions, requiring *no* adjustable parameters, are shown by the solid lines in figure 5.13 and figure 5.14, for the unsieved bead and sieved bead group velocities, respectively. Excellent quantitative agreement with the data is seen in both cases. The difference between the two curves, quite apparent at higher frequencies, is a consequence of the different distributions of bead sizes involved in the unsieved and sieved bead samples. The polydispersity for the unsieved beads was about 15% while that of the sieved beads was about 5%. In the theoretical calculations, the bead distribution used for the unsieved beads had a Gaussian functional form, based on the measured distribution of bead sizes shown in figure 3.2, while for the sieved beads an asymmetric functional form appropriate to the slice of the original bead distribution selected by the sieving was used. For the case of the unsieved beads, the factor of three increase in the polydispersity, coupled with a more diffuse bead distribution, has a "washing out" effect (figure 5.13) on

the more rapid frequency variations in the ballistic propagation velocities apparent at high frequencies in the sieved bead case (figure 5.14).

As a concluding observation, the group velocities over most of the frequency range investigated are significantly less than the sound speeds in the material constituents, as was the case for the phase velocities. The physical significance of these slow velocities, the consequence of agreement between the velocity data and the theory, as well as the matching of the minima between the mean free path and the group velocity, are discussed in the next section.

5.2.4 Discussion

At this point it is appropriate to summarize what has been presented thus far, regarding the propagation of the ballistic pulse through the scattering medium, with a view to elucidating the physical origin of the behaviour. This is done within the context of the theoretical predictions of the pulse behaviour. To set the stage for this discussion, however, a few introductory remarks are in order. The behaviour of the ballistic pulse was investigated in the intermediate frequency regime, where the size of the inhomogeneities (i.e. the glass beads) were comparable to the wavelength of the wave – specifically, for wavelengths ranging from about 0.6 times the bead radius to about 6 times the bead radius. The large attenuations of the ballistic pulses on these length scales, and the correspondingly large dispersion, have implications for the *nature* of the propagation. This has been recognized in the work of Sommerfeld (1914) and Brillouin (1953, 1960), and the determination of the speeds of propagation has remained a classic problem,

particularly the group velocity which is strictly well defined only when the dispersion is not too large (Jackson, 1975). That the scattering in the medium has affected the ballistic propagation is undeniable, as the group velocity, though well defined, is *not* intermediate between that of the glass and the water. How is it then that the temporal and spatial coherence between the transmitted and incident pulses is maintained? The answer to this question begins with the understanding of the behaviour of the scattering mean free path.

The scattering mean free path was found to exhibit pronounced dips (e.g. figure 5.3), the positions of which correspond almost exactly to the minima observed in the measured group velocity (e.g. figure 5.13). The origin of these dips was determined from a calculation of the total scattering cross section of a coated sphere using the GCPA approach. These calculations, which faithfully reproduced the frequency variation in the data (though not their magnitude), allowed the dips in l_s to be identified with resonances in the total scattering cross section of a *single* scattering unit (i.e. coated sphere) embedded in the medium. These resonances must then also be the origin of the dispersion in the group velocity.

The most surprising feature of the group velocity data was the remarkably slow velocities of the spatially and temporally coherent transmitted pulse at the resonant frequencies of the single coated-spheres. The agreement of the calculated group velocity with the data suggests a physical interpretation of the coherent transport at such slow speeds. The group velocity was calculated from the dispersion curve determined from the peaks in the DOS. The DOS itself was found by embedding a single coated-sphere in an effective medium whose properties were determined through the application of the GCPA. This *renormalized* the scattering, and the resonances of the coated sphere were thus

modified by their coupling to the embedding medium. The degree of renormalization depends on the strength of the scattering; the greater the scattering, the greater the modification. This assertion is supported by the following rationale. For a dilute concentration of scatterers, the individual scattering resonances would be strong and well defined, and the material properties of the embedding medium would be distinct from those of the scatterer. However, if the concentration of scatterers were to increase, then it is physically plausible that the material properties of the embedding medium would approach those of the scatterers themselves. The diminishing effective contrast between the scatterer and the embedding medium would inevitably lead to weakened individual scattering resonances. Thus, in the limit of the embedding medium having the same properties as the scatterers, the individual resonances must vanish entirely. This is the origin of the uniform properties of the medium, whose renormalization determines the group velocity. The theoretical approach followed identifies the frequencies and wave vectors of the minima in the coupled scattering resonances, thus yielding the dispersion curve. This procedure directly indicates how a propagating wave of frequency ω is forced by the renormalization of the embedding medium to select the wave vector k that allows it to propagate through the medium with the least scattering. The theoretical approach taken correctly describes the renormalization of the effective medium by the strong resonant scattering, and thus explains the physical origin of the remarkably low velocities of ballistic propagation.

5.3 Ultrasonic speckle

One of the experimental challenges in measuring multiply scattered ultrasonic radiation arises from the rapid spatial fluctuations that occur in the phase and amplitude of the scattered sound in the detecting plane. These fluctuations are caused by the interference between the ultrasonic waves that have traveled different paths through the sample, resulting in acoustic speckles that are analogous to the more familiar case of optical speckles (Goodman, 1976). Since piezoelectric transducers measure the ultrasonic *field* across the surface of the detector (see Sec. 4.2), these rapid spatial fluctuations will give rise to spurious phase cancellation effects if conventional large diameter transducers are used, leading to grossly inaccurate results. This serious experimental limitation has been overcome by the use of the miniature hydrophone, whose diameter is less than the ultrasonic wavelength, to detect the scattered radiation over a single coherence area.

The spatial fluctuations that occur are illustrated in figure 5.15 for a cross section of the acoustic speckle pattern of the multiply scattered sound arising from the transmission of an incident continuous wave through a 20-mm-thick sample containing 0.5-mm-radius glass beads. The frequency of the incident wave was f = 2.5 MHz, implying an ultrasonic wavelength in water of λ = 0.6 mm. These data were collected by scanning the small hydrophone across the face of the sample. They confirm that the width of the coherence area over which the ultrasonic signal is essentially constant is approximately equal to the ultrasonic wavelength λ. The spatial fluctuations of the multiply scattered sound exiting a square region 4 mm on a side are illustrated in figure

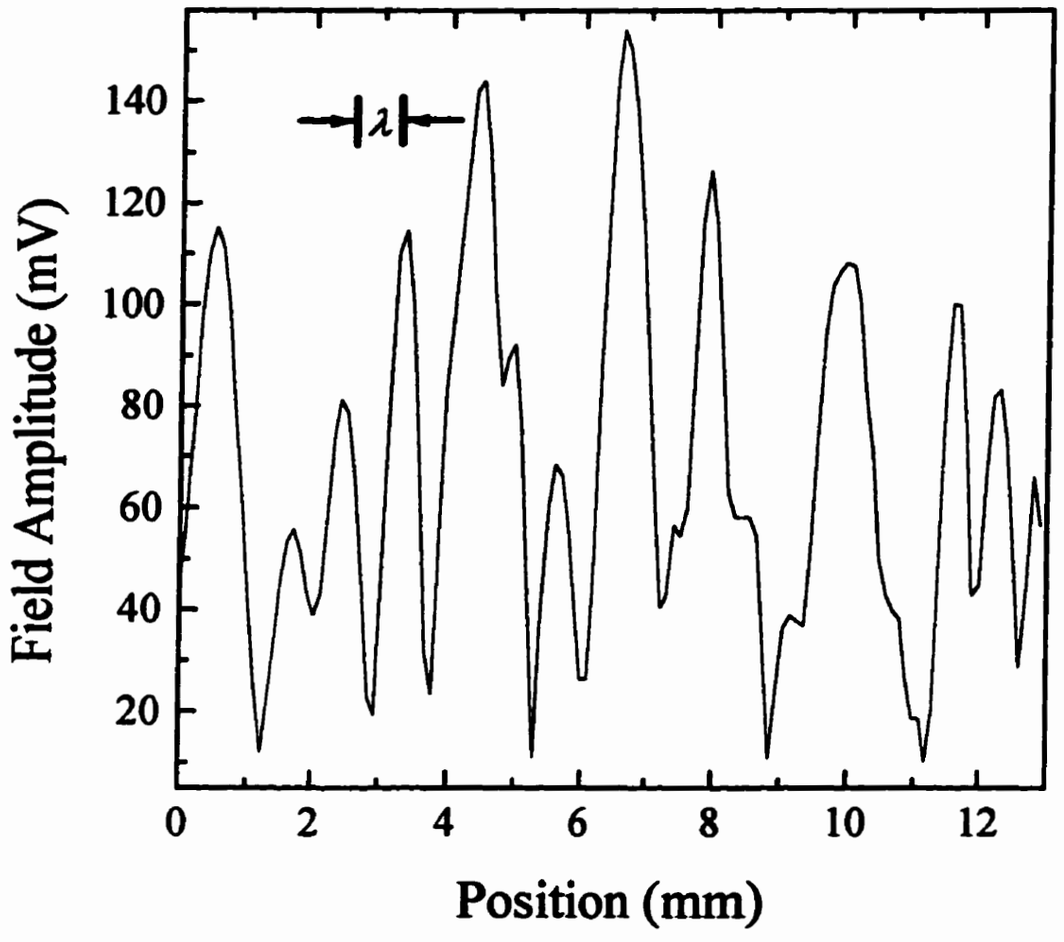

Figure 5.15 Typical cross section of the acoustic speckle pattern for multiply scattered sound exiting a 20 mm thick sample of 0.5 mm radius glass beads in water. The coherence area is approximately λ^2, where $\lambda = 0.6$ mm is the wavelength in water.

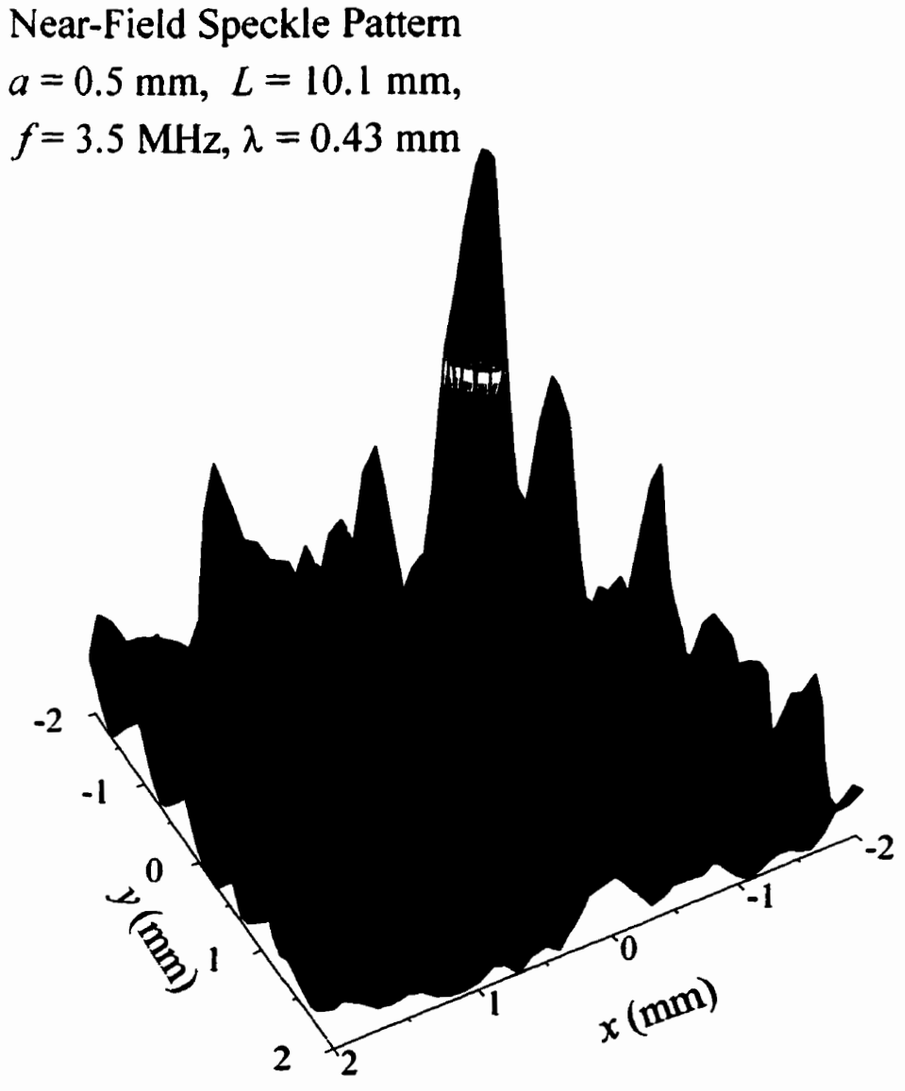

Figure 5.16 The near field speckle pattern of multiply scattered sound, for a 10 mm sample containing 0.5 mm radius glass beads in water, detected over a square region approximately nine wavelengths wide, where $\lambda = 0.43$ mm (corresponding to a frequency of $f = 3.5$ MHz).

5.16, for a 10 mm sample containing 0.5 mm radius glass beads in water, at a frequency of f = 3.5 MHz, corresponding to an acoustic wavelength in water of λ = 0.43 mm. The resolution is 100 pixels/mm. with red denoting a region of high intensity (a "bright" speckle), and blue a region of low intensity (a "dark" speckle).

In practice, it is not possible to predict the actual intensity variations in a speckle pattern for a particular scattering microstructure. It is therefore necessary to discuss the properties of speckle patterns in statistical terms. The statistics describe the behaviour of the scattering as defined by an ensemble of scattering systems, all with the same macroscopic properties but differing in microscopic detail. In the context of the transmission of multiple scattered ultrasonic waves through randomly close-packed glass beads in water, this implies samples of the same thickness and occupied volume fraction (of the glass beads), but with different arrangements of the glass bead disorder. The measured intensity at a specific position, for a particular time, is then not exactly predictable given a *single* sample, but its statistical properties over an ensemble of samples *can* be described.

The development of a statistical model for speckle follows from its equivalence to the random walk problem in a plane (Goodman, 1976). This equivalence is valid provided two quite reasonable assumptions hold true. The first assumption is that not only should individual members of the ensemble be unrelated, but the strength of a particular scattered component should bear no relation to its phase. The second assumption is that there should be no preferred phase – the phase distribution should have uniform probability over the interval from $-\pi$ to π. If these two assumptions hold true, and if the ensemble is

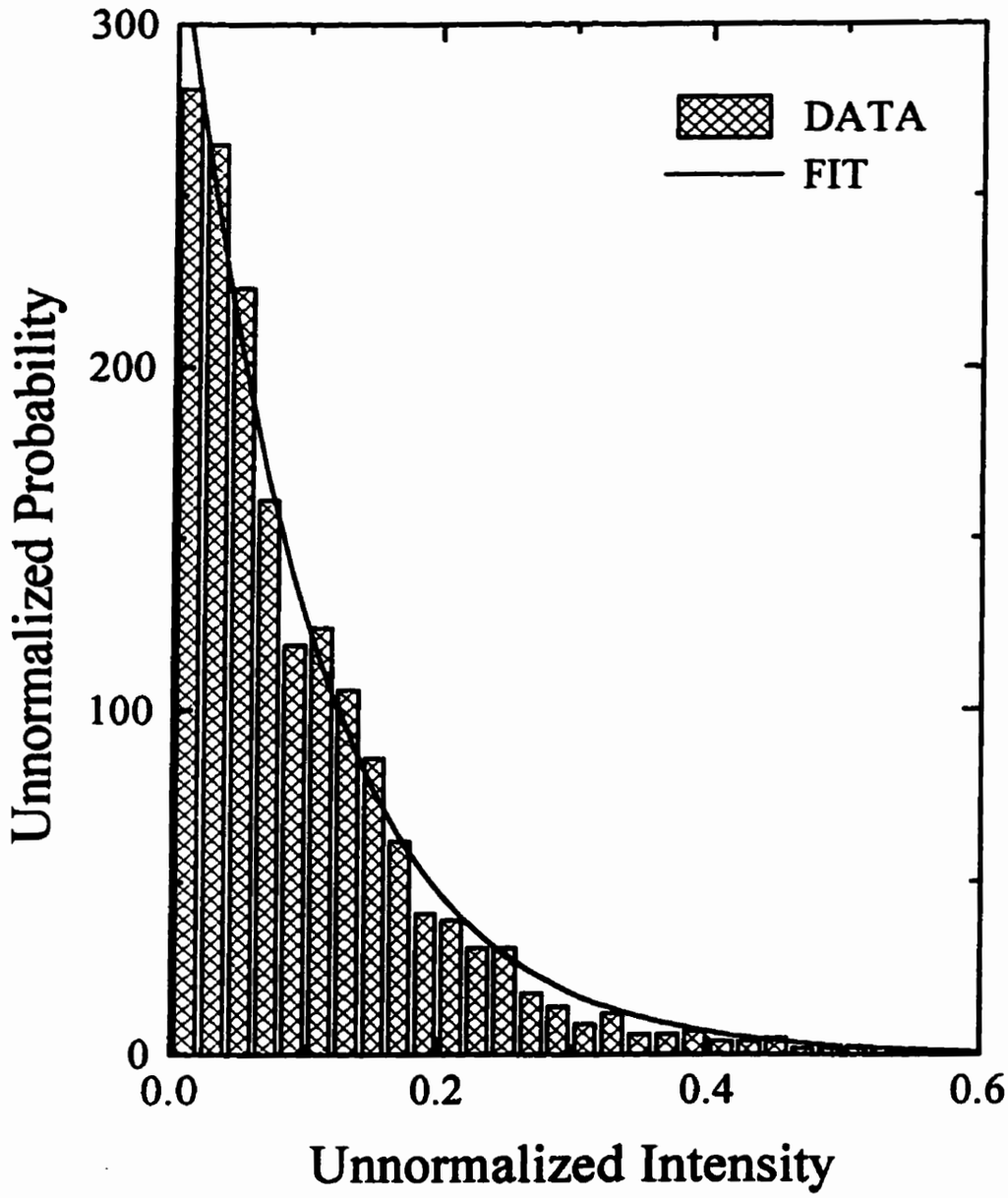

Figure 5.17 Probability distribution of the intensity in the speckle pattern shown in figure 5.16. The solid curve is a fit to the exponential distribution function.

sufficiently large, the probability distribution of the intensity will obey an exponential distribution function of the form

$$P(I) = \frac{1}{\overline{I}} \exp\left(-I/\overline{I}\right), \tag{5.5}$$

where $\overline{I}$ is the mean intensity. The speckle pattern illustrated in figure 5.16 has a mean intensity of 0.1025, in arbitrary units, as determined by direct calculation. Under the assumption that the 1600 pixels consist of uncorrelated members of an ensemble, the (unnormalized) probability distribution of the intensity in the speckle pattern, shown in figure 5.17, can be fit to the predicted negative exponential form. An unweighted fit, shown by the solid curve, yields a mean intensity of $\overline{I} = 0.1025$, in excellent agreement with the result determined by direct calculation. A consequence of this agreement is the implicit verification of the assumption that individual intensity measurements, at different positions on the same sample, can be treated as independent members of an ensemble, provided that the number of speckles sampled is sufficiently large. Physically, this indicates that each speckle is the result of a very different realization of possible path lengths, implying that the correlation between neighbouring speckles is weak, at best (Jones, 1996).

Inspection of figure 5.16 correctly gives the impression that the variation in the intensity is a significant fraction of the mean. The exponential distribution function, equation (5.5), has the characteristic that its standard deviation precisely equals its mean, implying that the contrast of a speckle pattern, as defined by

$$C = \sigma_I / \overline{I}, \tag{5.6}$$

where σ_I is the standard deviation, is then always unity (Goodman, 1976). The standard deviation of the intensity for the speckle pattern shown in figure 5.16 is $\sigma_I = 0.115$, yielding a value for the contrast 12% in *excess* of unity. This is presumably due to the fact that the averaging (though over 1600 pixels) covers only 80 –90 speckles, at best. This presumption is supported by further speckle data, spanning a wide range of sample thicknesses and frequencies, where the contrast has been observed to vary randomly, both above and below unity, by amounts usually less than the square root of the number of speckles sampled.

5.4 Temporal fluctuations

In the previous section, the propagation of an incident continuous wave through the sample produced an ultrasonic speckle pattern that was constant over time. This is not the case for the transmission of a very short pulse. The signal detected within a single coherence area should be spread out over time as longer and longer scattering paths impinge on the detector. Such behaviour is illustrated in figure 5.18 for the propagation of various short pulses through a 10-mm-thick sample containing unsieved 0.5-mm-radius glass beads in water. The incident pulses, shown to the left of their transmitted signals, were centred at a frequency of 2.45 MHz, and varied in width from about 1 μs to about 5 μs. Inspection of these figures shows that the transmitted signals are spread out over time intervals in excess of 70 μs, due to the progressively longer paths traveled as a consequence of the multiple scattering. An important consequence of the interference effects of the multiply scattered sound transmitted along different paths are the large temporal fluctuations in the amplitude that modulate the more rapid 2.45 MHz carrier frequency oscillations. The characteristic periods of these fluctuations in the waveform envelopes are on the order of the input pulse width, and represent the time over which the magnitude and phase of the detected fields remain essentially unchanged. This results from the range of possible scattering paths, whose limits are set by the width of the incident pulse, that contribute at a given instant on the detector. Hence, the maximum overlap of the paths contributing at any time is determined by the width of the incident pulse, so that as the incident pulse width is increased, the characteristic width of these

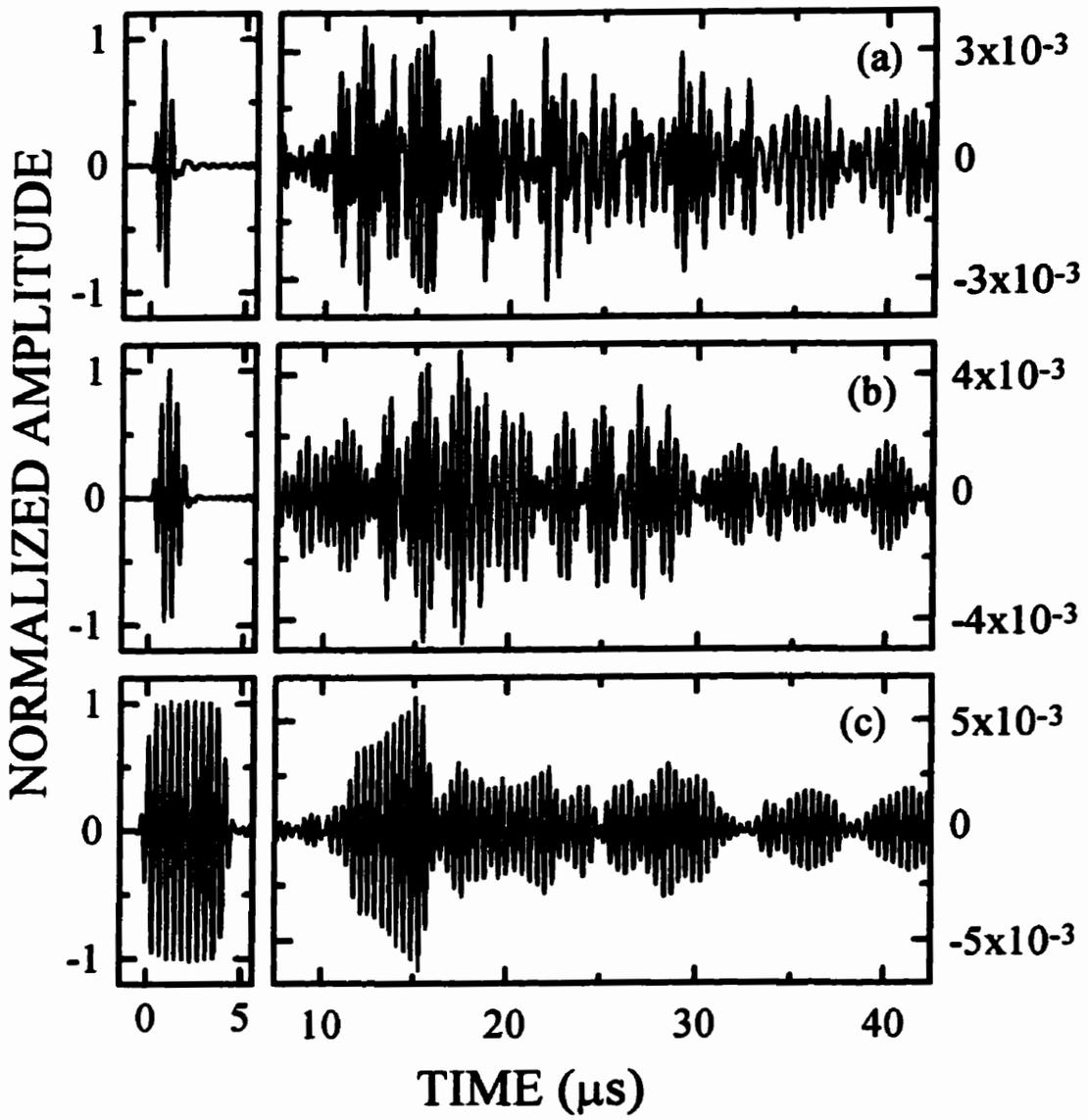

Figure 5.18 Time evolution of the transmitted ultrasonic fields in a single speckle (right) for three different incident pulse widths (left), showing the temporal fluctuations of the multiply scattered fields.

temporal fluctuations also increase proportionately. This is illustrated by the progression in figure 5.18 which shows the signal transmitted through the same sample when the pulse width is increased from about 2 oscillations [figure 5.18(a)], to about 4 oscillations [figure 5.18(b)], and then to about 10 oscillations [figure 5.18(c)]. In all cases, the temporal fluctuations of the envelope vary on a time scale that corresponds to the increasing input pulse widths. The interference effects of the waves, transmitted along different paths, that give rise to these temporal fluctuations, can thus be directly measured using sound because both the amplitude and phase of the scattered waves are detected.

The interference effects originate from the sum of the ultrasonic fields of the overlapping path distributions in the sample. If the incident pulse width exceeds the longest transit times for the scattered sound to travel through the sample, the interference effects approach those of continuous wave input. This is illustrated in figure 5.19, which shows the effect of increasing the incident pulse width to 100 μs. The incident pulse is shown in figure 5.19(a), normalized for comparison with the transmitted signals to an amplitude of ± 1. Figures 5.19(b) and 5.19(c) show the relative amplitudes of the signals transmitted through a 10-mm-thick glass bead sample. The data in figures 5.19(b) and 5.19(c) were taken for two different positions of the detector, corresponding to bright and dark speckles, respectively. Fluctuations in the transmitted signals are still observed during the first 50 – 60 μs, whereupon the entire distribution of different path lengths becomes simultaneously "filled" and the signal level becomes constant, as would be expected for continuous wave transmission (cf. Sec. 4.3.3.1). Unlike the continuous wave

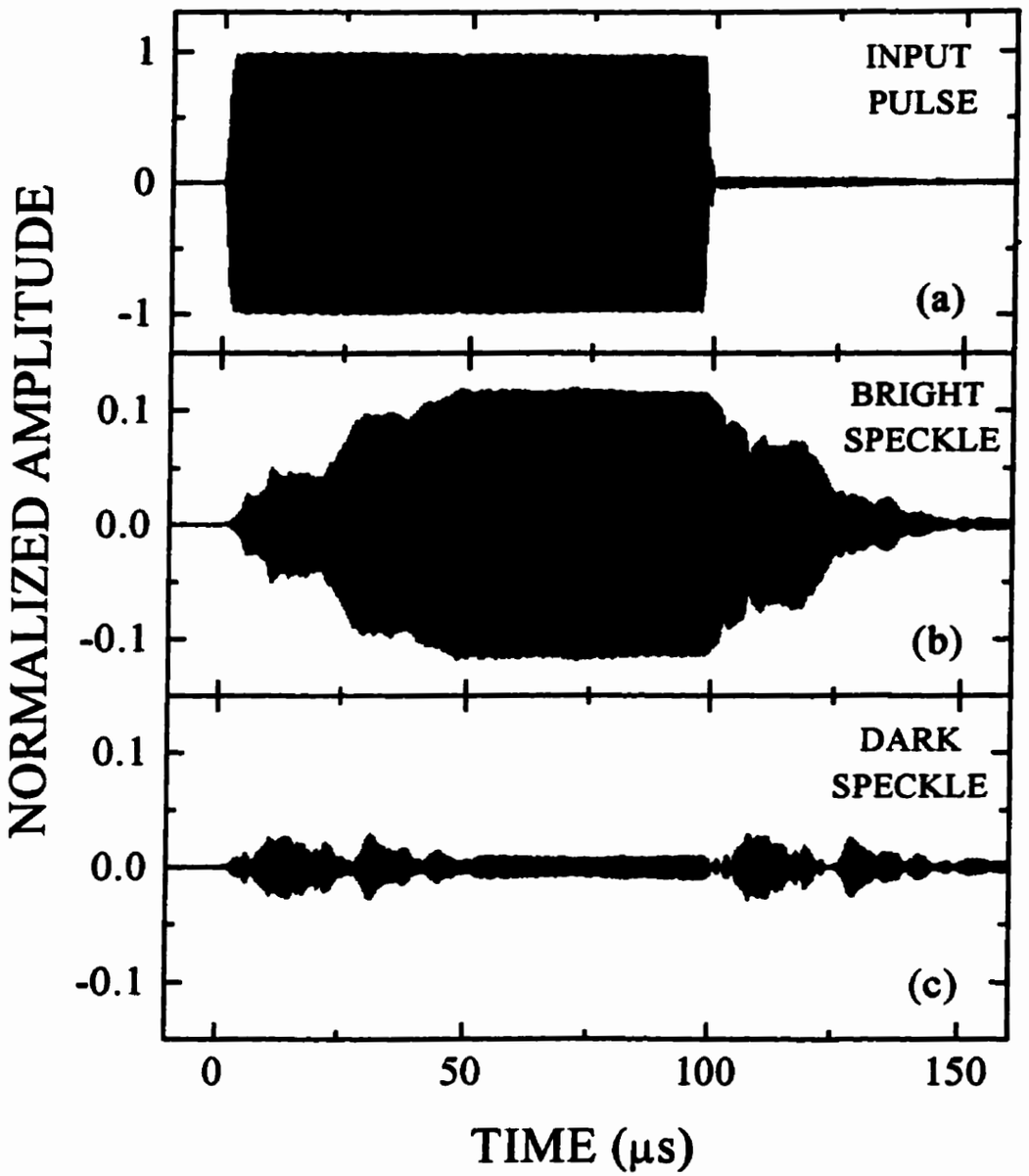

Figure 5.19 Transmitted ultrasonic field in a single speckle for an incident pulse width of 100 μs. The incident pulse is shown in (a), and the transmitted field in typical bright and dark speckles are shown in (b) and (c).

situation, however, this plateau lasts only until the end of the input pulse, after which rapid fluctuations are again observed as the paths impinging on the detector from earlier temporal positions in the incident pulse begin to decay away. The time interval over which these fluctuations persist is similar to the time for the sound to diffuse through the sample in the short pulse experiments, again showing the temporal interference effects that are directly observable in ultrasonic experiments.

5.5 Diffusive transmission

5.5.1 Dynamic measurements (pulse mode): D and τ_a

5.5.1.1 Ensemble averaging: the diffusive pulse

An understanding of the propagation of acoustic waves, beyond that described by the ballistic pulse, is afforded by studying the mean behaviour of the multiply scattered sound intensity. Since each particular scattering microstructure provides a unique distribution of path lengths between a source point and detector, a general description of the propagation must of necessity involve many statistically independent *ensembles* of such scatterers. This is indeed what the mathematical formalism of diffusive propagation presupposes when characterizing the acoustic intensity (Sec. 2.2.7.1; cf. Sec. 2.2.2).

An example of the experimental determination of this diffuse acoustic intensity (the "diffusive pulse") is presented for the transmission of an incident plane wave, with a 1.55 MHz central frequency and a 5 μs pulse width [figure 5.21(a)], through a 7 mm thick sample composed of the sieved glass beads in water. The transmitted signals were detected over time within different coherence areas, yielding both phase and amplitude behaviour, as figure 5.20 illustrates for three typical speckles. Again, as discussed in Sec. 5.4, the transmitted signals are spread out over time intervals in excess of 70 μs and exhibit temporal fluctuations on the order of the input pulse width. The important point here is that there seems to be no similarity between the speckles, reflecting the unique set of path lengths traversed as a consequence of the different scattering microstructure and

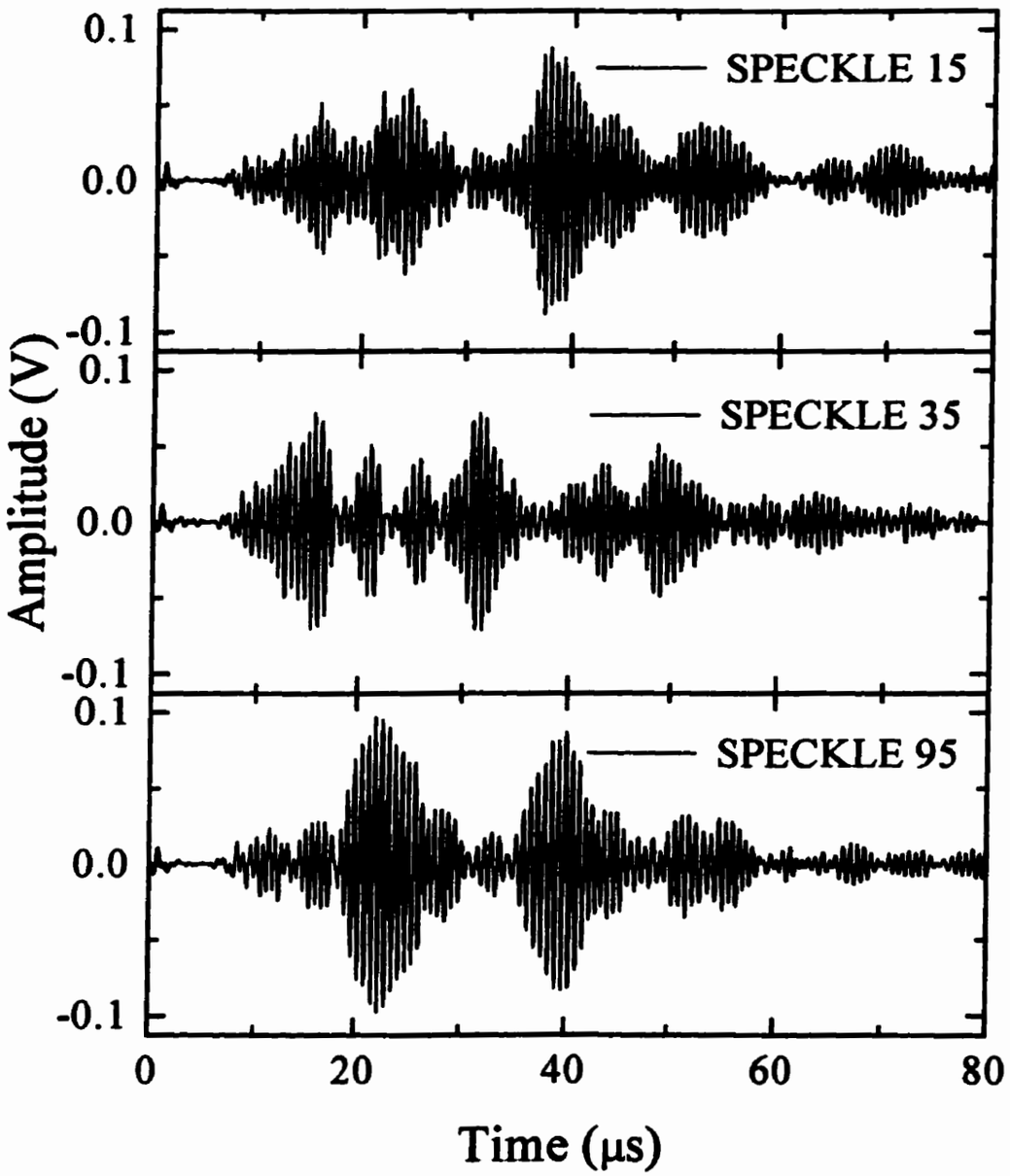

Figure 5.20 Typical ultrasonic fields detected, from three different coherence areas, due to the propagation of a 1.55 MHz incident plane wave pulse through a 7 mm sample containing sieved glass beads in water.

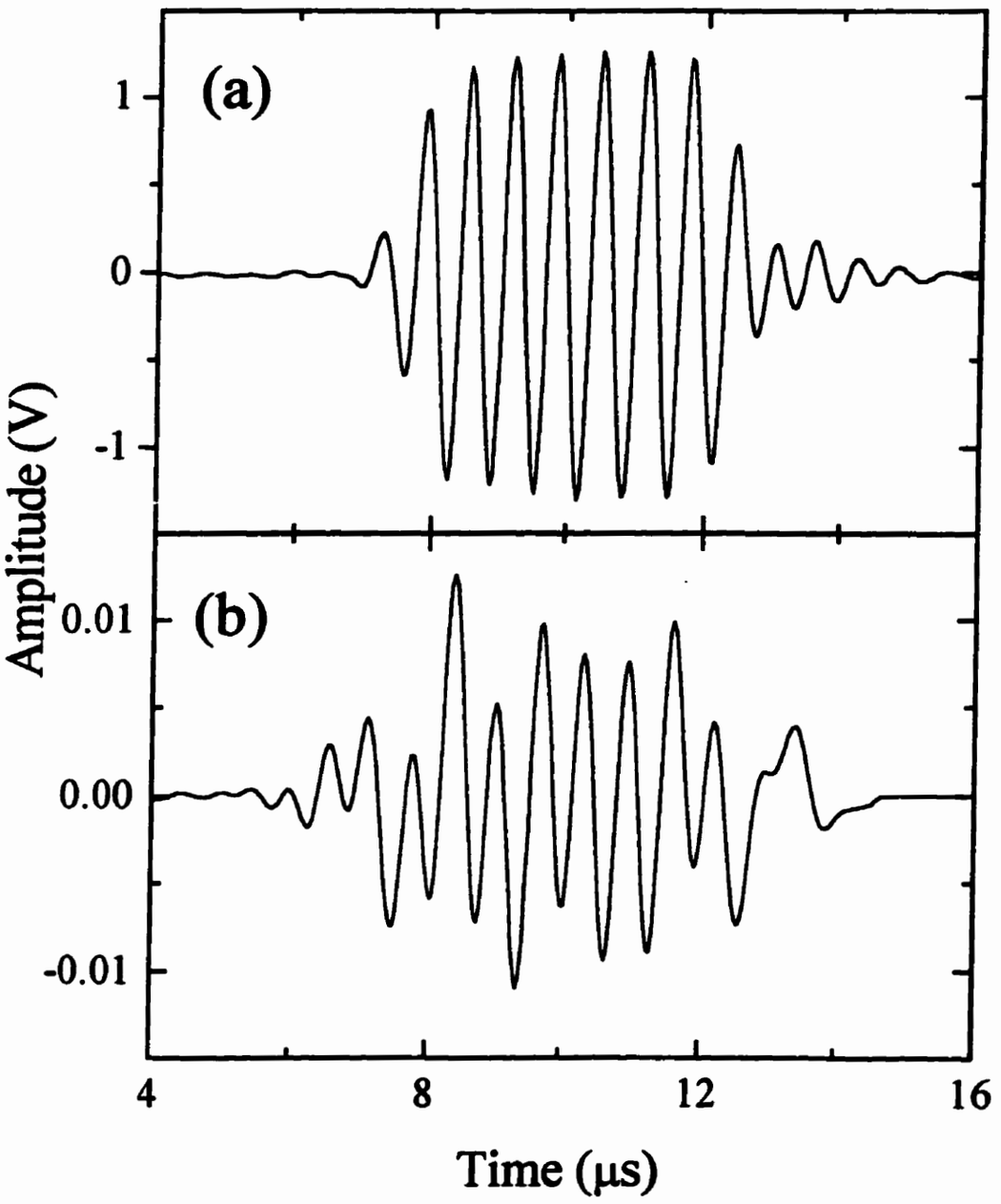

Figure 5.21 (a) The incident pulse for those ultrasonic fields presented in figure 5.20. (b) The ballistic remnant used to correct the fields.

implying that the speckles may constitute independent members of an ensemble. This will be discussed quantitatively in Sec. 5.5.1.2.

The signal detected within each coherence area is, in principle, composed of both the ballistic and the diffusive signal, though the ballistic signal was usually extremely small. The behaviour of the multiply scattered sound being of interest, these two often needed to be decoupled. This required, first, the determination of the ballistic pulse (Sec. 5.2.1). For the example discussed above, the ballistic pulse resulting from the averaging of the ultrasonic fields of 121 speckles is presented in figure 5.21(b). The ballistic remnant is seen to be about 40 dB smaller than the incident pulse [figure 5.21(a)], and roughly 20 dB smaller than the mean size of the temporal fluctuations in the speckle. Moreover, though not shown in figure 5.21(b), the size of the ballistic remnant is comparable to the size of the remaining fluctuations in the averaged multiply scattered field. This point will be discussed further. The temporal extent of the ballistic pulse was identified by comparing it with the incident pulse, and then setting the amplitude of the remaining fluctuations to zero [e.g. the amplitude for all times greater than 14.5 μs in figure 5.21(b)]. The ultrasonic field of the ballistic pulse was then subtracted from the ultrasonic fields of the individual speckles, leaving the purely diffusive component. It should be noted that, regardless of the necessity of removing the ballistic component, each waveform was first corrected for a small baseline offset (~ 2 mV), thus eliminating the slight drift in the baselines (< 1 mV) between signals. This was done by averaging the positive and negative field excursions and then subtracting the result from each field to properly zero the waveform.

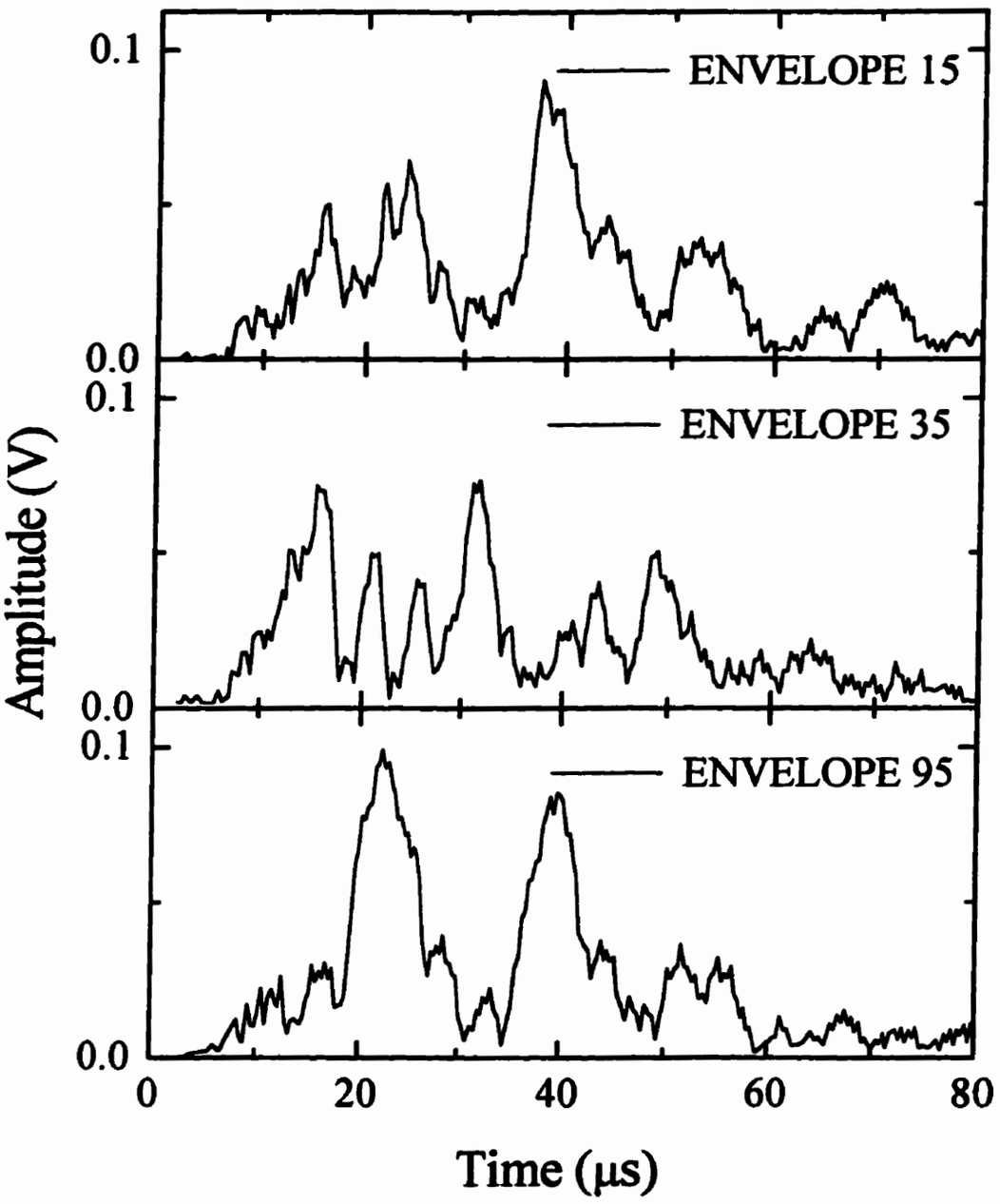

Figure 5.22 The waveform envelopes of those ultrasonic fields presented in figure 5.20.

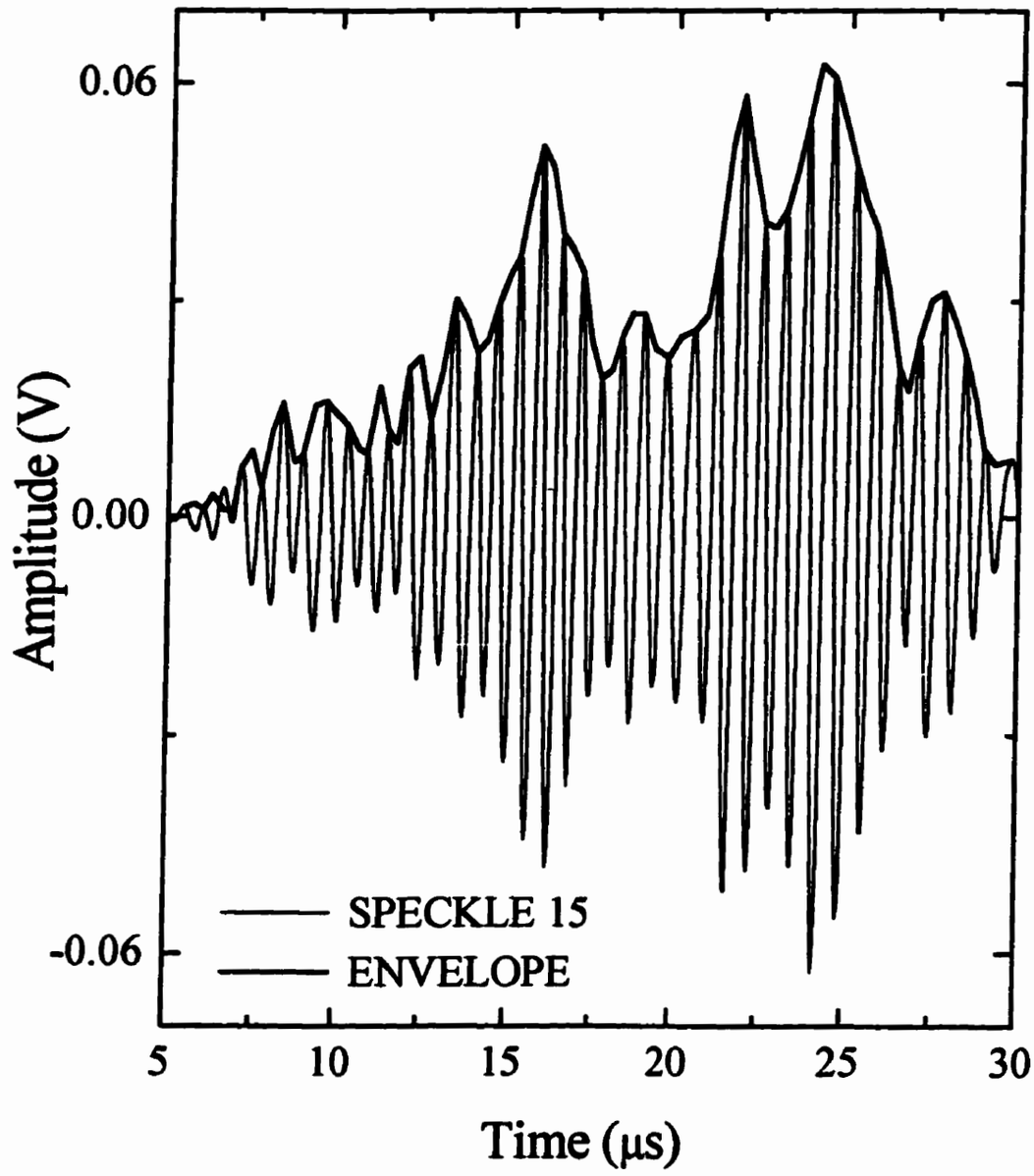

Figure 5.23 An expanded view at early times of the scattered field from speckle 15 (figure 5.20, upper panel), with its waveform envelope shown by the bold curve.

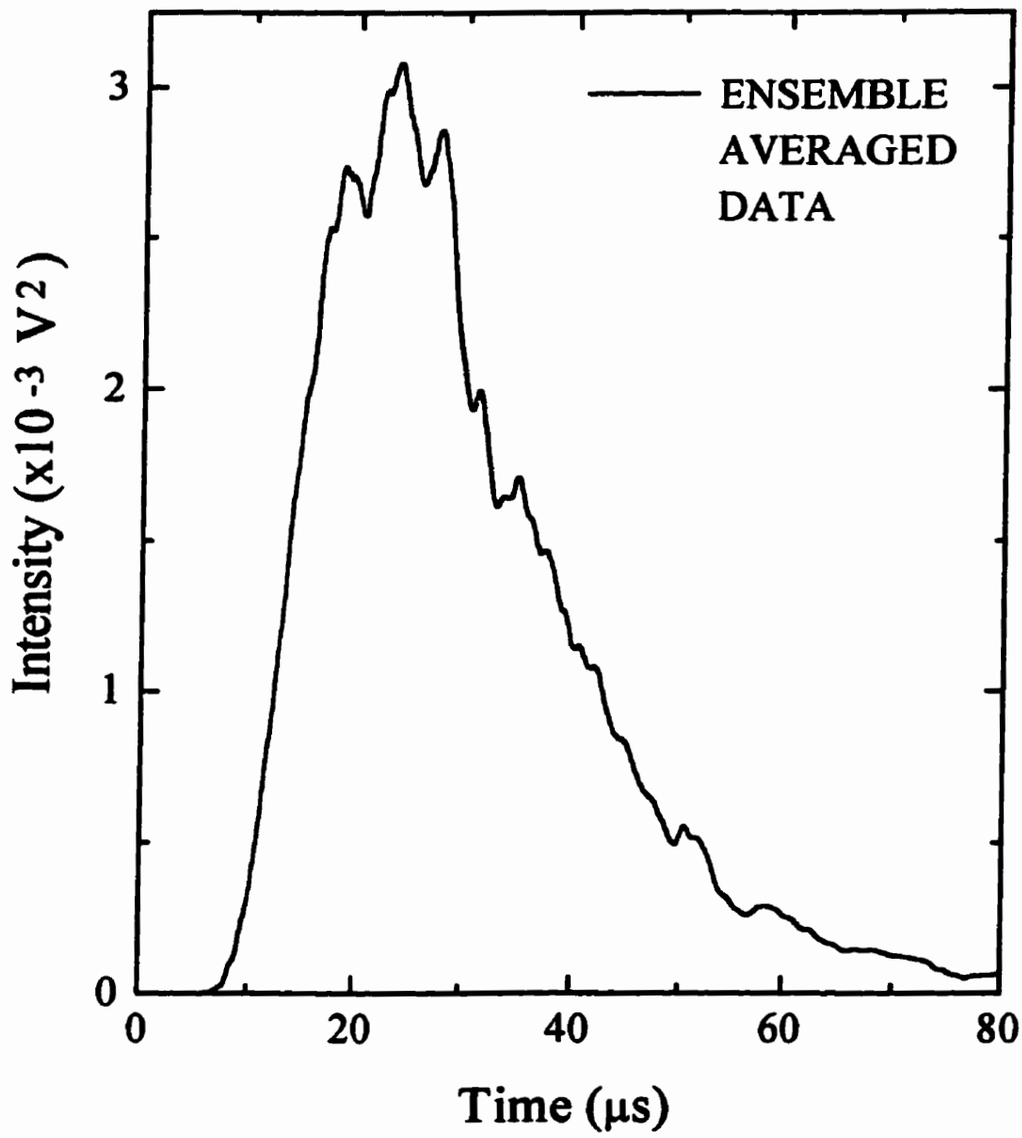

Figure 5.24 A typical diffusive pulse (unnormalized, no timing corrections) produced by the ensemble averaging of the scattered intensities from 121 separate speckles, due to a 1.55 MHz plane wave incident pulse transmitted through a 7 mm sample containing sieved glass beads in water.

To construct the mean diffuse intensity, the phase information contained in the individual speckles was ignored and the waveform envelopes determined. To double the temporal resolution of the envelope, the absolute value of the field was taken, and a peak search program used to identify the maxima of the individual oscillations. Figure 5.22 shows the envelopes of those fields presented in figure 5.20; figure 5.23 provides an enlarged view of one of these fields with its envelope. The envelopes were then squared, to give an intensity, and then averaged together to produce the ensemble averaged diffuse intensity. An example of such a diffusive pulse, for the propagation of the 1.55 MHz incident plane wave pulse through the 7 mm thick sample composed of the sieved glass beads in water, is illustrated in figure 5.24. The normalization and timing corrections needed by the diffusive pulse, before the diffusion parameters can be ascertained, are discussed in Sec. 5.5.1.3.1.

It now becomes quite apparent why even very small ballistic remnants must be removed from the signal. They would yield a temporal "fluctuation" of fixed position in all speckles, whereas the temporal fluctuations arising from the diffusive component are "randomly" positioned with respect to one another. Averaging many speckle intensities together would magnify the ballistic intensity relative to the mean diffuse intensity, and produce a peak at the rising edge of the diffusive pulse.

5.5.1.2 $\sqrt{N}$ fluctuations

Inspection of the diffusive pulse shown in figure 5.24 reveals small fluctuations in its intensity. It seems quite reasonable that the magnitude of these fluctuations depends upon the number of envelopes averaged to produce the pulse. Clearly, the fluctuations

will be larger if this number is small, and smaller if this number is large. A quantitative description of the fluctuations is, however, only feasible using statistical arguments. The statistical character of ultrasonic speckle was discussed in Sec. 5.3. In particular, the contrast (or average normalized intensity fluctuations) within a spatial speckle pattern was seen to equal unity [equation (5.6)]. The diffusive pulse may be thought of as being constructed from a large number of uncorrelated *temporal* speckle patterns, each with unity contrast (cf. figure 5.22). Since the sum of N real-valued, identically distributed, uncorrelated random variables has a mean value which is N times the mean of any one component, and a standard deviation which is $\sqrt{N}$ times the standard deviation of any one component (Bhattacharyya and Johnson, 1977), the addition of N temporal speckle patterns on an intensity basis reduces the contrast in accordance with

$$C = \frac{\sigma_{\langle I \rangle}}{\langle I \rangle} = \frac{\sqrt{N}\sigma_I}{N\overline{I}} = \frac{1}{\sqrt{N}}. \tag{5.7}$$

To verify that the fluctuations in the diffusive pulse diminish with the increase of further intensity envelopes in the manner described by equation (5.7), two 10 mm thick samples, composed of the unsieved 0.25 mm radius glass beads in water, were studied in the point source geometry, using short pulses of about 10 oscillations and a central frequency of 3.5 MHz. Diffusive pulses were determined for many different values of N, with the fluctuations at each point in the pulse being determined by a computation of the standard deviation at that point, normalized to the pulse intensity at that point. These normalized fluctuations were then averaged over the entire temporal extent of the diffusive pulse. Figure 5.25 presents the results of such analysis, for values of N ranging from 9 to 196, in

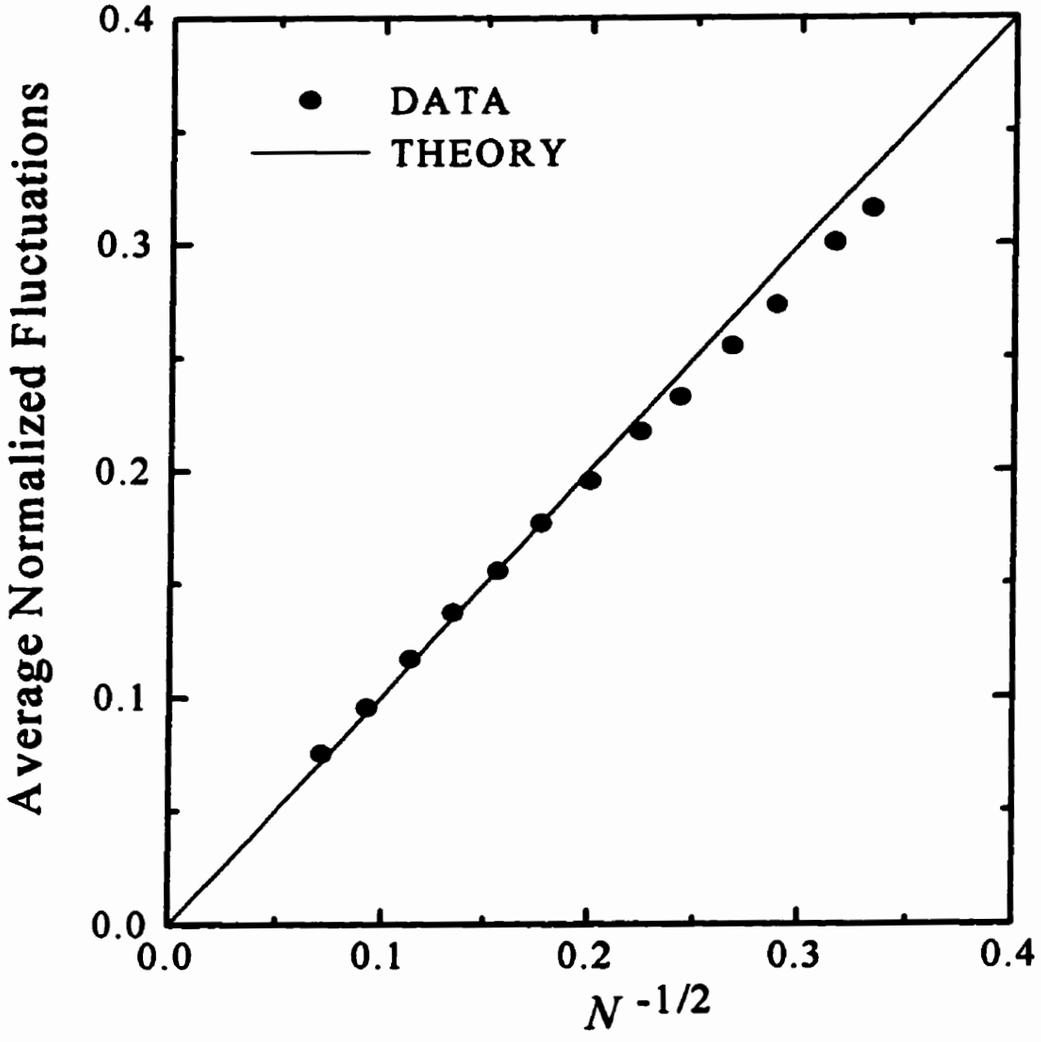

Figure 5.25 Average normalized fluctuations remaining on a diffusive pulse as a function of the number of intensity envelopes in the ensemble. The straight line indicates the expected behaviour, and the dots the measured behaviour, for values of N ranging from 9 to 196, using point source data at 3.5 MHz for two 10 mm thick samples composed of unsieved 0.25 mm radius glass beads in water.

comparison with the expected behaviour (straight line). Good agreement is seen, though the data are systematically lower than expected for small N. This is a consequence of the way the diffusive pulse was found for each set of N envelopes – every temporal speckle at small N was also an element of the ensemble at large N. This trend is removed if the members of the ensemble are chosen at random from the parent population. Furthermore, the scatter in the data may be lessened if M independent ensembles of N speckle envelopes are averaged together, as some values will be higher, and some lower. Such behaviour has been verified, as mentioned in Sec. 5.3.

5.5.1.3 Fitting the diffusive pulse

5.5.1.3.1 Some preliminaries

The functional form of the diffusive pulse, described in Sec. 2.2.7.1, assumed an instantaneous diffusive source a distance z_0 into the sample at time $t = 0$. As a consequence of the experimental restrictions under which the data were acquired, the diffusive pulse needed timing and normalization corrections before it would meet these conditions. To maintain the greatest accuracy in the timing, the distance between the generating transducer and detector remained the same for both the reference pulse and the transmitted data. For convenience, the temporal origin was initially taken to be when the midpoint of the incident pulse impinged upon the sample face (i.e. $t = 0$ at $z = 0$, not $z = z_0$). Ignoring, for the moment, the existence of the plastic walls, by maintaining stationary transducers the reference pulse has been delayed by the time required to traverse a water path equivalent to the sample thickness. The effect of the cell walls were to introduce additional delays because sound traveled faster through plastic than water.

For each wall, the additional delay was the time required to transit a wall thickness of water less the time it actually took to travel through the wall. Hence, the total delay was

$$\begin{aligned} t_{delay} &= t_{sample}^{water} + \left(t_{wall\,1}^{water} - t_{wall\,1}^{plastic}\right) + \left(t_{wall\,2}^{water} - t_{wall\,2}^{plastic}\right) \\ &= t_{cell}^{water} - t_{walls}^{plastic} \end{aligned}, \tag{5.8}$$

where t_{cell}^{water} was the time required to transit a total *cell* thickness (sample plus walls) of water, and $t_{walls}^{plastic}$ was the time actually required to go through both plastic walls. The diffusive pulse should thus also be delayed by this amount to synchronize with the reference pulse. In fact, if the centre of the reference pulse was at some non-zero time t_{ref}, a time shift

$$\Delta t = t_{delay} - t_{ref}, \tag{5.9}$$

was added to the time axis of the diffusive pulse (i.e. a shift to the right for $\Delta t > 0$). This timing correction put the temporal origin of the incident pulse at the sample face ($z = 0$), and not at $z = z_0$ — in effect, setting the reference time too early. Shifting further the diffusive pulse (to the left) by subtracting a time

$$t_{shift} = z_0 / v_{group} \tag{5.10}$$

finally positions the pulse properly. This last time shift does, though, introduce a difficulty, since z_0 is not yet known. Further discussion of this point will be reserved for Sec. 5.5.1.3.3, where all the parameters needed to fit the diffusive pulse are considered.

The proper normalization of the diffusive pulse presented practical difficulties, and for this reason the amplitude of the pulse was treated as an adjustable parameter in the fit. In some cases, these difficulties could be overcome, and the amplitude could be treated as fixed once the normalization was determined. The difficulty lay in the accurate

determination of the amplitude of the incident pulse in the point source geometry. As discussed in Sec. 4.2.4, a focusing transducer does not actually focus to a point, but rather to a narrow and elongated focal zone (figure 4.7) defined within the -6 dB limits. The peak intensity of the incident wave was easily determined, but the mean intensity (a more appropriate quantity to use) was more difficult to ascertain. Since an absolute normalization is not crucial for diffusive pulse measurements (Sec. 5.5.1.3.3), this difficulty was ignored, and the peak intensity of the incident (reference) pulse was used. There is, of course, no such concern in the planar source geometry. All diffusive pulses were normalized, with respect to a one volt incident pulse, by division by

$$V_R^2 \, 10^{(R-T)/10}, \tag{5.11}$$

where V_R was the peak amplitude of the reference pulse, and R-T the difference in the precision attenuator settings when collecting the reference and the transmitted signals (cf. figure 4.12). Even neglecting the additional correction factors discussed earlier (Sec. 4.3.3.2; see also Appendix B), this normalization was within an order of magnitude of its true value – sufficient for the purpose of fitting the pulse. Further discussion of this point (regarding the planar source diffusive pulses) may be found in Sec. 5.5.1.3.7 and Appendix C.2.

The expressions for the transmitted flux found in equations (2.98) and (2.100) were based on a delta-function source of incident waves. The particular shape and finite width of the incident pulse required its convolution with the predicted diffusive pulse, as described in equation (2.101). To accomplish this, the envelope of the incident pulse intensity was found, and its maximum normalized to unity. The centre of the incident pulse, previously determined to be t_{ref} (see above), was then set at $t = 0$. It should be

noted that t_{ref} was usually determined from the midpoint of the -6 dB points on the rising and falling edges of the incident pulse envelope, though for cases where the incident pulse evidenced asymmetry, it was found by requiring half the integrated intensity under the envelope to lie to either side; this ensured that the convoluted diffusive pulse predicted by the fit would remain unbiased by the asymmetry of the incident pulse.

5.5.1.3.2 The influence of D and τ_a on diffusive pulse shapes

An understanding of the physical significance of variations in the diffusive parameters D and τ_a may be gained by returning to the infinite medium. In an infinite medium with an instantaneous point source at the origin, the flux directed in the positive z direction and detected at $r = (0, 0, L)$ is

$$J^+(L) = \frac{2\pi DL}{(4\pi Dt)^{5/2}} e^{-t/\tau_a} e^{-L^2/4Dt}, \qquad (5.12)$$

[using equations (2.66) and (2.97), and explicitly including the absorption]. This expression has been plotted, in figure 5.26, for various values of D and τ_a, assuming L = 10 mm. Figure 5.26(a) shows the behaviour of the diffusive pulse as a function of D, having neglected absorption entirely ($\tau_a \to \infty$). The small time behaviour of the pulse being dominated by $e^{-L^2/4Dt}$, the effect of decreasing D is to delay the onset of the diffusive pulse and to cause the pulse to rise much less sharply, resulting in a shift of the peak to later times and a depression in its amplitude. The long time behaviour of the pulse is dominated by $(4\pi Dt)^{-5/2}$, so the effect of decreasing D elevates the tail end of the

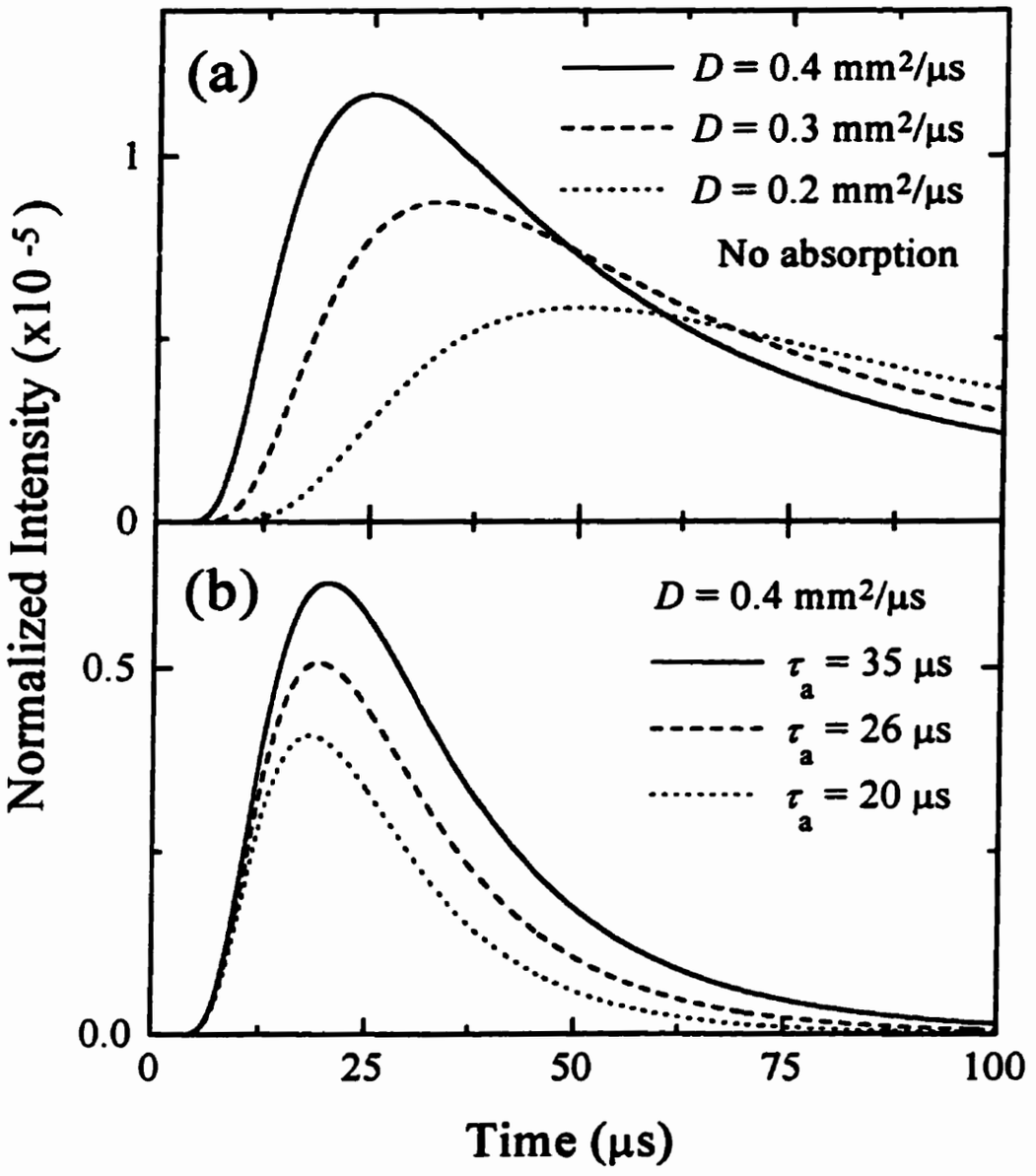

Figure 5.26 The behaviour of the diffusive pulse for various values of D and τ_a. (a) The effect of varying D, neglecting absorption, and (b) the effect of varying τ_a, while holding D fixed.

pulse, in accordance with energy conservation arguments. Figure 5.26(b) shows the effect of increasing absorption (decreasing τ_a) on the shape of the diffusive pulse, for fixed D. The absorption is seen to dominate the pulse shape at long times, whereas the diffusion coefficient D dominates at short times.

5.5.1.3.3 The multi-parameter fit

The diffusion parameters D and τ_a were determined by finding the best fit of the functional form predicted via diffusion theory [after convolving equation (2.98) (for the point source), or equation (2.100) (for the plane-wave source), with the incident pulse] to the experimentally obtained diffusive pulse. This numerical task was accomplished using a *C* program that employed a nonlinear least-squares fit algorithm. The input parameters to the program will first be considered, followed by a general description of the program, with emphasis on the fit function, and concluding with a discussion of the trustworthiness of the diffusive parameters thus obtained.

Since the penetration depth was initially unknown, the diffusive parameters were found by performing fits over a range of z_0, with the "correct" value later determined from the self-consistency requirements imposed on the diffusive parameters for samples of different thicknesses. This is illustrated more fully in Sec. 5.5.1.3.4. With z_0 chosen, the fitting program was able to calculate the last timing correction to the diffusive pulse [equation (5.10)], and the values of D and τ_a (for this particular choice of z_0) were then ascertained. Zhu *et al.* (1991) have determined that $z_0 \cong l^*$ (to within $\pm 30\%$), and numerical simulations by Durian (1994) have confirmed this equality. The consistency

requirement that establishes z_0 then also determines l^*, which is itself a fitting parameter. All other fixed parameters required in the fit were known; they were the group velocity v_g, the sample thickness L, and the reflection coefficient R. The group velocity and the sample thickness were measured parameters, and the reflection coefficient was a calculated value based on measured quantities.

The program was provided with "starting values" of D, τ_a, and the normalization factor. A diffusive pulse was then calculated, using these values and the fixed parameters, and then convoluted with the measured time profile of the incident pulse intensity envelope, and integrated over the area of the detector. The calculated pulse was then compared to the experimentally determined pulse to see if it matched (within some given degree of accuracy). If not, better values of the adjustable parameters were determined and the process repeated until convergence was attained. The determination of these better values was the responsibility of the nonlinear least-squares fit algorithm *"nllsq"* (Kornblit, 1979).

Let the set of n data points (for the diffusive pulse) be denoted by $y(t_i)$, and the functional form by $f(t_i)$. The principle of least-squares asserts that the optimum value of the adjustable parameters is achieved if

$$\Phi = \sum_{i=1}^{n} w_i \left[f(t_i) - y(t_i) \right]^2 \tag{5.13}$$

is minimized, where w_i is the weight of the ith data point. If $\boldsymbol{b} = (b_1, b_2, \ldots, b_k)$ are the estimates of the k adjustable parameters, then the minimum in Φ is obtained when

$$\frac{\partial}{\partial b_j}\Phi = \frac{\partial}{\partial b_j}\sum_{i=1}^{n} w_i\left[f(t_i) - y(t_i)\right]^2 = 0, \tag{5.14}$$

for all $j \in [1, k]$ (Bevington, 1969). Closed-form solutions to equation (5.14) are not, in general, possible if $f(t)$ is not linear in the parameters b_j, as in the present case; alternate methods must then be used to find the minimum of Φ. These methods all rely on the calculation of correction vectors δb to move towards the absolute minimum on the Φ surface in parameter space, beginning from certain trial parameters.

The two most common methods employed in non-linear curve fitting are the Taylor expansion method (Newton's method), and the Gradient method (method of steepest descent). The former method expands the function $f(t)$ in a first-order Taylor's expansion as a function of the parameters b_j. The expanded function is then linear in the parameter increments δb_j, and conventional methods of linear least-squares may then be used to find the condition for a minimum in Φ as

$$\frac{\partial \Phi}{\partial(\delta b_j)} = 0, \tag{5.15}$$

for all $j \in [1, k]$. This method leads to rapid convergence if the calculations of δb_j are carried out in the neighbourhood of the minimum of Φ, but may lead to a possible divergence if δb_j is too large to justify the first-order expansion. The Gradient method, however, works well when the starting point is far from the minimum of Φ. Here all parameters are adjusted simultaneously so that the correction vector δb is parallel to the largest local negative gradient of Φ in parameter space:

$$\delta b_j = -\frac{\partial \Phi}{\partial b_j}, \tag{5.16}$$

for all $j \in [1, k]$. Convergence is slow near the minimum though, as the near-zero derivatives in this region yield a small correction vector. The fit algorithm *"nllsq"* employs the Marquardt method, which combines the best features of both of the above methods, to determine the correction vector. It does this by introducing a parameter which allows an interpolation between the correction vectors calculated by the two common methods. Details are provided by Kornblit (1979), and references therein.

As is evident from the behaviour of the diffusive pulse shapes shown previously (figure 5.26), the temporal profile of the ensemble-averaged diffuse intensity depends sensitively on both the diffusion coefficient and the absorption time, with the initial rise of the pulse determined by D and the decay strongly influenced by τ_a. These parameters being thus largely uncorrelated, an accurate determination of their values is expected when using the fitting program. This holds true even if a normalization factor is included as an adjustable parameter, since its effect is merely to rescale the intensity over all times. The principle cause of the uncertainty in the fitting parameters is *not* the accuracy with which the fitting subroutine can determine the minimum of Φ in parameter space, but rather the influence on D and τ_a of uncertainties in the *fixed* parameters. Fortunately, this dependence on the fixed parameters was, in general, weak, at least over most of the frequencies and sample thicknesses studied, with the effect on D being only about half that of the effect on τ_a. It would be necessary, for example, to vary the reflection coefficient R by about a factor of two from its calculated value to produce a ±10% uncertainty in D (±20% in τ_a); for realistic uncertainties in R (±20%), the resulting uncertainty in D is ±2% (±5% in τ_a), which is negligible. Of slightly greater effect is the uncertainty in the

group velocity v_g (used in the final timing correction – see above) and the sample thickness. In both cases, for typical uncertainties, the resulting uncertainty in D is ±5% (±10% in τ_a), using typical sample thicknesses. For thin samples, however, the uncertainty in L has a large effect on the uncertainty in τ_a, and to a lesser extent, also on D. A 5% uncertainty in L [e.g. ΔL = 0.25 mm (the maximum possible absolute uncertainty in L), with L = 5 mm] gives a maximum possible uncertainty in D of ±15% (±40% in τ_a). Final typical uncertainties in D are thus about 7%, and for τ_a about 15%. The uncertainties in D and τ_a arising from the uncertainty in z_0 are made apparent in Sec. 5.5.1.3.4 and Sec. 5.5.1.3.7

5.5.1.3.4 Point source results

Ensemble-averaged diffusive pulses were determined, in the point-source geometry, at many distinct frequencies, and for samples of different thicknesses. Their time profiles were then fit to the predictions of diffusion theory, as discussed above. Since at each frequency, the values of D and τ_a should be completely independent of sample thickness, fitting the data for different values of z_0 should allow their actual values to be determined. This is illustrated in figure 5.27, where the values of D and τ_a thus obtained are shown for samples of three different thicknesses (L = 5.31, 10.3, and 20.5 mm) over a range of values of z_0. These data were acquired using unsieved glass bead (radius, a = 0.5 mm) samples within the on-axis point source geometry, for incident pulses at central frequencies of 2.5 MHz, and pulse widths of 4.2 μs. Inspection of figure 5.27 reveals that

the dependence of the fitting parameters D and τ_a on the penetration depth z_0 is strong for the thin samples, but weak for the thick samples, where the dominance of long diffusion path lengths make the data relatively insensitive to z_0. A reasonably narrow range of values for z_0, between about 0.7 and 1 mm, is seen where consistent values of D and τ_a are observed. These self-consistent fits yield $D = 0.435 \pm 0.015\,\mathrm{mm}^2/\mu\mathrm{s}$ and $\tau_a = 12.0 \pm 0.5 \mu s$. Furthermore, this range of values for z_0 allows the transport mean free path to be estimated as $l^* \approx 0.85 \pm 0.15\,\mathrm{mm}$ (for this frequency and bead size), since $l^* \approx z_0$ to an excellent approximation (Zhu *et al.*, 1991; Durian, 1994). The experimentally determined temporal profiles of the diffuse intensities for these three sample thicknesses are shown by the open symbols in figure 5.28. The smooth solid curves, obtained with the diffusion theory using the above values, are shown to be excellent fits to the data for all three thicknesses. The diffusive pulses resulting from the transmission of narrow incident pulses (~10 oscillations), at four different frequencies, through a 10.3 mm thick sample comprised of the unsieved 0.5 mm radius glass beads, are shown in figure 5.29. As illustrated, the diffusion theory was found to well describe the data for all frequencies investigated. A qualitative inspection of the four diffusive pulses reveals that the absorption appears to be monotonically increasing with frequency. The behaviour of the diffusion coefficient is not quite as apparent, though it is clear that D is significantly smaller at 1.5 MHz than at the three higher frequencies (because the initial rise of the pulse is later in time; cf. Sec. 5.5.1.3.2). The diffusion coefficients at the various frequencies will be summarized in Sec. 5.5.3, as will the absorption times, where the frequency variations and their physical origins are presented.

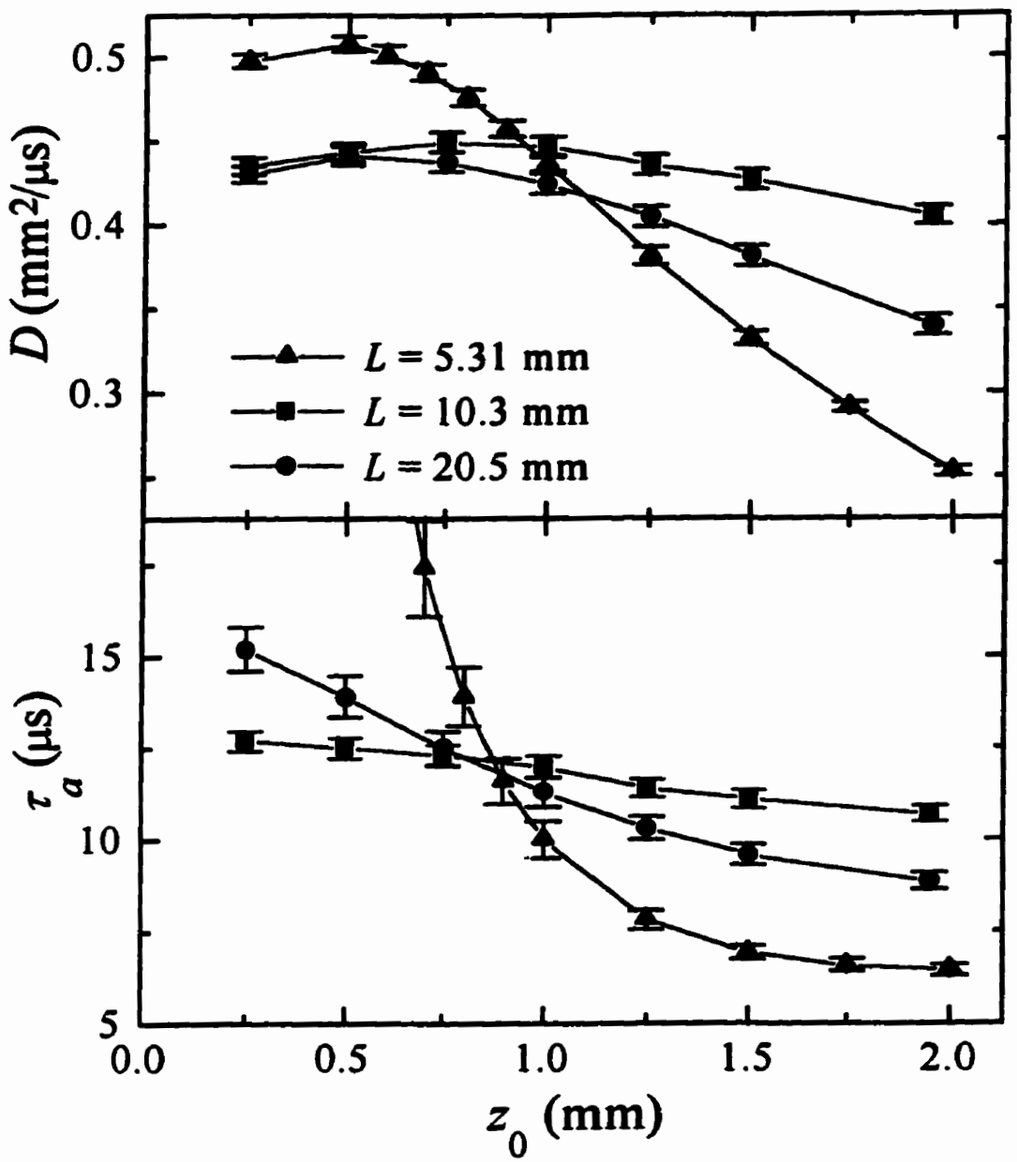

Figure 5.27 Dependence of the fitted parameters D and τ_a on the diffusive origin z_0, at a frequency of 2.5 MHz, for unsieved glass bead (radius, $a = 0.5$ mm) samples at three different thicknesses. The consistency of the fitted parameters for z_0 between 0.7 and 1 mm gives an estimate for l^* of 0.85 ± 0.15 mm.

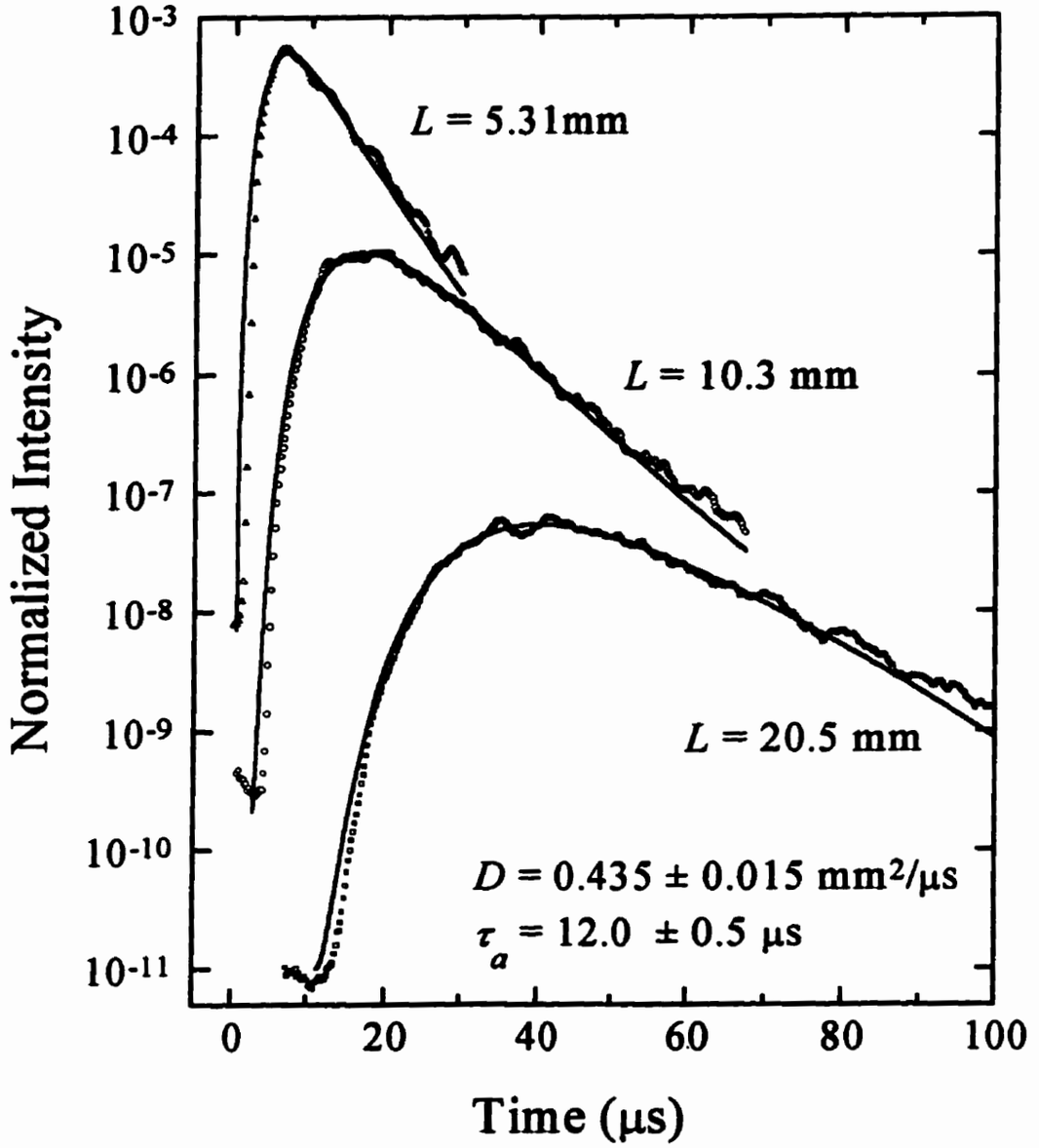

Figure 5.28 Time profiles of the normalized ensemble-averaged intensities transmitted as discussed in figure 5.27. The open symbols are the data, while the smooth solid curves are the best least-squares fits to the diffusion theory at $z_0 = 0.85$ mm.

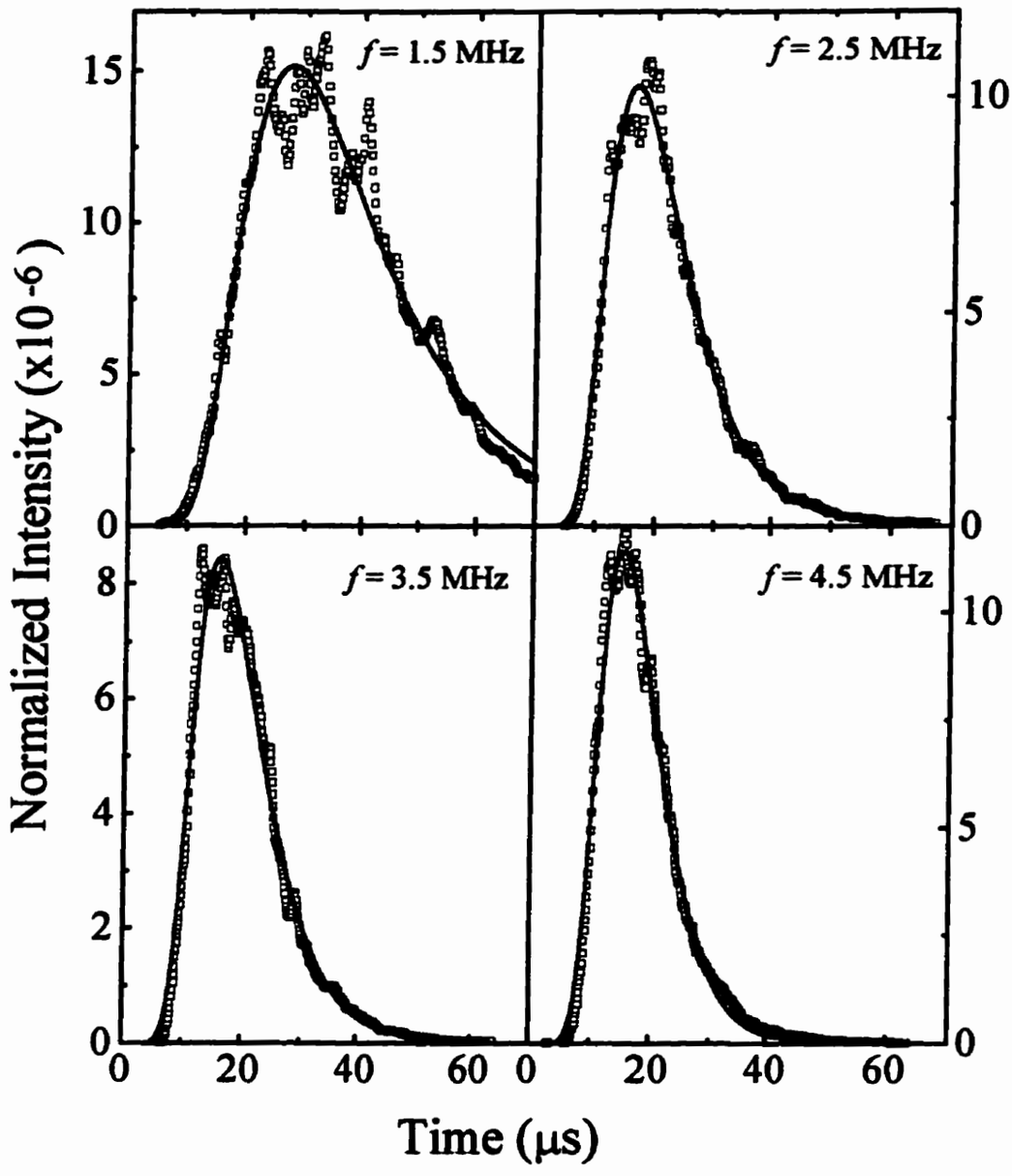

Figure 5.29 Point source diffusive data, at four different frequencies, for the transmission of a narrow pulse through a 10.3 mm thick sample composed of unsieved glass beads of radius 0.5 mm. The solid curves are the fits to diffusion theory.

5.5.1.3.5 Effect of the displaced point source: diffusive pulse ratios

As a consistency check on the applicability of diffusion theory in the description of the transport of multiply scattered sound, the use of a point source and a point detector is exploited. If the detector is displaced transversely from the axis of the source (figure 4.10, with the hydrophone in the off-axis position), the ensemble-averaged transmitted intensity is expected to decrease by

$$\exp\left[-\left((x-x_0)^2+(y-y_0)^2\right)/4Dt\right], \tag{5.17}$$

independent of all other variables, in accordance with equation (2.98), where (x_0, y_0) is the source position and (x, y) the detector position. Thus, the ratio of the ensemble-averaged diffuse intensity detected off-axis to that detected on axis will be independent of absorption, and hence τ_a, and independent of boundary effects, and hence z_0 and R.

Experimental verification of the predicted behaviour of the intensity ratios is illustrated with data acquired at 2.5 MHz using three different 10.2 mm thick samples containing the 0.5 mm radius unsieved glass beads. One hundred speckles were measured for each sample, with the 200μm diameter hydrophone detecting the transmission of short pulses, of about 10 oscillations, generated by a focusing transducer. The scattered sound was measured with the detector displaced a distance r from the axis of the source, with r equal to 0, 10.2, and 15.2 mm. Diffusive pulses were constructed (as described in Sec. 5.5.1.1) from the 300 speckles at each transverse position of the hydrophone; the time dependencies of these ensemble-averaged intensities are shown in figure 5.30(a), where the intensity is plotted logarithmically to facilitate comparison between the three different pulses. The intensities are markedly reduced for the off-axis detector positions, with the

peaks of the diffusive pulses being shifted to later times for greater displacements of the detector. Physically, the reduction in the signal reflects the fact that scattered waves arriving at the same time for each position of the detector must follow paths of the same length and so fewer paths impinge on the off-axis detectors; likewise, the shift of the diffusive pulse peaks reflects the lengthening of the dominant scattering paths resulting from the effective increase in the sample thickness.

In figure 5.30(b), the ratios of the ensemble-averaged intensities for the two off-axis positions to that obtained for the detector on axis are shown. As expected from the individual diffusive pulses shown in figure 5.30(a), the ratio is much smaller for the detector further off axis, thus verifying the reduction in the number of paths that reach the detector as the distance r from the axis is increased. The smooth lines in figure 5.30(b) are the fits to the predicted exponential form. These fits were obtained by convolving equation (5.17) with the measured input beam profile and then integrating the result over the effective area of the detector (assumed square, for ease of calculation). The input beam distribution, which resembles the diffraction-limited pattern for a circular aperture, had a 6 dB beam diameter of about 1.5 mm [see equation (4.10)]. For the 10.2 mm axial displacement, this correction was important, improving the fit at small times and reducing the value found for D by about 5%. Correcting for the effective area of the detector yielded a similar effect, and the net result was a value for D consistent with the results for the larger displacement. Both modifications of the pure exponential form [equation (5.17)] were minimal for the 15.2 mm axial displacement.

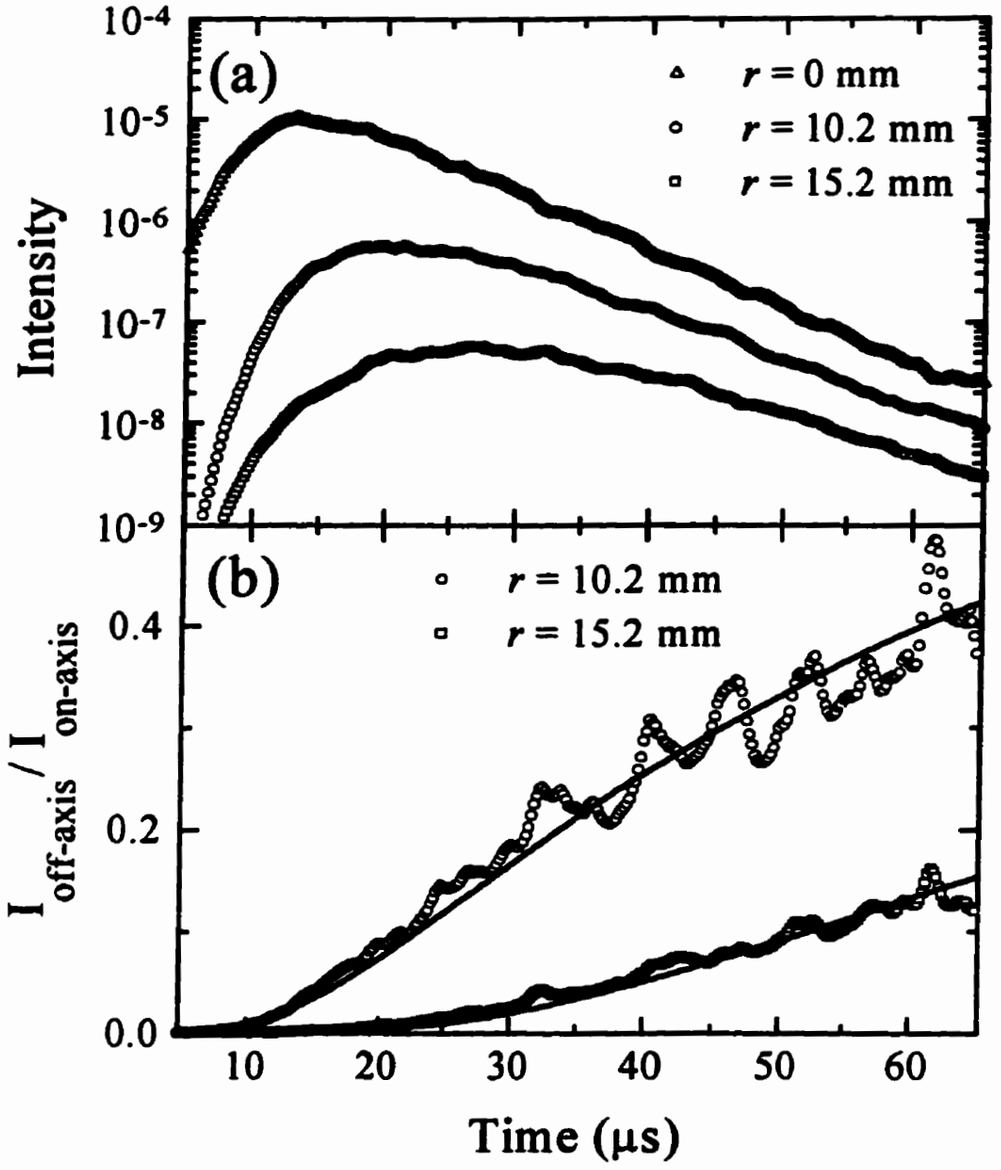

Figure 5.30 (a) The time dependencies of the ensemble-averaged intensities for displacements r from the source axis, plotted logarithmically, and (b) the ratio of off-axis to on-axis intensity, with the expected exponential reduction shown by the solid curves providing a measure of D.

The effective area of the detector is related to the angular sensitivity of the hydrophone, and to the distance between the hydrophone and the sample interface; it thus corresponds to the area of the sample over which signals are detected. The hydrophone was positioned 2.0 mm back from the sample interface (the cell wall thickness being 1.5 mm), and is sensitive over a cone whose half-angle is about 50° (at the frequency employed); this results in an effective area of ±2 mm on a side. The necessity for considering the detector to be effectively larger is a consequence of the loss of axial symmetry with the source point. The fits shown in figure 5.30(b) were determined by chi-square minimization, yielding values for D of 0.44 ± 0.03 mm$^2/\mu s$ for the 10.2 mm axial displacement, and 0.46 ± 0.03 mm$^2/\mu s$ for the 15.2 mm axial displacement, the uncertainties in D being determined by allowing the reduced chi-square to vary by a factor of two. These values are in excellent agreement with $D = 0.435 \pm 0.015$ mm$^2/\mu$s, the value presented earlier for the on-axis data (Sec. 5.5.1.3.4; see figure 5.28).

5.5.1.3.6 Comparing point source and planar source diffusive pulses

In the above section, the applicability of diffusion theory for the description of the ensemble-averaged transport of multiply scattered sound through sieved glass bead samples was noted for the incident planar geometry. Specific mention was made of the agreement between the fitting results, at 2.5 MHz, for the point and planar sources, although the diffusion coefficients required scaling by the bead radii before this became apparent. Because the diffusive pulses are determined for different geometries, it is expected that their shapes differ noticeably, although the values of the parameters remain

unchanged. An explicit and unambiguous demonstration of this is afforded by comparing data obtained with a planar source and a point source, again at 2.5 MHz, for samples containing the unsieved glass beads, with L = 10.2 mm,. The point source diffusive pulse has been constructed from 484 speckles over four different sample cells, and the planar source diffusive pulse from 1600 speckles over one of these sample cells. In figure 5.31, in addition to reaching its peak value at a later time, the diffusive pulse acquired in the planar geometry is seen to be noticeably longer than that obtained in the point source geometry. This reflects the larger contribution of sound waves traveling over longer paths from the planar source. The smooth solid curves through the data are the best non-linear least squares fits with $z_0 = 0.85\,\text{mm}$, using equation (2.98) and equation (2.100) for the point and planar source data, respectively. For the point source data, the fitting parameters found were $D = 0.435 \pm 0.015\,\text{mm}^2/\mu\text{s}$ and $\tau_a = 12.0 \pm 0.5\mu\text{s}$; these values are in excellent agreement with those found for the planar source, namely $D = 0.43 \pm 0.02\,\text{mm}^2/\mu\text{s}$ and $\tau_a = 11 \pm 1\mu\text{s}$. Furthermore, comparison of the above two equations reveals that the planar source form differs from that of the on-axis point source form only by the multiplicative factor $4\pi Dt$, thus predicting that the ratio of the diffusive pulses increases linearly with time. The linear time dependence of this ratio is indeed well obeyed, as is shown in figure 5.32. The data are from the ratio of those measured diffusive pulses shown in the previous figure, and the straight line is the best linear fit to this ratio. Unfortunately, the uncertainty in the normalization of the point source data precludes obtaining a precise estimate of D from the slope of the line. Nonetheless, the

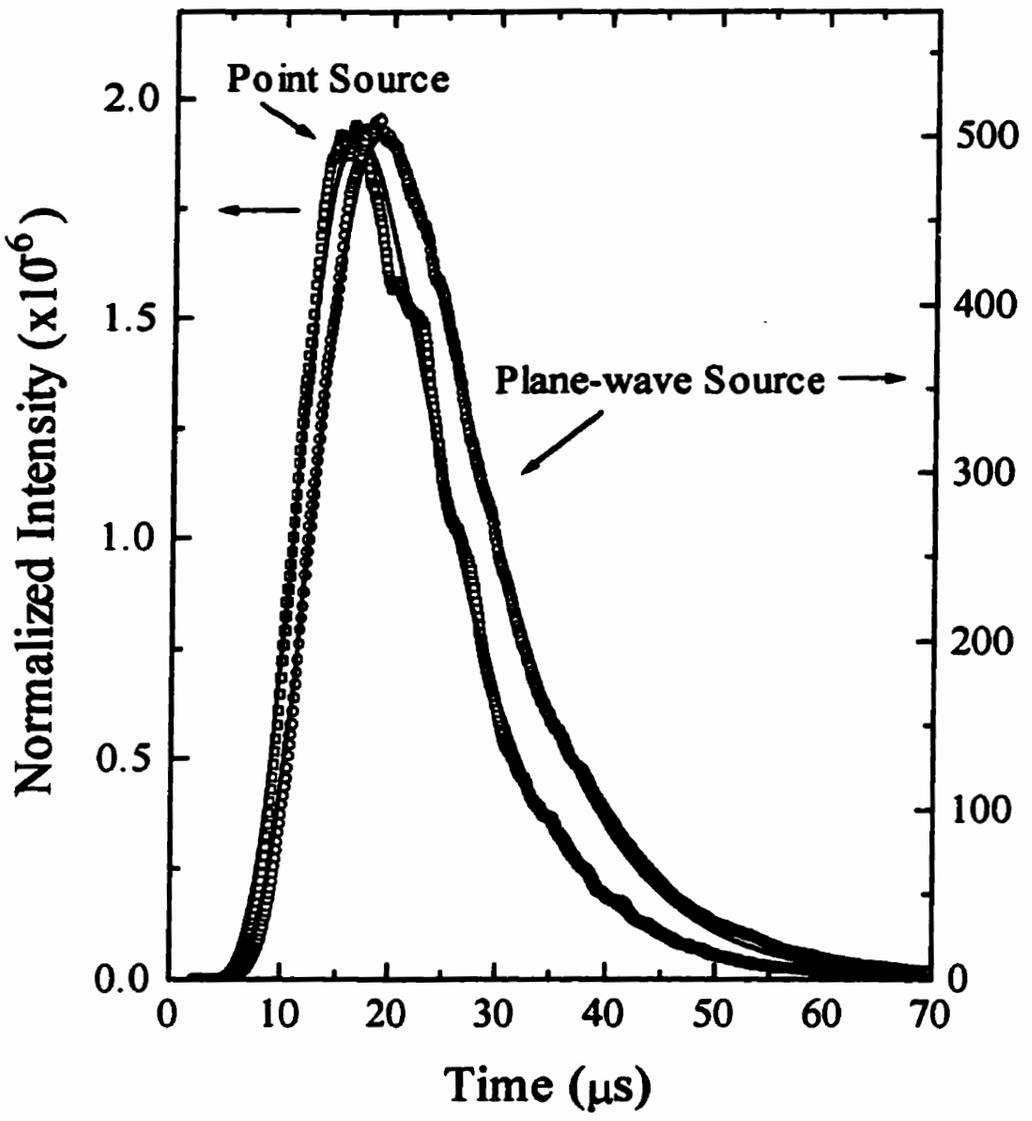

Figure 5.31 Comparison of the temporal profiles of the ensemble-averaged diffuse transmission, at 2.5 MHz, through 10.2 mm thick samples composed of unsieved glass beads, for a point source and a planar source. The smooth solid curves are fits to the corresponding expressions given by diffusion theory.

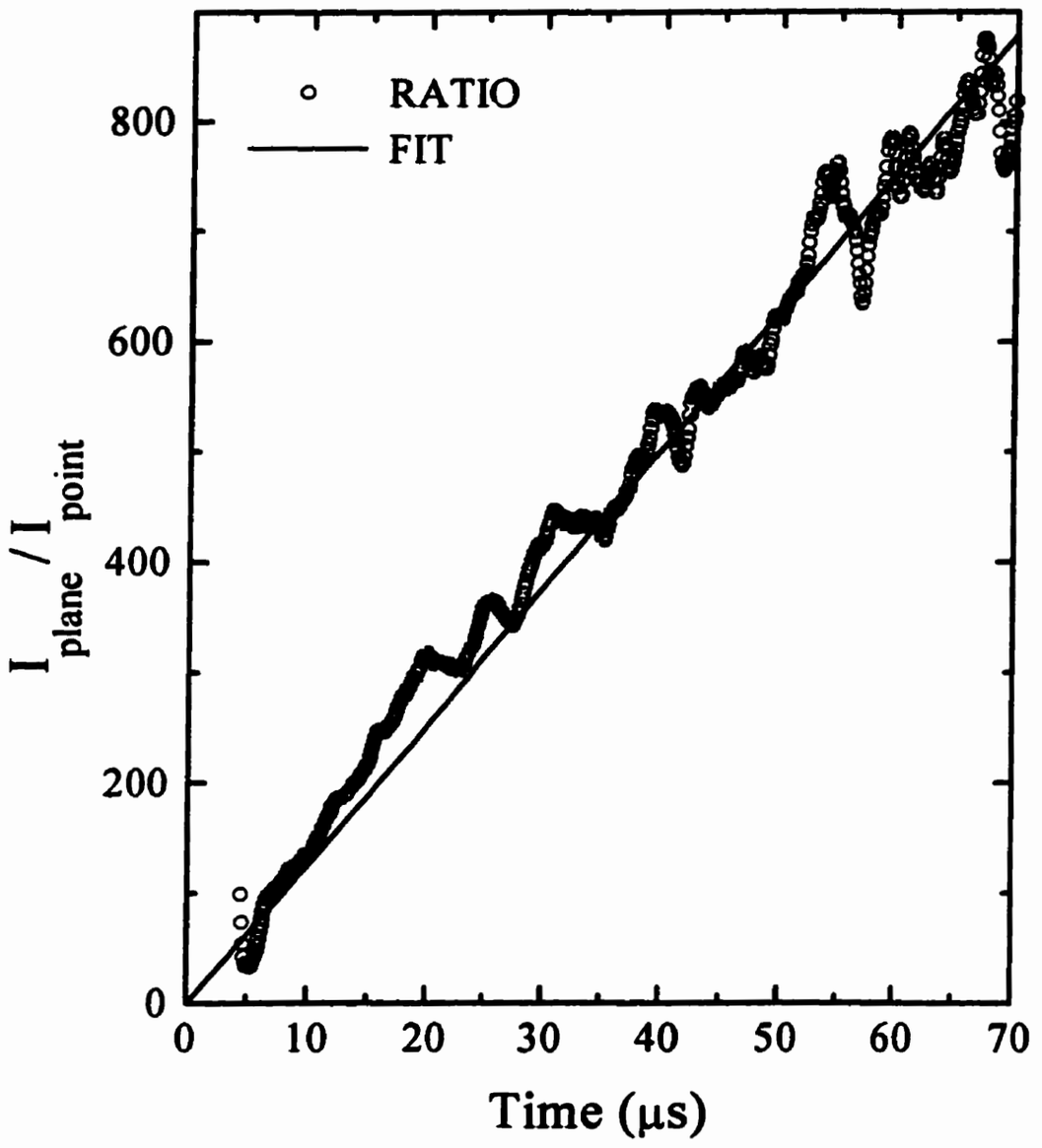

Figure 5.32 The ratio of the planar to point source diffusive pulses (from figure 5.46). The straight line, being the best linear fit to this ratio, demonstrates the consistency of the diffusion approximation in describing the fit for different incident pulse geometries.

robustness of the fit and the applicability of the diffusion approximation to the description of the propagation remains explicitly confirmed.

5.5.1.3.7 Typical planar source results

The ensemble-averaged diffusive pulses realized from the data acquired in the planar source geometry were obtained and analyzed in like manner to that of the point-source data. With the exception of the data presented in the previous section (Sec. 5.5.1.3.6), all plane-wave diffusive pulse measurements were performed on sieved-bead samples (of 7.1, 10.1, and 15.2 mm thicknesses). This point is re-emphasized since the slight difference between the mean radii of the unsieved (a = 0.45 mm) and sieved glass beads (a = 0.47 mm) will result in a small difference in D, since D should scale with l^* and thus also with the bead radius.

Within the planar source geometry, the sound intensity incident upon the sample could be accurately determined, and an absolute normalization of the diffusive pulse achieved by incorporating known correction factors (Sec. 4.3.3.2; see also Appendix B). This altered the normalization factor in the fit from an adjustable to a fixed parameter, leaving only D and τ_a as fitting parameters (z_0 being treated as described previously). The planar wave diffusive pulses were fit with both free and fixed normalization factors, and the results for the variation of D and τ_a with z_0 were compared. Diffusive pulses were acquired, at six distinct frequencies ranging from 1 to 3.5 MHz (in about 0.5 MHz increments), for samples of three different thicknesses (L = 7.1, 10.1, and 15.2 mm). A more detailed analysis of planar wave data (at 1.5 MHz and 3.5 MHz) may be found in

Appendix C.2, where careful attention is paid to the effect of the normalization factor. The fitting results at 2.5 MHz are summarized below.

The values of D and τ_a obtained by fitting the 2.5 MHz data for a range of z_0 are shown in figure 5.33 (free normalization fit) and figure 5.34 (fixed normalization fit). The curves through the determined parameters show no common intersection point. Moreover, D and τ_a are less sensitive to variations in z_0 than was the point-source data. This appears to be a universal characteristic of all planar source data and is likely due to the greater dependence on increased path lengths imposed by the source geometry. For the free normalization fit, assuming $z_0 = 0.85\,\text{mm}$, the spreads in D and τ_a, almost entirely due to the thinnest sample, are 10% and 30%, respectively. Fixing the normalization results in a increase in both parameters, for all sample thicknesses. This increase is small (~10%) for the thicker samples, but quite pronounced (~25% for D, and ~50% for τ_a) for the thinnest sample, and as a consequence the spreads in the parameters are greatly reduced (~6% for D, and ~12% for τ_a). The weak dependence on z_0 for the samples investigated, combined with small systematic variations in sample thickness, have precluded using the consistency condition to determine z_0. However, using the fixed normalizations, consistent results for D and τ_a could be obtained over a large range of z_0 precisely because of this weak dependence.

The diffusive pulses for the 2.5 MHz data are shown in figure 5.35, plotted on a logarithmic scale, for all three sample thicknesses. The smooth solid curves are the best fixed normalization fits to the data for $z_0 = 0.85\,\text{mm}$. These fits are quite good, and yield

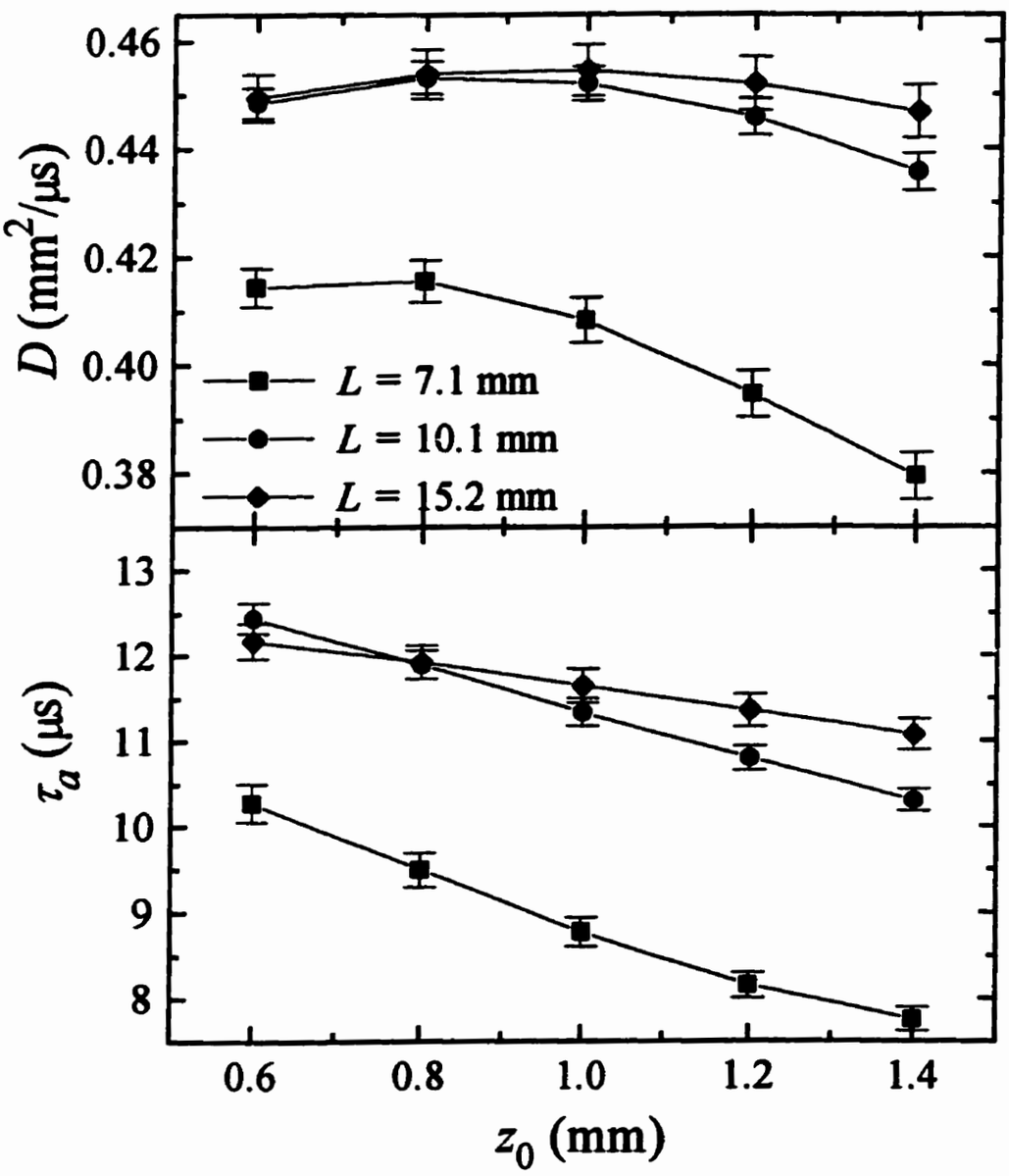

Figure 5.33 Dependence of the fitted parameters D and τ_a on the penetration depth z_0, allowing free normalization in the fit, for samples at three different thicknesses, using planar source data at a central frequency of 2.5 MHz.

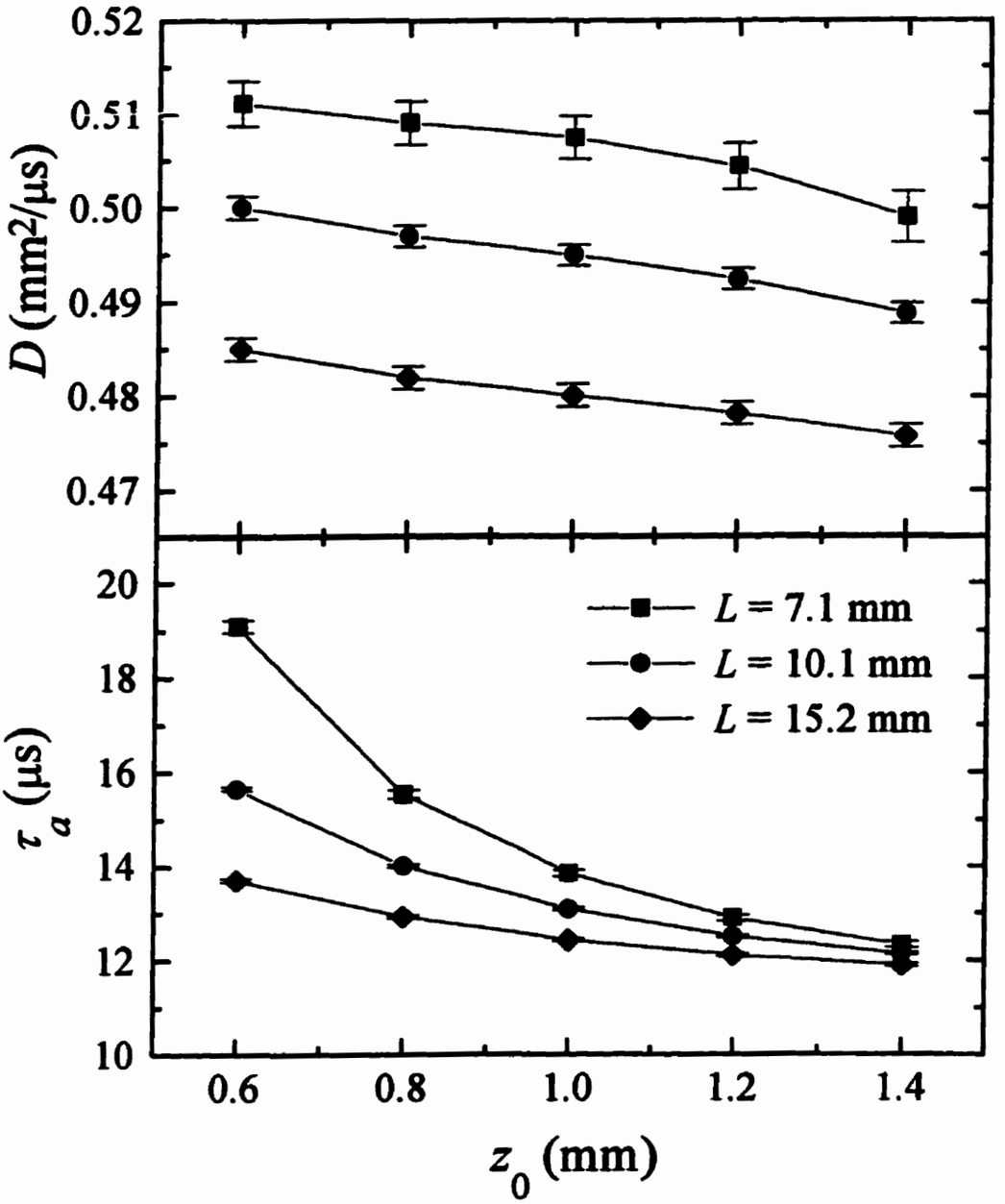

Figure 5.34 Dependence of the fitted parameters D and τ_a on the penetration depth z_0, requiring fixed normalization in the fit, for samples at three different thicknesses, using planar source data at a central frequency of 2.5 MHz.

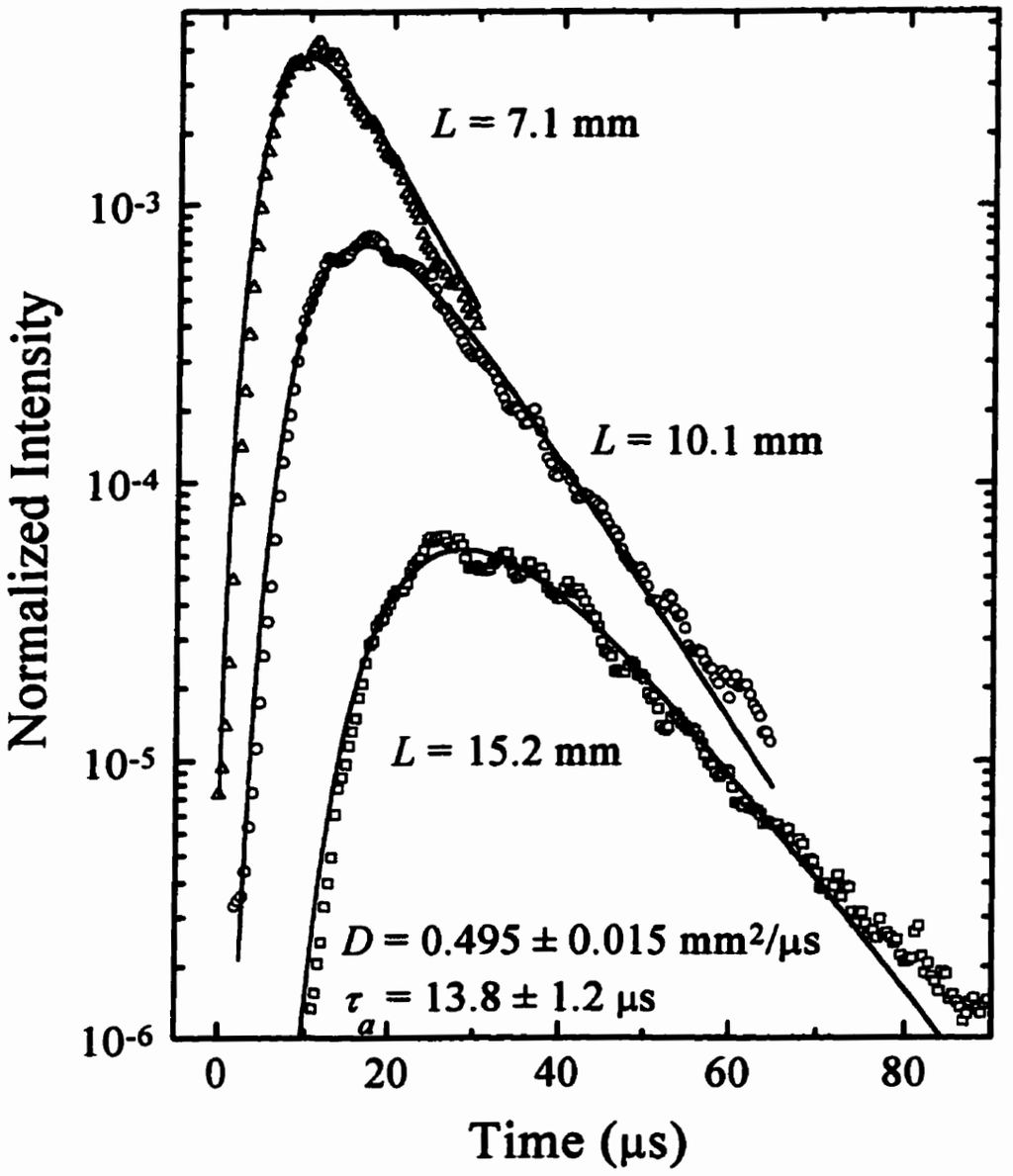

Figure 5.35 Time profiles of the normalized ensemble-averaged intensities transmitted as discussed in figure 5.34. The open symbols are the data, while the smooth solid curves are the best least-squares fixed normalization fits to the diffusion theory at $z_0 = 0.85$ mm.

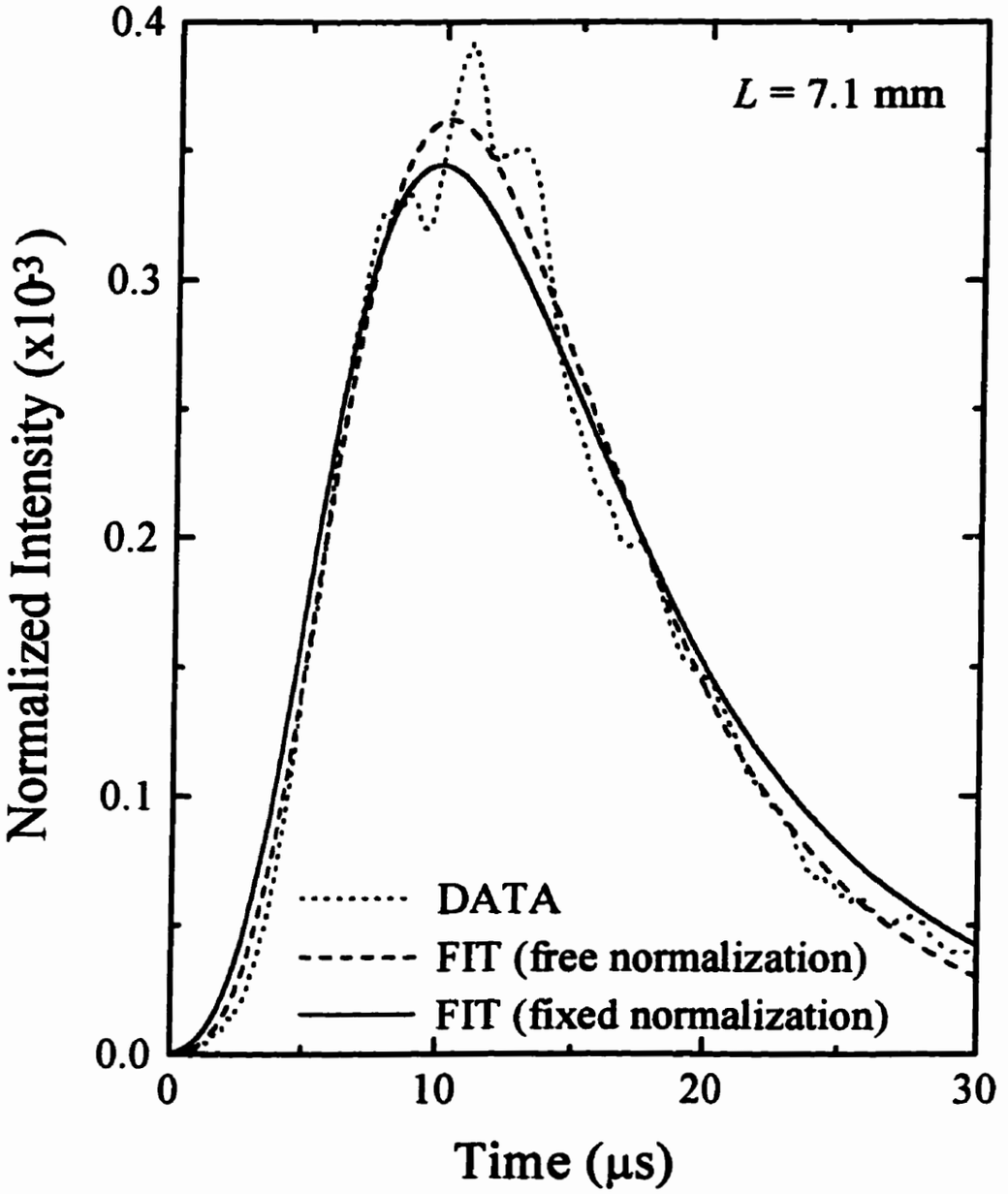

Figure 5.36 Comparison of the free and fixed normalization fits, at $z_0 = 0.85\,\text{mm}$, to the diffusive pulse determined from transmission through the $L = 7.1$ mm sample at 2.5 MHz.

values for D and τ_a of $0.495 \pm 0.015\,\mathrm{mm}^2/\mu\mathrm{s}$ and $13.8 \pm 1.2\,\mu\mathrm{s}$, respectively. The diffusion coefficient is in agreement with the value presented earlier for the point source on-axis data ($D = 0.435 \pm 0.015\,\mathrm{mm}^2/\mu\mathrm{s}$, Sec. 5.5.1.3.4) if both are scaled by their respective bead radii, whence $D/a = 1.04 \pm 0.04\ \mathrm{mm}/\mu\mathrm{s}$ (planar wave: fixed normalization) and $D/a = 0.97 \pm 0.04\ \mathrm{mm}/\mu\mathrm{s}$ (point source). The absorption time is also consistent with the value presented earlier ($12.0 \pm 0.5\,\mu\mathrm{s}$). Agreement is markedly improved by weighting the fitting results from the thicker samples more than those of the thinner one.

The differences between the free normalization fits and the fixed normalization fits for the two thickest samples are not readily apparent to the eye. For the thinnest sample, however, the pronounced decrease in D and τ_a means the two fits should be distinguishable. This is what is observed in figure 5.36, where the 7.1 mm data are represented by the dotted line, and the free and fixed normalization fits by the dashed and solid curves, respectively. Clearly, the fixed normalization fit shows a greater departure from the data than does the free normalization fit, especially at early and late times; it represents perhaps the greatest allowable discrepancy between data and fit. Poor experimental technique *may* explain the anomalous behaviour of this sample *vis-à-vis* the thicker samples. If there was significant bowing of the sample walls (which can happen after packing if thin samples are improperly handled) then the thickness would be greater than originally measured. Employing an incorrect, smaller, sample thickness results in a reduction in D and τ_a. This may explain why the 7.1 mm parameters are lower in figure 5.33 than the parameters for the thicker samples. In turn, fixing the normalization, though forcing consistency between the samples, consequently results in a poorer fit. Though

bowing has occurred, periodic checks of the thickness usually caught such a systematic error. A second possibility is a partial debond of the cell wall allowing water to leak out. The water would, of course, then be replaced by air bubbles, which scatter sound very strongly, thus also leading to a reduction in D and τ_a. Air bubbles have not been noted when preparing samples since the glass beads wet quite well; however, the polystyrene walls wet less well and bubbles may be entrapped at the wall/bead interface (depending on the location and size of the leak, sample storage and handling) rather than rise to the top of the cell. Such entrapped bubbles could not be formed when the sample was originally made, since the water was put in first and the beads then followed (chapter 3). In those samples that were known to have a leak, the cell wall invariably catastrophically debonded upon handling. Appendix C.2 treats the anomalous behaviour of this sample in more detail when discussing the 3.5 MHz data, where similar behaviour is noted for the thin sample. This anomalous behaviour is actually of minor importance since such inconsistencies were rare, and confined to the thinner samples. Moreover, since the dependence of D and τ_a on z_0 was much weaker for the thicker samples, greater weight was accorded their values, and a consistent determination of D and τ_a was obtained for all planar wave data.

5.5.2 Steady state measurements (cw mode): l^* and v_e

The first attempt at obtaining diffusion parameters by experimental determination of the steady state transmission was done by Genack (1987) for optical propagation through randomly distributed titania microcrystals at large volume fractions (though the

treatment of the boundaries was inadequate). Garcia *et al.* (1992) later performed total transmission measurements of the microwave intensity through dense random ensembles of polystyrene spheres, showing that diffusion theory gave an excellent description of the transport (the boundary conditions were now properly done). This allowed the transport mean free path to be determined, and was also exploited to get D from intensity autocorrelation measurements, thus allowing the energy velocity at one frequency to be obtained. Li *et al.* (1993) also demonstrated the validity of the diffusion approximation for the description of the steady state optical transport in random media. Their experiments on a sintered alumina wedge allowed the simultaneous determination of the penetration depth and the transport mean free path at a single frequency, although the energy velocity could not be determined as independent measurements of D were not performed. Such single frequency determinations of l^* and v_e have provided, to date, only limited experimental data (Genack *et al.*, 1993). This situation provides the motivation for the current measurements of the absolute transmission of acoustic waves through the glass bead samples, allowing the transport mean free path l^* to be determined under the constraint of consistency with the pulse measurements of D and τ_a. The self-consistent determination of these three diffusion parameters has *for the first time* enabled the energy velocity v_e to be experimentally ascertained over a wide frequency interval. The means whereby the absolute transmission was confidently obtained is first reviewed, and then the procedure followed to extract l^* and v_e is explained. For convenience, all discussions are illustrated by focusing only on the sieved bead data. Measurements will be described on samples ranging from 3 to 15 mm in thickness, across a frequency range

from 1 MHz ($k_w a \approx 2$) to 3.5 MHz ($k_w a \approx 7$). A summary and discussion of the frequency dependence of *all* the diffusion parameters obtained may be found in Sec. 5.5.3.

Measuring the total transmission required very long incident planar pulses that approximated continuous waves. If the incident pulse was longer than the time taken for most of the scattered sound to diffuse through the sample, a constant signal amplitude would be attained, as explained in Sec. 5.4. An example of such a situation was earlier indicated in figure 5.19. To determine these constant levels, the minimum incident pulse width was determined for each frequency, and at each sample thickness. The pulse width was then increased by 20 to 50 μs, and measurements performed as discussed in Sec. 4.3.3.1.

Since it is the mean behaviour of the steady state transmission that is of interest, measurements must be made over an ensemble of statistically equivalent samples, as previously indicated in the context of short pulse transmission (Sec. 5.5.1.1). The procedure for determining the transmitted intensity is similar to that described for the diffusive pulses (Sec. 5.5.1.1), though now, of course, any ballistic remnant is an integral part of the transmission. As phase information was thus not required, the waveform envelopes in the 20–50 μs wide flat region in the middle of the pulse were calculated in real time and subsequently averaged to yield the mean amplitude at that detection point. This quantity was squared, thus yielding an intensity, and normalized by the intensity of the incident planar wave at that point; the provisional total transmitted intensity per unit area, for that sample at that frequency, was then found by averaging these normalized intensities over all N detection points. This gives the mean intensity of the speckle pattern (cf. figure 5.16). On average, the standard deviation was found to be equal to the mean,

thus verifying that the contrast of a speckle pattern is unity (Sec. 5.3). Since the average over the speckle pattern is equivalent to the ensemble-average over uncorrelated speckles, the uncertainty in the transmitted intensity may be equated with the reduction in contrast, which is the mean over the square root of N (cf. Sec. 5.5.1.2). Thus, the uncertainty in the transmission is the standard error rather than the standard deviation.

Great care was taken to ensure an accurate determination of the incident intensity (Sec. 4.3.3.1), as this was crucial for such absolute transmission measurements. Moreover, all possible points of departure between the experimental reality and the conditions set forth in the theory were quantitatively identified. These considerations involved the effect of the sample walls, that of the input beam distribution, and the detector efficiency, as described in Sec. 4.3.3.2. The details of these corrections, and their net effect, are further expounded in Appendix B. At each frequency, the provisional total transmitted intensity was multiplied by the relevant net correction factor to yield the *absolute* total transmitted intensity per unit area. The absolute transmission at each frequency was plotted against sample thickness and fit to the expectations of diffusion theory [equation (2.114)], subject to certain constraints.

The predicted transmission involves the product $D\tau_a$, a consequence of the absorption in the sample [equations (2.112) –(2.114)]. The fitting of the transmission data is thus subject to the constraint imposed by the prior knowledge of this product obtained from the diffusive pulse experiments. Before discussing the manner in which this constraint was applied, the behaviour of the transmission in the absence of absorption must be understood, particularly for thick samples. Ignoring absorption, the predicted transmission indicated by equation (2.114) reduces to that presented in equation (2.111).

For thick samples, the ballistic remnant effectively vanishes and the exponential term may be ignored. As z_e (the extrapolation length) is on the order of unity, the transmission through a thick sample in the absence of absorption may be approximated by

$$T \cong l^*/L. \tag{5.18}$$

Under these conditions, a log-log plot of the transmission against sample thickness is linear, with negative slope, and the vertical positioning of the line is governed by l^*. The inclusion of absorption causes this line to bend downwards, with the curvature governed by the correlation function $g_1(\tau_a)$ [equation (2.112)]. In addition to the sample thickness L and the reflectivity R (both known quantities), $g_1(\tau_a)$ depends upon both $D\tau_a$ and l^* (the latter through the extrapolation length and the penetration depth), but with the former being dominant. The procedure followed in the fitting was to choose a reasonable starting value for l^*, and then adjust $D\tau_a$ (subject to the constraints, further discussed below) to accommodate the curvature in the data. The range of $D\tau_a$ so determined was subsequently verified to be insensitive to the precise values of l^* after the latter was determined from the optimal vertical positioning of the curve. In this manner, it was possible to acquire a range of values which yielded acceptable fits.

The constraints on the fitting imposed by the results of the diffusive pulse measurements will now be discussed by illustration with the 2.5 MHz planar wave data presented in Sec. 5.5.1.3.7. Consistency requires that the fixed normalization fitting results be employed in determining the most probable range of values for the products $D\tau_a$, since these normalizations derive from the net correction factors involved in the absolute transmission. Consider the dependence of D and τ_a on the penetration depth z_0,

shown, for example, in figure 5.34. The products $D\tau_a$ are determined over a range of z_0 within which l^* can confidently be expected to lie; at 2.5 MHz, this is $0.6 < z_0 < 1.4$ mm. The results are $9.8 < D\tau_a < 6.15$, $7.8 < D\tau_a < 6.0$, and $6.65 < D\tau_a < 5.65$ for the 7.1 mm, 10.1 mm, and 15.2 mm thick samples, respectively. The self-consistent range for $D\tau_a$, established by the diffusive pulse measurements, thus lies between 6.15 and 6.65 mm^2 at 2.5 MHz. Ranges for all the frequencies of interest are summarized in table 5.1. It should be noted that these constraints were not regarded as unyielding; if the transmission data

f	$k_w a$	$D\tau_a$ (pulse)	$D\tau_a$ (cw)	l^*	D	v_e
MHz		(mm^2)	(mm^2)	mm	($mm^2/\mu s$)	(km/s)
1.02	2.03	4.20 – 5.20	4.75 – 5.25	0.80 ± 0.15	0.190 ± 0.020	0.71 ± 0.15
1.55	3.07	5.90 – 6.90	6.50 – 7.00	1.15 ± 0.35	0.285 ± 0.015	0.75 ± 0.25
2.01	3.98	4.95 – 5.55	5.55 – 5.95	1.00 ± 0.15	0.345 ± 0.035	1.05 ± 0.20
2.50	4.96	6.15 – 6.65	6.15 – 6.55	0.93 ± 0.13	0.490 ± 0.020	1.58 ± 0.23
3.00	5.95	7.50 – 8.50	8.00 – 8.50	1.00 ± 0.10	0.560 ± 0.060	1.68 ± 0.25
3.50	6.94	4.90 – 5.70	4.50 – 5.00	0.95 ± 0.15	0.500 ± 0.010	1.58 ± 0.25

Table 5.1 Summary of the constraints [$D\tau_a$ (pulse)], the fitting results for the diffusive pulse (D), and the absolute transmission data [$D\tau_a$ (cw), l^*], thus yielding v_e over a wide frequency range.

clearly evidenced curvatures outside the indicated range, the cw determination for $D\tau_a$ was allowed to deviate by as much as 10% of the mean constraint. Regardless, some degree of overlap was always demanded, albeit vanishingly small.

The log-log plots of the transmission versus sample thickness are shown in figure 5.37 through figure 5.42, for the six different frequencies indicated. The data are indicated by the solid circles, and the best fits by the solid curves. At each frequency, the range of allowed curvatures dictated by $D\tau_a$ was first ascertained, and then the permissible variation in magnitude governed by l^* was determined. These quantities are summarized in table 5.1. A few remarks on the individual fits in question are in order. For the 1.02 MHz data, the 5-mm-thick sample was accorded very little weight, as it clearly could not be accommodated in the otherwise excellent fit. Its inclusion at anywhere near normal weight required values for $D\tau_a$ significantly in excess of the maximum constraint and produced a very poor fit; by contrast, the remaining data yielded values for $D\tau_a$ that agreed well with the constraint (table 5.1). At 1.55 MHz, the scatter in the data made the imposition of the constraint an absolute necessity, with the most believable fits occurring for the upper half of the constraint range. The large error bars on l^* reflect the spread necessary to best fit the data for either the thinner or the thicker samples. The 2.01 MHz data unequivocally insisted on less curvature than that urged by the constraint. The constraint was thus relaxed by 10%, allowing larger values of $D\tau_a$ to be used. Aside from some scatter at intermediate thicknesses, the resulting fit is quite good. The fit to the data at 2.5 MHz is seen to be excellent, and the curvature expressed

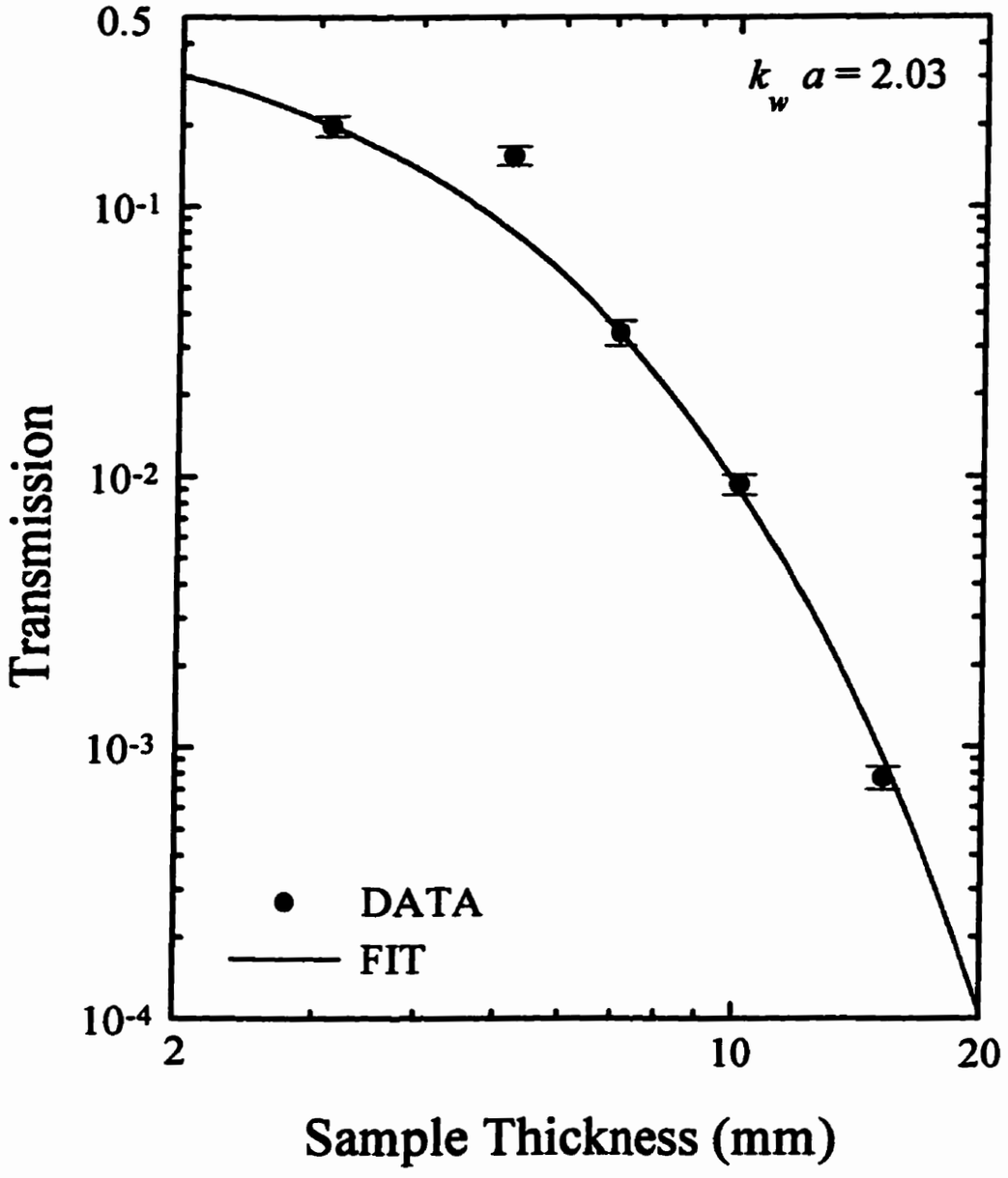

Figure 5.37 Dependence of the absolute transmission on sample thickness at 1.02 MHz. The fit shown is for $D\tau_a = 5.00$ mm^2 and $l^* = 0.80$ mm.

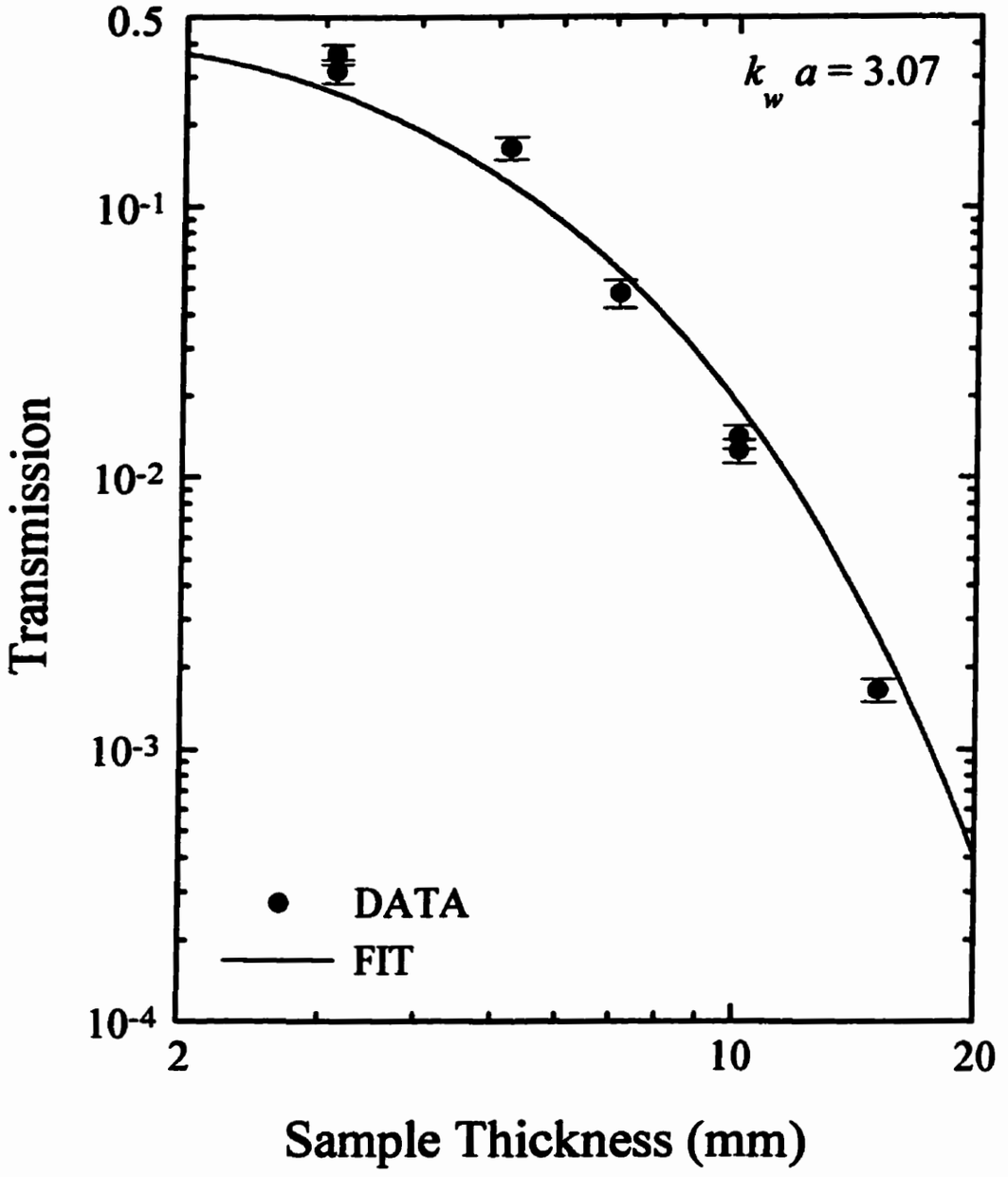

Figure 5.38 Dependence of the absolute transmission on sample thickness at 1.55 MHz. The fit shown is for $D\tau_a = 6.75$ mm^2 and $l^* = 1.15$ mm.

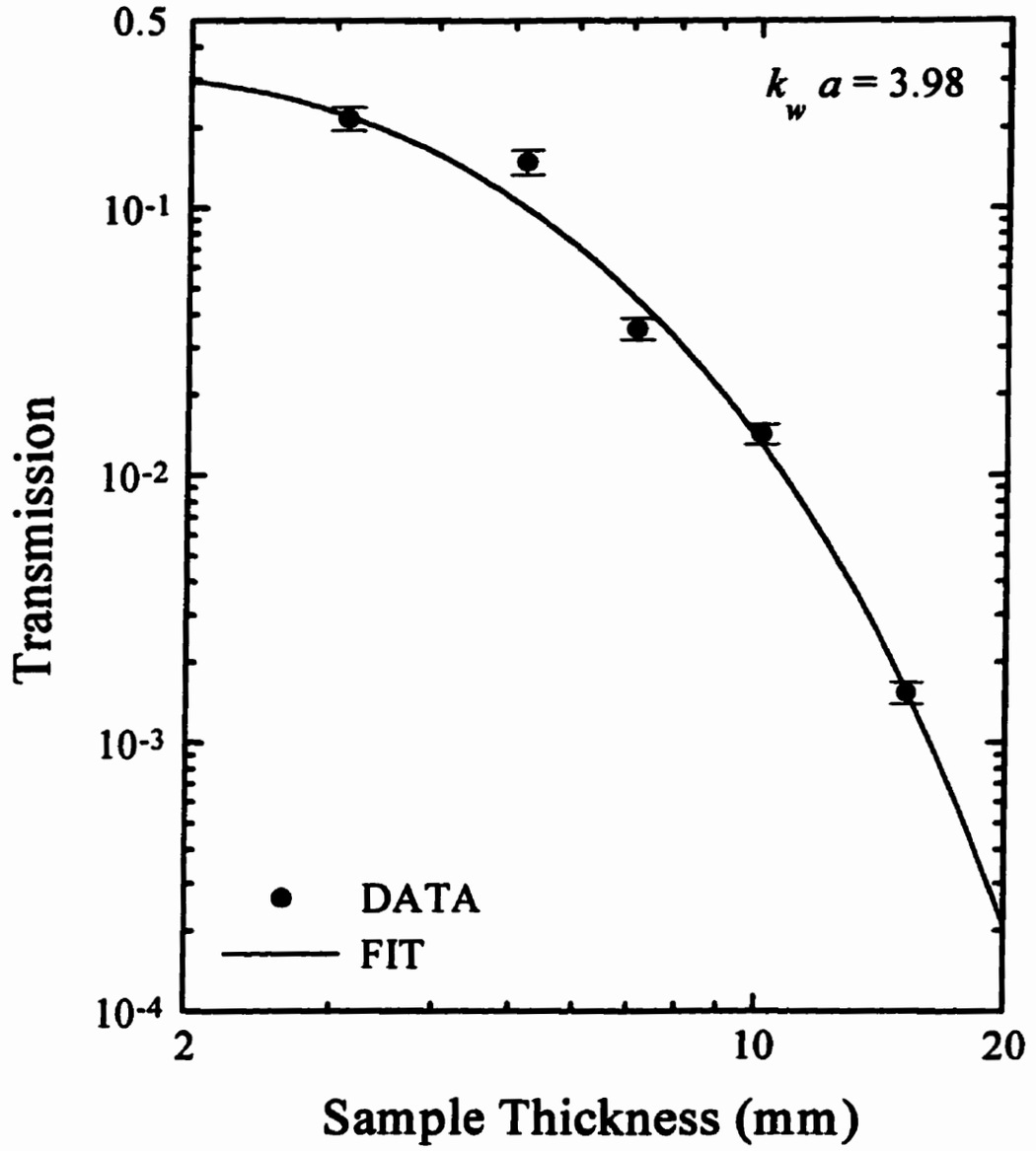

Figure 5.39 Dependence of the absolute transmission on sample thickness at 2.01 MHz. The fit shown is for $D\tau_a = 5.75$ mm^2 and $l^* = 1.00$ mm.

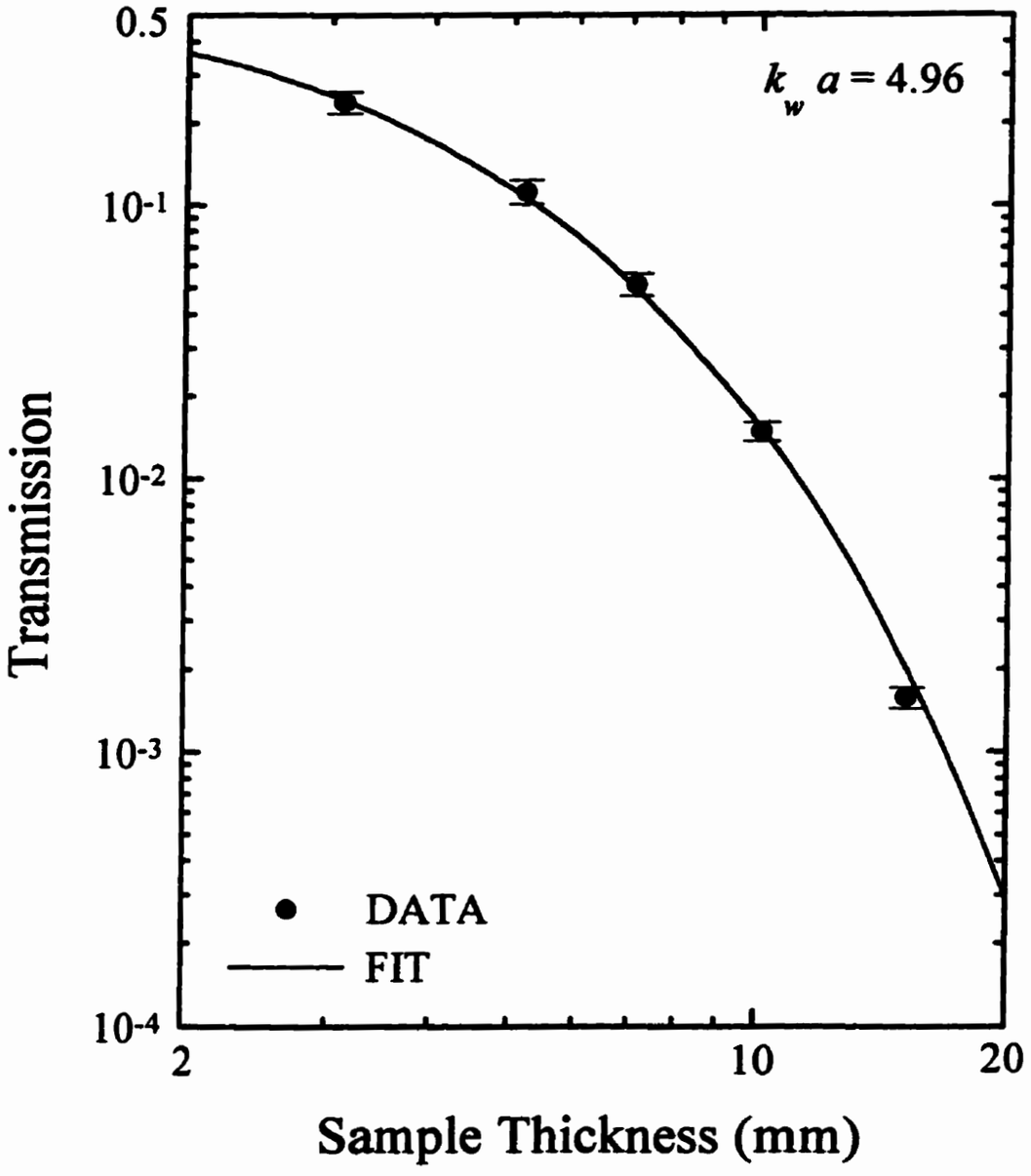

Figure 5.40 Dependence of the absolute transmission on sample thickness at 2.5 MHz. The fit shown is for $D\tau_s = 6.35$ mm^2 and $l^* = 0.93$ mm.

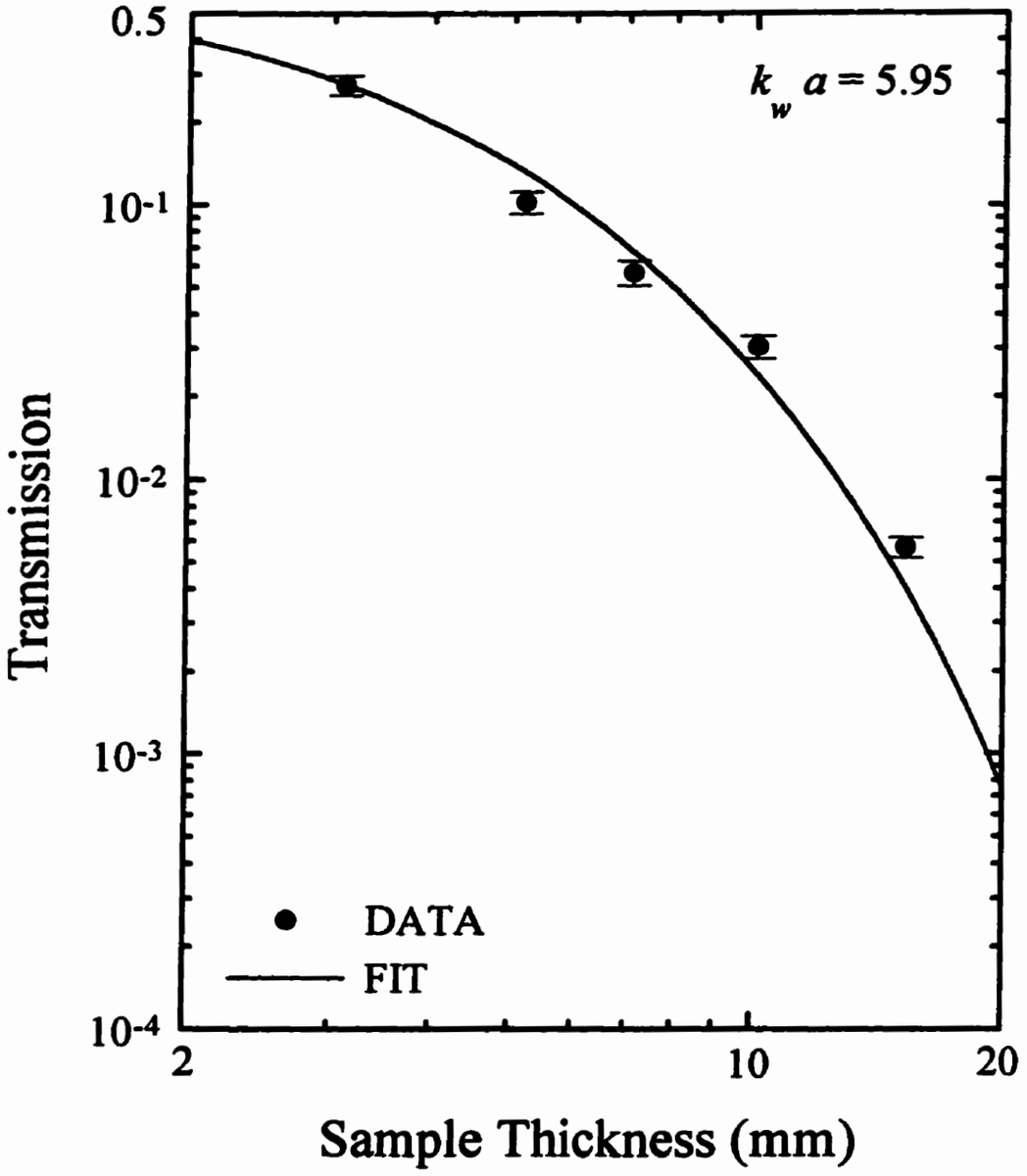

Figure 5.41 Dependence of the absolute transmission on sample thickness at 3.0 MHz. The fit shown is for $D\tau_s = 8.25$ mm^2 and $l^* = 1.00$ mm.

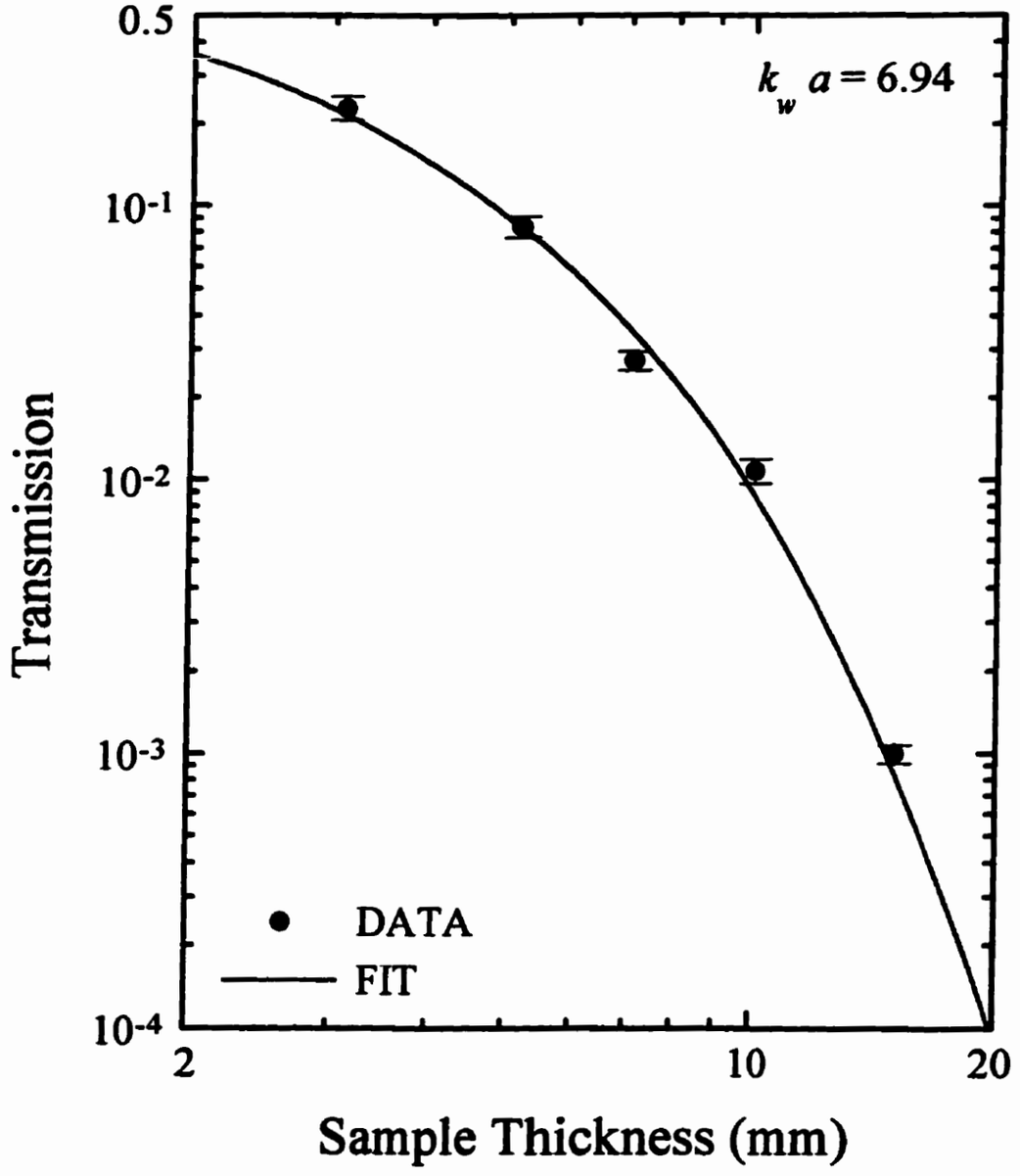

Figure 5.42 Dependence of the absolute transmission on sample thickness at 3.5 MHz. The fit shown is for $D\tau_a = 4.75$ mm^2 and $l^* = 0.95$ mm.

by the cw determination of $D\tau_a$ was found to be in full accord with the constraint (table 5.1). It was also unnecessary to invoke the constraint at 3.0 MHz, despite the slight scatter in the data; the resulting fit is clearly acceptable. At the highest frequency probed, 3.5 MHz, the transmission data necessitated more curvature than strictly allowed by the constraint. The constraint was thus relaxed by 10%, allowing smaller values of $D\tau_a$ to be used, so producing an excellent fit.

Having reliably determined both the transport mean free path l^* and the diffusion coefficient D, the energy velocity v_e may simply be calculated from equation (2.66). The results are illustrated in table 5.1 for the sieved bead data under consideration. A discussion of these data, and the relation of the energy velocity to the group velocity, is deferred to Sec. 5.5.3.2, so that all the diffusive parameters may be presented concurrently and their frequency dependencies examined in light of a unified physical picture.

5.5.3 Summary and discussion

5.5.3.1 The absorption rate τ_a^{-1}

The absorption in the glass bead samples is much greater than expected for either water or pure glass. The origin of this large absorption is explored by plotting the absorption rates τ_a^{-1} directly against the central frequency of the incident pulse, for samples with different bead size (a = 0.25 mm and a = 0.5 mm). Figure 5.43 shows that the absorption rate varies roughly linearly with frequency (the straight line being a guide to

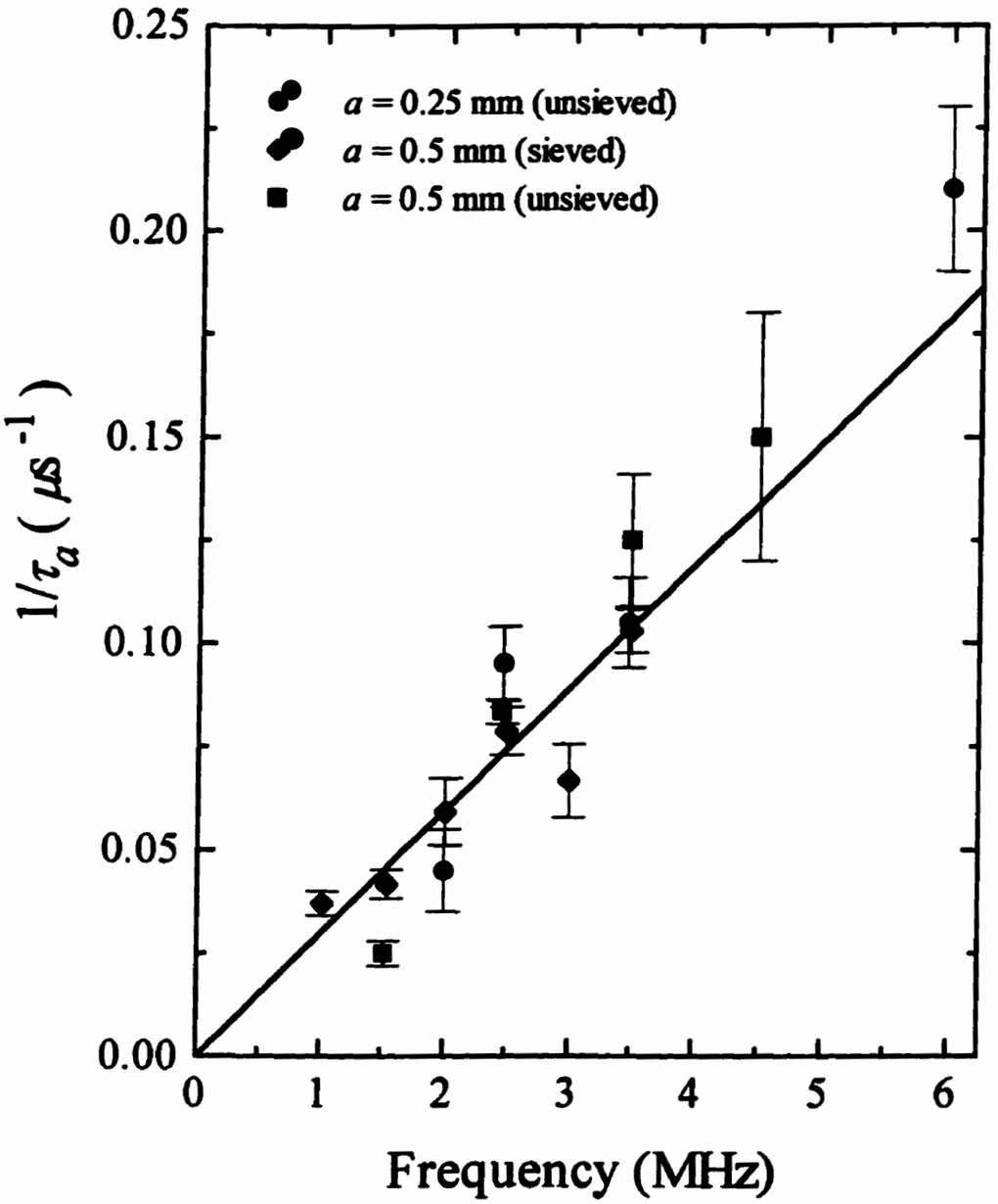

Figure 5.43 Variation in the absorption rate with frequency for data at both bead sizes. The straight line is a guide to the eye.

the eye), and is *independent* of the bead size. The interfacial area in the glass bead samples is large, and one might thus expect viscous losses to be responsible for the significant absorption. Viscous losses in a fluid near a fluid-solid interface are, however, expected to vary as (Landau and Lifshitz, 1959)

$$\frac{1}{\tau_a} \propto \sqrt{\omega \eta} \frac{S}{V}, \tag{5.19}$$

where η is the viscosity of the fluid, V the volume of the fluid, and S the surface area of the solid. This predicts an absorption proportional to a^{-1} for close-packed spheres, and a square root frequency dependence, neither of which are observed. The measured absorption appears intrinsic to the glass beads themselves, and presumably results from the method by which the spheres were manufactured.

The absorption *length* may be defined as $l_a = v_e \tau_a$. Over the range of frequencies for which data were acquired (at specific bead sizes), this implies $250 > l_a/a > 25$. These values are at least an order of magnitude greater than mean free path measurements (Sec. 5.2.2 and Sec. 5.5.3.2), implying that the attenuation of the ballistic pulse results from scattering and not absorption (for the range of sample thicknesses studied).

5.5.3.2 The diffusion parameters l^*, v_e, and D

Summaries of the frequency dependence of the experimentally determined diffusion parameters are presented, and compared with the theoretical predictions of the effective medium model (Sec. 2.2.8), allowing the underlying physics of the ballistic and diffusive transport to be explained on a microscopic basis. As the bulk of the data

presented are for the sieved beads, the theoretical predictions have been averaged over the smaller variation in bead size (~5%; see Sec. 3.2).

The variation in the transport mean free path l^* (scaled by the bead radius) with normalized frequency $k_w a$ (where k_w is the acoustic wave vector in water) is shown in figure 5.44; for comparison, the scattering mean free path l_s is also displayed. The solid symbols are the measured values for l^*, whereas the open symbols are the data for l_s. Comparison of the scattering and transport mean free paths reveal them to be indistinguishable at low frequencies, where the scattering is isotropic. At higher frequencies, the anisotropy of the scattering is clearly exposed, and l^* is seen to exceed l_s, as expected [equation (2.67)]. Note that the distance required to randomize the propagation direction is comparable to the bead *diameter* across the entire frequency range investigated, whereas the distance between scattering events can drop to less than the bead *radius*. Theoretical predictions of the transport mean free path, obtained using equation (2.116), are indicated by the solid curve in figure 5.44. Since l^* and l_s share the same scattering environment, the scaling parameter used in the calculation of l_s (Sec. 5.2.2) was also applied to the prediction of l^*. Good agreement is seen between experiment and theory.

The variation in the energy velocity v_e with normalized frequency $k_w a$ is shown in figure 5.45; for comparison, the group velocity v_g is also displayed. The measured values for v_e, determined using equation (2.66) (see table 5.1), are shown by the solid

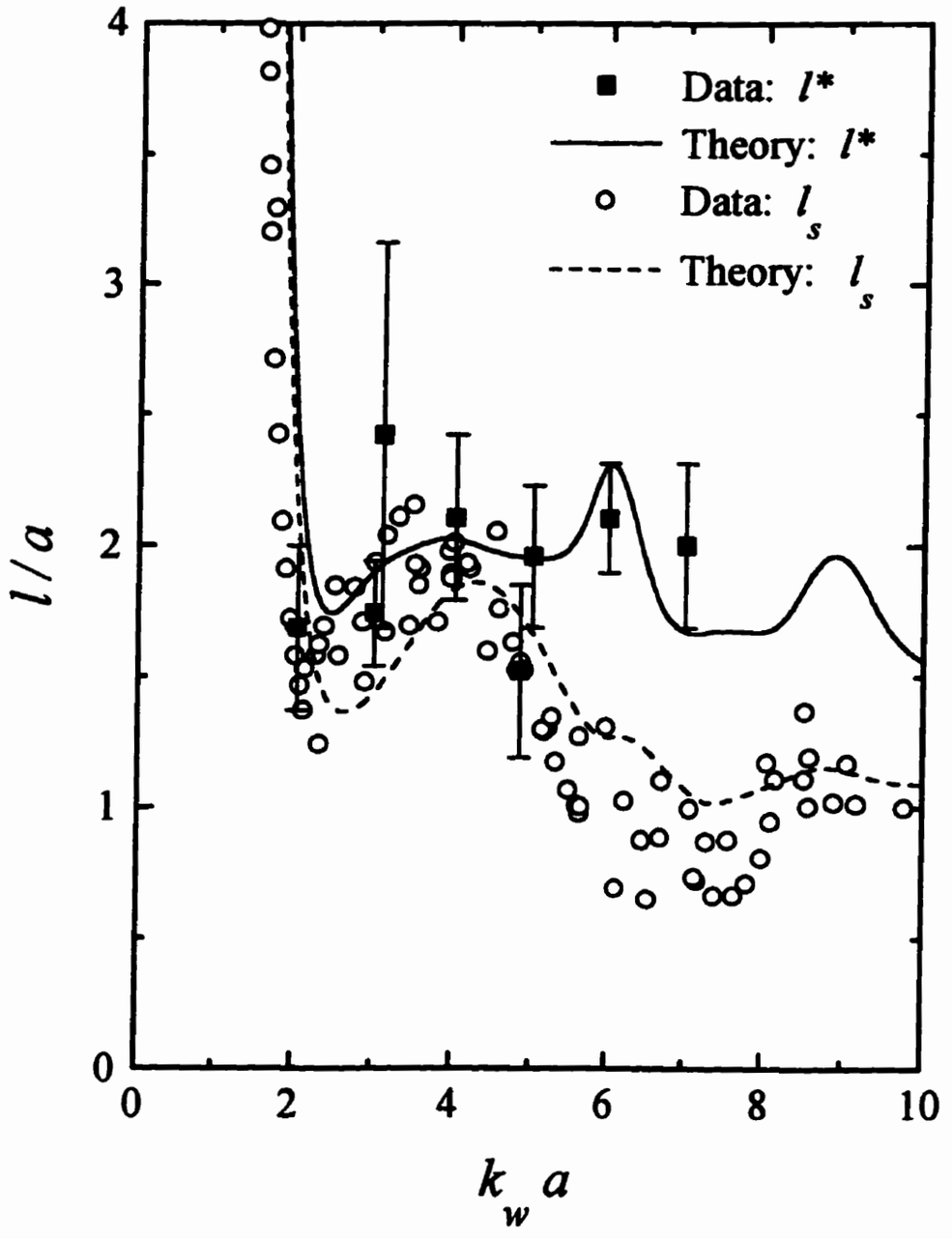

Figure 5.44 Frequency dependence of the transport and scattering mean free paths (solid and open symbols, respectively), compared with the predictions of the effective medium model (solid and dashed curves).

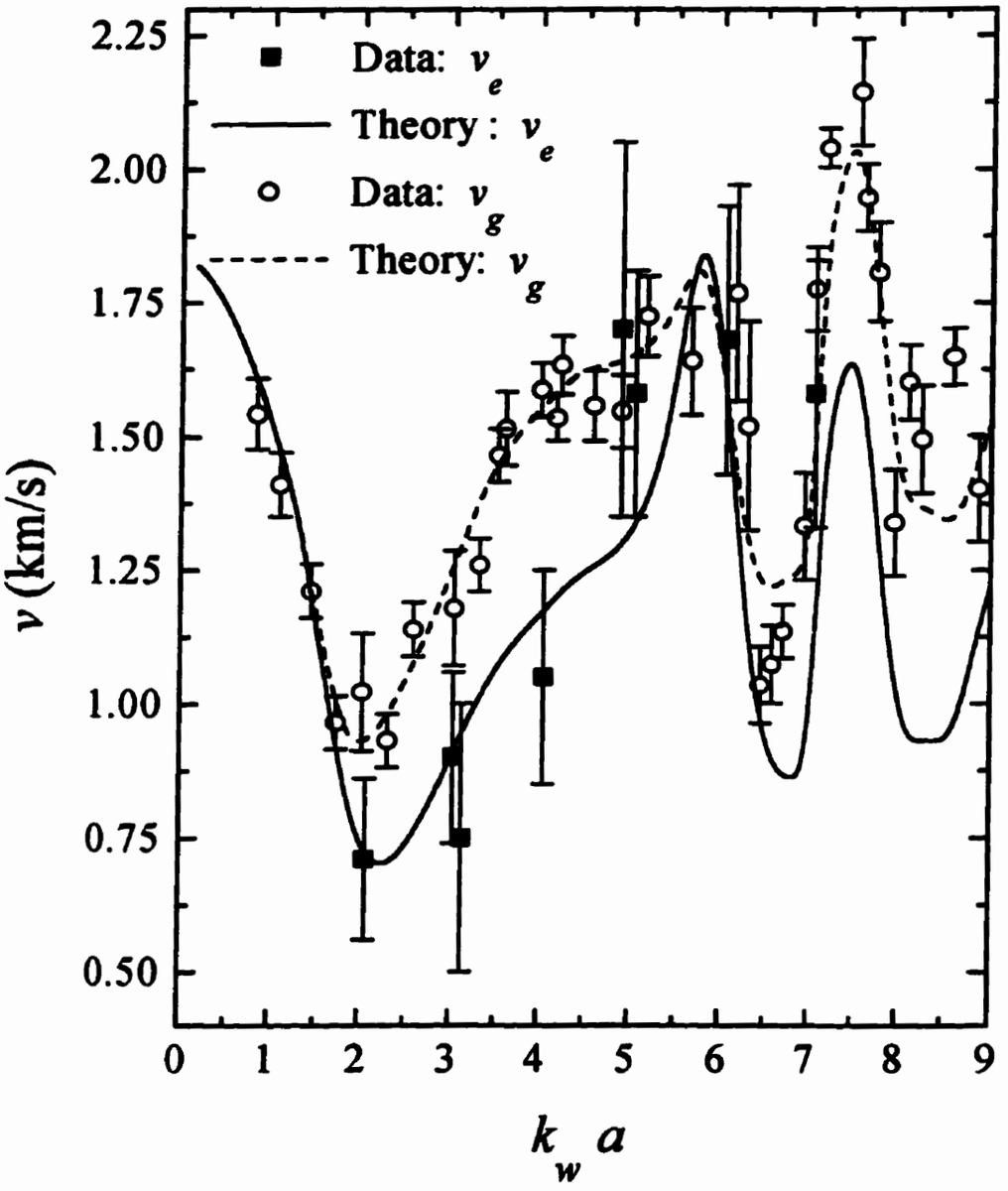

Figure 5.45 Frequency dependence of the energy and group velocities (solid and open symbols), compared with the predictions of the effective medium model (solid and dashed curves).

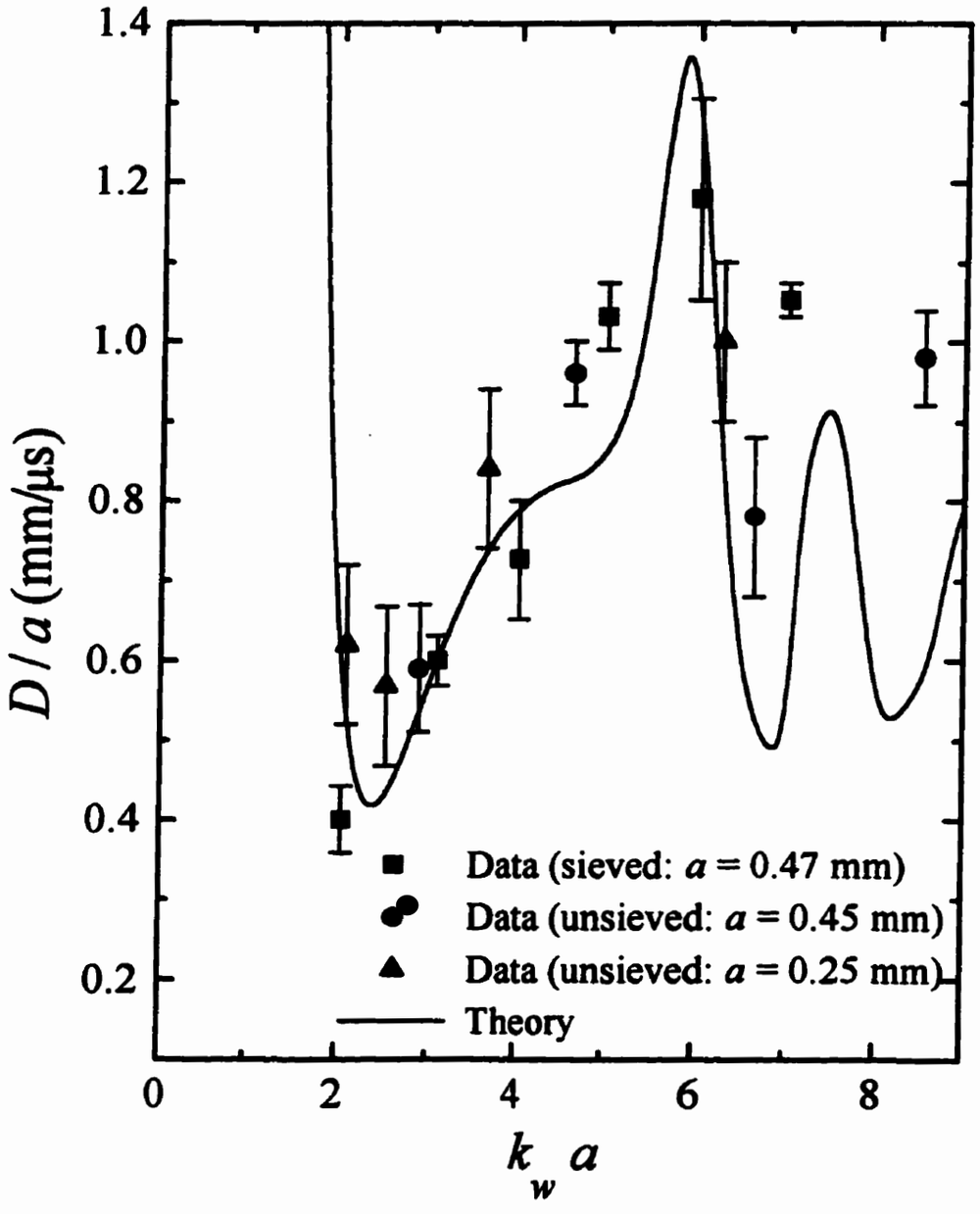

Figure 5.46 Frequency dependence of the diffusion coefficient (symbols), compared with the predictions of the effective medium model

symbols, whereas the open symbols are the data for v_g. The energy velocity is seen to be similar in magnitude to the group velocity over the entire frequency range investigated. In addition, the velocities exhibit strong frequency dispersion, varying by about a factor of three. The minima in the velocities may be attributed to the effects of scattering resonances, as they occur at the same frequencies as dips in the scattering mean free path (figure 5.44). The energy velocity is seen to be slower than the already quite slow group velocity in the neighbourhood of the first minimum, where the scattering mean free path is less than half the wavelength, while at the higher frequencies, the two velocities are indistinguishable within experimental error. The slow transport velocities are a consequence of a portion of the wave energy dwelling in the resonant scatterers for some period of time. Due to the angular dependence of the scattering amplitude, the dwell times of wave pulses that have forward scattered can differ from those that have scattered through finite (non-zero) scattering angles, thus explaining the small difference between v_e and v_g. Theoretical predictions for the energy velocity [equation (2.121)], shown by the solid curve in figure 5.45 (the dashed curve is the predicted behaviour for v_g), involve *no* adjustable parameters and are thus in remarkably good agreement with the experimental data. The calculations accurately predict the considerable structure in v_e and correctly show that v_e falls below v_g for $2 < k_w a < 4$, and that v_e approaches v_g for $5 < k_w a < 6$.

The behaviour of the diffusion coefficient D (scaled by the bead radii), with normalized frequency $k_w a$, is summarized in figure 5.46. The data are shown by the solid symbols, and the predictions of the effective medium theory (constructed from that of l^*

and v_e) by the solid curve. It should be noted that, aside from the phenomenological scaling constant in l^*, theoretical predictions of D involve no adjustable parameters. The agreement between theory and experiment is very good; the theory not only captures all the observed structure in D, but also generally predicts the correct magnitude. The experimentally determined diffusion coefficients from unsieved bead (circle, triangle) and sieved bead (squares) samples should be quite similar, at least for $k_w a < 7$. This is expected since the unsieved and sieved bead *group* velocities (figure 5.13 and figure 5.14, respectively) exhibit the same behaviour, except at the highest frequencies. Furthermore, the transport mean free paths for the two types of samples should also be equivalent since their scattering mean free paths are indistinguishable (figure 5.3 and figure 5.4). The above observations justify the inclusion of both types of data on the same plot. Theoretical predictions do not quite manifest quantitative agreement with the data at the highest three frequencies, though the frequency behaviour appears to be correctly captured. This seems to suggest that, at the highest frequencies, the difference between the group and energy velocities may be less than predicted.

The experimental results for the diffusive transport of acoustic waves through a glass-bead system with a high volume fraction of scatterers have convincingly demonstrated strong structure in the energy velocity. This structure is considerably greater than predicted by Kafesaki and Economou (1997) using a CPA model. In addition, their model provides an unphysical prediction for the energy velocity over most of the strong scattering regime investigated, giving values considerably greater than both our measured and calculated *group* velocities. This is quite likely due to the inherent

shortcomings of the CPA approach in the intermediate frequency regime (see Sec. 2.1.6.3 and Sec. 2.2.8).

The similarity of the strong dispersion found in the energy velocity to that seen in the group velocity is explained using our new approach to model their behaviour theoretically (Schriemer *et al.*, 1997). From their behaviour emerges a unified physical picture of the energy transport by ballistic and diffusive waves, which has its roots in the velocity of propagation of a wave pulse. The coupling between the resonant scatterers leads to an effective renormalization of the scattering. The result is weakened scattering from the coated spheres embedded in this renormalized homogeneous medium. This ensures that the group velocity remains well defined and allows it to be calculated within the GCPA. The energy velocity can then be quantitatively predicted by extending this approach to account for the angular dependence of the scattering delay experienced by this wave pulse. The appealing but generally unrecognized feature presented by this treatment is the near equivalence between the group and energy velocities; there exists a common origin in the velocity of propagation of a wave pulse, which is in the forward direction for the coherent transport, and locally between scattering events for diffusive transport.

6 Conclusions

A definitive study of the ballistic and diffusive transport of acoustic waves through resonantly scattering inhomogeneous media, composed of randomly close-packed glass beads immersed in water, was successfully accomplished in the normalized intermediate frequency range $1 < k_w a < 10$. This work is the first comprehensive undertaking in the intermediate frequency regime over such a wide range of frequencies. It has consequently allowed fundamental questions regarding the transport of energy to be conclusively addressed. The salient features of the investigations are summarized below.

The ballistic transport was accurately determined from the coherent transmission of short ultrasonic pulses through thin samples, enabling the scattering mean free path, the phase velocity, and the group velocity to be measured. A new effective medium theory, which overcomes the limitations inherent in the coherent potential approximation, has proven highly successful in predicting the transport behaviour of the ballistic pulse. Our generalized coherent potential approximation (GCPA) has resulted in the identification of the peaks in the spectral function with the propagating (quasi)modes of the renormalized homogeneous medium. The resulting dispersion relation enabled successful quantitative predictions of the highly dispersive phase and group velocities to be made, without any adjustable parameters. Both velocities were found to be substantially less than the speed of sound in either the water or the glass over most of the frequency range. From a calculation of the total scattering cross section for the coated sphere, the dips in the scattering mean free path were identified with resonances in the single particle scattering, thus explaining the origin of the dispersion in the group velocity. The quantitative

prediction of the experimentally determined group velocity by this approach, where the coupling between the resonant scatterers leads to an effective renormalization of the scattering within the medium, resolves a long-standing problem in the definition of the group velocity in strongly scattering materials. The group velocity remains well defined and calculable within the GCPA because, relative to the effective medium in which the coated spheres are embedded, the scattering from the spheres has been weakened by this effective renormalization.

Guided by the recent insight gained from the study of diffusing light, the diffusive transport of acoustic waves was accurately determined by measuring the multiple scattering of both short and quasi-continuous-wave ultrasonic pulses through glass bead samples at different thicknesses. A very small detecting transducer was used to probe the scattered sound fields within single spatial coherence areas, thus avoiding the spurious signal reductions due to phase cancellation effects in the larger element diameter transducers. This allowed the observation of ultrasonic speckle. Using short ultrasonic pulses, the temporal fluctuations in the multiply scattered fields, within a single speckle, were found to roughly correspond to the incident pulse width. The time dependence of the ensemble-averaged transmitted intensity, found from the multiply scattered sound detected over many uncorrelated speckles, allowed critical tests of the diffusion approximation to be performed. For short incident pulses and various different detection geometries, the shape of the ensemble-averaged transmitted intensity was found to be accurately described by the diffusion equation (with boundary conditions properly accounting for the reflectivity at the interfaces), and the diffusion coefficients D and absorption times τ_a consistently determined. The absorption was found to be intrinsic to

the glass beads, the absorption rate being linearly dependent on the frequency, and independent of the size of the glass beads used. The frequency behaviour of the diffusion coefficient, successfully predicted by extending the same theoretical approach used in the ballistic transport, was seen to be highly dispersive, being strongly slowed down in the neighbourhood of the single coated-sphere resonances.

The total transmitted intensity for steady state propagation of incident quasi-continuous waves was also accurately described by the diffusion equation, using the same boundary conditions as in the pulse geometry. A careful consideration of all relevant correction factors allowed an accurate experimental determination of the transport mean free path l^* from the dependence of the absolute transmission on sample thickness. Results found for the product $D\tau_a$ were consistent with findings from the pulse geometry, further attesting to the validity of the diffusion approximation in the description of the propagation for multiply scattered sound. A calculation of the full angular dependence of the scattering amplitude of the coated elastic sphere embedded in the homogeneous medium successfully predicted the frequency dependence of the transport mean free path.

By combining the results of these dynamic and static measurements, the energy transport velocity of the diffusing sound was experimentally determined. The energy velocity was found to exhibit strong structure as a function of frequency, being even slower than the group velocity at the first scattering resonance, and indistinguishable from the group velocity at the higher frequencies studied. By extending the model used in describing the ballistic transport to account for the angular dependence of the scattering delay, the energy velocity was quantitatively predicted and remarkably good agreement with the data was shown. From the approach used to model the dispersive behaviour of

the transport velocities emerges a unified physical picture of the energy transport by ballistic and diffusive waves, which has its roots in the velocity of propagation of a wave pulse. An effective renormalization of the scattering, which depends directly on the strength of the scattering (and the volume fraction of scatterers), results from the coupling between the resonant scattering units, and is responsible for the strong dispersion observed in these transport velocities through the closely packed glass bead samples. Our measurements are the first to establish the close connection between the ballistic and diffusive transport of energy.

These acoustic measurements of the diffusive transport have stimulated further investigations, both theoretical and experimental, into the nature of the propagation (Jones, 1996; Zhang *et al.*, 1997). The results presented in this thesis open up interesting new possibilities for using acoustic waves in future studies of multiply scattered sound. For example, scatterers with less intrinsic absorption, but stronger scattering resonances, may permit the observation of such non-classical propagation effects as scale dependent diffusion coefficients which are the signature of localization. On the technological side, new nondestructive testing techniques using diffusing sound could be of benefit in some situations. For example, the feasibility of using diffusing sound to investigate the dynamics of a scattering medium has recently been demonstrated (Jones, 1996) using a technique analogous to diffusing wave spectroscopy of light (Pine *et al.*, 1988). This acoustic technique could potentially be quite useful for the remote monitoring of large scale industrial chemical reactions.

The experimental and theoretical approach in this thesis has focused on acoustic waves, where strong scattering is relatively easy to achieve, and the full field (including all

phase information) can be simply detected. However, the basic features of the transport should, in principle, be observed for any classical wave propagating in disordered materials. Confirmation of similar behaviour by electromagnetic waves, such as light or microwaves, would provide an important generalization of these results.

Appendices

A Determination of the reflection coefficient

A.1 The angular dependent reflection coefficient, $R(\theta)$

In Sec. 2.2.6, the mean reflection coefficient is defined within the context of the boundary conditions imposed on the diffuse energy density [equations (2.87) – (2.89)]. The calculation of the mean reflection coefficient requires first a knowledge of its angular dependence, which we now proceed to determine. For simplicity, we consider a boundary between two fluid media, such as a gelled sample immersed in water, where the physics is quite straightforward (e.g. no mode conversion). A more sophisticated calculation, for reflection at the interfaces of a fluid-like sample, a rigid wall, and the water, yields remarkably similar results. An acoustic wave incident on a boundary between two dissimilar fluid media will undergo both reflection and transmission, the relative proportions of which are determined by the acoustic impedance mismatch between the two media. The acoustic impedance of a medium is the product of its density ρ and the phase velocity v of the propagating wave. Figure A.1 shows a wave in medium 1, at an angle of incidence θ_1, undergoing both reflection and refraction at the boundary with medium 2. Landau and Lifshitz (1959) have shown that, for a two-fluid medium, the reflection coefficient $R(\theta_1)$ is

$$R(\theta_1)=\left(\frac{\rho_2 v_2\cos\theta_1-\rho_1\sqrt{v_1^2-v_2^2\sin^2\theta_1}}{\rho_2 v_2\cos\theta_1+\rho_1\sqrt{v_1^2-v_2^2\sin^2\theta_1}}\right)^2, \qquad \text{(A.1)}$$

where v_1 and v_2 are the phase velocities, and ρ_1 and ρ_2 the densities, in media 1 and 2, respectively.

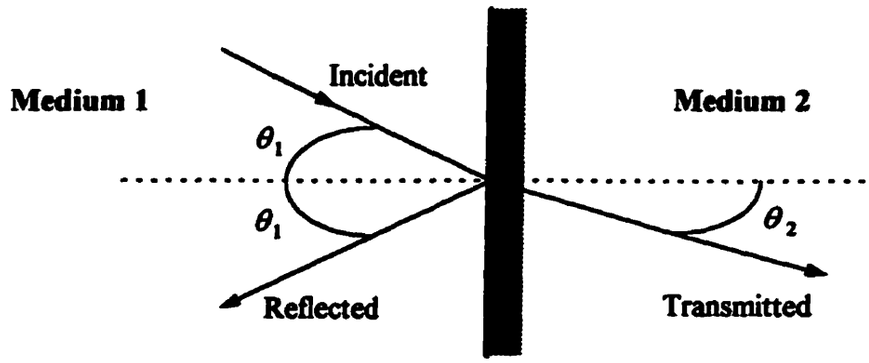

Figure A.1 Reflection and transmission at the boundary between two fluid media.

Using $R(\theta_1) + T(\theta_1) = 1$ (conservation of energy), with equation (A.1) and Snell's law,

$$\frac{1}{v_1}\sin\theta_1 = \frac{1}{v_2}\sin\theta_2, \tag{A.2}$$

the transmission coefficient $T(\theta_2)$, which gives the transmission as a function of the *exit* angle, is given as

$$T(\theta_2) = 1 - \left(\frac{\rho_1 v_1 \cos\theta_2 - \rho_2 \sqrt{v_2^2 - v_1^2 \sin^2\theta_2}}{\rho_1 v_1 \cos\theta_2 + \rho_2 \sqrt{v_2^2 - v_1^2 \sin^2\theta_2}} \right)^2 . \tag{A.3}$$

Equation (A.1) and equation (A.3) are used to correct for the effects of reflections (internal and incident, respectively) on the absolute transmission at the interfaces (Appendix B.3).

A.2 The mean reflection coefficient, R

Having shown, in the previous section, how the angular dependent reflection coefficient $R(\theta)$ may be determined, we now proceed to the determination of the mean reflection coefficient. We first determine the reflected flux $R(\theta)J(\theta)$, for a given angle of incidence θ, at $z = 0$. Consider once again the flux through dS due to dV, as done in equations (2.81) through (2.83). Integrating over r and ϕ only, we obtain

$$J(\theta) = \tfrac{1}{2} U v_e \sin\theta \cos\theta + \tfrac{1}{2} v_e l^* \frac{\partial U}{\partial z} \sin\theta \cos^2\theta, \tag{A.4}$$

The total flux in the z direction (due to reflections) at $z = 0$ is thus found by integration:

$$J^+ = \int_0^{\pi/2} d\theta \, J(\theta) R(\theta). \tag{A.5}$$

Away from the boundary, J^+ is given by equation (2.86); within the diffusion approximation, these two expressions for J^+ must be equal *near* the boundary at $z = 0$. Equating equations (2.86) and (A.5), using (A.4), yields the boundary condition at $z = 0$ in the following form:

$$U - l^* \left(\frac{\frac{1}{3} + C_2}{\frac{1}{2} - C_1} \right) \frac{\partial U}{\partial z} = 0, \tag{A.6}$$

where

$$C_1 \equiv \int_0^{\pi/2} d\theta \, R(\theta) \sin\theta \cos\theta \tag{A.7}$$

and $$C_2 \equiv \int_0^{\pi/2} d\theta\, R(\theta)\sin\theta\cos^2\theta\ . \tag{A.8}$$

The analogous form for the boundary condition at $z = L$,

$$U + l^*\left(\frac{\frac{1}{3}+C_2}{\frac{1}{2}-C_1}\right)\frac{\partial U}{\partial z} = 0, \tag{A.9}$$

may be found in a similar fashion. We see that equations (A.6) and (A.9) are identical to the boundary conditions previously determined, equations (2.87) and (2.88), provided we require

$$h = l^*\left(\frac{\frac{1}{3}+C_2}{\frac{1}{2}-C_1}\right). \tag{A.10}$$

An expression for the parameter R which depends only on the impedance mismatch between the media on either side of the boundary is found by comparing equations (2.89) and (A.10). This gives

$$R = \frac{3C_2 + 2C_1}{3C_2 - 2C_1 + 2}. \tag{A.11}$$

I am indebted to Michael L. Cowan for justifying, using a more sophisticated calculation, the employment of the simple two-fluid model. These more realistically determined values of R were used in fitting the diffusive pulses, although the difference with the more simply determined values was slight.

B Correction factors for absolute transmission measurements

B.1 Effect of the sample walls

The discussion of the wall correction has been presented in Sec. 4.3.3.2.1. Little needs to be added to what has already been discussed, save for mention of the actual values of this correction at the frequencies of interest. The wall corrections, which are the ratios of the transmission through gelled samples (Sec. 3) without and with walls, are presented in table B.1 for the sieved bead samples.

f(MHz)	Correction
1.0	2.43
1.55	2.92
2.0	2.84
2.5	4.85
3.0	3.14
3.5	3.15

Table B.1 Wall correction factors at various frequencies of interest.

It should be mentioned that, in addition to the limitation imposed on sample thickness by the structural rigidity of the gel, the reason the bulk of the measurements were not performed on such samples was the limited quantity of sieved beads (in particular) available. This was a constraint because the beads could not be extracted from the gel and conveniently cleaned. Though it is possible to dissolve the gel, the process is extremely slow given the quantity of gel involved, and the glass beads may be affected (and hence their resonant properties) by the chemicals used.

B.2 Detector (hydrophone) efficiency

B.2.1 Angular response of the hydrophone and initial reflective loss

The hydrophone angular response correction was introduced, and the method by which it was determined described, in Sec. 4.3.3.2.2. To calculate these quantities, the angular dependence of the probability $P(\theta)$ of a diffusely transmitted wave (phonon) arriving at a "small" area dS on the interior surface of the sample must first be found (see Sec. 2.2.6, figure 2.7). Since the flux through dS is just the integral of this probability over all solid angles and sample positions, equation (2.82) will allow us to extract this probability. Away from source terms, the steady state diffuse energy density U must vary linearly with $z = r\cos\theta$ in such a manner as to reach zero a distance $h = z_e l^*$ outside the sample. Substituting $U \propto h + r\cos\theta$ into equation (2.82) gives [using l^* rather than l_s, as is appropriate (Sec. 2.2.6)]

$$
\begin{aligned}
J &\propto \int_0^{\pi/2} d\theta \int_0^{\infty} dr\, e^{-r/l^*} (h + r\cos\theta)\cos\theta \sin\theta \\
&\propto \int_0^{1} d\mu \int_0^{\infty} dr\, e^{-r/l^*} (h + r\mu) \\
&\propto \int_0^{1} d\mu\, (z_e\mu + \mu^2)
\end{aligned}
\qquad \text{(B.1)}
$$

The probability of the phonon striking dS at an angle between $\theta = \arccos(\mu)$ and $\theta + d\theta = \arccos(\mu + d\mu)$ is thus

$$P(\mu)d\mu = C\left(z_e\mu + \mu^2\right)d\mu, \qquad \text{(B.2)}$$

or

$$P(\theta)d\theta = C\sin\theta\left(z_e\cos\theta + \cos^2\theta\right)d\theta \qquad \text{(B.3)}$$

(Durian, 1994; Vera and Durian, 1996). Employing Snell's law, the dependence of the probability on the *exit* angle becomes

$$P(\theta_2)d\theta_2 = C\sin\theta_2\cos\theta_2\left[z_e + \sqrt{1 - \left(\frac{\nu_2}{\nu_1}\sin\theta_2\right)^2}\right]d\theta_2, \qquad \text{(B.4)}$$

where the subscript 1 refers to the sample and the subscript 2 to the surrounding water, ν being the phase velocity in each medium, and a quantity $(\nu_2/\nu_1)^2$ has been absorbed into the constant of proportionality C. Equation (B.4) neglects reflections at the interfaces which decreases the fraction of the incident wave transmitted through the sample. Multiplying equation (B.4) by the boundary transmission $T(\theta_2)$ from equation (A.3) and then integrating gives the flux incident on the detector as

$$n = \int_0^{\pi/2} P(\theta_2) T(\theta_2) d\theta_2 . \qquad \text{(B.5)}$$

There is a dependence on $\cos\theta_2$ that follows from equation (2.82) in the derivation of $P(\theta_2)$. This arises from the assumption that the angular acceptance of dS (which is equivalent to the detector area) is entirely due to the effective area presented to the incoming wave, as the steady state diffusion theory assumes. However, if the angular response of the hydrophone $D(\theta_2)$ is *not* entirely geometric, the measured flux becomes

$$M = \int_0^{\pi/2} \frac{n(\theta_2) D(\theta_2)}{\cos\theta_2} d\theta_2 . \qquad \text{(B.6)}$$

The angular response correction factor is then given by the ratio n/M. Figure B.1 shows the angular dependence of the relative flux at 1.5 MHz both incident upon $[n(\theta_2)]$ and measured by $[M(\theta_2)]$ the 400 μm diameter hydrophone; also provided are the boundary transmission $T(\theta_2)$, and the detector response $D(\theta_2)$ divided by $\cos\theta_2$. Examples of the measured $D(\theta_2)$ are provided in figure B.2 for the 200 μm diameter hydrophone at frequencies of 1.5 MHz, 2.5 MHz, and 3.5 MHz. These angular responses are fit to Gaussians to allow the integrations [equation (B.6)] to be more easily performed.

The correction for the initial reflective loss of the incident wave is the inverse of $T(\theta_2 = 0)$. Multiplying the measured total transmission by $T^{-1}(\theta_2 = 0)$ and the ratio n/M (equation B.5 and equation B.6) thus corrects the measurements for impedance mismatch at the sample boundaries and the actual detectors used.

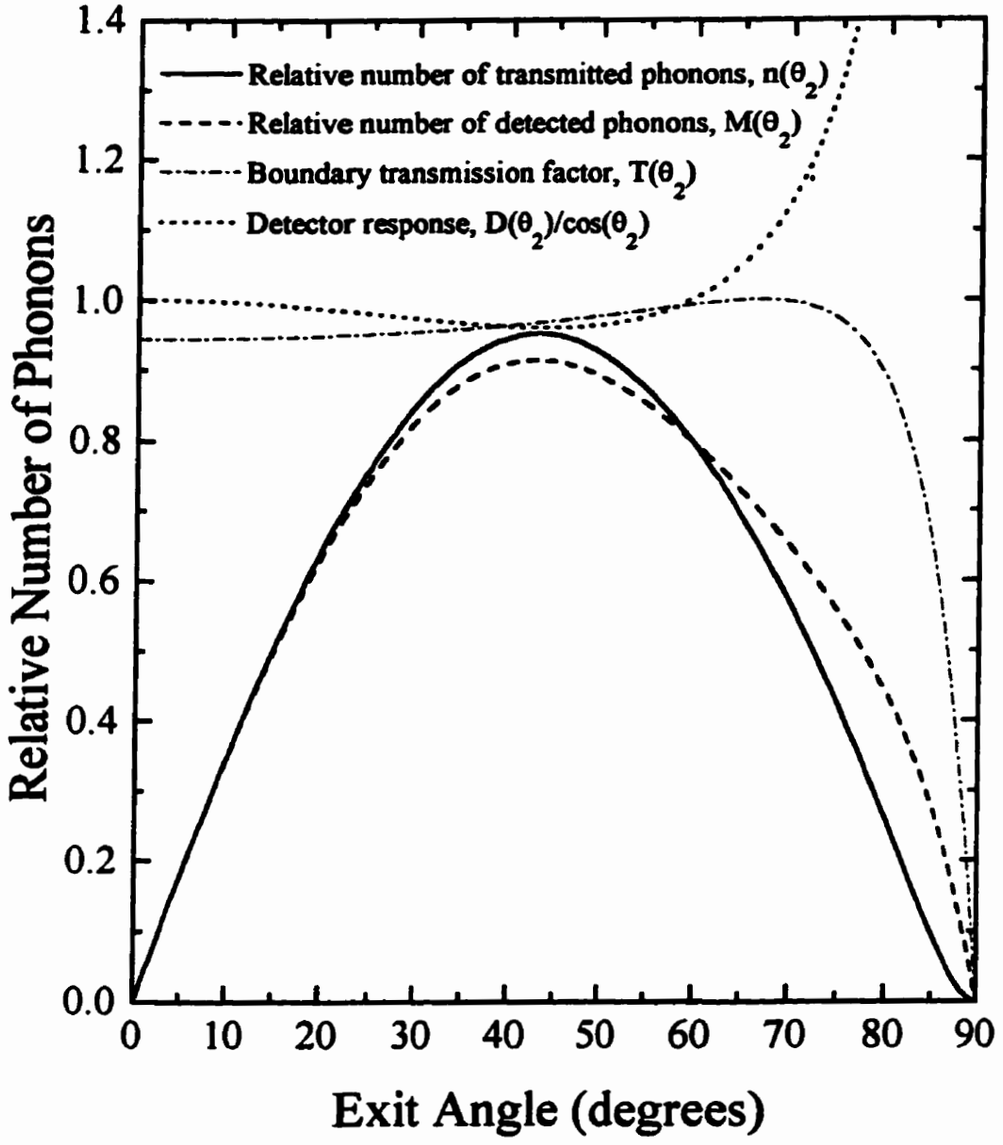

Figure B.1 The relative flux at 1.5 MHz incident on (solid curve), and detected by (dashed curve) the 400 μm diameter hydrophone. The angular dependence of the boundary transmission $T(\theta_2)$ (dot-dashed curve), and the detector response divided by $\cos(\theta_2)$ (dotted curve), are also provided.

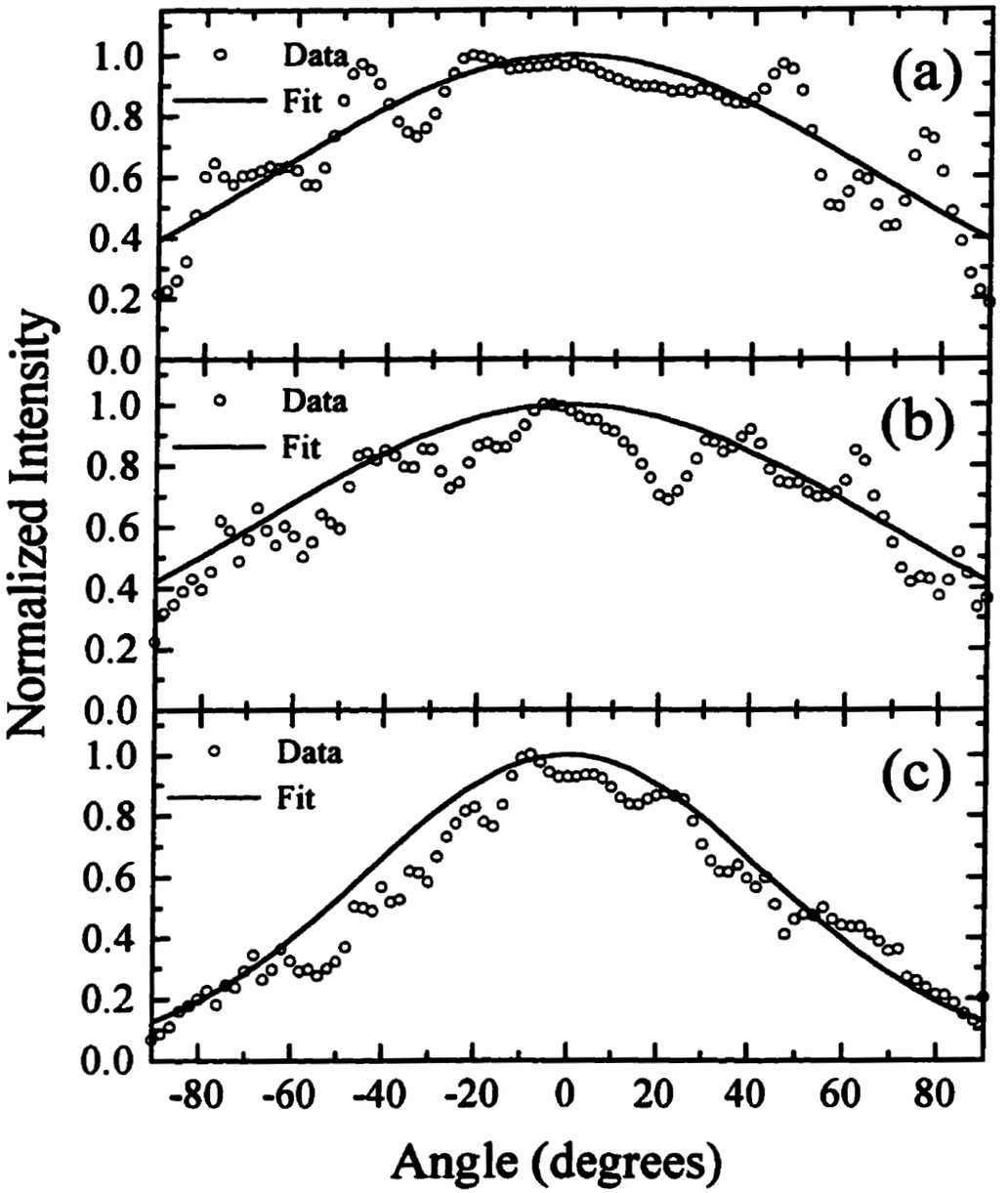

Figure B.2 The angular responses of the 200 μm diameter hydrophone at (a) 1.5 MHz, (b) 2.5 MHz, and (c) 3.5 MHz. The data are indicated by the open circles and the Gaussian fits by the solid curves.

B.2.2 Interference across the hydrophone face

The discussion of the hydrophone interference correction was introduced in Sec. 4.3.3.2.3. Due to the multiple scattering, the intensity displays considerable variation across the sample face, resulting in the well-known phenomenon of speckle (Sec. 5.3). If the *phase* of the detected signal demonstrates significant change over the detector area, then destructive interference occurs and the signal amplitude is decreased. The consequence is a spurious reduction in the total transmission that requires estimation. We have been working under the implicit assumption that the phase is "constant" within a coherence area, and that strong change is only exhibited when moving from one speckle to another. We now quantify the degree to which this is so, and determine the multiplicative factor to apply to the total transmission data to correct for the anomalous signal reduction.

The transmitted ultrasonic field of the multiply scattered sound, arising from a 1.5 MHz planar quasi-cw wave, incident on a 10 mm thick sample composed of the sieved glass beads, was detected with the 200 μm diameter hydrophone. At this frequency, the coherence area, having a diameter about that of a wavelength (Sec. 5.3; see figure 5.15), is five times wider than the detector, so spurious reductions in signal are assuredly minimal. The hydrophone acquired data at 800 positions along a 2.4 cm length of the sample diameter, giving a distance between points of 30 μm. These data were scaled to higher frequencies and the destructive interference and consequent transmission loss ascertained. This first required extracting the phase and amplitude data from all the transmitted ultrasonic fields. Since the data were collected in the steady state mode, this could be

accomplished at any common time. The transmitted field at a particular time t may be represented by

$$S(t) = A\cos(\omega t + \phi), \tag{B.1}$$

where A is the field amplitude, and ϕ the phase. Here, $\omega = 2\pi f$, where f is the frequency of the incident wave. The data [as represented by equation (B.1)] were then multiplied by a sinusoidal reference, given by $R_1(t) = \sin(\omega t)$, and expanded as

$$\begin{aligned} S(t)R_1(t) &= A\cos(\omega t + \phi)\sin(\omega t) \\ &= -\tfrac{1}{2}A\sin\phi + \tfrac{1}{2}A\sin(2\omega t)\cos\phi + \tfrac{1}{2}A\cos(2\omega t)\sin\phi \end{aligned} \tag{B.2}$$

This was repeated, using as a reference $R_2(t) = \cos(\omega t)$, and expanded as

$$\begin{aligned} S(t)R_2(t) &= A\cos(\omega t + \phi)\cos(\omega t) \\ &= -\tfrac{1}{2}A\cos\phi + \tfrac{1}{2}A\cos(2\omega t)\cos\phi + \tfrac{1}{2}A\sin(2\omega t)\sin\phi \end{aligned} \tag{B.3}$$

The resulting signals, represented by equations (B.2) and (B.3), were then digitally low-pass filtered, leaving only the zero frequency components

$$\alpha = \tfrac{1}{2}A\cos\phi, \tag{B.4a}$$

and

$$\beta = -\tfrac{1}{2}A\sin\phi. \tag{B.4b}$$

The phase was thus found from

$$\tan\phi = -\frac{\alpha}{\beta}, \tag{B.5}$$

and the amplitude from

$$A = 2\sqrt{\alpha^2 + \beta^2}. \tag{B.5}$$

The variation in these quantities, for the case under consideration, are shown in figures B.3 and B.4 for a portion of the data. Panels (a) show the variation in amplitude (solid

curves) and phase (dashed curves) as a function of hydrophone position along 5 mm segments of the sample diameter. Though the phase exhibits minimal variation across bright speckles, it *does* vary dramatically in the "dark" regions. This is pointed out more clearly in panels (b), where the rate-of-change of the phase with detector position is contrasted with the amplitude variation. The dramatic phase variations occur where the amplitude is low, implying that the distortion in the total transmission will be minimal even for detectors of finite (but small) area because the major component of the total transmission arises from areas where the phase varies little.

To extract the actual reduction in transmission at higher frequencies (where the wavelengths are shorter), the phase cancellations across the detectors were calculated. Relative to the 1.5 MHz data and the 200 μm diameter hydrophone, higher frequency waves see a hydrophone of larger diameter. The rescaled diameter was given by the ratio of the frequency f in question to that of the 1.5 MHz reference frequency, f_{ref}. The phase and amplitude data at f_{ref} were used to calculate the ratios of the mean intensities from a point detector and the rescaled detector, thus providing the transmission correction factor. The mean intensity from a point detector was found by squaring the amplitude and averaging over the entire detector displacement (800 pixels in 24 mm). The calculation for the rescaled detector was a little more involved. First the data needed to be transformed from one into two dimensions. This was done by assuming, for all points along the detection line, that the variation in amplitude and phase was the same in both orthogonal directions, in essence performing a 90° rotation of the line about itself at each

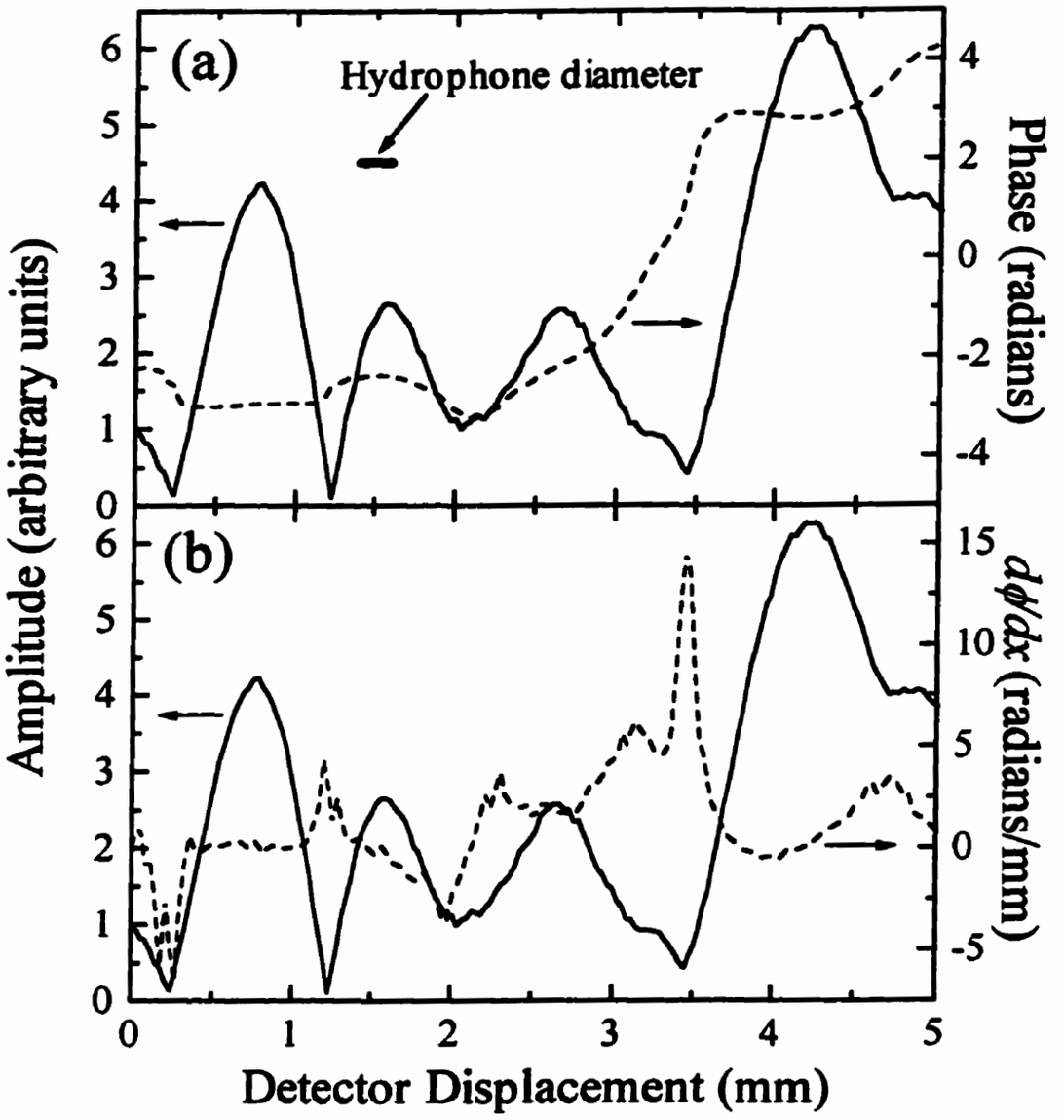

Figure B.3 (a) The amplitude (solid curve) and phase (dashed curve) variation along a 5 mm length of the sample diameter, at 1.5 MHz (L = 10 mm; a = 0.47 mm, sieved beads). (b) The rate-of-change of the phase (dashed curve) as compared to the amplitude variation (solid curve).

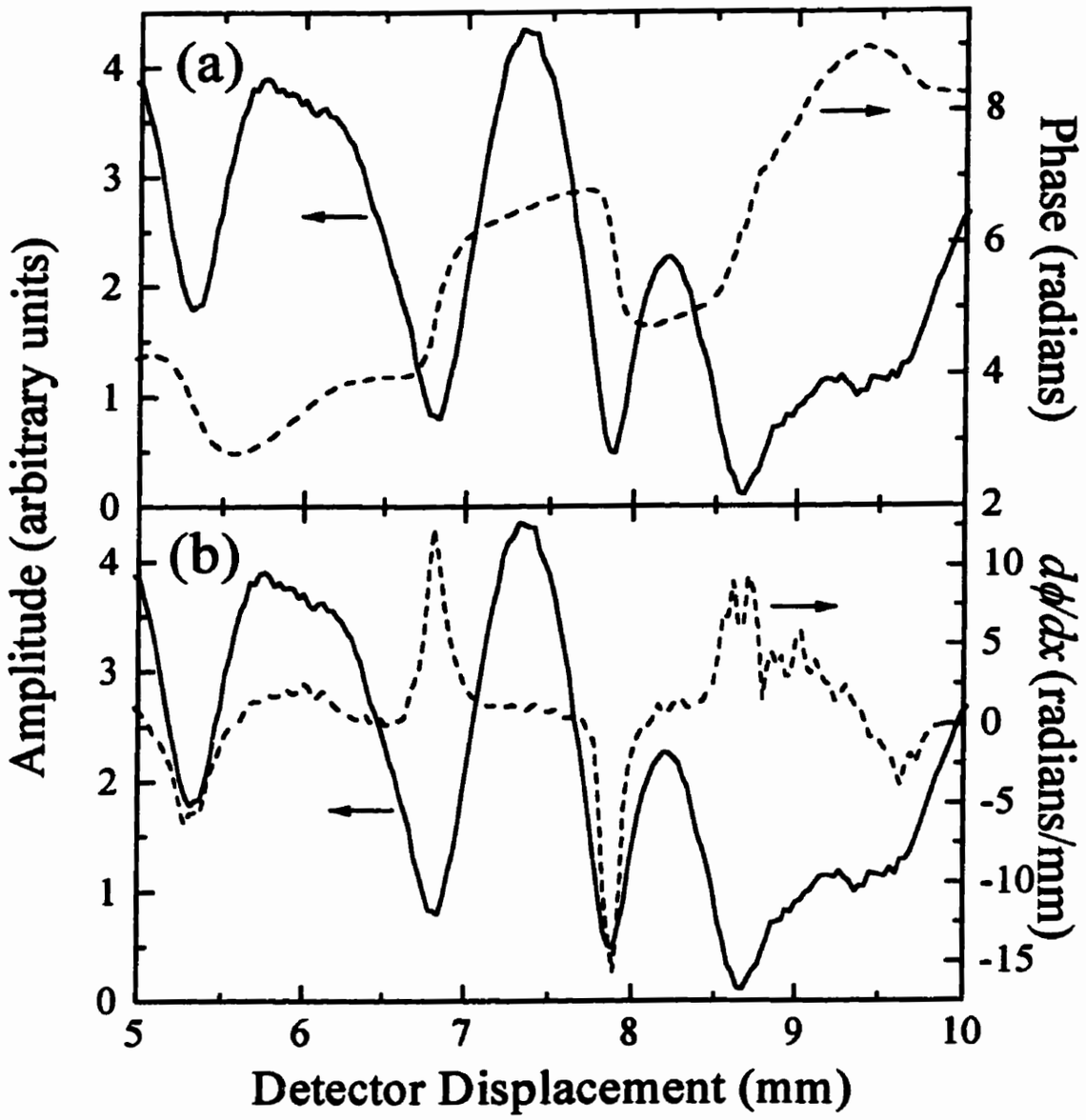

Figure B.4 (a) The amplitude (solid curve) and phase (dashed curve) variation along a further 5 mm length of the sample diameter, at 1.5 MHz (L = 10 mm; a = 0.47 mm, sieved beads). (b) The rate-of-change of the phase (dashed curve) as compared to the amplitude variation (solid curve).

point. While not exact, this assumption suffices to obtain very reliable results since the averaging is performed over many speckles for which the phase variations are similar. The number of pixels to average over was determined as

$$N = \left[\sqrt{\frac{\pi}{4}} \left(\frac{200\mu\text{m}}{30\mu\text{m}} \right) \left(\frac{f}{f_{ref}} \right) \right]^2 , \tag{B.6}$$

where 30 μm is the step size (pixel length), $(200\mu\,\text{m})\left(f/f_{ref}\right)$ the rescaled diameter of the detector, and $\sqrt{\pi/4}$ the correction required due to assuming a square (not circular) detector. The average field across the detector may be represented by

$$\begin{aligned} S(t) &= A\cos(\omega t + \phi_{av}) \\ &= \left(A\cos\omega t\right)\left(\cos\phi_{av}\right) - \left(A\sin\omega t\right)\left(\sin\phi_{av}\right) \\ &= \left(\cos\phi_{av}\right) N^{-1} \sum_{i=1}^{N} A_i \cos(\omega t + \Delta\phi_i) - \left(\sin\phi_{av}\right) N^{-1} \sum_{i=1}^{N} A_i \sin(\omega t + \Delta\phi_i) \end{aligned} , \tag{B.7}$$

where ϕ_{av} is the average phase across the detector, $\Delta\phi_i$ the phase in the *ith* pixel (with respect to the average), A_i the field amplitude in the *ith* pixel, and A the resultant amplitude of the average field. Since equation (B.7) holds for all times t, at $t = 0$ we find

$$A = N^{-1} \sum_{i=1}^{N} A_i \cos(\Delta\phi_i) . \tag{B.8}$$

Squaring equation (B.8) to produce an intensity and then averaging over the entire grid (a strip the width of the detector) gives the total transmission based on a finite detector area. The effect on the 3.5 MHz transmitted intensity, of using a 200 μm diameter hydrophone rather than a "point detector," is illustrated in figure B.5. The dashed curve represents the intensity as a function of the position of a point detector (i.e. no interference), while the

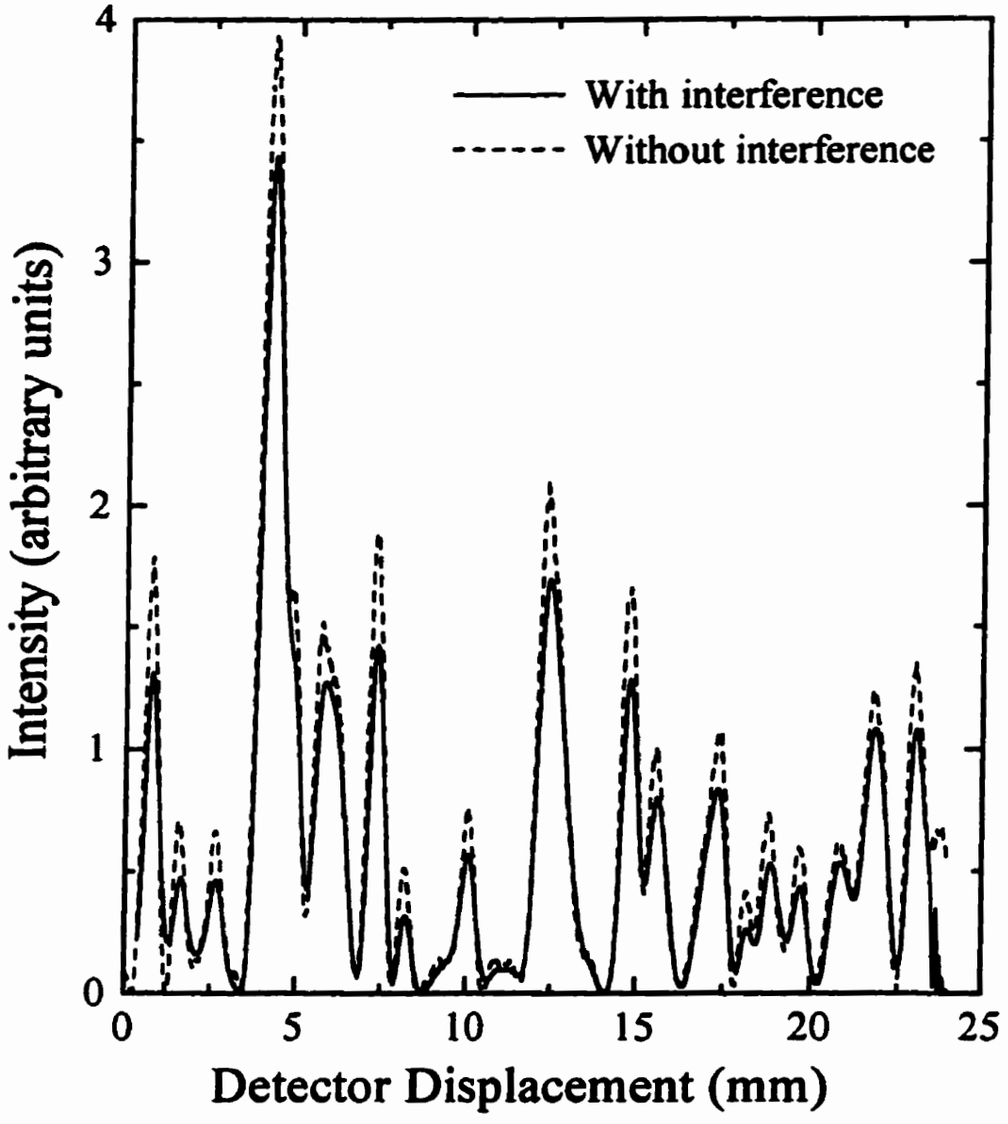

Figure B.5 Effect of finite detector area on the transmitted intensity at 3.5 MHz, based on rescaling the 1.5 MHz transmission data to the higher frequency. The solid curve indicates the spurious reduction in the transmission, due to a 200 μm diameter detector, as compared to that expected for a point detector (dashed curve).

solid curve shows that of the finite detector; 85% of the area under the dashed curve lies beneath the solid curve. The spurious reduction in the transmission for the 1.55 MHz reference data, due to interference across the detector, was estimated to be 4% on the basis of the application of the above procedure to itself. This 4% was added to the transmission ratios at higher frequencies to correct for the slight inadequacy in the reference data. Table B.2 shows the resultant correction factors at various frequencies of interest, assuming a 200 μm diameter hydrophone.

f(MHz)	Correction
1.55	1.04
2.0	1.10
2.5	1.13
3.0	1.17
3.5	1.21

Table B.2 Correction factors for spurious phase cancellation across a 200 μm diameter hydrophone at various frequencies of interest.

B.3 Effect of the input beam distribution

The steady state diffusion theory (Sec. 2.2.7.2) assumes a planar wave arriving at the sample with normal incidence. Although the experimental configuration gives rise to a

good approximation of such a condition (Sec. 4.3.3.1), *absolute* measurements make it crucial to quantify the effect on the transmission due to the departure of the *measured* input beam distribution from that of a planar wave. This is easily done by comparing the calculated transmissions for planar waves and measured distributions, using typical values of the diffusive parameters at each frequency.

The dependence of the incident intensity on the detector position, over a square region 900 cm^2 in area, is shown in figure B.6 for a frequency of 1.55 MHz, a distance of 75 cm away from a 0.64 cm diameter planar transducer, where the detector position is the radial distance from the propagation axis of the incident wave. For convenience, the intensity has been fit to a Gaussian, allowing the integration over the beam distribution to be easily performed when determining the transmission from equation (2.98). Transmissions were calculated for typical square detection grids containing 121 point with nearest neighbour distances of 2 mm. Figure B.7 illustrates the normalized (to the on-axis position) transmission, at a number of different detector positions within the grid, through a sample at 1.5 MHz (using typical values for the parameters), showing conclusively its dependence on the intensity of the incident wave. The solid curve is the fit to the beam distribution (open circles), more fully shown in the previous figure. Note that this curve fits the transmission (solid diamonds) very well. It should be noted that the fit to the input intensity was merely used to *calculate* the transmission so as to allow a comparison between the two; how well a Gaussian function fits the input beam distribution is *not* of importance. This means that normalizing the measured transmission at each point by the incident intensity at that point is equivalent to having a planar incident wave. However,

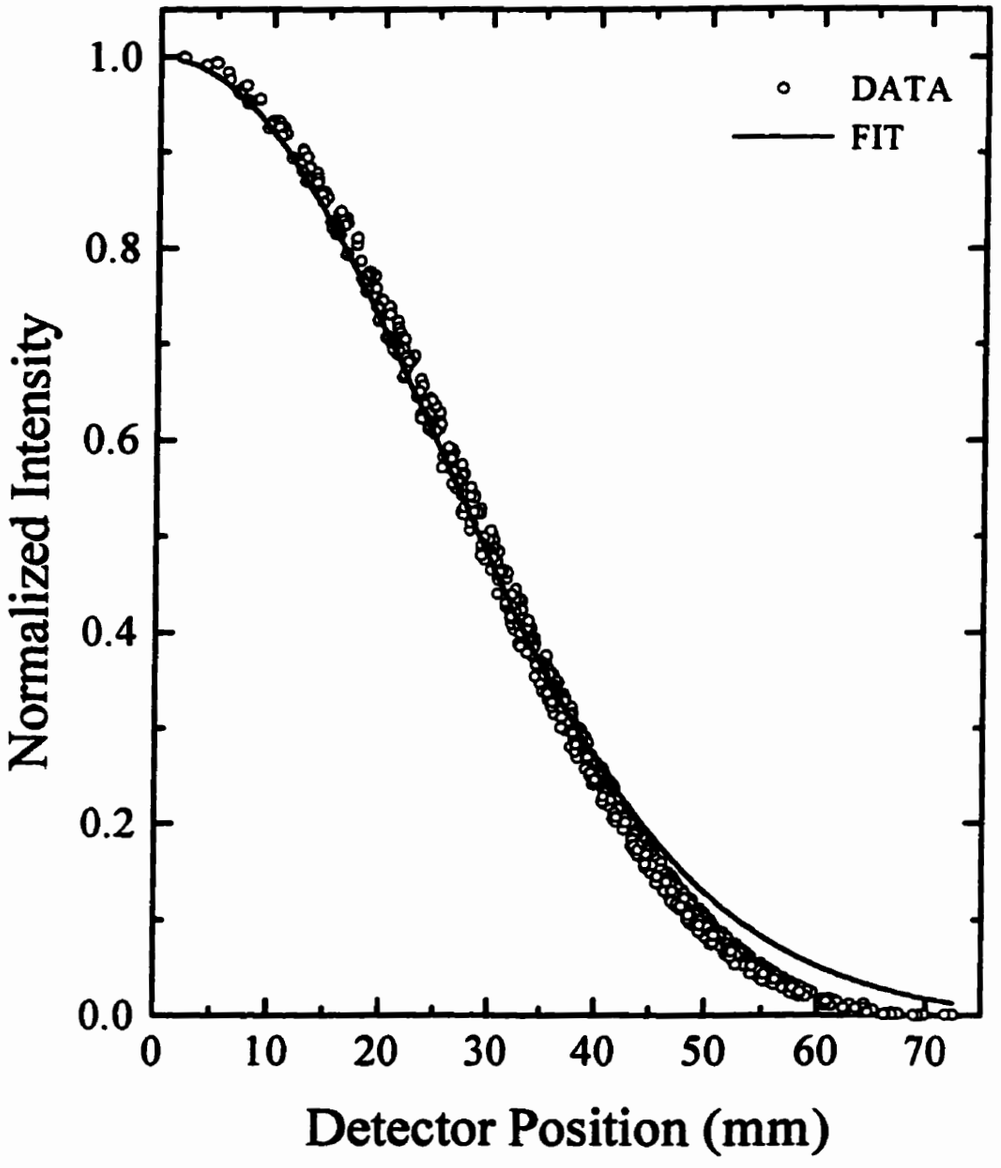

Figure B.6 Variation of the incident intensity at 1.55 MHz, for a 6.4 mm diameter generating transducer 75 cm from the detector. The beam distribution has been fit to a Gaussian for convenience.

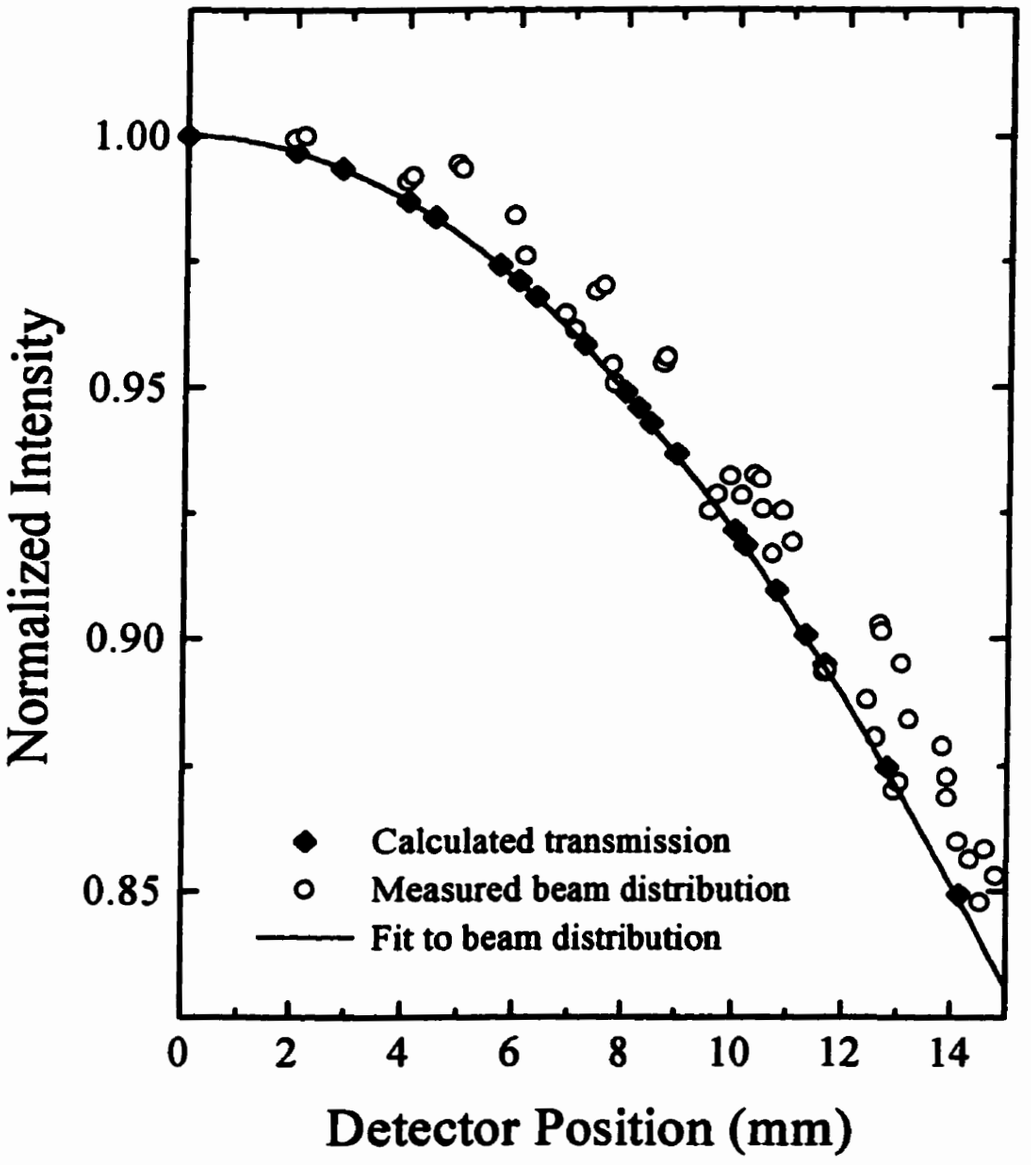

Figure B.7 The calculated transmission at 1.55 MHz, using typical values for the diffusive parameters and normalized to unity on-axis, compared with the measured beam distribution and its fit (figure 5.6).

when one compares the calculated transmission at the on-axis detection position with that calculated for a true planar wave, the latter is still slightly greater, implying that this method of normalizing the data has failed to fully capture the effect of the incident beam distribution. This arises because, within the immediate neighbourhood of any detection point, the mean incident intensity is *lower* than it is at the point itself. Qualitatively, the transmitted intensity is dominated by the incident intensity in the immediate region (circle) around the point since more paths of equivalent length come from the perimeter than from the centre (as long as the paths are not to long). Quantitatively, this correction is given by the ratio of the calculated transmission for a true planar wave to that calculated for the actual beam distribution. This, the smallest of all the corrections considered, varied from 1.02 (at 1.0 MHz, for a 12.7 mm diameter generating transducer), to 1.07 (at 3.5 MHz, for a 6.4 mm diameter generating transducer).

C Further results

C.1 Effect of filtering the diffusive pulse data

In Sec. 5.5.1.3.4, the results of the analysis of the 2.5 MHz point source data were presented for the variation of D and τ_a with z_0 for different sample thicknesses (figure 5.27), allowing a self-consistent value of z_0 to be determined. Unfortunately, such self-consistent determinations of the penetration depth could not be made so reliably at all frequencies. One of the reasons for this was dispersion in the scattered sound, as a consequence of the frequency continuum within the incident pulse due to its finite width. The effects of dispersion can be minimized by filtering the data before the ensemble average is constructed. To illustrate the manner in which consistent values for D and τ_a are achieved, we consider the effect of filtering at a frequency where the dispersion is particularly acute.

Short pulses at a central frequency of 1.55 MHz were transmitted through unsieved glass bead (radius, a = 0.5 mm) samples within the on-axis point source geometry, and the ensemble averaged diffusive pulses obtained, without filtering, for three different sample thicknesses (L = 5.06, 10.3, and 25.4 mm). In figure C.1, the resulting values of D and τ_a, over a range of values of z_0, are shown. The curves through the data (which are guides to the eye) show no common "intersection point" from which to ascertain z_0. Indeed, the findings of diffusion theory show no agreement at *any* value of z_0 for even the maximum permissible uncertainties in D and τ_a. In this regard, the discrepancies in the absorption times found at each thickness are especially large. The ballistic measurements of the intensities (Sec. 5.2) provided the first indication that

filtering was necessary, and subsequently the diffusion coefficient was found to be strongly dependent on frequency (Sec. 5.5.3.2). Consequently, the data were Gaussian FFT filtered (cf. Sec. 5.2.3.1) to reduce the frequency content of the scattered signals. Using a bandwidth of 0.2 MHz, the individual waveforms from each coherence area were filtered before the envelopes and diffusive pulses were found. Figure C.2 (plotted on the same scale as figure C.1) shows the results of repeating the fitting process to again find D and τ_a over a range of values of z_0, and comparison with figure C.1 reveals a significant increase in the consistency of the parameters. The effect of the filtering is seen to be strongly dependent on sample thickness, with the greatest effect occurring for the thickest sample. For values of D and τ_a in the neighbourhood of $z_0 = 1$ mm, D has been reduced by 20% and τ_a by 50% for the 25.4 mm thick sample, but both parameters remain virtually unchanged for the two thinner samples. This behaviour is consistent with the anticipated effects of dispersion, which are exacerbated by increasing the sample thickness. For the thinner samples, the filtering acts to reduce the dependence of D and τ_a on z_0 by flattening the slope of the curves (i.e. the primarily effect is at low or high values of z_0). Thus, in even highly dispersive regimes, filtering the data proves not to be necessary except for the thickest of the samples studied. Figure C.3 indicates the quality of the fits for the 25.4 mm thick sample; the diffusion theory is seen to provide a more accurate fit to the filtered data [figure C.3(b)], especially at early times, than it does for the unfiltered data [figure C.3(a)]. Fitting both the unfiltered and the filtered data at $z_0 = 0.85$ mm results in the reduction of D from 0.33 to 0.27 $mm^2/\mu s$, and in the reduction of τ_a from

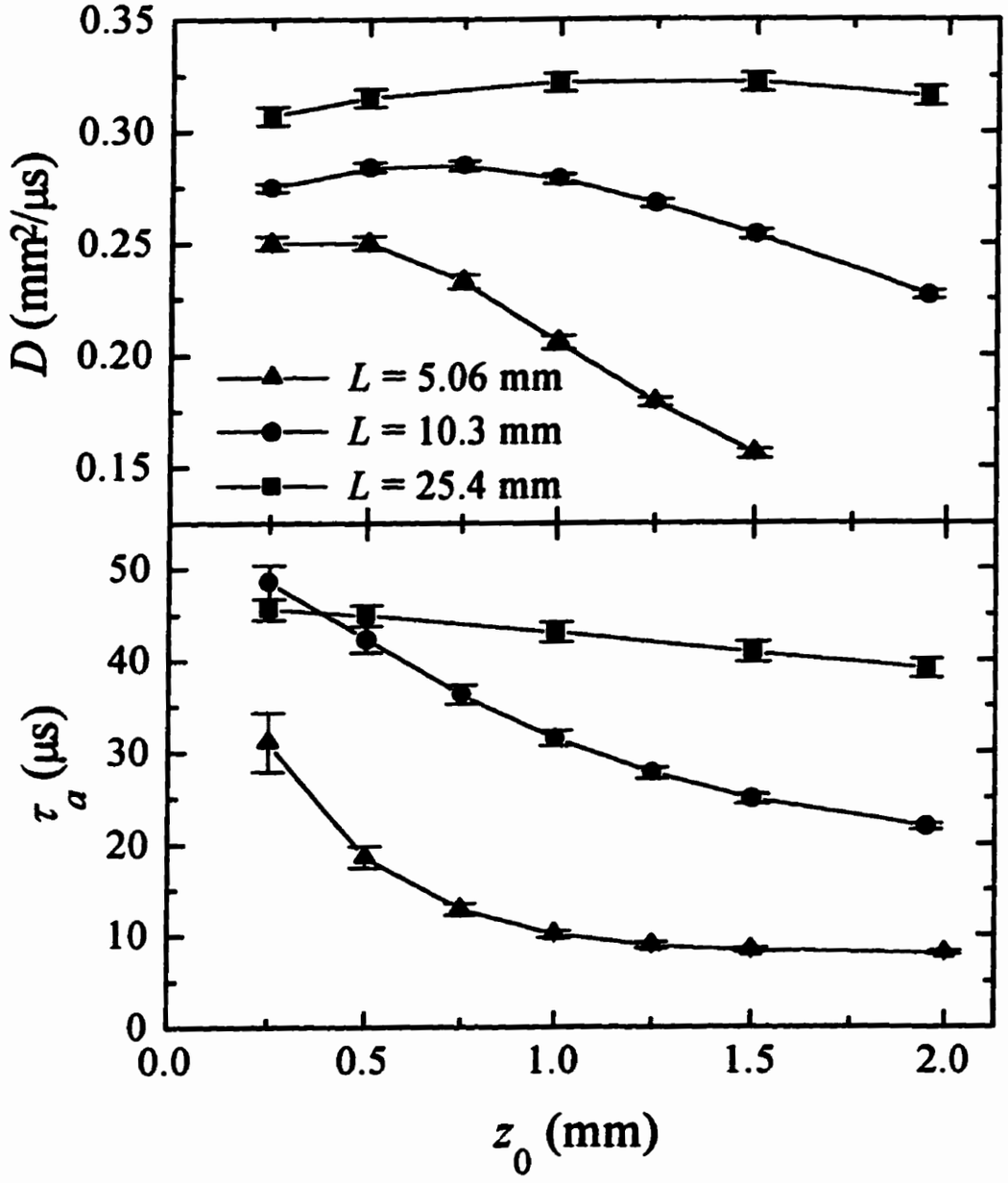

Figure C.1 Dependence of the fitted parameters D and τ_a on the penetration depth z_0, for unsieved glass bead (radius, a = 0.5 mm) samples at three different thicknesses, using unfiltered point-source data at a central frequency of 1.55 MHz.

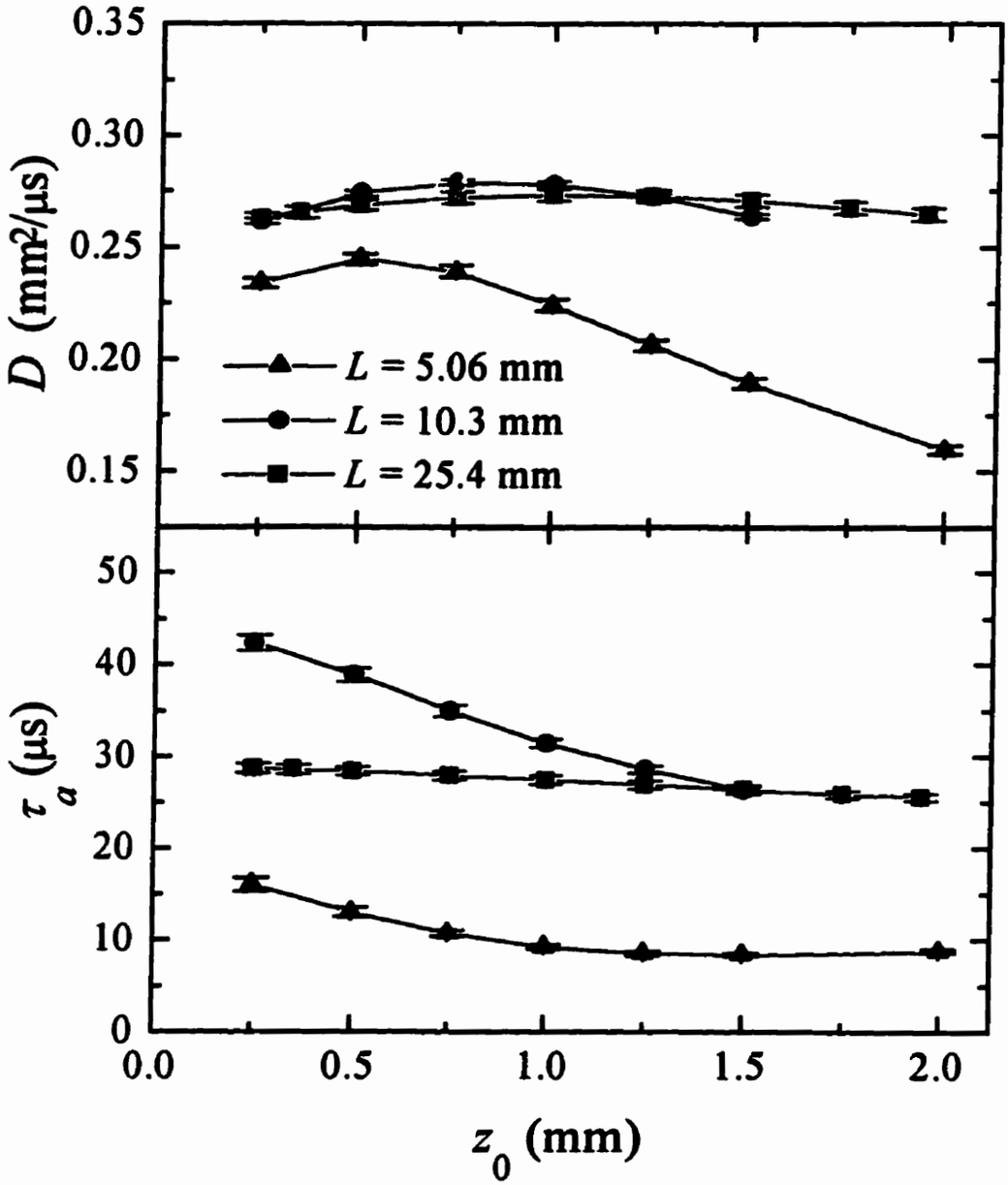

Figure C.2 Dependence of the fitted parameters D and τ_a on the penetration depth z_0, using the same data as for figure C.1, but now filtered at a bandwidth of 0.2 MHz (and central frequency of 1.55 MHz).

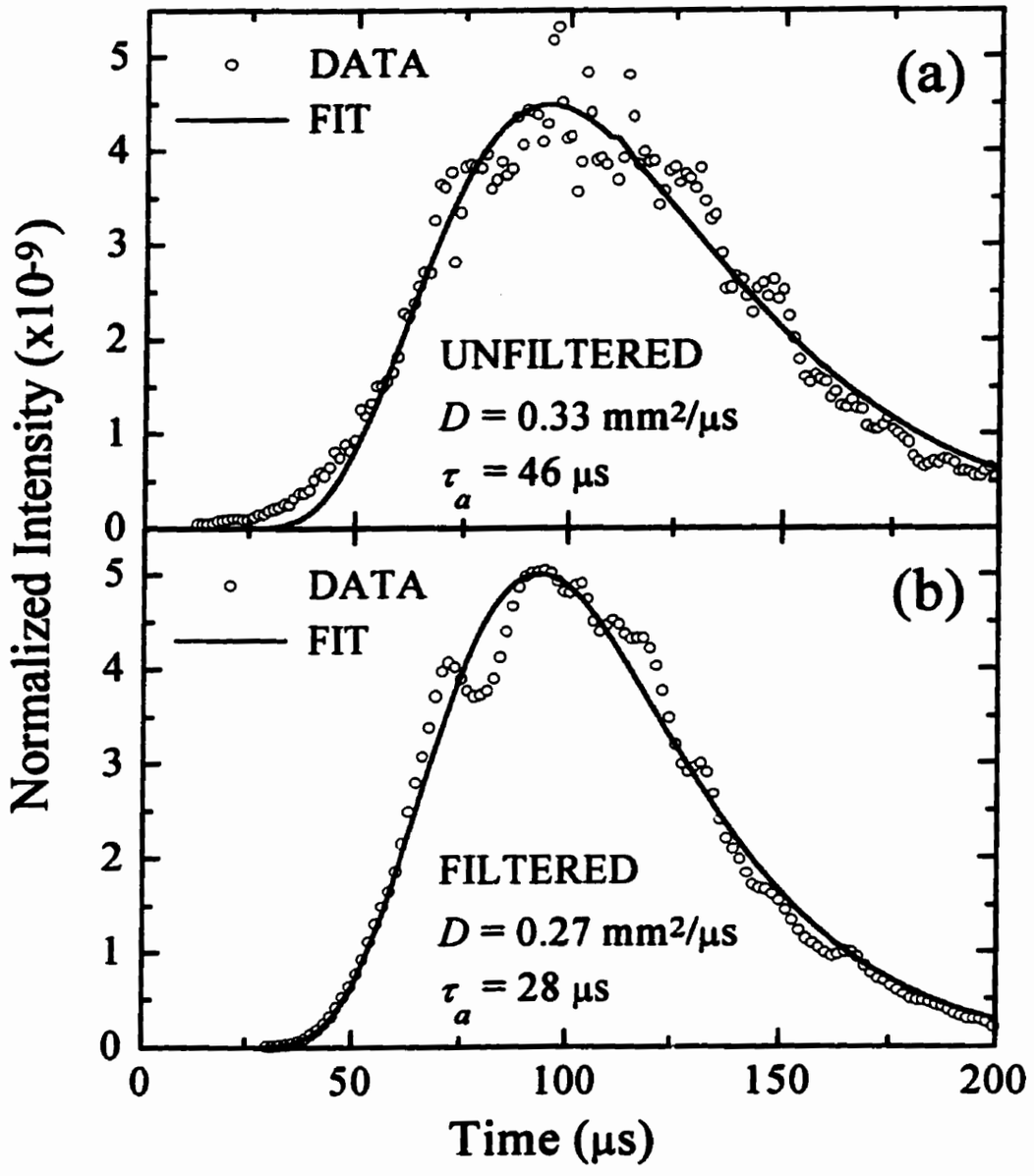

Figure C.3 The diffusive intensities for transmission through the 25.4 mm thick sample at a central frequency of 1.55 MHz: (a) unfiltered data, and (b) filtered data. The smooth solid curves are the best least-squares fits to the diffusion theory at $z_0 = 0.85$ mm.

46 to 28μs, respectively; the latter values are consistent with those found for the 10.3 mm thick sample. Consistency with the 5.06 mm thick sample is not possible without assuming unreasonable uncertainties in the parameters for that sample. The diffusion approximation, however, begins to break down for samples less than about three or four transport mean free paths thick (Zhang *et al.*, 1997). The fitting results for the thinnest sample are thus inherently suspect, as the diffusion approximation may not be accurate at this point. Using only the two thicker samples, the penetration depth may be estimated as $z_0 = 1.0 \pm 0.5\,\mathrm{mm}$. Since $l^* = z_0$ to an excellent approximation, the supposition the diffusion approximation begins to fail for the thinnest sample is plausible. Consistent values for D and τ_a are obtained using the two thicker samples.

C.2 Analyzing the planar diffusive pulse data

The values of D and τ_a obtained by fitting the 1.55 MHz data for a range of z_0 are shown in figure C.4 (free normalization fit) and figure C.5 (fixed normalization fit). For the free normalization fits, the spread of the diffusion parameters shows a dependence on sample thickness similar to that of the point-source data (figure C.1, albeit interpolated to common sample thicknesses); at $z_0 = l^* = 1.2\,\mathrm{mm}$, D varies by 20% (which is excessive), and τ_a by 30%. A large part of this variation may be explained by the different normalization factors ascertained by the fit for each sample thickness. As table C.1 shows, the free normalization parameter varies by a factor of two at 1.55 MHz (for $z_0 = 1.2\,\mathrm{mm}$). Asserting a consistent fixed normalization for all three sample thicknesses,

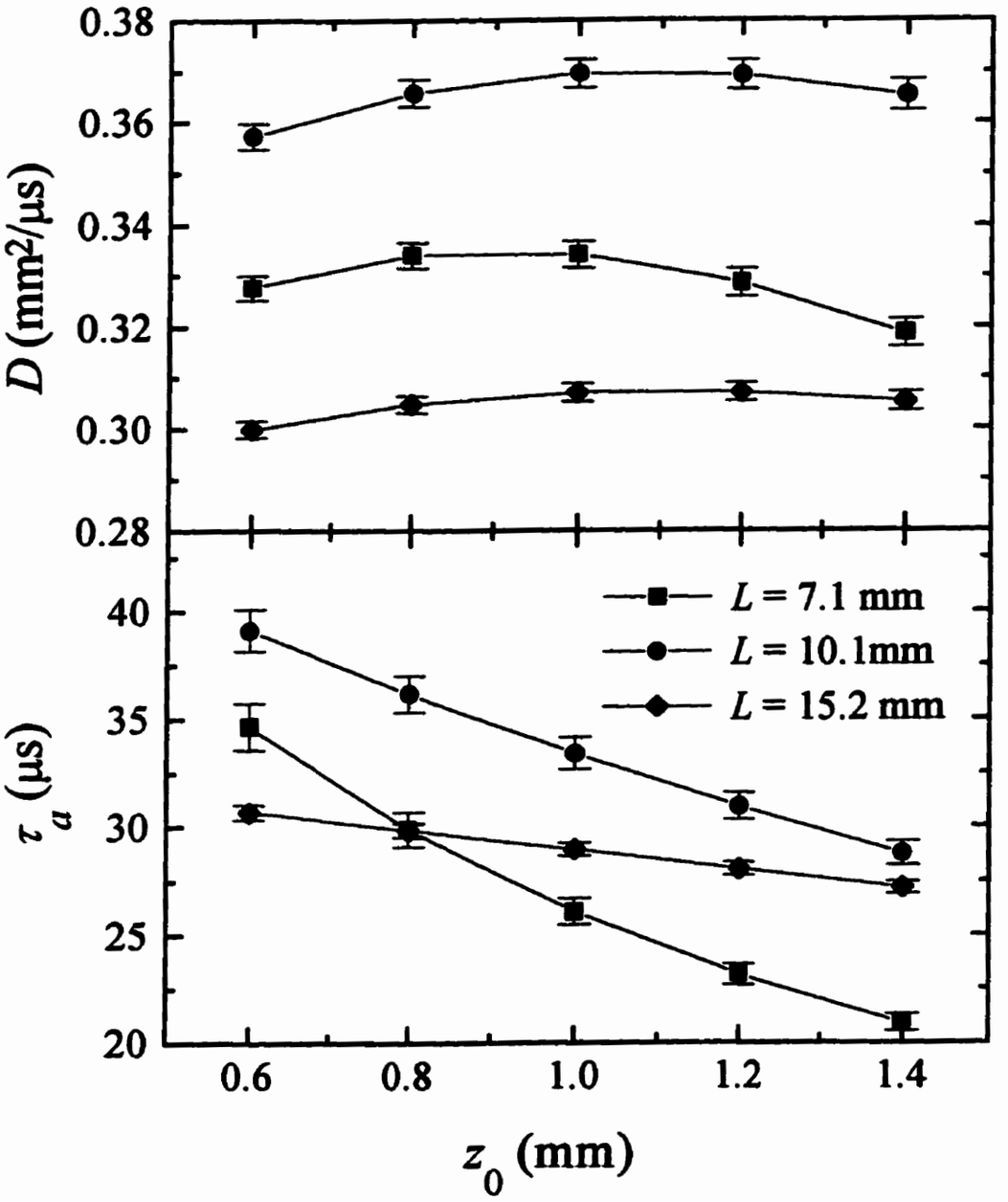

Figure C.4 Dependence of the fitted parameters D and τ_a on the penetration depth z_0, allowing free normalization in the fit, for samples at three different thicknesses, using planar source data at a central frequency of 1.55 MHz.

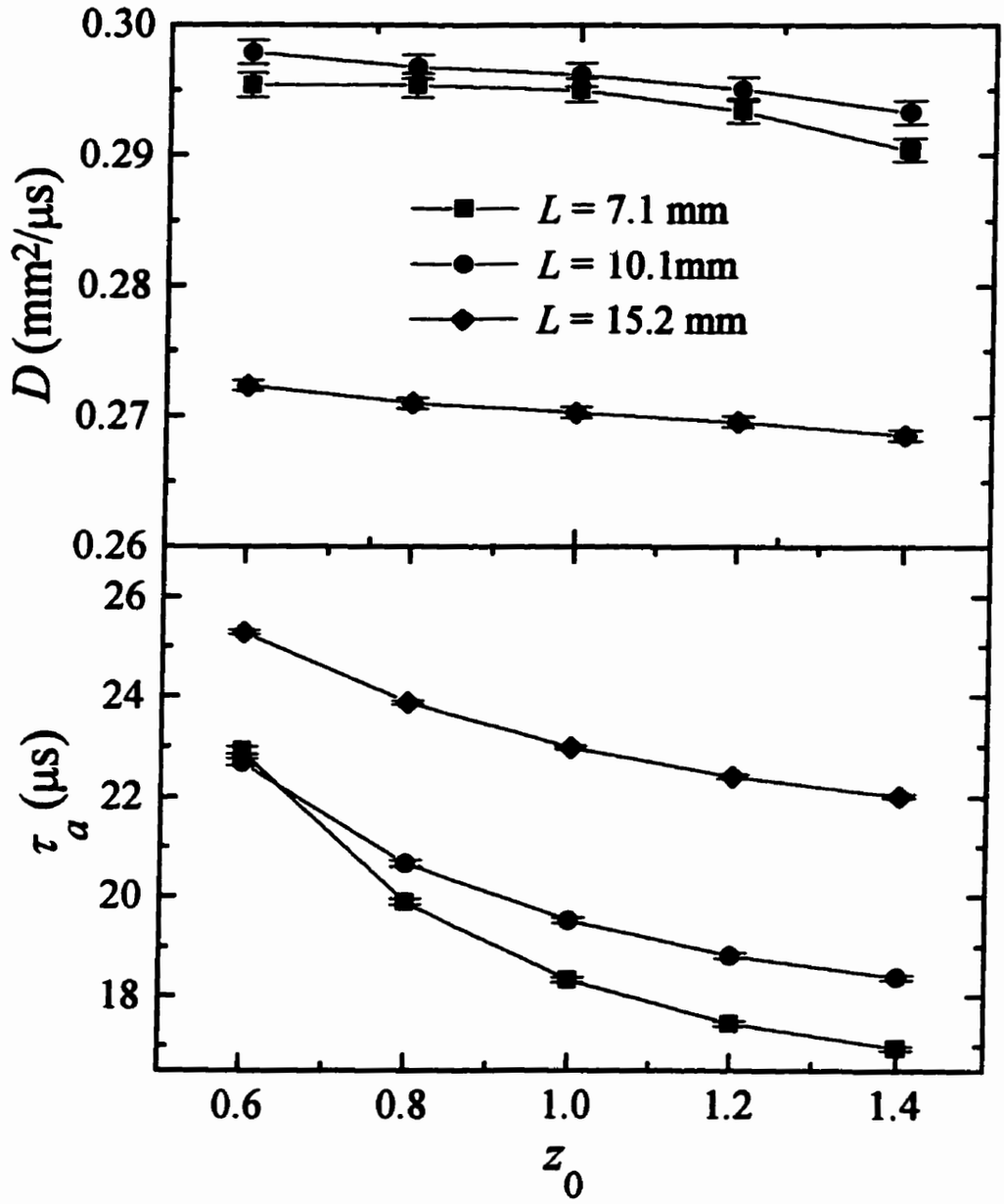

Figure C.5 Dependence of the fitted parameters D and τ_a on the penetration depth z_0, requiring fixed normalization in the fit, for samples at three different thicknesses, using planar source data at a central frequency of 1.55 MHz.

though further lessening the sensitivity of D and τ_a to variations in z_0 (due to changes in the normalization parameter with z_0), also markedly reduces the spread in the fitted values, particularly for D (figure C.5 – note the difference in scale to figure C.4). The effect of the fixed normalization fit is manifested as a distinct decrease in D and τ_a, with the amount dependent upon the magnitude of the departure between the free and fixed normalization factors. Thus the dominant contribution to the reduction in the spread is from refitting the 10.1 mm thick sample.

(a)

	Normalization
f = 1.55 (MHz)	0.256
f = 2.5 (MHz)	0.206
f = 3.5 (MHz)	0.190

(b)

	f = 1.55 MHz	f = 2.5 MHz	f = 3.5 MHz
L = 7.1 mm	0.163	0.463	0.866
L = 10.1 mm	0.088	0.316	0.265
L = 15.2 mm	0.105	0.305	0.320

Table C.1 (a) Fixed normalization factors, and (b) free normalization factors, used when fitting the diffusive pulses at three different frequencies.

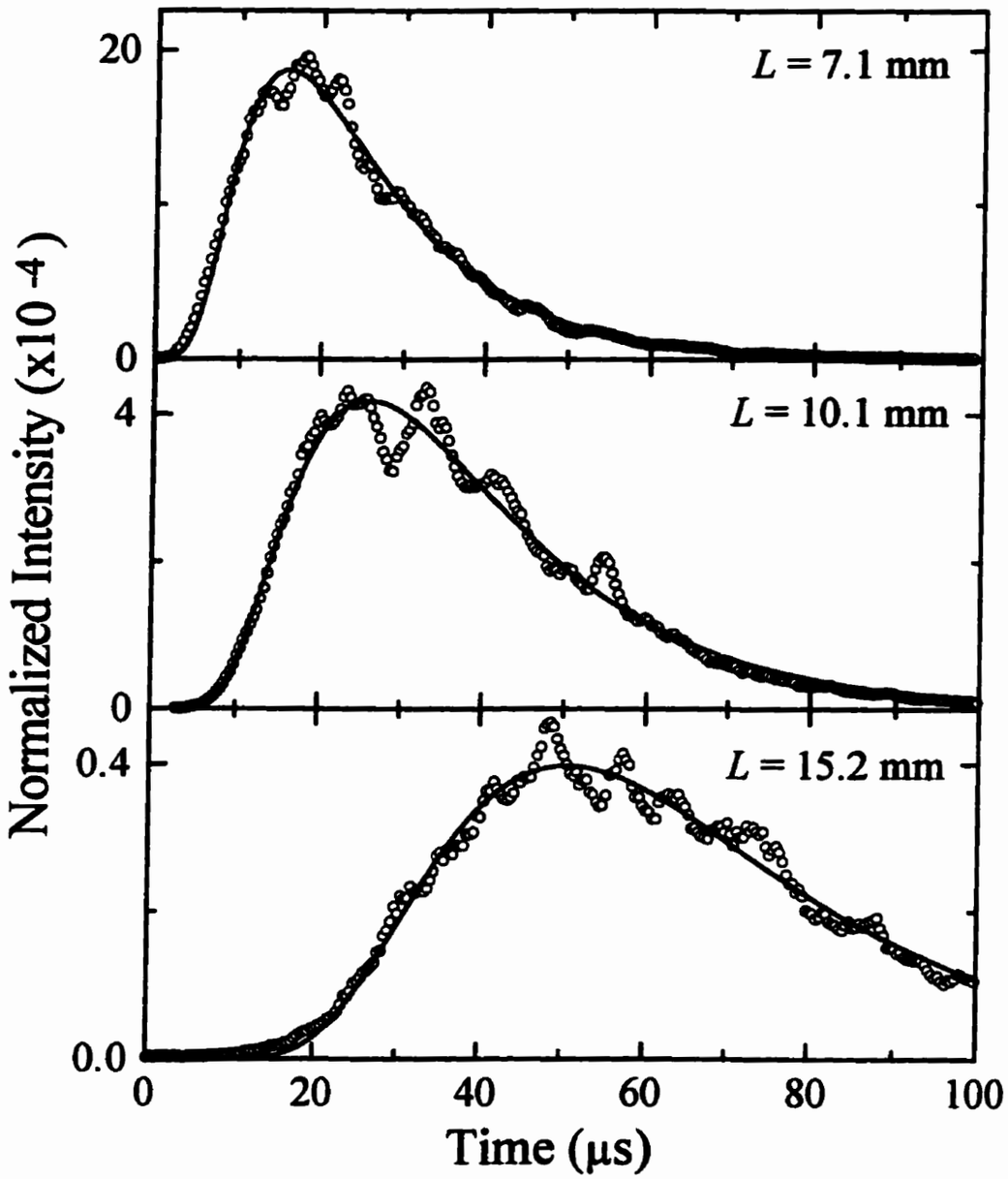

Figure C.6 Time profiles of the normalized ensemble-averaged intensities transmitted as discussed in figure C.4. The open symbols are the data, while the smooth solid curves are the best least-squares fits using *free* normalization, at $z_0 = 1.2$ mm.

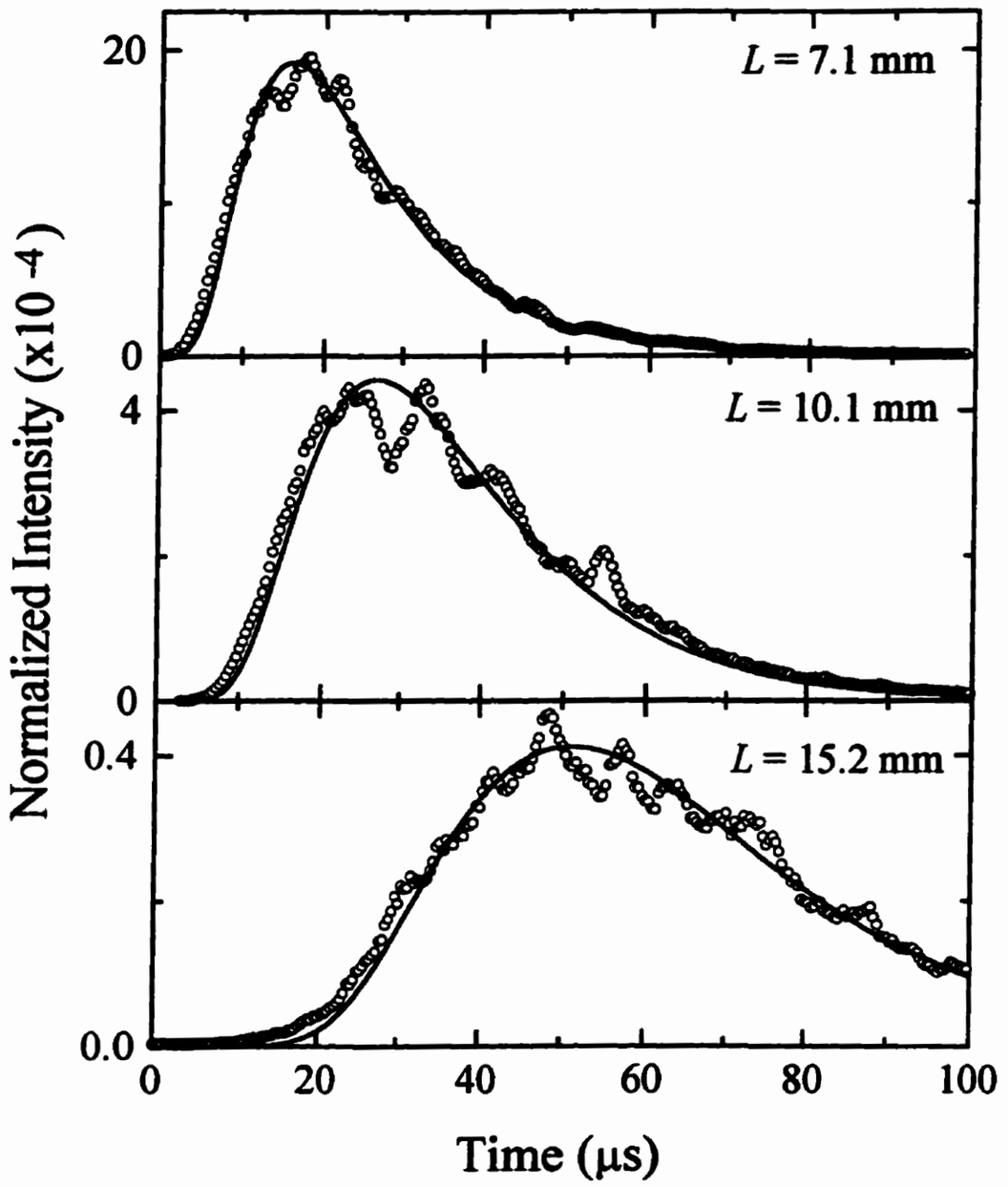

Figure C.7 Time profiles of the normalized ensemble-averaged intensities transmitted as discussed in figure C.5. The open symbols are the data, while the smooth solid curves are the best least-squares fits using *fixed* normalization, at $z_0 = 1.2$ mm.

The quality of the fits, for both free and fixed normalizations, at $z_0 = 1.2\,\text{mm}$, are shown in figure C.6 and figure C.7, respectively, for all three sample thicknesses. The free normalization fits are seen to be excellent, while the fixed normalization fits appear to be less so. The principle effect seems to be an effective displacement of the leading edge to later times, evidenced as a reduction in D. The fixed normalization fits, though acceptable, no longer appear quite as convincing a demonstration of the accuracy of the diffusion approximation as was earlier seen. This appearance is false. The justification for this statement may be found in the dispersive behaviour of D in this frequency range, which was alluded to in Appendix C.1. There, filtering the diffusely transmitted sound resulted in an improved fit with smaller values for D and τ_a (figure C.3). For reasons discussed in Sec. 5.5.3, the effect of filtering was only apparent for the thickest of samples ($L = 25.4$ mm). Comparing the filtered fit with the unfiltered data in figure C.3 produces something not unlike that revealed in figure C.7 for the fixed normalization fits. It is suggested that this similarity betrays a common origin, namely significant dispersion in D. If so, fixing the normalization forces the fit to select the "dominant" diffusion parameters from the "smeared out" diffusive pulse. Whether the precise frequency at which these dominant parameters are selected corresponds to the central frequency of the input pulse depends on the shape of the dispersion, and to a lesser extent, on the frequency dependence of the normalization correction factor.

The discussion of the planar source diffusive data is concluded with the presentation of the behaviour at 3.5 MHz. As was seen in Sec. 5.5.3, the diffusion coefficient exhibits strong dispersion in the neighbourhood of 3.5 MHz ($k_w a \approx 7$), hence

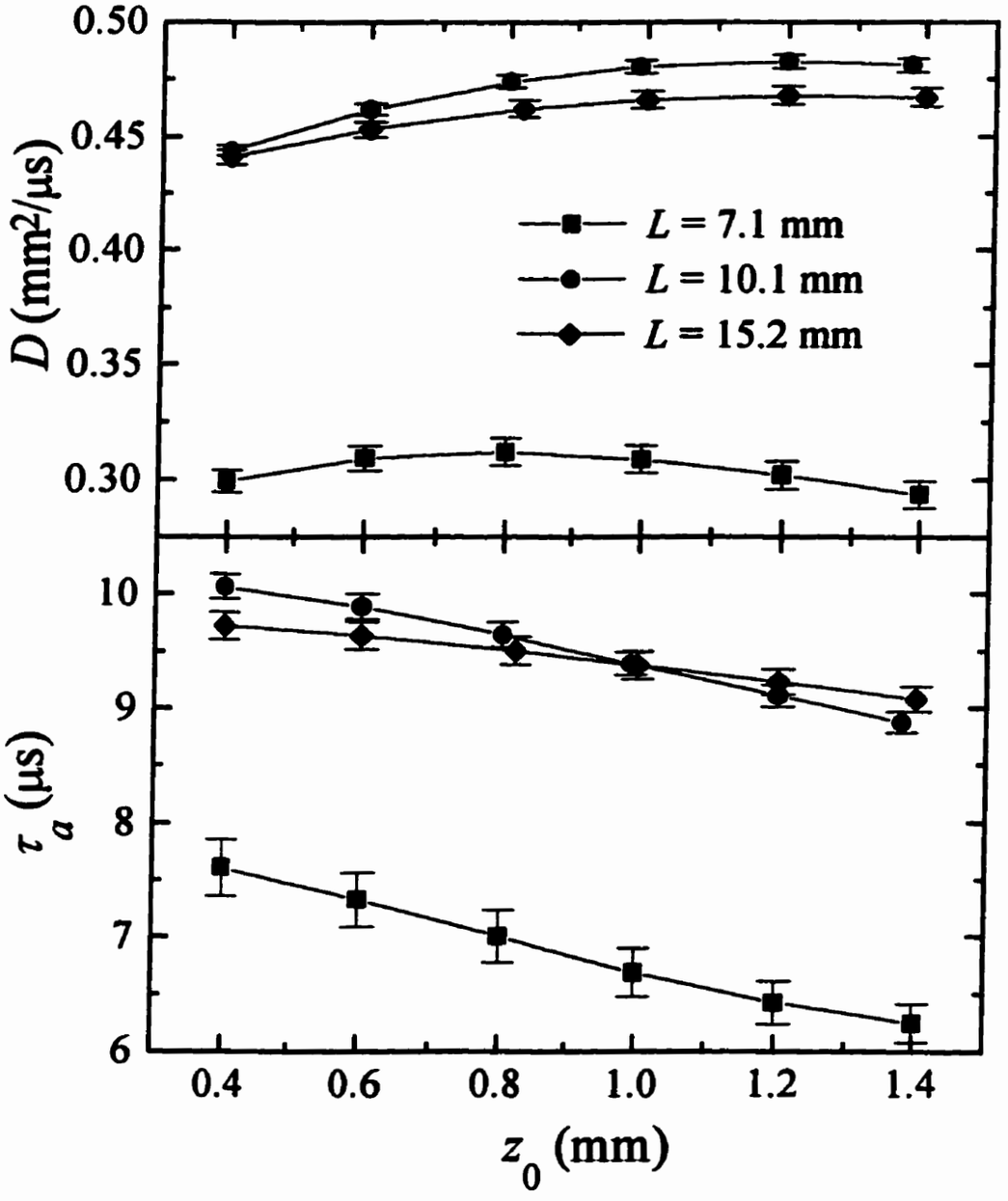

Figure C.8 Dependence of the fitted parameters D and τ_a on the penetration depth z_0, allowing free normalization in the fit, for samples at three different thicknesses, using filtered planar source data at a central frequency of 3.5 MHz.

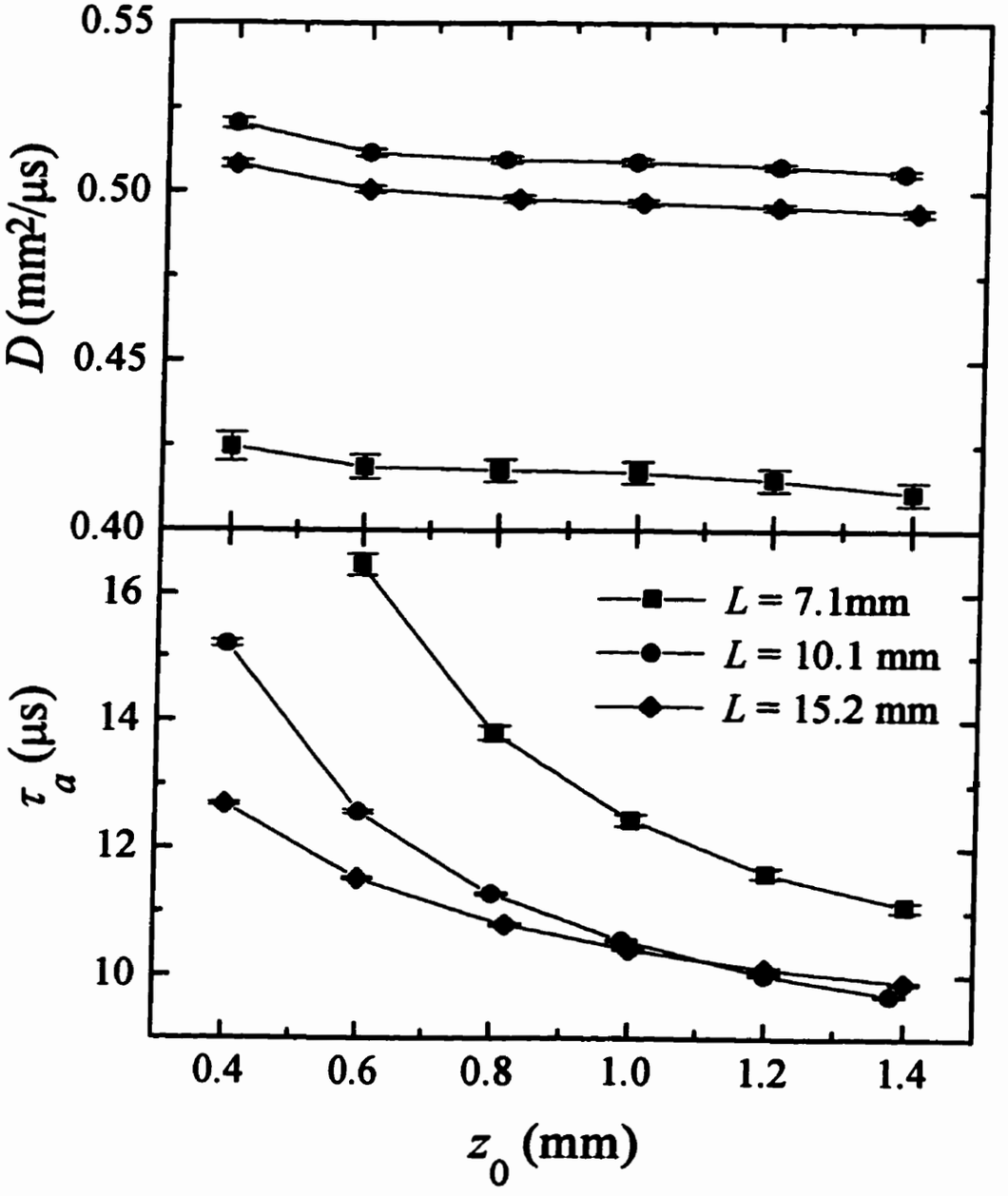

Figure C.9 Dependence of the fitted parameters D and τ_a on the penetration depth z_0, requiring fixed normalization in the fit, for samples at three different thicknesses, using filtered planar source data at a central frequency of 3.5 MHz.

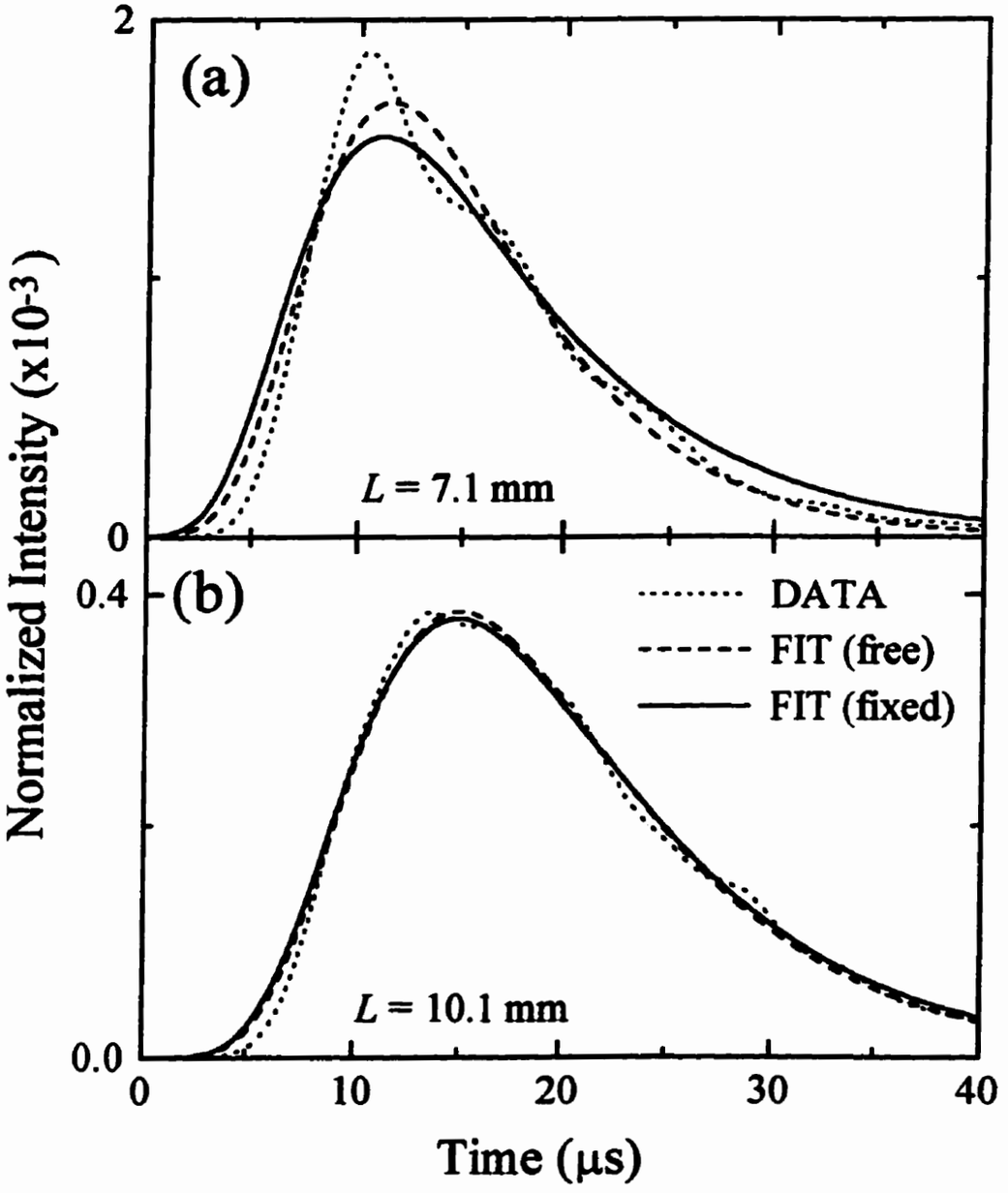

Figure C.10 Comparison of the free and fixed normalization fits, for $z_0 = 1.0\,\text{mm}$, to the diffusive pulse determined from transmission through (a) the $L = 7.1$ mm sample and (b) the $L = 10.1$ mm sample, at 3.5 MHz.

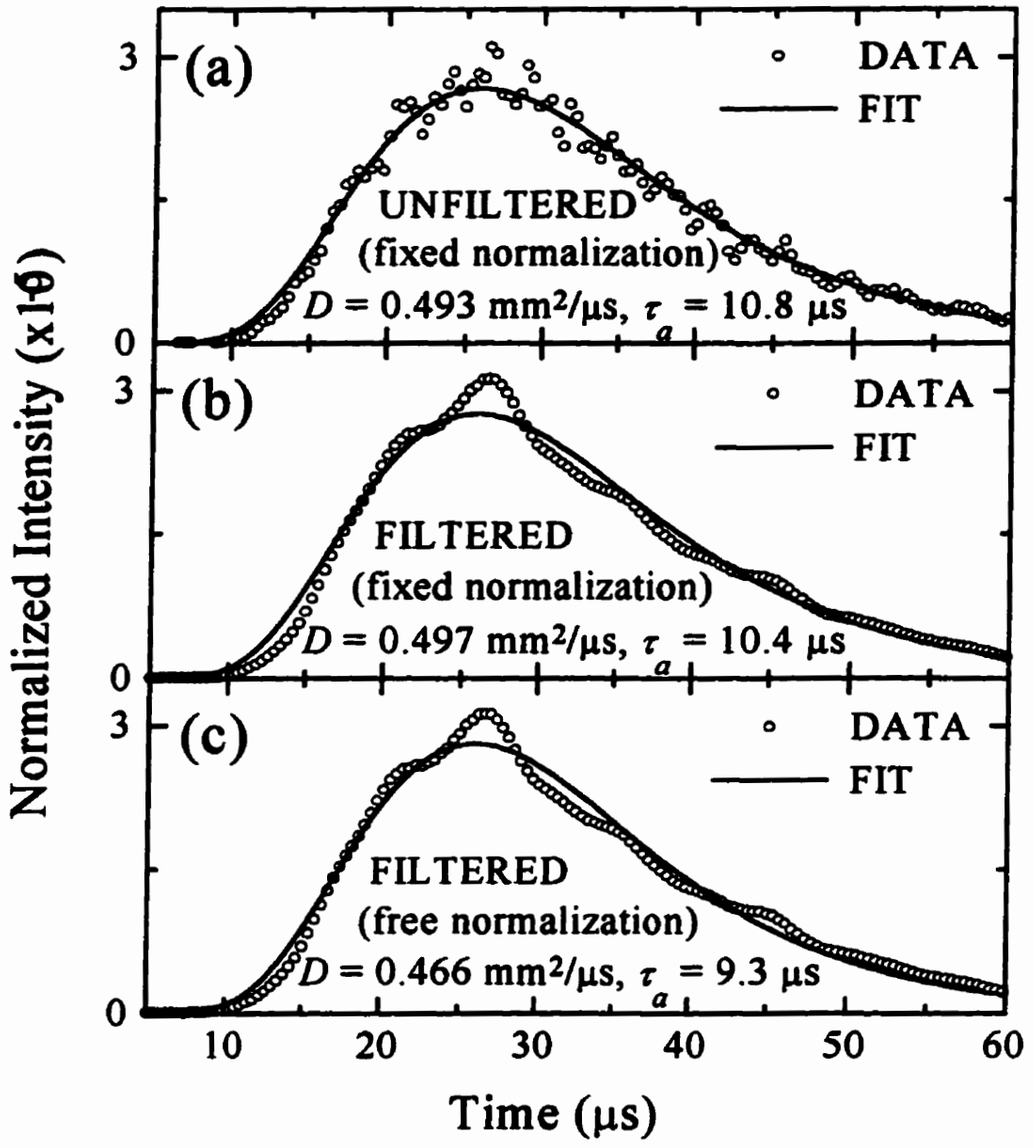

Figure C.11 The diffusive intensities for transmission through the 15.2 mm thick sample at a central frequency of 3.5 MHz. The smooth solid curves, and indicated parameters, are the result of the best least-squares fits to the diffusion theory at $z_0 = 1.0\,\text{mm}$. Comparison of panels (a), (b) and (c) show the effect of filtering the data, and fit normalization.

the decision to filter the data. Unless explicitly stated otherwise, the data presented result from Gaussian FFT filtering the transmitted sound with a 0.2 MHz bandwidth. The values of D and τ_a obtained by fitting the diffusive pulses for a range of z_0 are shown in figure C.8 (free normalization fit) and figure C.9 (fixed normalization fit). Behaviour similar to that noted at 2.5 MHz (Sec. 5.5.1.3.7) is found, with the thinnest sample providing results again inconsistent with those of the thicker samples. Figure C.10(a) and figure C.10(b) compare the free and fixed normalization fits to the diffusive pulse data for the 7.1 mm and 10.1 mm thick samples, respectively, at $z_0 = 1.0\,\text{mm}$. Both the free and fixed normalization fits for the 7.1 mm sample do not agree with the data on the rising edge of the pulse. A systematically low sample thickness, or the presence of air bubbles, has been suggested (Sec. 5.5.1.3.7) to account for the anomalous reduction in D and τ_a. These suggestions do not explain why the free normalization factor is so much larger for the thin sample than for the thicker samples (which are well within a factor of two of the fixed normalizations), namely ~2.2 and ~4.6 times larger at 2.5 MHz and 3.5 MHz, respectively (Table C.1). The fact that the discrepancy in the normalization is worse at 3.5 MHz explains why the fits shown in figure C.10(a) are worse than those shown in figure 5.36. Such behaviour is consistent with the presence of very low bead density regions in the sample (i.e. large water-filled voids), where the scattering is low and the transmission thus increased. However, the position of the rising edge of the diffusive pulse data seems to suggest a small value for D, which would likely be inconsistent [equation (2.65)] with the requirement that l^* must then *increase*. One positive, definitive, statement can be made to conclude this discussion. A significant departure of the free normalization factor from the expected value indicates problems with the sample. Hence, the free normalization

factor may be of some use in material characterization of multiple scattering systems (nondestructive testing applications).

It was earlier noted (Appendix C.1) for the 1.55 MHz data ($k_w a \approx 3$) that filtering was only beneficial for the thickest of samples ($L \approx 25$ mm). Accordingly, to ascertain whether filtering at 3.5 MHz ($k_w a \approx 7$) has had an effect on the quality of the fit and the diffusive parameters found, the diffusive pulse for the L = 15.2 mm sample was determined from the unfiltered data, fit at $z_0 = 1.0\,\text{mm}$, and compared to the filtered results. The unfiltered fit (fixed normalization) is presented in figure C.11(a), and the filtered fit (likewise fixed normalization) in figure C.11(b). Excellent agreement is noted, with the two values for D (as well as τ_a) differing only in the third significant digit. For completeness, the free normalization filtered fit is shown in figure C.11(c). In all three plots, the diffusion theory appears to fit the data tolerably well.

References

Neil W. Ashcroft and N. David Mermin, *Solid State Physics*, W. B. Saunders Company, Philadelphia (1976)

Rama Bansil and Manoj K. Gupta, "Effect of varying crosslinking density on polyacrylamide gels," *Ferroelectrics* **30**, 63-71 (1980)

Yu. N. Barabanenkov and V. D. Ozrin, "Problem of light diffusion in strongly scattering media," *Phys. Rev. Lett.* **69**, 1364-6 (1992)

George I. Bell and Samuel Glasstone, *Nuclear Reactor Theory*, Van Nostrand Reinhold Company, New York (1970)

Philip R. Bevington, *Data Reduction and Error Analysis for the Physical Sciences*, McGraw Hill, New York (1969)

Gouri K. Bhattacharyya and Richard A. Johnson, *Statistical Concepts and Methods*, John Wiley & Sons, New York (1977)

L. Brillouin, *Wave Propagation in Periodic Structures*, Dover, New York (1953)

L. Brillouin, *Wave Propagation and Group Velocity*, Academic Press, New York (1960)

K. Busch, C. M. Souloulis, and E. M. Economou, "Transport and scattering mean free paths of classical waves," *Phys. Rev. B* **50**, 93-8 (1994)

K. Busch and C. M. Souloulis, "Transport properties of random media: a new effective medium theory," *Phys. Rev. Lett.* **75**, 3442-5 (1995)

K. Busch and C. M. Souloulis, "Transport properties of random media: an energy density CPA approach," *Phys. Rev. B* **54**, 893-9 (1996)

H. S. Carslaw and J. C. Jaeger, *Conduction of Heat in Solids*, 2nd ed., Oxford University Press, London (1959)

G. Cwilich and Y. Fu, "Scattering delay and renormalization of the wave-diffusion constant," *Phys. Rev. B* **46**, 12015-12018 (1992)

J. M. Drake and Azriel Z. Genack, "Observation of nonclassical optical diffusion," *Phys. Rev. Lett.* **63**, 259-62 (1989)

D. J. Durian, "Influence of boundary reflection and refraction on diffusive photon transport," *Phys. Rev. E* **50**, 857-66 (1994)

E. N. Economou, *Green's Functions in Quantum Physics*, 2nd ed., Springer-Verlag, Berlin, (1983)

E. N. Economou and C. M. Soukoulis, "Optical localization: calculational techniques and results," in *Scattering and Localization of Classical Waves in Random Media*, Ping Sheng, ed., 404-22 (1990)

Albert Einstein and Leopold Infeld, *The Evolution of Physics*, 2nd ed., Simon & Schuster, New York (1966)

R. J. Elloit, J. A. Krumhansl, and P. L. Leath, "The theory and properties of randomly disordered crystals and related physical systems," *Rev. Mod. Phys.* **46**, 465-543 (1974)

Daniel S. Fisher, Geoffrey M. Grinstein, and Anil Khurana, "The theory of random magnets," *Physics Today* **41** (12), 56-67 (1988)

N.Garcia, A. Z. Genack, and A. A. Lisyansky, "Measurement of the transport mean free path of diffusing photons," *Phys. Rev. B* **46**, 14475-79 (1992)

Azriel Z. Genack, "Optical transmission in disordered media," *Phys. Rev. Lett.* **58**, 2043-6 (1991)

Azriel Z. Genack, *et al.*, p. 23, in *Photonic Band Gaps and Localization*, ed. by C. M. Souloulis, Plenum Press, New York (1993)

J. W. Goodman, "Some fundamental properties of speckle," *J. Opt. Soc. Am.* **66**, 1145-50 (1976)

Akira Ishimaru, *Wave Propagation and Scattering in Random Media, Vol 1*, Academic Press, New York (1978)

John David Jackson, *Classical Electrodynamics*, 2nd ed., John Wiley & Sons, New York, (1975)

Xiaodun Jing, Ping Sheng, and Minyao Zhou, "Theory of acoustic excitations in colloidal suspensions," *Phys. Rev. Lett.* **66**, 1240-3 (1991)

Xiaodun Jing, Ping Sheng, and Minyao Zhou, "Acoustic and electromagnetic quasimodes in dispersed random media," *Phys. Rev. A* **46**, 6513-34 (1992)

Ian P. Jones, "Acoustic correlation spectroscopy of strongly scattering media," *M.Sc Thesis*, University of Manitoba (1996)

M. Kafesaki and E. N. Economu, "Acoustic waves in random media," *Europhys. Lett.*, **37**, 7-12 (1997)

Miles V. Klein and Thomas E. Furtak, *Optics*, John Wiley & Sons, New York (1986)

Eugene Kogan and Moshe Kaveh, "Diffusion constant in a system near resonance," *Phys. Rev. B* **46**, 10636-40 (1992)

A. Kornblit, *nllsq– Non Linear Least Square Fit in C*, Bell Laboratories Technical Memorandum 78-1525-prelim. (1979)

Ad Lagendijk, Rob Vreeker, and Pedro De Vries, "Influence of internal reflection on diffusive transport in strongly scattering materials," *Phys. Lett. A* **136**, 81-8 (1989)

L. D. Landau and E. M. Lifshitz, *Fluid Mechanics*, Pergamon, Oxford (1959)

Melvin Lax, "Multiple scattering of waves," *Rev. Mod. Phys.* **23**, 287-310 (1951)

J. H. Li, A. A. Lisyansky, T. D. Cheung, D. Livdan, and A. Z. Genack, "Transmission and surface intensity profiles in random media," *Europhys. Lett.* **22**, 675-80 (1993)

D. Livdan and A. A. Lisyansky, "Transport properties of waves in absorbing random media with microstructure," *Phys. Rev. B* **53**, 14843-8 (1996)

G. Maret and P. E. Wolf, "Multiple light scattering from disordered media. The effect of Brownian motion of scatterers," *Z. Phys. B* **65**, 409-13 (1987)

Eugen Merzbacher, *Quantum Mechanics*, John Wiley & Sons, Inc., New York (1970)

Roger G. Newton, "Optical theorem and beyond," *Am. J. Phys.* **44**, 639-42 (1976)

J. H. Page, H. P. Schriemer, A. E. Bailey, and D. A. Weitz, "Experimental test of the diffusion approximation for multiply scattered sound," *Phys. Rev. E* **52**, 3106-14 (1995)

J. H. Page, Ping Sheng, H. P. Schriemer, I. Jones, Xiaodun Jing, and D. A. Weitz, "Group velocity in strongly scattering media," *Science* **271**, 634-7 (1996)

Panametrics, *Ultrasonic Transducers for Nondestructive Testing*, Panametrics Inc., Waltham, MA (1993)

Wolfgang K. H. Panofsky and Melba Phillips, *Classical Electricity and Magnetism*, 2nd ed., Addison-Wesley Publishing Co., Reading, Massachusetts (1962)

D. J. Pine, D. A. Weitz, P. M. Chaikin, and E. Herbolzheimer, "Diffusing wave spectroscopy," *Phys. Rev. Lett.* **60**, 1134-7 (1988)

D. J. Pine, D. A. Weitz, G. Maret, P. E. Wolf, E. Herbolzheimer, and P. M. Chaikin, "Dynamical correlations of multiply scattered light," in *Scattering and Localization of Classical Waves in Random Media*, Ping Sheng, ed., 312-72 (1990)

J. W. S. Rayleigh, *The Theory of Sound*, 2nd ed. revised (1894), Dover Publications, New York (1945)

V. M. Ristic, *Principles of Acoustic Devices*, John Wiley & Sons, New York (1983)

H. P. Schriemer, M. L. Cowan, J. H. Page, Ping Sheng, and D. A. Weitz, "Energy velocity of diffusing waves in strongly scatterin media," submitted to *Phys. Rev. Lett.* (1997).

Ping Sheng (ed.), *Scattering and Localization of Classical Waves in Random Media*, World Scientific, Singapore (1990)

Ping Sheng, Xiaodun Jing, and Minyao Zhou, "Beyond the effective medium: quasi modes in disordered media," *Physica A* **207**, 37-45 (1994)

Ping Sheng, *Introduction to Wave Scattering, Localization, and Mesoscopic Phenomena*, Academic Press, San Diego (1995)

A. Sommerfeld, "Uber die fortpflanzung des lichtes in dispergierenden medien: I," *Ann. Phys. (Leipzig)* **44**, 177-202 (1914)

C. M. Soukoulis, S. Datta, and E. M. Economou, "Propagation of classical waves in random media," *Phys. Rev. B.* **49**, 3800-10 (1994)

Meint P. van Albada and Ad Lagendijk, "Observation of weak localization of light in a random medium," *Phys. Rev. Lett.* **55**, 2692-5 (1985)

Meint P. van Albada, Bart A. van Tiggelen, Ad Lagendijk, and Adriaan Tip, "Speed of propagation of classical waves in strongly scattering media," *Phys. Rev. Lett.* **66**, 3132-5 (1991)

Bart A. van Tiggelen, "Multiple Scattering and Localization of Light," *Doctoral Thesis*, University of Amsterdam (1992)

Bart A. van Tiggelen, Ad Lagendijk, Meint P. van Albada, and Adriaan Tip, "Speed of light in random media," *Phys. Rev B* **45**, 12233-43 (1992)

Bart A. van Tiggelen and Ad Lagendijk, "Rigorous treatment of the speed of diffusing classical waves," *Europhys. Lett.* **23** 311-xxx (1993)

M. U. Vera and D. J. Durian, "Angular distribution of diffusely transmitted light," *Phys. Rev. E* **53**, 3215-24 (1996)

Richard L. Weaver and Wolfgang Sachse, "Diffusion of ultrasound in a glass bead slurry," *Theoretical and Applied Mechanics Report No. 742, UILU-ENG-93-6040, University of Illinois at Urbana-Champaign* (December 1993)

Eugene Wigner, "Lower limit for the energy derivative of the scattering phase shift," *Phys. Rev.* **98**, 145-7 (1955)

Zhao-qing Zhang and Ping Sheng, "Wave diffusion and localization in random composites," in *Scattering and Localization of Classical Waves in Random Media*, Ping Sheng, ed., 137-78 (1990)

Z.-Q. Zhang, I. P. Jones, H. P. Schriemer, J. H. Page, D. A. Weitz, and Ping Sheng, "Wave transport in random media: the ballistic to diffusive transition," submitted to *Phys. Rev. Lett.* (1997).

J. X. Zhu, D. J. Pine, and D. A. Weitz, "Internal reflection of diffusive light in random media," *Phys. Rev A* 44, 3948-59 (1991)